polymers

Nano- and Microcomposites for Electrical Engineering Applications

Edited by
Frank Wiesbrock

Printed Edition of the Special Issue Published in *Polymers*

www.mdpi.com/journal/polymers

MDPI

Frank Wiesbrock (Ed.)

Nano- and Microcomposites for Electrical Engineering Applications

This book is a reprint of the Special Issue that appeared in the online, open access journal, *Polymers* (ISSN 2073-4360) in 2016, available at:

http://www.mdpi.com/journal/polymers/special_issues/nano_microcomposites

Guest Editor
Frank Wiesbrock
PCCL—Polymer Competence Center Leoben GmbH
Austria

Editorial Office
MDPI AG
St. Alban-Anlage 66
Basel, Switzerland

Publisher
Shu-Kun Lin

Assistant Managing Editor
Lynn Huang

Assistant Editor
Tian Li

1. Edition 2016

MDPI • Basel • Beijing • Wuhan • Barcelona • Belgrade

ISBN 978-3-03842-292-1 (Hbk)
ISBN 978-3-03842-293-8 (electronic)

Table of Contents

List of Contributors

Valentina Allodi Department of Computer Science, University of Verona, Strada le Grazie 15, 37134 Verona, Italy.

Natascha Andraschek Polymer Competence Center Leoben (PCCL), Roseggerstraße 12, Leoben 8700, Austria.

Sergio Brutti Department of Sciences, University of Basilicata, V.le dell'Ateneo Lucano 10, 85100 Potenza, Italy.

Sheng Chen School of Ocean Science and Biochemistry Engineering, Fuqing Branch of Fujian Normal University, 1 Longjiang Road, Fuqing 350300, China.

Rui Ding College of Environmental Science and Engineering, Fujian Normal University, 8 Shangsan Road, Fuzhou 350007, China.

Catharina Ebner Chair of Polymer Chemistry, Montan University Leoben, Otto-Glöckl-Strasse 2, Leoben 8700, Austria.

Xiaoping Fan College of Environmental Science and Engineering, Fujian Normal University, 8 Shangsan Road, Fuzhou 350007, China.

Michael Feuchter Institute of Material Science and Testing of Polymers, Montanuniversitaet Leoben, 8700 Leoben, Austria; Polymer Competence Center Leoben, 8700 Leoben, Austria.

Martin Fimberger Polymer Competence Center Leoben, Rosseggerstrasse 12, Leoben 8700, Austria; Institute for Chemistry and Technology of Materials, Graz University of Technology, NAWI Graz, Stremayrgasse 9, Graz 8010, Austria.

Ulf W. Gedde Fiber and Polymer Technology, School of Chemical Science and Engineering, KTH Royal Institute of Technology, Stockholm SE-100 44, Sweden.

Marco Giarola Department of Computer Science, University of Verona, Strada le Grazie 15, 37134 Verona, Italy.

Stanislaw M. Gubanski Division of High Voltage Engineering, Department of Materials and Manufacturing Technology, Chalmers University of Technology, Gothenburg SE-41296, Sweden.

Anh T. Hoang Division of High Voltage Engineering, Department of Materials and Manufacturing Technology, Chalmers University of Technology, Gothenburg SE-41296, Sweden.

Ilho Kang Research Center, NEPES AMC, 99 Seokam-ro, Iksan, Chonbuk 54587, Korea.

Roman Kochetov Department of Electrical Sustainable Energy, Delft University of Technology, Mekelweg 4, 2628 CD Delft, The Netherlands; Asea Brown Boveri (ABB) Corporate Research, Segelhofstrasse 1k, 5405 Baden-Daettwil, Switzerland.

Ling Bing Kong School of Materials Science and Engineering, Nanyang Technological University, 50 Nanyang Avenue, Singapore 639798, Singapore.

Dai Soo Lee Division of Semiconductor and Chemical Engineering, Chonbuk National University, Baekjedaero 567, Deokjin-gu, Jeonju, Chonbuk 54896, Korea.

Xiuzhu Lin School of Ocean Science and Biochemistry Engineering, Fuqing Branch of Fujian Normal University, 1 Longjiang Road, Fuqing 350300, China.

Dongming Liu Fiber and Polymer Technology, School of Chemical Science and Engineering, KTH Royal Institute of Technology, Stockholm SE-100 44, Sweden.

Shaohui Liu School of Science, Henan Institute of Engineering, Zhengzhou 451191, China; Key Laboratory of Advanced Civil Engineering Materials of Ministry of Education, Functional Materials Research Laboratory, School of Materials Science & Engineering, Tongji University, 4800 Caoan Road, Shanghai 201804, China.

Zhimin Luo Jiangsu Key Laboratory for Organic Electronics & Information Displays and Institute of Advanced Materials (IAM), Nanjing University of Posts and Telecommunications, Nanjing 210046, China.

Xiuling Ma College of Chemistry and Chemical Engineering, Fujian Normal University, 8 Shangsan Road, Fuzhou 350007, China.

Gino Mariotto Department of Computer Science, University of Verona, Strada le Grazie 15, 37134 Verona, Italy.

Andreas Moser Institute of Material Science and Testing of Polymers, Montanuniversitaet Leoben, 8700 Leoben, Austria.

Michael Muhr Institute of High Voltage Engineering and System Performance, Graz University of Technology, Inffeldgasse 18/I, Graz 8010, Austria.

Maria Assunta Navarra Department of Chemistry, Sapienza University of Rome. P.le Aldo Moro 5, 00185 Rome, Italy.

Petru V. Noţingher Faculty of Electrical Engineering, Electrotechnical Material Laboratory, University Politehnica of Bucharest, Splaiul Independentei 313, Bucharest 060042, Romania.

Love Pallon Fiber and Polymer Technology, School of Chemical Science and Engineering, KTH Royal Institute of Technology, Stockholm SE-100 44, Sweden.

Stefania Panero Department of Chemistry, Sapienza University of Rome. P.le Aldo Moro 5, 00185 Rome, Italy.

Ilona Pleşa Polymer Competence Center Leoben GmbH (PCCL), Roseggerstrasse 12, Leoben 8700, Austria.

Gisbert Riess Chair of Polymer Chemistry, Montan University Leoben, Otto-Glöckl-Strasse 2, Leoben 8700, Austria.

Sandra Schlögl Polymer Competence Center Leoben GmbH (PCCL), Roseggerstrasse 12, Leoben 8700, Austria.

Yuriy V. Serdyuk Division of High Voltage Engineering, Department of Materials and Manufacturing Technology, Chalmers University of Technology, Gothenburg SE-41296, Sweden;Division of High Voltage Engineering, Department of Materials and Manufacturing Technology, Chalmers University of Technology, Gothenburg SE-412 96, Sweden.

Mirko Sgambetterra Department of Chemistry, Sapienza University of Rome. P.le Aldo Moro 5, 00185 Rome, Italy.

Bo Shen Key Laboratory of Advanced Civil Engineering Materials of Ministry of Education, Functional Materials Research Laboratory, School of Materials Science & Engineering, Tongji University, 4800 Caoan Road, Shanghai 201804, China.

Johan J. Smit Department of Electrical Sustainable Energy, Delft University of Technology, Mekelweg 4, 2628 CD Delft, The Netherlands.

Gwang-Seok Song Division of Semiconductor and Chemical Engineering, Chonbuk National University, Baekjedaero 567, Deokjin-gu, Jeonju, Chonbuk 54896, Korea.

Christof Sumereder Institute of Energy, Transport and Environmental Management, University of Applied Science–FH Joanneum, Werk-VI-Straße 46, Kapfenberg 8605, Austria.

Ioannis-Alexandros Tsekmes Department of Electrical Sustainable Energy, Delft University of Technology, Mekelweg 4, 2628 CD Delft, The Netherlands.

Alun S. Vaughan Department of Electronics and Computer Science, University of Southampton, Southampton SO17 1BJ, UK.

Andrea Johanna Wanner Polymer Competence Center Leoben (PCCL), Roseggerstraße 12, Leoben 8700, Austria.

Frank Wiesbrock Polymer Competence Center Leoben, Rosseggerstrasse 12, Leoben 8700, Austria.

Shaomei Xiu Key Laboratory of Advanced Civil Engineering Materials of Ministry of Education, Functional Materials Research Laboratory, School of Materials Science & Engineering, Tongji University, 4800 Caoan Road, Shanghai 201804, China.

Liqun Xue School of Ocean Science and Biochemistry Engineering, Fuqing Branch of Fujian Normal University, 1 Longjiang Road, Fuqing 350300, China.

Celia Yeung Department of Electronics and Computer Science, University of Southampton, Southampton SO17 1BJ, UK.

Jiwei Zhai Key Laboratory of Advanced Civil Engineering Materials of Ministry of Education, Functional Materials Research Laboratory, School of Materials Science & Engineering, Tongji University, 4800 Caoan Road, Shanghai 201804, China.

About the Guest Editor

Frank Wiesbrock received his doctorate at the Technical University of Munich, Germany, in 2003 for his work on metal ß-amino carboxylates under the supervision of H. Schmidbaur. His subsequent biannual postdoctoral stay with U.S. Schubert at the Eindhoven Technical University focused on block copoly(2-oxazoline)s from microwave-assisted synthesis. He worked as a project manager at Chemspeed Technologies AG in Augst, Switzerland, and returned to academia in 2007 as a Marie Curie ToK researcher with T. Calogeropoulou at the National Hellenic Research Foundation in Athens, Greece. Since 2008, he has been an assistant professor/lecturer at the Graz University of Technology, Austria, where he completed his Habilitation in 2012. Currently he is employed as a senior researcher at the Polymer Competence Center Leoben (PCCL), Austria. His research interests comprise microwave-assisted polymerizations, poly(2-oxazoline)s, biopolymers and biocompatible polymers, and nanocomposites for electronic applications.

Preface to "Interdisciplinary Approaches towards Materials with Enhanced Properties for Electrical Engineering"

Frank Wiesbrock

Reprinted from *Polymers*. Cite as: Wiesbrock, F. Interdisciplinary Approaches towards Materials with Enhanced Properties for Electrical Engineering. *Polymers* **2016**, *8*, 307.

The *internationally growing demand for electrical energy* is one of the most prominent triggers stimulating research these days. In this *highly interdisciplinary research area*, electrical engineers, material scientists and chemists collaborate for the design and fabrication of the next generation of high-voltage machinery and electro-technical devices. *Nanocomposites with enhanced thermal conductivity and improved electric properties* are in the center of these joint research activities. Hence, in this Special Issue of the open-access journal *Polymers*, the state-of-the-art research and technology of the area '*micro- and nanocomposites for electrical engineering applications*' has been summarized in three review articles, while the current research trends and the development and characterization of novel materials have been described in eight original research articles.

State-of-the-art of research and technology. The comprehensive review article by Plesa et al. addresses with dedication the *structure-property relationships of composite materials with special respect to their electric properties* and the resulting potential application fields [1]. Originating from the high demands regarding the reliability and lifetime expectance of high-voltage engineering machineries such as generators and transformers, *the mechanical properties of insulating resins and the corresponding micro- and nanocomposites* are of prime importance; this topic has been summarized in the review article by Moser and Feuchter [2], in which epoxy-based resins are discussed in detail. *Mica/epoxy composites* are the most commonly used insulation materials in *high-voltage rotating machines*, and their properties as well as the *possibly occurring failure mechanisms* of the composite material have been described in the review article by Andraschek and colleagues [3].

Novel composites based on epoxy resins or on low-density polyethylene. The preparation as well as the isotropic electrical properties (in the case of additionally present silver nanowires) of *epoxy-based nanocomposites containing in-situ formed silver nanoparticles* was reported by Kang, Lee, and Song [4]. Vaughan and Yeung described the effect of *siloxane-mediated surface functionalization of silica nanoparticles* [5]; the corresponding epoxy-based nanocomposites exhibited breakdown strengths that were increased by approx. 50% compared to the unfilled

epoxy resin. Gubanski et al. reported the *decrease of the direct current conductivity of low-density polyethylene composites* containing inorganic fillers such as magnesium oxide and aluminum oxide [6]. In a subsequent study [7], a *bipolar charge transport model* was employed to investigate this reduction, from which the *reduced charge injection at electrodes* was identified as the most important parameter causing the observed effects.

Materials based on polymers from renewable resources and composites based on (per-) fluorinated polymers. Smit, Wiesbrock et al. reported the synthesis of crosslinkable copoly(2-oxazoline)s from *fatty acids such as castor oil and coconut oil* [8]. The crosslinked copolymers exhibited *electric properties similar to those of polyamides*, which renders them medium insulators. The in-situ preparation of *reduced graphene oxide/carboxymethyl chitosan composites* was described by Luo, Chen, and colleagues [9]. An electrode modified with this composite showed a *high detection performance for bivalent copper ions*. Nanocomposites of *poly (vinylidene fluoride) and cube-shaped surface-hydroxylated $Ba_{0.6}Sr_{0.4}TiO_3$ nanoparticles* were reported by Zhai et al. to show an *increased dielectric constant and improved breakdown strength* compared to the unfilled polymer [10]. Mariotto and colleagues described composites of *Nafion and nano-sized sulfated titanium dioxide* [11], in which they found that the inclusion of 2 wt % of fillers yielded structures that consisted of *filler-rich regions, which were separated by areas of almost pure Nafion*. This structural arrangement does not easily provide any *proton percolation path*, and, hence, a higher resistance was expected for this composite.

In summary, this Special Issue of *Polymers* compiles the current state-of-the-art of research and technology in the area of '*micro- and nanocomposites for electrical engineering applications*' and highlights prominent current research directions in the field. We very much hope that you enjoy reading it.

Acknowledgments: This work was performed in the K-Project PolyComp at the Polymer Competence Center Leoben GmbH within the framework of the COMET-program (Competence Centers for Excellent Technologies) of the Federal Ministry for Transport, Innovation and Technology and Federal Ministry for Economy, Family and Youth. Funding is provided by the Austrian Government and the State Government of Styria.

Author Contributions: Frank Wiesbrock wrote the editorial.

Conflicts of Interest: The author declares no conflict of interest.

References

1. Pleşa, I.; Noţingher, P.V.; Schlögl, S.; Sumereder, C.; Muhr, M. Properties of Polymer Composites Used in High-Voltage Applications. *Polymers* **2016**, *8*, 173.
2. Moser, A.; Feuchter, M. Mechanical Properties of Composites Used in High-Voltage Applications. *Polymers* **2016**, *8*, 260.

3. Andraschek, N.; Wanner, A.J.; Ebner, C.; Riess, G. Mica/Epoxy-Composites in the Electrical Industry: Applications, Composites for Insulation, and Investigations on Failure Mechanisms for Prospective Optimizations. *Polymers* **2016**, *8*, 201.
4. Song, G.-S.; Lee, D.S.; Kang, I. The Effects of in Situ-Formed Silver Nanoparticles on the Electrical Properties of Epoxy Resin Filled with Silver Nanowires. *Polymers* **2016**, *8*, 157.
5. Yeung, C.; Vaughan, A.S. On the Effect of Nanoparticle Surface Chemistry on the Electrical Characteristics of Epoxy-Based Nanocomposites. *Polymers* **2016**, *8*, 126.
6. Hoang, A.T.; Pallon, L.; Liu, D.; Serdyuk, Y.V.; Gubanski, S.M.; Gedde, U.W. Charge Transport in LDPE Nanocomposites Part I—Experimental Approach. *Polymers* **2016**, *8*, 87.
7. Hoang, A.T.; Serdyuk, Y.V.; Gubanski, S.M. Charge Transport in LDPE Nanocomposites Part II—Computational Approach. *Polymers* **2016**, *8*, 103.
8. Fimberger, M.; Tsekmes, I.-A.; Kochetov, R.; Smit, J.J.; Wiesbrock, F. Crosslinked Poly(2-oxazoline)s as "Green" Materials for Electronic Applications. *Polymers* **2016**, *8*, 6.
9. Chen, S.; Ding, R.; Ma, X.; Xue, L.; Lin, X.; Fan, X.; Luo, Z. Preparation of Highly Dispersed Reduced Graphene Oxide Modified with Carboxymethyl Chitosan for Highly Sensitive Detection of Trace Cu(II) in Water. *Polymers* **2016**, *8*, 78.
10. Liu, S.; Xiu, S.; Shen, B.; Zhai, J.; Kong, L.B. Dielectric Properties and Energy Storage Densities of Poly(vinylidenefluoride) Nanocomposite with Surface Hydroxylated Cube Shaped $Ba_{0.6}Sr_{0.4}TiO_3$ Nanoparticles. *Polymers* **2016**, *8*, 45.
11. Allodi, V.; Brutti, S.; Giarola, M.; Sgambetterra, M.; Navarra, M.A.; Panero, S.; Mariotto, G. Structural and Spectroscopic Characterization of A Nanosized Sulfated TiO2 Filler and of Nanocomposite Nafion Membranes. *Polymers* **2016**, *8*, 68.

Properties of Polymer Composites Used in High-Voltage Applications

Ilona Pleşa, Petru V. Noţingher, Sandra Schlögl, Christof Sumereder and Michael Muhr

Abstract: The present review article represents a comprehensive study on polymer micro/nanocomposites that are used in high-voltage applications. Particular focus is on the structure-property relationship of composite materials used in power engineering, by exploiting fundamental theory as well as numerical/analytical models and the influence of material design on electrical, mechanical and thermal properties. In addition to describing the scientific development of micro/nanocomposites electrical features desired in power engineering, the study is mainly focused on the electrical properties of insulating materials, particularly cross-linked polyethylene (XLPE) and epoxy resins, unfilled and filled with different types of filler. Polymer micro/nanocomposites based on XLPE and epoxy resins are usually used as insulating systems for high-voltage applications, such as: cables, generators, motors, cast resin dry-type transformers, *etc.* Furthermore, this paper includes ample discussions regarding the advantages and disadvantages resulting in the electrical, mechanical and thermal properties by the addition of micro- and nanofillers into the base polymer. The study goals are to determine the impact of filler size, type and distribution of the particles into the polymer matrix on the electrical, mechanical and thermal properties of the polymer micro/nanocomposites compared to the neat polymer and traditionally materials used as insulation systems in high-voltage engineering. Properties such as electrical conductivity, relative permittivity, dielectric losses, partial discharges, erosion resistance, space charge behavior, electric breakdown, tracking and electrical tree resistance, thermal conductivity, tensile strength and modulus, elongation at break of micro- and nanocomposites based on epoxy resin and XLPE are analyzed. Finally, it was concluded that the use of polymer micro/nanocomposites in electrical engineering is very promising and further research work must be accomplished in order to diversify the polymer composites matrices and to improve their properties.

Reprinted from *Polymers*. Cite as: Pleşa, I.; Noţingher, P.V.; Schlögl, S.; Sumereder, C.; Muhr, M. Properties of Polymer Composites Used in High-Voltage Applications. *Polymers* **2016**, *8*, 173.

1. Introduction

In the last two decades, the design of composite materials comprising either micro-scaled or nano-scaled inorganic particles has gained increased attention in

power and high-voltage engineering [1–8]. Particularly, the use of micro- and nanotechnologies offers new approaches towards improved insulation systems that operate at higher temperatures and electrical stress. Along with material performance, basic research and development of "advanced" materials in the field of polymer base composites also pursue energy-efficient and low cost manufacturing routes in order to bring new material concepts into marketable products [1].

Composite materials typically consist of two or more components that comprise significantly different physical and/or chemical properties. Due to the controlled combination of the components, new materials are obtained with distinct properties from the individual components [2]. If at least one of the components has nanometric dimensions, these materials are termed nanocomposites [3]. In Reference [3] a nanocomposite is defined as "a multiphase solid material where one of the phases has one, two or three dimensions of less than 100 nanometers (nm), or structures with repeating distances between the different phases in nanoscale that form the material". Nanocomposites differ from traditional composites in three major aspects: (i) they contain a small amount of filler (usually less than 10 wt % *vs.* more than 50 wt % for composites); (ii) the filler size is in the range of nanometers in size (10^{-9} m *vs.* 10^{-6} m for composites) and (iii) they have tremendously large specific surface area compared to micro-sized composites [4]. Thus, nanocomposites are characterized by distinctive advantages including homogenous structure, no fiber rupture, and optical transparency, improved or unchanged processabillity [4]. Depending on the matrix material, nanocomposites can be classified in three major categories: ceramic matrix nanocomposites, metal matrix nanocomposites and polymer matrix nanocomposites [5]. In Reference [4], polymer matrix nanocomposites are considered as "polymers in which a small amount of nanometer size fillers ($\leqslant$ 10 wt %) is homogeneously dispersed".

Composite materials are typically desired to be employed instead of traditional materials due to their enhanced materials performance involving high strength, toughness, heat resistance, light weight, impermeability against gasses, thermal endurance and stability in the presence of aggressive chemicals, water and hydrocarbons, high resistance to fatigue and corrosion degradation, re-processing recyclability and less leakage of small molecules such as stabilizers, *etc.* [4]. In particular, in the field of plastic engineering, composite materials are selected as a function of Young's modulus *versus* density or yield strength *versus* density [4]. For numerous applications in automotive, aircraft or maritime industry, light-weight materials with increased mechanical strength are preferred to be used. The present review addresses polymer based micro- and nanocomposites that are employed in high-voltage applications and gives an overview of electrical, mechanical and thermal properties of composite materials in dependence on the material structures and compositions.

In the power industry, inorganic filler (particularly aluminum nitride (AlN), boron nitride (BN), silicon dioxide or silica (SiO_2), aluminum oxide or alumina (Al_2O_3), titanium oxide or titania (TiO_2), silicon carbide (SiC) and zinc oxide (ZnO), *etc.*) are usually incorporated into electrical insulating polymers to achieve specific electrical, mechanical, and thermal properties [1,6]. As an example, the resistance of nanocomposites to partial discharges and electric treeing enables the design of new insulation systems with enhanced electrical breakdown strength. Beside electrical properties, mechanical strength as well as thermal conductivity play an important role in selected applications such as insulation systems of large electrical machines. In addition, permittivity and dissipation factor are desired to be as low as possible for electrical insulation whilst for capacitors, loss factor should be as high as possible. Flame retardancy is a property desired for cables insulation used in the radiation field in tunnels, while tracking resistance is very important for outdoor insulators [4].

The present study highlights the most recent studies and results concerning micro- and nanocomposites materials used in high-voltage applications and possible future work on these materials as the distinctive advantages of polymer based (nano) composites (*i.e.*, high temperature performance, improved dielectrics, structural properties and designability) offer promising concepts for the next generation of large motors, generators, transformers and other electrical devices, such as coil forms, slot liners and multifunctional components [7] (see Figure 1).

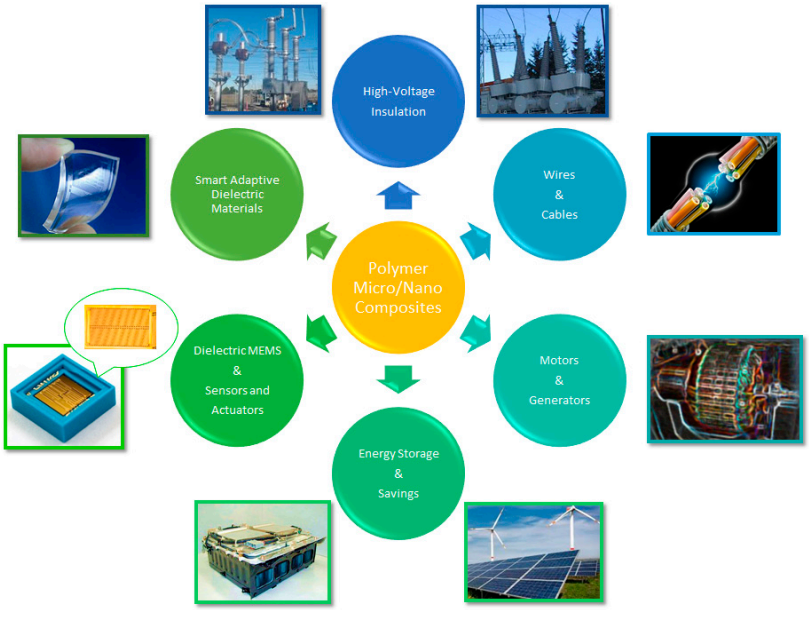

Figure 1. The next generation of high-voltage applications employing polymer based nanocomposites.

2. From Micro to Nanocomposites in Electrical Engineering

In 1987, Ashley described a perspective on advanced materials and the evolution of engineering materials (see Figure 2) [8]. It is obvious that the time scale is non-linear and in 2020, the estimation on materials usage is in a continuous increasing and the rate of change is far faster today than any previous time in history. The rapid rate of change offers opportunities that cannot be ignored by materials scientists, engineers and chemists. As a prominent example, engines efficiency increases at high operating temperatures and this requires high temperature resistant structural materials. However, new materials for rotating machines electrical insulation systems are not only faced by higher operation temperatures, but also by increased electrical, environmental and mechanical stresses. Further examples are nuclear power plants that require advanced materials for electrical equipment which are resistant to low- and high-energy radiations. In addition, developments in optical communication strongly rely on optical fibers that absorb light negligibly and on structural materials that are strong as metals and resist corrosion as plastics.

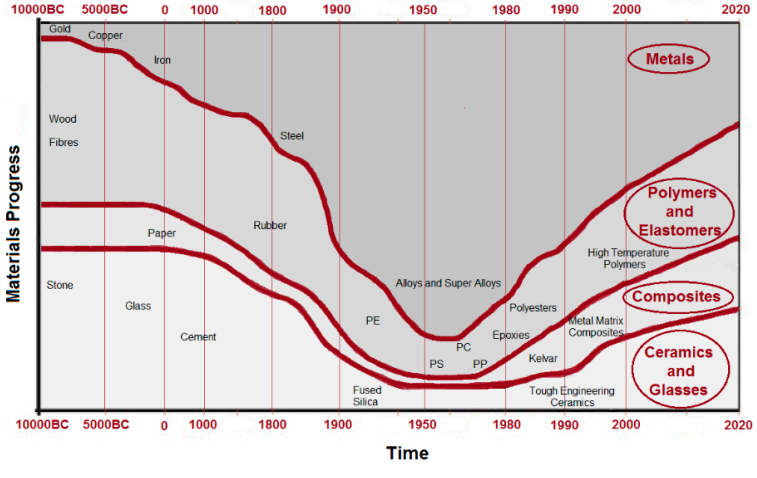

Figure 2. Evolution of the engineering materials (Redraw and adapted figure from [8]).

In electrical engineering, the first insulation systems were composite materials based on natural fibers of cellulose, silk, flax, cotton, wool, asbestos, sand, mica, quartz, *etc.* and natural resins derived from trees, plants, insects and petroleum deposits including pitch, shellac, rosin or linseed oil [9]. The fillers were applied as individual strands for wires and in combined forms as in nonwoven papers and woven cloths. The fact that in the early years of electrical industry, the focus was on renewable materials and trial experimentation to find systems which met

minimum design criteria has to be take into account. Thus, operating temperatures, mechanical and electrical stresses were kept low to accommodate the limitations of these materials [9].

During the First World War, mica splittings were combined with bitumen or asphalts, supported on both sides by a fine grade of cellulose paper. The so-called Kraft paper was formed by muscovite mica splittings bonded with natural shellac [9]. Mica is an inorganic crystalline natural substance occurring commonly in bedrock. Chemically, mica is a complex silicate of aluminum with traces of other elements. The most employed varieties of mica are muscovite ($K_2O \cdot 3Al_2O_3 \cdot 6SiO_2 \cdot 2H_2O$) and phlogopite ($K_2O \cdot 7MgO \cdot Al_2O_3 \cdot 6SiO_2 \cdot 3H_2O$). The structure of mica is complex and consists of silicon atoms layers (placed in the centers of some tetrahedrons formed by oxygen atoms) and aluminum, bounded together by oxygen atoms. Potassium atoms and hydroxyl groups ($-OH$) provide the connections between layers. This structure enables the flakes to be split into thin strips [10]. The thermal endurance of mica is very high. Mica starts to lose its water at a temperature of 500 °C, although some types endure even above 1100 °C. These values are more adequate for electrical machines, since the highest permitted temperatures for their parts are usually above 200 °C at the maximum [10]. Both dielectric strength and surface resistance of mica are high whilst the dielectric losses are low. Mica is characterized by a higher resistance to creepage currents and partial discharges in comparison to the best organic insulators. Taking into consideration all the properties described above, mica is almost a compulsory material in high-voltage electrical machines [10].

Initially, mica was used as insulating material, in the way of small flakes and later for the manufacture of composite materials based on mica with natural (shellac, bitumen, *etc.*) and synthetic (bakelite, epoxy, polyester, *etc.*) resins used for the insulation systems of medium and high power electrical machines. Nowadays, mica is used mainly for mica paper and is composed of extremely small flakes of mica and produced in the same way as paper [11]. The composites were prepared by using a vacuum, impregnation and pressurized process, call also VPI (vacuum pressure impregnation) process and they were employed in groundwall insulation of turbine generator stator coils (see Figure 3) [9].

Micafolium insulation systems were being manufactured in the same time as the asphaltic mica systems and at the beginning, they were applied for sheet wrapping of high-voltage coils and shaped insulating parts. Park [12] synthesized epoxy resin/mica composites and estimated their electrical breakdown, in order to use the composite materials for manufacturing the insulation systems of high-voltage machines. In particular, mica particles with dimensions of 5–7 μm and different concentrations (20, 30 and 40 wt %) were applied. To reduce the composites viscosity, a plasticizer or a low molecular aliphatic epoxy was used [12]. The electrical breakdown strength (measured with a sphere-to-sphere electrodes system) was

increasing by the addition of mica filler and an optimum was achieved for a mica content of 20 wt % [12]. The electrical breakdown strength of the system with an aliphatic epoxy was higher than of the system with a plasticizer [12].

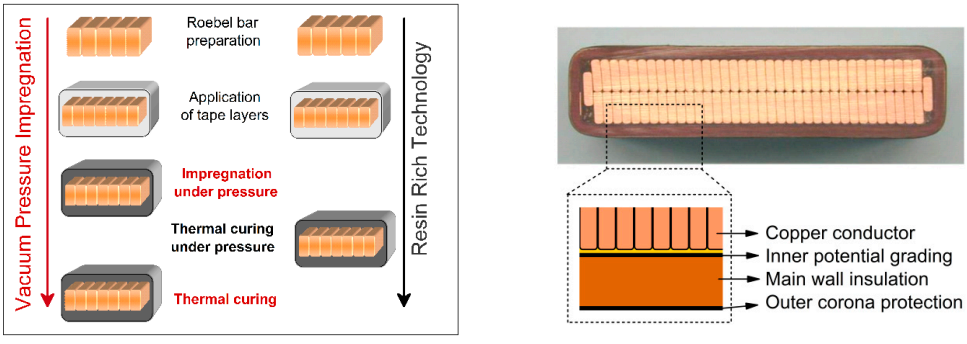

Figure 3. Vacuum pressure impregnation and resin rich processes in manufacturing high-voltage insulation composites of rotating machines stator bars (Redrawn and adapted figure from [13,14]).

The beginning of synthetic products for insulations started in 1908 with phenol-formaldehyde resins, which were used in different electrical applications. Between the 1920s and 1940s, other synthetic products were introduced in the electrical engineering industry, including alkyd resins, aniline-formaldehyde, polyvinyl chloride (PVC), urea-formaldehyde, acrylic, polystyrene (PS) and nylon and melamine-formaldehyde, glass fibers, *etc.*, which lead to an explosion of new applications in electrical insulation. During the 1940s and the 1950s, the availability of numerous types of synthetic polymers and resins increased tremendously. Polyesters and polyethylenes (PEs) were introduced in 1942, fluorocarbons and silicones in 1943, epoxies in 1947 and polyurethane (PUR), polypropylene (PP) and polycarbonate (PC) in the 1950s [9]. In the 1950s, the insulation engineers started to investigate the proliferation of new materials made from synthetic plastic films and, later, polymer fiber based nonwovens were employed for induction motors. Another major development was the replacement of solvent-borne natural and synthetic resins with solventless synthetic resins, such as polyesters, epoxy resins, silicones, acrylates, imides, blends of phenolics and other resins, which make their application more environmentally friendly and less likely to form voids within the insulation systems [9]. Historically epoxy-based composites have been widely used in both, the power as well as the microelectronics industry due to their generally superior electrical, mechanical and thermal properties along with their economical and convenient processability. In power industry, epoxy resin is still the most popular applied material for stator groundwall insulation systems. Epoxy

resins with micro-scaled inorganic fillers (quartz flour) are particularly applied for dry distribution transformers and for voltage and current transformers. Previous work has demonstrated that the properties of epoxy/inorganic filler composites are governed by the chemical nature, physical structure, shape and dispersion of the inorganic filler within the epoxy matrix [1].

The composites industry began to mature in the 1970s, when improved plastic resins and reinforcing fibers (*i.e.*, Kevlar [9]) were developed and since then it has been in a continuous evolution. The first sign of "new materials" was given in the 1990s by Toyota research group that developed the first polymer nanocomposites based on clay and nylon-6 with improved thermal and mechanical performances, for timing belt covers [15].

Although the concept of "nanometric dielectrics" [16] or simply "nanodielectrics" [17] was introduced for the first time in 1994 by Lewis [16], it did not became clear how electrical insulation would benefit by the potential property changes due to nano-sized filler inclusion. Numerous studies regarding electrical phenomena in nanodielectrics, their electrical and thermal properties and the fabrication of different devices and systems with novel properties obtained due to their nanometric structures were achieved [16,18]. In 1988, Johnston and Markovitz [19] showed that some advantages could be obtained for mica-based systems used for the groundwall insulation of the form-wound generators. In 1999 Henk *et al.* [20] made similar investigations on SiO_2 nanoparticles which are improving the voltage endurance of polymer insulation when they are dispersed in polymers. Even so, the potential application of nanodielectrics in the area of high-voltage and power engineering did not draw too much attention from researchers and material engineers until the pioneer experimental work of Nelson and Fothergill *et al.* [21,22]. A series of experimental work was performed in order to obtain a fundamental understanding of the way in which nanoparticles interact in a polymer matrix (especially, epoxy resin) to modify the dielectric properties.

Nanodielectrics analyzed by Fréchette *et al.*, in their work [17], were used to explore nanometric dielectrics and dielectrics associated with nanotechnology and to produce molecularly tailored materials [17]. Starting from these experimental results, intensive work and research has been invested on preparation, evaluation, and characterization of this new generation of materials, called nanodielectrics [23]. The interest in researching nanodielectrics materials has been increased in the last 10 years and different working groups were formed all over the over the world, as CIGRE WG D1.24 who investigated the potential of polymer nanocomposites as electrical insulation [24–26]. The first review articles on the nanodielectrics results was published in 2004 [4,18,27]. The studies suggested that the unique properties of polymer nanocomposites used as dielectrics in high-voltage applications are due to the interfaces, which play a key role in determining dielectric performance.

In addition, several publications indicated that self-assembly is a crucial process in the formulation of nanocomposites [28,29].

The "interfaces" between inorganic fillers and the organic polymers (see Figure 4), such as epoxy resin systems, represent the key to understand the mechanisms and phenomena which control the properties of nanocomposites used as advanced dielectrics [1]. Therefore, interfacial control is critical for achieving good coupling between the inorganic filler and the base polymer. The present goal of the research studies in this field is to optimize these benefits and to provide a better understanding of the physical and chemical structure of the interface region [1]. In this case, there is a promise of new and enhanced properties, which are derived from the interactions between fillers and polymer matrices. Due to the complexity of nano-, meso- and micro-materials interactions, there is a large number of variables to tailor novel properties, which could be interesting for scientists and material engineers [1].

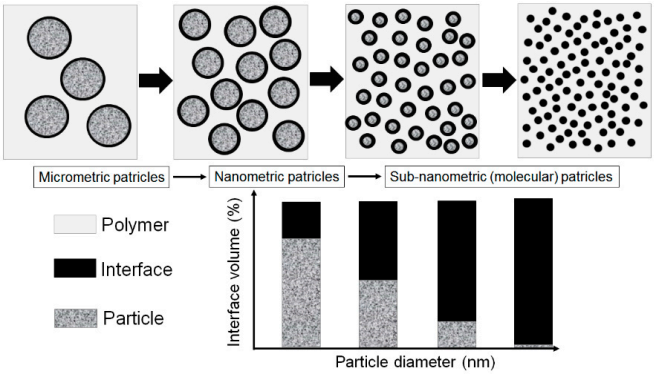

Figure 4. Schematic representation of the ratio particles/interfaces changes with the size of the filler (Redrawn and adapted figure from [30]).

In order to describe the scientific development of micro and nanocomposites electrical features desired in power engineering, the review article is focused on the electrical, mechanical and thermal properties of the insulating materials, especially cross-linked polyethylene (XLPE) and epoxy resins, unfilled and filled with different types of particles. Polymer micro/nanocomposites based on XLPE and epoxy resins are usually used as insulating systems for high-voltage applications, such as cables, electrical machines (especially power generators and motors), dry transformers, *etc.*

3. Nanocomposite Used in High-Voltage Applications

Among properties enhancement, perhaps the most important property of the composites is the change in electric strength that is found when the filler particles attain nanometric dimensions [1]. Recent investigations have shown that the epoxy

based nanocomposites [31] demonstrate some advantages in both mechanical and dielectric properties compared to pure resin systems and epoxy resin composites with micro-fillers at low concentration (1–10 wt %) [4,32,33]. It was found that over a wide range of frequency, the permittivity values of epoxy nanocomposites were reduced significantly compared to the base resin and epoxy micrometer-size filler at lower concentration. It was revealed that the reduction of the permittivity values strongly depends on filler type as well as filler size [33–35]. On the other hand, the presence of nanofillers in epoxy resin affects the space charge accumulation in polymer matrix [26,36–38]. The accumulation of space charge has a huge influence on dielectric properties of insulation systems. Earlier researcher in this field showed that the accumulation of space charge could affect the internal electric field which can present important local intensifications and may lead to partial discharges, electrical treeing and to an early breakdown of the insulation [31,39,40]. Consequently, it is very important to reduce space charge accumulation and its influence on dielectric behavior of insulating materials. Several works revealed that epoxy nanocomposites could accumulate less charge than neat epoxy resins [26,31]. It was also observed that epoxy nanocomposites provide faster charge dynamics, especially for negative charges [41]. Thus, it is important to study the influence of matrices and the chemical structure of fillers on the space charge accumulation in order to avoid and/or reduce their influence on the lifetime of polymer composites used in electrical engineering.

Gröpper *et al.* [42] showed that with the utilization of specially treated spherical SiO_2 nanoparticles as part of the well-approved epoxy-mica stator winding insulation for large electrical machinery it is possible to improve significantly the properties of the high-voltage insulation system. Resistance to partial discharge erosion and electrical treeing is greatly increased and results in a longer lifetime (until electrical breakdown). In addition, the mechanical and thermal properties, which are important for stator windings of large turbine and hydro generators, showed increased values due to the application of nanocomposites [42]. The mica-based impregnating resin includes an epoxy resin/anhydride mixture and nanoparticles filler, as SiO_2 and/or Al_2O_3 modified by a silanizing agent. Further, a method of producing the mica-based impregnating resin is provided, too [43]. To improve the partial discharge resistance, Gröpper *et al.* [44] have used an insulating tape comprises a mica paper and a carrier material that are glued to each other by means of an adhesive The adhesive comprises at least one nanoparticulate filler material and the insulating tape wound about the conductor is impregnated with plastic resin [44].

Nowadays, the topic of interest and technical importance in electrical power generators industry is thermal conductivity of the VPI insulation [1]. In order to improve the performance of a generator or motor, the thermal conductivity of the insulation must be improved for increased thermal power dissipation capability of the stator slot [1]. In order to obtain all these performances, the increase in

thermal conductivity of insulation systems components is very important for the manufacturing process of electrical rotating machines. The improvements of thermal conductivity is generally achieved by the dispersion of high thermal conductive (HTC) particles, such as BN, SiC and Al_2O_3 within a conventional resin [1]. However, for successful approaches in medium and high-voltage electrical insulation, it is necessary to obtain a clear understanding of the influence of particle size and shape distribution and also, the role of the interface between particles and neat resin system on the composite properties.

There are several studies on the improvements of thermal conductivity for high-voltage electrical insulation applications [1]. Lee *et al.* [45] investigated various inorganic fillers including AlN, wollastonite, SiC whisker and BN. Particles with different shape and size were used alone or in combination to prepare thermally conductive polymer composites. With respect to AlN, a titanate-coupling agent was employed for the surface treatment of the inorganic fillers. The application of hybrid fillers resulted in an increase of composites thermal conductivity, which was attributed to the connectivity enhancement offered by structuring fillers. For the same content of filler, the use of larger and surface treated particles has lead to an enhanced thermal conductivity of composite materials. On the other hand, the surface treatment of filler allowed the production of composites with lower coefficient of thermal expansion.

Zweifel *et al.* [46] investigated the potential advantages and uses of submicron and micron-sized fillers (BN, SiC and diamond) for thermal management in reinforced composites applied in electrical insulation systems. Particularly, the effect of type, size, concentration and dimensions of the fillers on the properties (electrical, thermal, mechanical, *etc.*) of reinforced epoxy laminates was determined in detail. It was also found that an improvement of thermal properties of the corresponding composite material could be accomplished whilst a minimal change in the dielectric properties was observed. Zhang *et al.* [1,47] studied the overall thermal conductivity of epoxy resin composites with the addition of selected inorganic fillers (BN, Al_2O_3, SiO_2, diamond). These individual fillers have high thermal conductivity and their average size span the nano to micro dimensions. In order to obtain high thermal conductivity systems, these fillers were used singly or combined with other fillers in the epoxy resins. The results suggest that the size of BN (BN-Micro, BN-Meso and BN-Nano) is not necessary crucial to the thermal conductivity of the epoxy/hardener/filler composites at low to moderate concentrations. In terms of α-Al_2O_3, nano-diamond, nano β-SiC and nano amorphous silicon nitride (Si_3N_4) the results evidenced that the performance of these fillers is not so good as BN regarding the enhancement of the thermal conductivity of epoxy resin composites despite the fillers have comparable or in some cases higher conductivities than BN. Other studies [37,48] were performed on the thermal conductivity of different micro

and nanocomposites containing selected inorganic fillers such as Al_2O_3, AlN and magnesium oxide (MgO). It was observed that the thermal conductivity values of the nanocomposites depend on several factors including interfacial layer structure, dimensions, and specific surface area.

Along with epoxy based thermosetting resins, thermoplastics are another class of polymer materials that are employed in electrical applications. In particular, PE was used as insulating material for medium-voltage and high-voltage energy cables in the early 1970s. After the occurring of massive cable failures due to quality problems and moisture diffusion, insulating systems of cables based on PE were replaced by XLPE. First modern XLPE cables were mainly employed for alternating current (AC) applications due to space charge accumulation purposes, but nowadays the cable technology is sophisticated enough that also high-voltage direct current (HVDC) cables can be in used in service. At the beginning of the HVDC, a general-purpose of cable development was the addition of inorganic filler into the base polymer [49]. However, in the process of adapting the cable to higher voltage application, miniaturization, higher purification and higher distribution of the inorganic filler material were pursued.

First experiments on nanocomposite insulation materials with inorganic nanoparticles distributed uniformly into the polymer matrix were performed, in order to gain advanced properties, such as improved space charge accumulation, volume resistivity, thermal conductivity, direct current (DC) breakdown strength, and lifetime in service of the insulation system. Different types of nanofiller materials were used, such as layered silicate (LS), SiO_2, TiO_2, and Al_2O_3 [50]. An example of the achieved enhancements was described by Lee *et al.* [51], where conventional AC-XLPE, DC-XLPE and nano-DC-XLPE cable insulation materials properties were compared. The volume resistivity and space charge characteristics were investigated. Between AC and DC breakdown strength a factor of more than two was demonstrated whilst the volume resistivity and the electric field loading capacity could be enhanced significantly due to the addition of nanofillers. Regarding AC XLPE cables, voltages up to 550 kV and a rated power up to 1.5 GVA were realized. The cross section of the copper conductor is up to 2500 mm² and a cable length can be 1000 m without joints. At DC XLPE cables, voltages up to 320 kV and a rated power of 1 GVA have been realized as well as cables with a length of several 100 km for subsea projects. For example an Extra High-Voltage (EHV) cable of $\pm$ 320 kV DC was applied for the interconnection between Spain and France. Underground and submarine cables have been in use since the early stages of electricity transmission [52].

High-voltage alternating current (HVAC) underground transmission cables are usually employed in densely populated areas, in submarine connections and, in general, where the implementation of overhead lines is difficult or impossible. Due to the fact that cables are installed out of sight, underground in tunnels, or under

water, they have a reduced impact on the territory and a limited occupation of the soil. Terminal ends are often the only visible evidence for the presence of underground cables. The development of the power cable technology is a rather slow process. Due to the efforts of the cable industry in the recent years, a solid dielectric transmission cable with XLPE insulation is now available.

It is expected that the adoption of this type of cable will give a strong input to the realization of HVAC and HVDC underground transmission lines in the near future. Therefore, the trend towards nanodielectric research comes from the emerging need of power engineers to design new electrical insulation systems that are capable of withstanding higher voltage levels, such as HVAC and HVDC applications [53].

4. Polymers and (Nano)Fillers

4.1. Polymers Used in High-Voltage Applications

The polymer matrix, which can be incorporated into the structure of micro/nanocomposite materials used in high-voltage applications, can be divided into three major categories: thermoplastics, thermosets and elastomers. Polymers are classified in these categories as a function of their different properties, such as physical and chemical structure, thermal characteristics, mechanical and electrical behavior, *etc.*

Thermoplastic polymers are defined as plastics that become moldable above a specific temperature and solidify upon cooling. Typical examples are PE, PP, PVC, linear polyester and polyamides (PAs). Almost 85% from the global polymer production are thermoplastics and in dependence on their transition temperature characteristics, they can be divided into two large classes: amorphous and crystalline [54]. With respect to amorphous thermoplastics, such as PVC and polyamide-imide (PAI), their modulus decreases rapidly above glass transition temperature (T_g), and the polymer exhibits liquid-like properties. Crystalline or semicrystalline thermoplastics, such as low-density polyethylene (LDPE), ethylene-vinyl-acetate (EVA), polyetherketone (PEK), are normally processed above the melting temperature (T_m) of the crystalline phase and the T_g of the coexisting amorphous phase. Their degree of crystallinity is ranging from 20% to 90% and upon cooling, crystallization must occur quickly [54]. The large volume of low cost commodity types, such as PEs, isotactic polypropylene (i-PP), PS and PVC, represents over 70% of the total production of thermoplastics. Polymers such as acetals, PAs, PC, polyesters, polyphenylene oxide (PPO), blends and specialty polymers (liquid-crystal polymers, PEK, polyimide (PI), fluoropolymers, *etc.*) are increasingly used in high-performance applications [54].

Thermosetting polymers are pre-polymers, which form a three-dimensional polymer network upon a curing step. Curing can be accomplished either by heat

(generally, above 200 °C) or by high-energy irradiation. Examples of this type of polymers are epoxy resins, polyester resins fiberglass systems, PURs, PIs, urea, *etc.* Fillers or fibrous reinforcements are often applied to enhance both properties, thermal and dimensional stability of thermosetting resins [54]. Due to their excessive brittleness, many thermosetting polymers could be useless if they are not combined with fillers and reinforcing fibers [54].

Elastomers are flexible polymers that comprise a low crosslink density and generally have low Young's modulus and high failure strain compared to other materials. There are two main categories of elastomers: elastomer with C=C double bonds in their polymer structure (*i.e.*, styrene-butadiene copolymers, polybutadiene) and elastomers containing only saturated C–C bonds in their structure (*i.e.*, EVA, ethylene propylene diene rubber).

Among the most used polymers in micro and nanocomposites are PE (for power cables), epoxy resins, polyester, silicone and imide (for electric machines, dry transformers) and silicone rubbers (for electric insulators). PEs (low, medium or high density) hold very good electrical, mechanical and rheological properties, they are resistant to the environmental conditions, but they have low operating temperatures (below 90 °C) [11]. The addition of inorganic fillers increases the service temperature and improves their mechanical properties. Thermosetting resins have higher service temperatures (155 °C—epoxy resins, 175 °C—polyester resins, 200 °C—silicone resins, 240 °C—imide resins), but low thermal conductivity compared to that of metal parts that come in contact [11].

4.2. Fillers Used in Composites

Polymer composites represent a mixture of two or more components, with two or more phases, based on polymers and fillers. The fillers may have different geometries, such as fibrous, irregular flakes, spheres, acicular and plate-like in shape, cube, block, *etc.* and they are used in a reasonable large volume concentration in polymers (> 5 vol %) [54]. They can be *continuous*, such as long fibers embedded in the polymer in regular arrangements extended across the microcomposite dimensions or *discontinuous*, such as short fibers, flakes, platelets or irregularly shaped fillers (< 3 cm in length) arranged in the polymer in different and multiple geometric patterns forming a microcomposite [54].

An important diversity of fillers are in use, with different chemical compositions, shapes, forms, sizes and intrinsic properties. They are usually rigid materials, immiscible with the polymer matrix in molten or solid states forming different morphologies [54,55]. From the chemical aspects, fillers can be classified in *inorganic* (*i.e.*, oxides, hydroxides, salts, silicates, metals) and *organic* (*i.e.*, carbon, graphite, natural polymers and synthetic polymers) substances. Based on their origin, fillers can be *natural* (*i.e.*, mineral, such as asbestos and animal, such as silk, wool, cellulose,

etc.) and *synthetic* (*i.e.*, organic fibers including Kevlar, carbon black, graphene as well as inorganic fibers such as oxides and hydroxides: TiO_2, SiO_2, Al_2O_3, aluminum trihydroxide ($Al(OH)_3$), magnesium hydroxide ($Mg(OH)_2$), antimony trioxide (Sb_2O_3), *etc.*) as summarized in Table 1 [54].

Table 1. Examples of different types of fillers (Adapted table from [54]).

Origin	Chemical structure	Examples
Natural	Animal	Silk, Wool, Hair
	Mineral	Asbestos
	Cellulose	Wood, Seed, Leaf, Fruit, Stalk, Bast, Grass
Synthetic	Inorganic	Oxides: TiO_2, SiO_2, Al_2O_3, ZnO, MgO, Sb_2O_3 Hydroxides: $Al(OH)_3$, $Mg(OH)_2$ Metals: Al, Au, Ag, B, Sn, Cu, Steel Silicates: asbestos, talc, mica, nanoclay, kaolin Salts: $CaCO_3$, $BaSO_4$, $CaSO_4$, *etc.* Carbides and nitrides: AlN, BN, SiC
	Organic	Carbon and graphite fibers and flakes, carbon nanotubes, carbon black, graphene, graphene oxide Natural polymers: cellulose and wood fibers, cotton, flax, starch Synthetic polymers: aramid, polyester, polyamide, polyvinyl alcohol fibers

When the fillers are dispersed homogenously in the polymer matrix, in small concentrations (usually less than 10 wt %) and they are in the nanometric range, respectively with dimensions smaller than 100 nm (nanoparticles), than materials are known as nanocomposites. They are distinct from microcomposites due to their unique properties given by the interface zone formed between the polymer and nanoparticles. These interfaces are significantly increased compared to micro-sized composites, due to the nanometric scale of the particles. Because of their unique properties, nanocomposites have great potential for advanced applications.

Nanofillers can be classified in three main categories [56]:

- One-dimensional nanofiller: plates, laminas and shells,
- Two-dimensional nanofiller: nanotubes and nanofibers,
- Three-dimensional nanofiller: spherical nanoparticles.

Various nanoparticles, such as nanoclays (organomodified montmorillonite, *etc.*), nano-oxides (TiO_2, SiO_2, Al_2O_3, *etc.*), carbon nanotubes (CNTs), metallic nanoparticles (Al, Fe, Ag, and Au, *etc.*), semiconducting particles (SiC, ZnO, *etc.*) have been homogeneously dispersed in polymers, as provided in Table 2, due to the increasing demand for improvement in performances of thermoplastics and thermosetting polymer materials [56–58].

Table 2. Examples of different types of nanofillers (Adapted table from [56]).

Nanofiller type	Origins/Structure	Examples
Nano-clay	Phyllosilicates	Kaolinite, Smectite (Talc, Mica, Montmorillonite), Chlorite, Bentonite, Saponite, *etc.*
	PolySilicate	Natural (Magadiite, Ilerite, Zeolite, Silhydrite, Kanemite, Kenyaite) and Synthetic (Zeolite and FluoroHectorite)
	Double Lamellar Hydroxite	Synthetic (Hydrotalcite, *etc.*)
Nano-oxides	Organic	Diatomite;
	Inorganic	NanoTiO_2, nanoSiO_2, nanoAl_2O_3, nano-antimony-tin oxide (ATO)
Carbon nanotubes (CNTs)	Single-wall	Diameter between 1 and 2 nm;
	Double-wall	Diameter between 2 and 4 nm;
	Multi-wall	Diameter between 4 and 150 nm;
Other nanofillers	Metallic	Nanosilver, nanozinc, nanogold fillers, *etc.*;
	Magnetic	Oxide: ferrites, *etc.*
	Semiconducting	Nano-SiC, nano-ZnO *etc.*

The properties of polymer micro/nanocomposites are affected by the nature of polymer matrix and filler, their intrinsic properties, by the size and shape of the fillers, by the dispersion of the particles into the polymer matrix, by the surface functionalization and the thickness of the filler surface treatment and also, by the interactions and adhesion between the polymer matrix and the fillers.

Owned to their very small dimensions and large specific area, polymer nanocomposites possess different physical and chemical properties compared to traditional composites. Selection of the nanoparticles for a proper application depends on the desired electrical, mechanical and thermal properties. For example [59], CNTs improve the electrical and thermal resistivity and Al_2O_3 is usually selected for high thermal conductivity whilst TiO_2 nanoparticles (anastase) have photocatalytic properties. Calcium carbonate ($CaCO_3$) is typically used for low costs and high number of deposits and SiC is applied for mechanical strength, hardness, corrosion and non-linear electrical behavior. In particular, ZnO is employed in composites for electric stress control due to its high thermal conductivity and non-linear electrical characteristics. Nanofillers can improve or adjust significantly different properties, such as electrical, mechanical, thermal, and optical or fire-retardancy of the materials in which they are incorporated with the condition to be homogenously dispersed. A very good dispersion of the nanofillers into the polymer matrix can be achieved by using different methods and preparation techniques among them mechanical dispersion methods, including ultrasonic vibration or special sol-gel techniques, high shear energy dispersion mixing and/or through a tailored surface modification of the nanoparticles [59,60].

4.3. Fillers Surface Treatment

Homogeneous dispersion of the fillers into the polymer matrix is a challenge due to the immiscibility of polymer and particles [61]. Single particles tend to agglomerate due to their interfacial tension and the properties of composites are altered. Therefore, the surface treatment of the particles is very important to achieve homogenous distribution, to avoid any cluster formation in the polymer composite and to improve the adhesion between the polymer and filler [61]. Whilst surface treatment of numerous fillers are described in literature, account has to be taken into the fact that the thickness of the modified layer plays an important role in the composites properties changes [59]. Important research regarding the influence of particles surface modification on the electrical properties of composites [62–64] and, especially, nanocomposites was performed [61,65–67].

Techniques used for controlled surface modification include: (i) *chemical treatment* of the nanoparticles surface; (ii) *grafting* of functional polymeric molecules to the hydroxyl groups existing on the particles surface and (iii) *plasma* techniques, which make the surface of the particles more or less wettable, harder, rougher and more conducive to adhesion to the polymer [61].

Usually, for the *chemical treatment* of the particle surfaces, different types of silane coupling agents (*i.e.*, 3-aminopropyl triethoxysilane) are used (Figure 5). Silane coupling agents can react with the hydroxyl groups of inorganic and organic surfaces via condensation reaction [61,68]. The change in the surface polarity in conjunction with steric hindrance effects enables a better dispersion between the modified nanoparticles and polymer matrix [61]. Another typical coupling mechanism, similar to the one described before is titanate coupling agent (*i.e.*, tetra-isopropyl titanate), where the same effect is obtained [61].

Grafting of the functional polymeric molecules to the hydroxyl groups of the surface of nanoparticles is another technique to overcome the incompatibility between inorganic fillers and polymer matrix [70]. As provided in Figure 6, there are two different methods to prepare grafted surfaces. One the one hand side a polymer chain is directly coupled to the inorganic filler surface ("grafting onto" reactions) and on the other hand side the attachment of monomers on the surface and the subsequent polymerization of the polymeric chain ("grafting from" reactions) is accomplished [71]. Through this method, selected polymer chains are grafted to the nanoparticle surface by strong covalent bonding. Due to the covalent attachment of the polymer, the modified nanoparticles become either hydrophobic or hydrophilic and their miscibility is enhanced. Further separation of the nanoparticles partially results from the steric hindrance effect [61].

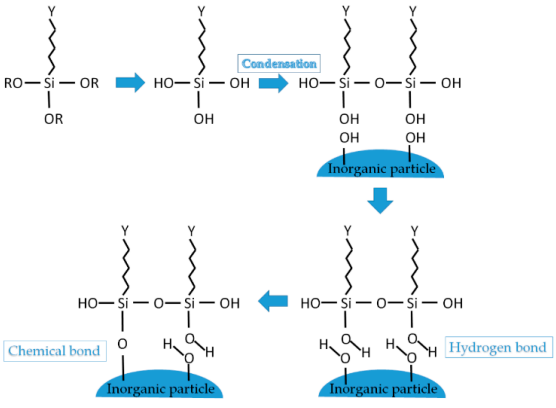

Figure 5. Schematic representation the surface functionalization of inorganic particles via condensation reaction of functional silanes (Redraw and adapted figure from [69]).

Plasma method is another technique that modifies chemically and physically the surface of the inorganic nanoparticles, without influencing the bulk properties of the fillers. In the presence of selected monomers, graft copolymerization and polymerization reactions can be carried out during plasma treatment enabling the preparation of particles with controlled surface properties. The limitation of this technique is that the experimental conditions require a very complicated vacuum system [61]. Surface modification of the inorganic particles trough these methods produces excellent integration and good adhesion between the polymer matrix and fillers [61].

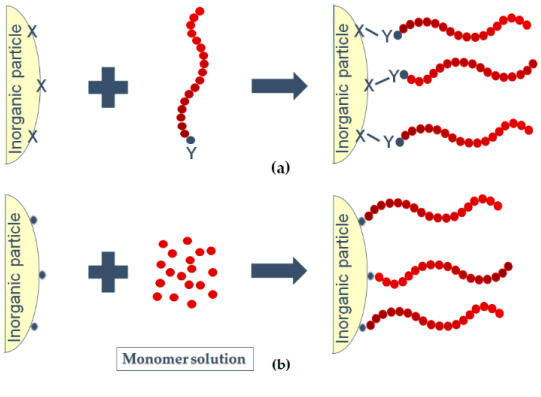

Figure 6. Schematic representation the surface functionalization of inorganic particles by (**a**) "grafting onto" and (**b**) "grafting from" reactions (Redraw and adapted figure from [72]).

4.4. The Role of the Interface

Interface regions formed between the polymer matrix and particles are considered to have a dominant role in the final properties of nanocomposites [23]. Some simple examples can clearly demonstrate the significance of the interface area, especially, at the nanometric and molecular levels [69]. Taking into consideration the example of Kickelbick [73], a cube composed by 16 × 16 × 16 atoms packed tight is illustrated in Figure 7.

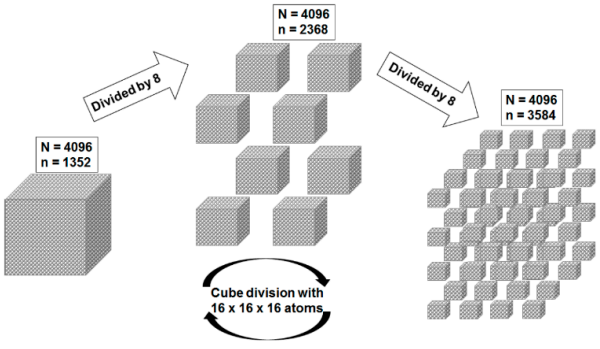

Figure 7. Surface statistic consequence of dividing a cube, where N is the total number of atoms and n is the number of surface atoms (Redraw and adapted figure from [73]).

The cube contains a number of 4096 atoms, from which 1352 are located on the surface, therefore ~33% of the atoms are surface atoms. In the case that the cube is divided into eight equal 8 × 8 × 8 cubes, the overall number is the same, but 2368 atoms are located at the surface, which means ~58% of the atoms are located on the surface. If the same operation is repeated, 3584 atoms are obtained at the surface, which means ~88% surface atoms.

The example shows how important the surface becomes when objects are becoming smaller and smaller in size. In terms of nanoparticles, which sizes are in the range of tens nanometers, nearly every atom is a surface atom that can interact with the polymer and therefore inner surface has a direct impact on the nanocomposite properties [73].

For a better understanding of the interface properties and its physico-chemical structure, several papers were published and focused on the models development in order to describe the interface between nanoparticles and polymer matrix. All the established models started from the fundamental theories and models of dielectric materials. When composite dielectric materials are manufactured with different shapes, sizes, dielectric properties and concentration of each component,

it is beneficial to predict through analytical and numerical models, the effective permittivity and the distribution of electric fields within the composite [74].

The first analytical models for estimation the effective permittivity of dielectrics were based on the effective medium theory (EMT), where the interface between the components was not considered [75]. These models assumed an elementary cell containing a spherical inclusion of an arbitrary radius embedded in a matrix, such as Maxwell–Garnett (MG) model [75]. Later, MG model was extended with different assumptions to consider the interactions between the different constituents, such as the symmetric Bruggeman model [75].

More recently analytical models were developed and among them exists the three-dimensional electromagnetic model developed by O'Connor *et al.* [74]. A software constructs a composite with thousands of distinct elements arranged according to the defined input parameters. The software provides the modeling composite systems without creating manually many individual composite elements and enables user specification over the simulation parameters, analyzing the results through a user interface. The permittivity of each composite element, concentration, shape, size, and density, are user-defined. The effective permittivity of the composite is determined by a capacitance of a plate capacitor containing the virtual composite. Comparisons between the simulated effective permittivity and the values calculated using classical equations for the effective permittivity of composites with various particle concentrations are presented. Finally, examples of how the electric field is distributed through the composite structure are included [74].

The above analytical and numerical models for predicting the effective permittivity of composite dielectric materials, do not take into account explicitly the electric charge distribution in composites, so this aspect could be one important limitation regarding the use of these models for polymer nanocomposites, in defining their dielectric properties [75].

4.4.1. Wilkes' Model

Wilkes published the first article with an interface model in 1989 [76]. The model describes the partially distribution of the silica nanoparticles into the outer polymer region formed by covalent bonds, which were generated by the end cap method, as depicted in Figure 8 [76]. Silica nanoparticles and the polymer matrix are combined to form a network structure of hydrogen bonds produced by the direct mixing methods [23].

4.4.2. Tsagaropoulos' Model

Another interface model is the one proposed by Tsagaropoulos *et al.* in Reference [77]. For a better understanding of the morphological and structural changes generated by the increase of the filler concentration within the polymer

matrix, which results in a decrease of the average interparticle distance, Tsagaropoulos proposed a model represented schematically in Figure 9 [77].

The incorporation of the nanoparticles into a polymer matrix creates interactions between the nanofillers and the polymer chains located in their vicinity, generating regions with restricted chain mobility around nanoparticles [78]. These restricted mobility regions possess their own glass transition temperature (T_g), according to the model for the morphology of ransom ionomers (EHM) and the model of Tsagaropoulos is focused on T_g behavior in different combinations of polymers and silica nanocomposites [77,78].

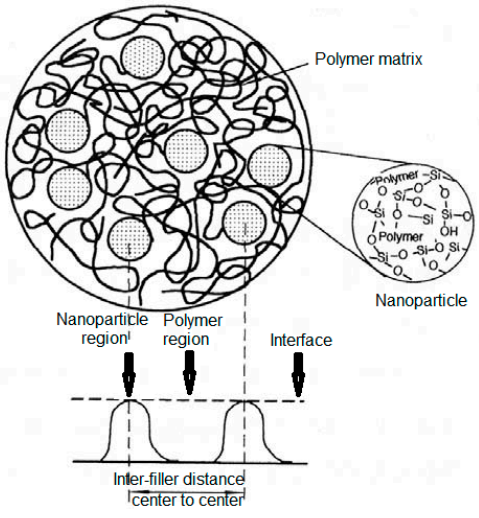

Figure 8. Wilkes' model of the interface formed between silica nanoparticles and polymer matrix (© 2016 IEEE. Reprinted, with permission, from [76]).

Tsagaropoulos' model assumes that silica particles (textured areas in Figure 9) are surrounded by a layer of polymer (grey areas in Figure 9) or tightly bound layer, which appears to be immobile in the temperature and frequency regimes and does not participate to the glass transition. The polymer chains capable to participate to the glass transition (textured light grey area in Figure 9) are called polymer of reduced mobility or loosely bound layer [77]. A series of experiments were accomplished on different polymer/silica nanocomposites and they revealed the existence of two glass transitions. One is the glass transition of the polymer and the other is the glass transition of the loosely bound layer. This conclusion came from the experimental appears of two tan δ peaks [77,78].

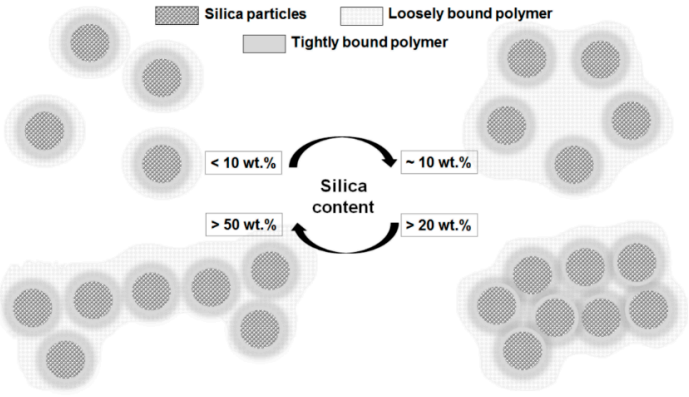

Figure 9. Tsagaropoulos' schematic representation model of the morphological changes in the polymer matrix filled with silica filler in different concentrations: (**a**) less than 10 wt %; (**b**) circa 10 wt %; (**c**) over 20 wt % and (**d**) over 50 wt % (Redraw and adapted figure from [77]).

4.4.3. Lewis' Model

In 1994, Lewis highlighted the importance of the interface considering them as regions with altered electrochemical and electromechanical behavior [16]. In 2004, Lewis defined an interface between two uniform material phases A and B, as illustrated in Figure 10 [79]. The intensity I_α of a chosen material property α associated with the forces is constant within each of the two phases A or B, but will become increasingly modified as the interface with another phase is approached [79,80]. In general, α can be any physical or chemical property (*i.e.*, electrochemical potential, the electric field, the local dielectric permittivity or an optical parameter) [79].

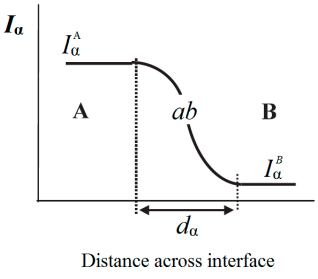

Figure 10. Intensity model of Lewis showing the interface *ab* between two phases A and B are defined by the intensity I_α and the changes of the property α suffered when crosses the interface (© IOP Publishing. Reproduced with permission. All rights reserved [79]).

The region over which the forces associated to a chosen property α is different from the bulk values in each phase is called interface *ab* where the intensity d_α changes from I_α^A in the bulk phase A to I_α^B in the bulk phase B [79,80]. Lewis also suggested that an electrical charge layer is formed around the nanoparticles in the interface region *ab*, as shown in Figure 11 [79].

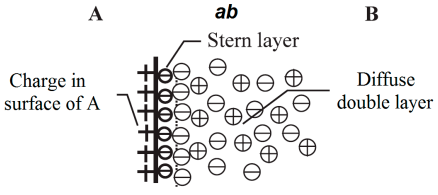

Figure 11. Distribution of the electrical potential in Stern layer and Gouy-Chapman diffuse mobile ion double layer of the interface *ab* in response to a charge A (© IOP Publishing. Reproduced with permission. All rights reserved [79]).

The interface *ab* consists of three charged layers (see Figure 11). On the side A of the interface *ab*, there is a double layer associated with the surface of phase A, which is formed by trapped carriers, mobile electrons and holes and immobile charged impurities [79]. Next to the first layer, a double layer with a higher charge density, termed Stern (Helmholtz) layer), exists. The A side of the Stern (Helmholtz) layer is formed by absorbed ions and dipoles, whilst its B side is determined by ions attracted by the excess of charge on phase A. Beyond the Stern (Helmholtz) layer there is the Gouy-Chapman layer, which is formed by the separation of mobile positive and negative charges from phase B. The interface *ab* charging involves electronic polarization and orientation of any permanent dipole and is described as Stern/Gouy-Chapman double layer model. The electrical double layer is composed by the compact Stern layer, formed by charges immediately adjacent to the surface A and Gouy-Chapman layer, which is the more distant diffuse part [79,80]. If medium B has a polar component, then the charge is significant. If medium B contains mobile ions, they will immigrate to establish a diffuse electric double layer around particle A [80].

4.4.4. Tanaka's Model

In 2005, Tanaka proposed a multi-core model in one of his paper [76] in order to understand better various properties and phenomena that polymer nanocomposites exhibit as dielectrics and electrical insulation. This model describes the physico-chemical and electrical structure of the interface regions formed between spherical nanoparticles and polymer matrix (see Figure 12) [76].

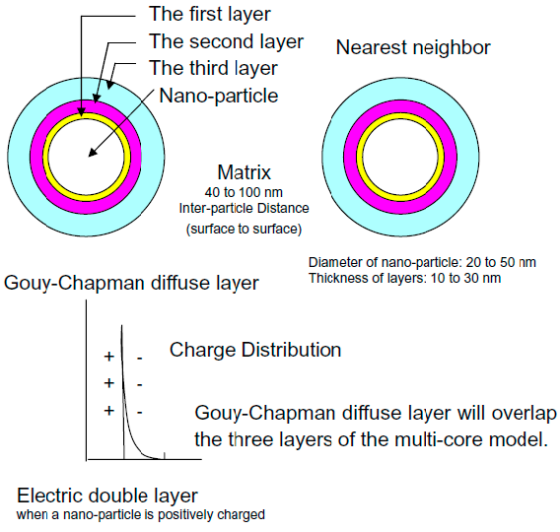

Figure 12. Tanaka's multi-core model (© 2016 IEEE. Reprinted, with permission, from [76]).

According to Tanaka's model, the interface is defined as a multi-layer of several tens nm and is formed by three layers: a bonded layer (the first layer), a bound layer (the second layer) and a loose layer (the third layer). A Gouy-Chapman diffuse layer is superimposed on the three layers of the interface and cause a far-field effect [76]. The first layer is a region of chemical bonding between the inorganic particles and organic polymer matrix. The second layer is an interfacial region consisting of a layer of polymer chains strongly bound and/or interacted with the first layer and the surface of inorganic nanoparticles. The third layer is a region loosely coupling and interacting with the second layer, with a different morphology compared to the others [76].

In polymer nanocomposites, the particles may interact electrically with the nearest neighbors' particles due to the far-field effect, resulting in a collaborative effect [76]. This model can explain different electrical properties, such as partial discharges resistance of PA/LS nanocomposites [76]. Some articles were published in order to show Lewis' contribution in the developments of Tsagaropoulos' and Tanaka's models, their differences and similarities and future challenges [81,82].

4.4.5. Other Models

Besides these four models of the interface region between nanoparticles and polymer matrix, various models were proposed, but the matching between models and experimental results is quantitatively poor. Computer simulation and numerical modeling are expected to generate more quantitative results.

Starting from Tanaka's model, in 2008 an electrostatic 3D model by Ciuprina *et al.* [75] was proposed in order to analyze the electric field distribution inside and outside of the spherical nanoparticles homogenously dispersed into a polymer matrix. In addition, this model can reveal the impact of the nanoparticles diameter and concentration, the thickness of the interface layers and the permittivity of the nanoparticles and layers on the polymer nanocomposites properties [83]. Starting from similar hypothesis, in 2012, Plesa [84] proposed a novel structural model of nanocomposites composed of LDPE filled with inorganic nanoparticles ($SiO_2/TiO_2/Al_2O_3$) (Figure 13) [84]. The thicknesses of the LDPE-nanofillers interfaces were assumed to differ in size. Types of electric dipoles present on the interfaces were identified depending on the chemical structures of the individual layers, and a calculation was done to estimate their concentration. The permittivity values of the interface layers were computed with the proposed model assuming no interaction between the dipoles. The achieved data were compared with the experimental results obtained on the same type of nanocomposites and they were used to explain the interface structure and the electrical properties of nanocomposites [84].

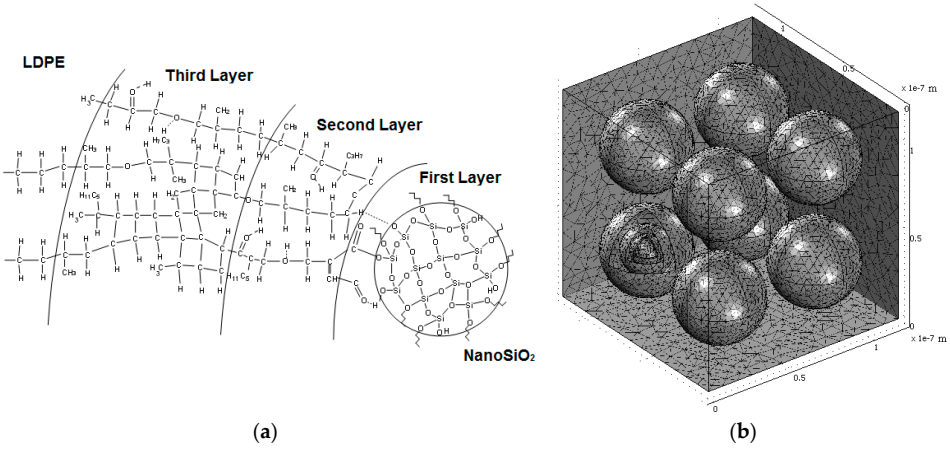

Figure 13. (**a**) Schematic representation of an interface LDPE—nanoSiO_2 chemical structure and (**b**) 3D electrostatic model (Reprinted, with permission, from author [84]).

Another model influenced by the multi-core model of Tanaka is the interphase volume model proposed by Raetzke in 2006. According to this model [80,85], the term interface is replaced by the term interphase of which characteristics depend on the particles size, filler concentration and type of polymers and nanofillers. Within the hypothesis of an ideally nanoparticles dispersion in a polymer matrix, a certain

interphase thickness is assumed and a maximum of interphase volume is reached for a distinct filling concentration (see Figure 14) [80,85].

Comparing the dependence of the interphase volume on the fillers concentrations with the dependence of the electrical properties of the polymer nanocomposites on the filler content, the interphase thickness within the nanodielectrics can be estimated [80,85].

The polymer chain alignment model proposed by Andritsch in 2011 [80,86] is based on experiments and describes the morphology of nanofilled epoxy resins (Figure 15).

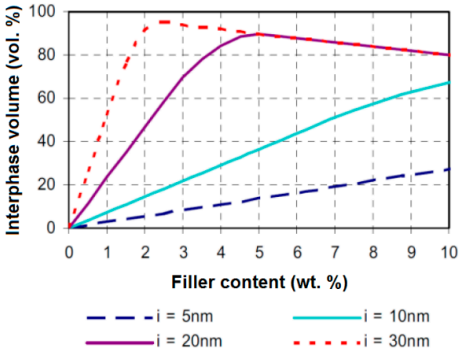

Figure 14. Interphase volume model of Raetzke for a silicone matrix and SiO_2 particles, with different interface thicknesses *i* (© 2016 IEEE. Reprinted, with permission, from [85]).

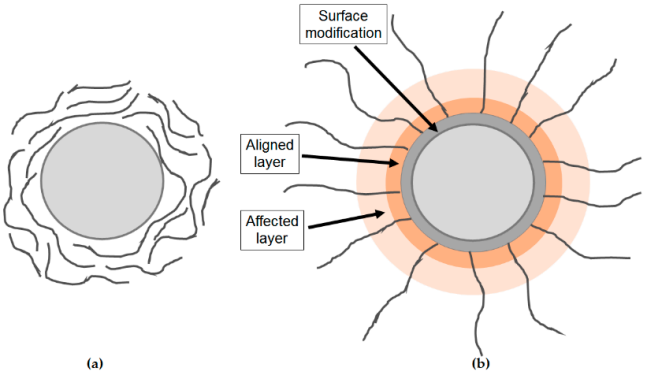

Figure 15. Polymer Chain Alignment Model by Andritsch: nanoparticles (**a**) without and (**b**) with surface modifications. (Redraw and adapted figure from [86]).

If the nanoparticles are unmodified (Figure 15a), the interactions between the nanoparticles and the polymer matrix are low. If the surfaces of nanoparticles are modified with a silane coupling agent (Figure 15b), a restructuring of the polymer matrix will take place due to the reactions between the polymer and the silane epoxy groups: an alignment layer of the polymer chains perpendicular to the nanoparticle surface appears and the polymer surrounding region is affected, too [80,86].

The water shell model proposed by Zou *et al.* in 2008 [87] is based on Lewis' and Tanaka's models and explains the effect of water absorption in epoxy nanocomposites, when they are exposed to humidity [78]. In this model is considered that the water molecules are concentrated around the nanoparticles and, in low concentrations, in the polymer matrix. If the water concentration around the nanoparticles is high, percolative paths are formed through overlapping water shells (Figure 16), which affect the dielectric properties of epoxy nanocomposites [78,87].

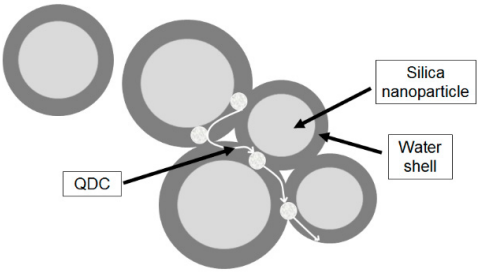

Figure 16. Schematic representation of the water shell model proposed by Zou. The percolative path passes through overlapping water shells, around nanoparticles (Redraw and adapted figure from [87]).

The models of polymer nanocomposites presented above give an idea about the physico-chemical and electrical properties of the interface between nanoparticles and polymer matrix. Parts of the experimental results were explained through these models, but with some limitation since the interface regions have not been made visible until now in polymer nanocomposites.

5. Preparation Methods

Preparation methods of microcomposites are relatively simple and these can be manufactured in large quantities [54]. Taking into consideration different types of polymer and fibers from which polymer microcomposites can be made, the preparation methods represent a broad subject [88]. The basic steps include impregnation of the fiber with the resin, forming of the structure, curing of thermosets or thermal processing of thermoplastic matrices and finishing [88].

Depending on the process, these steps may occur separately or continuously. For example, the starting material for many polymer microcomposites is a prepreg process, where fiber tapes or cloths that have been preimpregnated with resin, are partially cured. Pultrusion, impregnation, forming and curing are done in a continuous process. Some other important manufacturing techniques are: sheet molding (fast flexible technique), injection molding (fast technique, high volume of fibers in thermoplastics matrices), resin transfer molding (fast technique, complex parts and good control of fiber orientation), prepreg tape lay-up (slow and laborious technique, reliable, expensive), pultrusion (continuous technique, constant cross-section parts), filament winding (moderate speed technique, complex geometries and hollow parts) and thermal forming (fast, easy, repair and joining technique, reinforced thermoplastics) [88].

Over the last two decades, chemists and material scientists have shown significant interest and important development on the preparation methods of organic and/or inorganic nanocomposites [89]. Nanocomposite materials can be obtained using similar microcomposites design and synthesis techniques, which make them interesting from the production point of view [90]. The incorporation of nanoparticles into the polymer matrix can lead to novel high-performance compared to the unfilled or micro-filled polymers [89].

In order to obtain these high-performances in thermal, mechanical or electrical properties, nanofillers should be homogeneously dispersed into the polymer matrix and should be physically or chemically bounded by the surrounding polymer [89]. During the fabrication process, agglomerations of nanoparticles tend to appear due to the interfacial tension, accumulated on the nanofillers surface and due to the incompatibility of inorganic and organic components. It was recognized that the surface treatment of nanoparticles would bring a better dispersion in the polymer matrix [89]. The correctly chosen curing dispersion agent will bind the organic polymers and inorganic particles, which are immiscible [89]. Taking into consideration all these aspects, a certain number of techniques were developed in order to obtain improved nanocomposite materials.

Usually, the synthesis of polymers nanocomposites applies bottom-up or top-down methods [90]. Bottom-up methods involves chemical processes (sol-gel process, chemical vapor deposition, spray pyrolysis, *etc.*), where the precursors are used to construct and grow organized structures, from the nanometric level (see Figure 17a). Top-down techniques top-down are using in the most cases physical methods (LSs dispersion in polymer, *etc.*) and the bulk material is broken down into smaller pieces or patterning (see Figure 17b) [90].

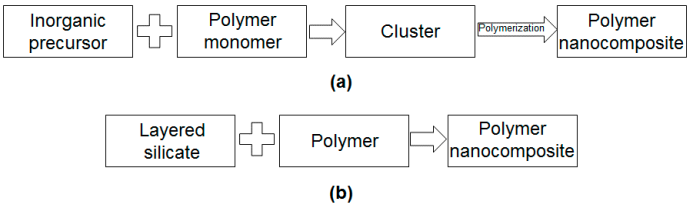

Figure 17. Schematic representation of (**a**) bottom-up and (**b**) top-down methods.

Inorganic nanofillers can be dispersed into the polymer matrices via four different ways: (i) *intercalation method* based on the exfoliation of LSs; (ii) *sol-gel process* which starts, at room temperature, with a molecular precursor and then forms by hydrolysis and condensation reactions a metal oxide framework; (iii) *in situ* formation of nanofillers and *in situ* polymerization of monomers in the presence of fillers previously obtained and (iv *direct mixing* of the polymer and the nanofillers, either as discrete phases (melt mixing), or in solution (solution mixing) [91]. In the following section, well-established preparation techniques to obtain nanocomposites materials are described.

5.1. Intercalation Method

Intercalation method is a typical top-down method based on the decreasing size of filler to the nanometric scale [92]. This method can be achieved by three ways: direct intercalation of polymer chains from solution, polymer melt intercalation and intercalation of monomers followed by *in situ* polymerization [73].

5.1.1. Direct Intercalation of Polymer Chains from Solution

Direct intercalation of polymer chains from solution is the procedure of dispersing layered fillers (*i.e.*, silicates) into a solvent in which the polymer is soluble and is known as exfoliation or adsorption process. When the solvent is eliminated from the polymer-clay complex through evaporation, the silicates sandwich the polymer to form a multi-layered structure (see Figure 18) [91,93].

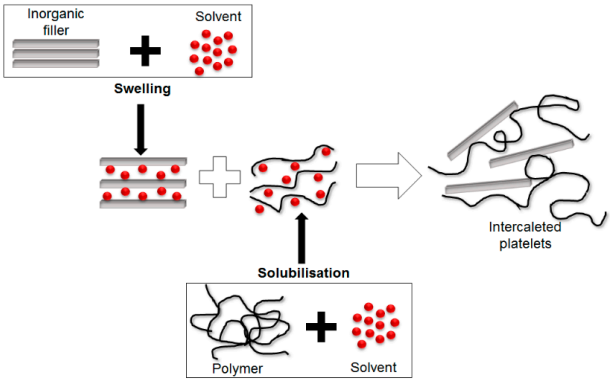

Figure 18. Schematic representation of the solution processing (Redraw and adapted figure from [93]).

5.1.2. Polymer Melt Intercalation

Polymer melt intercalation involves the mixing of the layered filler (*i.e.*, silicate) with the polymer in the molten state. If the surfaces of the silicate layers are sufficiently compatible with the polymer chains, the polymer can be inserted into the interlayer space, without any solvent, forming intercalated or exfoliated nanocomposites (see Figure 19) [91,93].

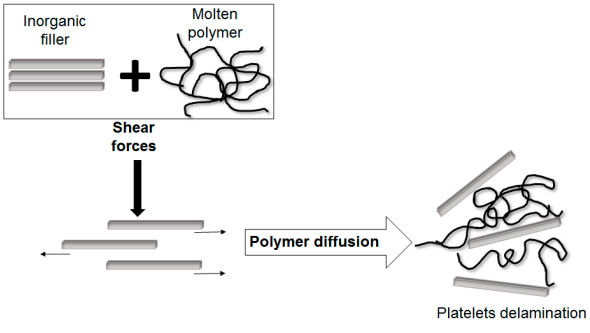

Figure 19. Schematic representation of the melt processing (Redraw and adapted figure from [93]).

5.1.3. Intercalation of Monomers Followed by *In Situ* Polymerization

Intercalation of monomers followed by *in situ* polymerization is the procedure that uses monomers with initiators, which are allowed to polymerize in the presence of the layered filler (one prominent example is clay). During the polymer chains growing, the clay layers are separated and the polymer chains enter the interlayer space, forming polymer/clay nanocomposites (see Figure 20) [91,93].

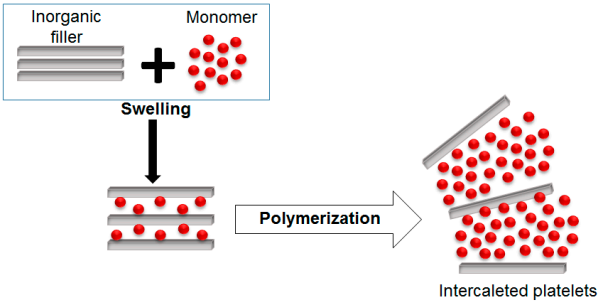

Figure 20. Schematic representation of the intercalation of monomers *in-situ* polymerization (Redraw and adapted figure from [93]).

5.2. Sol-Gel Method

Sol-gel method is a typical bottom-up method and is associated with two reactions steps, namely sol and gel. Sol represents a colloidal suspension of solid particles in a liquid phase and gel is the interconnected network formed between phases [90]. This process consists of two main reactions: hydrolysis of the metal alkoxides (Equation (1)) and condensation of the hydrolyzed intermediates (Equations (2) and (2′)) [90]:

- Hydrolysis: $$M(OR)_4 + H_2O \rightarrow HO - M(OR)_3 + ROH, \quad (1)$$
- Condensation: $$(OR)_3M - OH + OH - M(OR)_3 \rightarrow (OR)_3M - O - M(OR)_3 + H_2O, \quad (2)$$ $$(OR)_3M - OH + RO - M(OR)_3 \rightarrow (OR)_3M - O - M(OR)_3 + ROH. \quad (2')$$

Both are multi-steps processes and occur sequentially [90]. This method can be used in order to obtain inorganic metal oxides from organic metal alkoxides, esters, *etc.* and transparent films of organic-inorganic hybrid trough co-hydrolysis and polycondensation of alkyltrimethoxysilane- tetramethoxysilane mixtures [91]. The sol-gel procedure is a useful way to produce inorganic-organic hybrids [91].

5.3. In Situ Polymerization

Formation of nanoparticles via *in situ* polymerization is a method of synthetisation of nanoparticles via polymerization of colloidal sols containing metal ions and monomers. The size of the nanoparticles depends on the experimental conditions (temperature, thermal coagulation, *etc.*) and colloidal sols properties [91]. This method is used to prepare nanocomposites based on thermosetting polymers and nanoparticles, which are dispersed within monomer (or monomer solution) and the mixtures-polymerized by standard methods [92].

5.4. Direct Mixing of Nanoparticles with the Polymer

Direct mixing of nanoparticles with the polymer is a typical top-down approach and is the simplest method to obtain nanocomposites. This method involves, either direct mechanical mixing of the polymer with nanofillers (in the absence of any solvent), above the softening point of the polymer (termed melt-compounding method) or mixing the polymer and fillers as a solution (termed solution-mixing method) [23,92]. Due to the surface treatment of the nanoparticles and the development of mixing equipment, homogenous samples can be obtained through this method (see Figure 21).

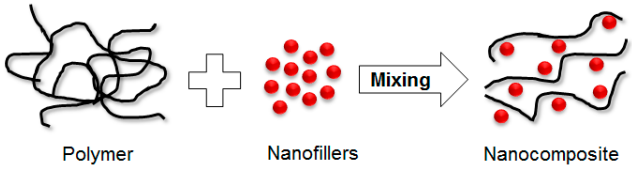

Figure 21. Schematic representation of the mechanical mixing of nanoparticles with the polymer.

Polymer nanocomposites represent very promising materials for applications as dielectrics and electrical insulations, from the viewpoint of their excellent properties [33]. Nevertheless, in order to move these materials from the lab to an industrial production, it is necessary to develop suitable methods towards the large-scale manufacturing of polymer nanocomposites. This will help to create reproducible and reliable data that are needed for expanding development of these advanced materials in the high-voltage applications.

6. Properties of (Nano)Composites

It is a challenge to design and optimize proper electrical insulation systems of electrical equipment, in the conditions when energy demands, voltage level and temperature values are increasing and on the other hand, the electrical components and equipment sizes are becoming smaller and more compact compared to the traditional ones, increasing the demands on the insulation systems. Thus, current research aims at systems that are expected to have better endurance and reliability compared to their conventional counterparts [94].

In the insulation engineering, polymer composites are the second generation of what is called filled resins and consists of polymers filled with a large amount (the order of 50 wt %) of inorganic microfillers [33]. They are traditionally designed to be used as structural materials [95]. Due to the rapid growth of the electrical engineering industry, composite materials were involved more and more in electrical applications,

as structural and electronic composites. However, there is a vast difference in their property requirements: while structural composites emphasis high strength and high modulus, electronic composites emphasis high thermal conductivity and low thermal expansion. Considering all these aspects, the industry is continuously looking for better alternative materials, which come at affordable prices to maintain the requisite price margin, besides considering the depleting natural resources of conventional materials [95].

Composite materials offers some advantages in terms of light-weight, resistance, ease of maintenance and better environmental protections, but also poses some disadvantages in terms of processing costs and the choice of materials. Composite materials offers the opportunity to provide the suitable product with required performance for the final application and thereby optimizing the price-performance ratio [95]. In high-voltage applications, solid electrical insulation materials, termed dielectrics, in the early days of electrical power applications were made of natural materials and ceramic materials [94,96]. There were two areas where few advances had been observed for cellulose-based paper, which is still the main insulation system in power transformers and sub-water cables applications and outdoor electric insulation materials for high-voltage lines and bushing [94]. However, polymer composites with better performance as well as lower weight than the conventional polymers were developed in the last several decades. Later, the use of plastics and epoxy resins in electrical engineering applications, allowed the manufacturing of insulation systems with controlled properties. In general, plastics are easier to be shape and process compared to glass and ceramics, but do not possess sufficient mechanical strength. Light-weight designs of polymer composites (containing inorganic fillers) with enhanced material properties were pursued in the last several decades. Epoxies offered new possibilities in developing electrical insulation, particularly to reach a more compact design in electrical power equipment [97]. Fillers have been introduced to improve the mechanical and other properties (electrical, thermal) of polymers [94]. Due to their good adaptability and simple manufacturing technology, mineral filled epoxies are the preferred materials for indoor and outdoor insulation. The disadvantage of these materials is long-term aging [97]. Nowadays, polymeric epoxy resins, hardeners and industrially available fillers are of good quality, but their internal interfaces, which lead to aging, cannot be avoided [97].

Newly born emerging advanced materials, called polymer nanocomposites are defined as polymers filled with a small amount of nanofillers (few wt % in content and 1 to 100 nm in size), which should be homogeneously dispersed in the polymer matrix and poses a tremendously large surface as compared to microfillers [33]. Therefore, in order to understand the characteristics that emerge due to nanostructuration, it is indispensable to investigate the interaction between nanofillers and polymer

matrix [33]. These materials possess a huge potential in applications, such as building, transportation, food packaging, electrical and electronics engineering, industries, *etc.* and could be used as high functional materials (coating and barrier-functional materials, flame-retardant and foamed materials, *etc.*) [33].

First experimental results on the electrical properties of polymer nanocomposites were reported by Nelson and Fothergill in 2002 [98]. Their investigations on epoxy systems filled with TiO_2 micro/nanoparticles concluded that: (i) nanofilled epoxy exhibits a flat loss tangent response at low frequency compared to microcomposites; (ii) nanofilled epoxy exhibits mitigated space charge behavior compared to microcomposites and (iii) the decay of charge for nanofilled epoxy is rapid compared with microfilled epoxy [53,98]. Whereas conventional microfilled materials reduce dielectric strength due to bulk charge accumulation, they reported [22] that the nanofilled epoxy exhibited a higher DC breakdown strength compared to microcomposites, but the values were close to the base polymer. Subsequent experimental findings on the use of nanocomposites in electrical insulation were overwhelming positive [53].

Various nanocomposite systems, such as PE/TiO_2, PP/LS, EVA/LS, epoxy/TiO_2, epoxy/Al_2O_3, epoxy/ZnO, were investigated and it was reported that space charge formation was mitigated upon nanostructuration and showed reduced charge accumulation at high fields when compared with the base polymer [53]. Meanwhile, the breakdown performance of various nanocomposite systems was found to be enhanced compared to equivalent microcomposites [53]. In addition, nanocomposites were generally more resistive to partial discharges compared to microcomposites and base polymers. Because microfillers are much less closely packed as nanofillers, erosion of the matrix around the nanofillers was assumed to proceed as in the unfilled polymer. Similar mechanisms were also suggested for tree-retardant effect found in nanocomposites [53]. Nanocomposites were found to exhibit lower permittivity and loss tangent compared to microcomposites and sometimes to unfilled polymer [53]. Mechanical and thermal properties, such as tensile strength, bending strength, elastic modulus, weight deflection temperature and heat decomposition temperature were found to be improved for various types of nanocomposites [33]. Long-term characteristics such as creep, stress relaxation and fatigue were obtained for different nanocomposites systems. Furthermore, some types of nanocomposites exhibit characteristics that are particularly important for selected target applications, such as paint performance, high biodegradability, gas barrier effect, flame retardancy, foaming ability, *etc.* [33].

Nanodielectrics are expected to possess unique dielectric properties due to the interfacial region between nanofillers and polymer, rather than a simple binary combination of properties, such as in conventional microcomposites. This distinct property lead to the idea of a new class of dielectric materials with combined electrical,

mechanical and thermal properties and can be an excellent class of material as far as AC and DC applications are concerned [53]. Nevertheless, many promising experimental results have been reported concerning the use of nanodielectrics as electrical insulation materials in high-voltage applications.

6.1. Electrical Properties

6.1.1. Electrical Conductivity

Imai *et al.* [99] investigated the electrical properties of micro/nanocomposites based on epoxy resin and LS/silica fillers. Figure 22a shows the relationship between absorption current and time.

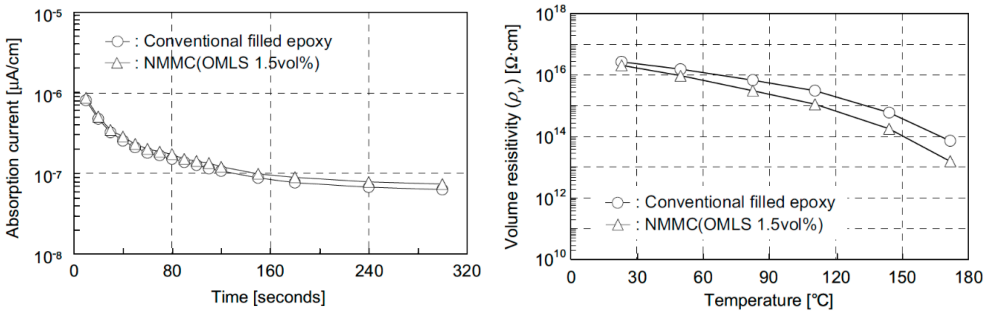

Figure 22. (**a**) Absorption currents in time after applying DC voltage (500 V) and (**b**) volume resistivity dependence with temperature (© 2016 IEEE. Reprinted, with permission, from [99]).

It was found that the damping curve of the nano- and micro- filler mixture composite (NMMC) with 1.5 vol % organically modified layered silicate (OMLS) is almost the same as that of the conventionally filled epoxy and a very small influence of modifier ions of LSs is observed on these results. At room temperature there was no significant difference between the results for conventional filled epoxy resin and the NMMC/1.5 vol % OMLS on volume resistivity values, but increasing the temperature, resistivity decrease slightly in the case of nanocomposites [99].

Castellon *et al.* [26] observed that the conduction currents are significantly influenced by the SiO_2 concentration compared to unfilled epoxy resin. The greater the concentrations of micro- and nanoparticles in the base polymer are, the greater the conduction currents are obtained [26]. All the obtained results were explained through the Schottky model approach.

Singha *et al.* [32] analyzed the variations of DC volume resistivity with respect to filler concentrations (TiO_2, Al_2O_3 and ZnO) in epoxy nanocomposites. Even

the introduction in the systems of free ions by adding inorganic particles, which can increase the DC conductivity of composites, their influence was not found to be significant in this study [32]. Patel *et al.* [100] performed similar studies on nanocomposites based on epoxy resin and Al_2O_3 nanofillers.

Lutz *et al.* [101] analyzed the influence of water absorption on volume resistivity of epoxy resin insulators. They proposed a model (based on Fickian diffusion) to simulate the dynamic process of volume resistivity decrease during humidity storage.

Roy *et al.* [102] studied the time dependent conduction characteristics of micro/nanocomposites based on XLPE and 5 wt % SiO_2, unfunctionalized and functionalized with aminosilane, hexamethyldisilazane (HMDS) and triethoxyvinylsilane, respectively. Samples with a thickness of 100–150 μm were prepared and an electric field intensity of 2 kV/mm was applied. As it can be observed from Figure 23, the curves of absorption currents in time for functionalized and untreated SiO_2 nanocomposites have the same slope, but the currents values are lower for functionalized materials. It was observed that the absorption currents are consistent with the loss tangent behavior in the low frequency region, which strongly suggests that the conductivity could be associated with the interfacial region and/or hydration effects, which are alerted by the enhanced coupling associated with the functionalized materials [102]. Similar results were obtained in other studies [103–106].

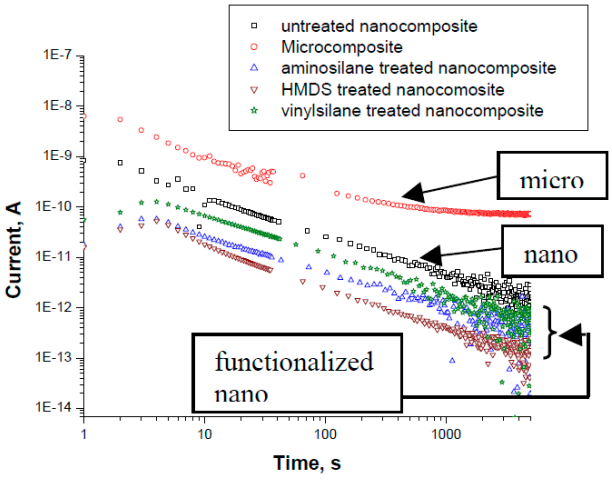

Figure 23. Absorption current dependent on time for XLPE/SiO_2 micro/nanocomposites (© 2016 IEEE. Reprinted, with permission, from [102]).

Lau *et al.* [107] investigated the absorption currents behavior of PE nancocomposites unfilled and filled with 2, 5 and 10 wt % nanoSiO_2, untreated and treated with trimethoxy(propyl)silane coupling agent (C3-treated). The results indicated that

the presence of nanoSiO_2 fillers influenced the values of absorption current. Thus, while the unfilled polymer showed a decrease in time of the absorption currents (in a conventional manner), all the analyzed nanocomposites systems reveal an initial decrease followed by a period in which the current values increase by rising the time of DC field application. It was observed that the time-current characteristics of all analyzed nanocomposites were different from the unfilled polymer and the rate of nanocomposites current values decrease was significantly greater compared to unfilled PE [107]. Using these experimental values, the charge carrier mobility was estimated for unfilled and nanoSiO_2 filled PE. The results on absorption currents measurements can be used to gain understanding of the relationship between space charge accumulation and movement [107].

6.1.2. Micro/Nanocomposites with Controlled Electrical Conductivity

In many high-voltage and medium-voltage applications such as cables accessories, generator or motor end windings or bushing, many problems with the electrical field stress concentrations can be noticed [108]. In order to avoid breakdown or flashover in these situations, it is necessary to control the electrical field throughout materials with tailored conductivity and non-linear conductivity. These termed field grading materials will reduce the local surface stress in the way which will not exceed the breakdown strength in any location. Even in the past time the field grading materials were used only in AC terminations for medium-voltage applications, nowadays they are involved in both medium and high-voltage applications, under AC and DC conditions because voltage requirements steadily increased and the size of equipment decreased [108].

The main components of a cable are conductor, insulation and grounded shield. In operation, the rated voltage (the potential difference between the conductor and the shield) occurs across the insulation system and the radial stress in this region is non-linear [108]. During the operation process, problems can occur in joints or at the end of the cable due to the fact that the shield has to be removed at cable terminations and the concentrated field in the insulation has to be spread out in a controlled manner in this discontinuity. If this action is not taken into consideration, the electric field stresses may cause flashover problems or breakdown [108]. One solution to solve this problem is called geometrical stress control and it refers to the shield bending and increasing the thickness of the insulation. The major drawback of this solution is the size and cost of the components, particularly in high-voltage applications. Another approach refers to the field grading material, which means that the material possess the ability to distribute the field by itself. Usually, the electrical properties of these materials must be field dependent. In terms of HVAC cables, the field grading materials provide field grading in two ways, either by non-linear resistivity or by capacitive field grading. In latter, the relative

permittivity becomes high enough to redistribute the field. For HVDC applications, field grading can be controlled trough a material with field dependent resistivity, which means that the material should become conductive at high fields and stay insulating at low fields [108,109]. In many high-voltage applications, conducting layers are used to obtain equipotential surfaces. Thus, with respect to medium and high-voltage cables, semiconducting layers for levelling and attenuation of high field local values, respectively for reduction of partial discharges phenomena are used. Conducting layers of large radius are commonly tied to the potential of a high-voltage termination to afford some protection from unwanted corona discharges, *etc*. Furthermore, the end windings of high-voltage machines are covered with a semiconducting layer to reduce the partial discharges and leakage [108,110]. As these layers do not have to carry currents, their resistivity does not need to be similar to a metal in order to be effective. For example, a graphite ink is used for rendering cellulose layers conductive as a substitute for metallic foils in the internal stress grading of high-voltage bushing [108]. Similar, semiconducting layers, arranged on both sides of the high-voltage or medium-voltage cable insulation, are manufactured of PE and carbon black or SiC [111,112]. The polymers that are employed for semiconductor layers (acrylates, acetates, PEs, *etc.*) have to exhibit a high thermal stability (up to 250–300 °C during the crosslinking process) to maintain the mechanical properties of the screen and the electrical nature of the inter carbon particle gap [113]. In addition, the polymer materials should comprise a reduced risk for scorching and lumping [112]. Account has to be also taken into the fact that protrusions of the semiconductive layer can push into the insulation and enhance the local electrical field (accelerating electrical aging). The smoothness of a semiconductive material is an important parameter to measure the material consistency and quality. Carbon black has a big influence on the surface smoothness (dispersion of the particles) and on the cleanliness of the semiconductive layers (ions and grit particles) [112]. Semiconductor layers resistivity depends on the polymer matrix nature (recently PE), the concentration of carbon black, process parameters for achieving technological semiconductor layers, temperature, *etc.* [114,115].

In other applications, such as shielding for electronic devices and electrostatic dissipation (ESD), encapsulating, electromagnetic and radio frequency interference (EMI/RFI), thin films coating, packing of electronic circuits, *etc.*, polymeric composite materials with high electrical conductivity are used. The matrixes of these composites are usually based on PE, PVC, PC, PS, epoxy resins, nylon 6.6, acrilonitril-butadien-stiren (ABS), *etc.* As fillers, AlN, carbon and graphite, aluminum, copper, steel or silver particles, polyacrylonitrile (PAN), barium titanate ($BaTiO_3$), *etc.*, are applied. [116,117].

Another alternative to impart some conductivity to conventional polymers can be offered by CNTs and nanofibers. As their conductivities can have values in a broad

range (from semiconducting to conducting materials), CNTs (single walled carbon nanotubes (SWCNTs) or multi-walled carbon nanotubes (MWCNTs)) can be used in many applications [108]. In literature, several studies on this subject [118–120] have been published and one early observation was that the electrical conductivities were not as high as expected given the conductivity of the nanotubes. One example is the study of Cravanzola *et al.* [121] on a piezoresistive sensor device, which has been made by integrating two piezoresistive fibers into two sandwiched PP panels. The fibers were prepared by extrusion from piezoresistive polymeric composites manufactured by melt mixing PP with expanded graphite (EG) and/or MWCNTs (1–2 wt %). It was shown that due to the applied loads mechanical deformation remarkably affected the resistivity of the materials. Haznedar *et al.* [122] investigated composites based on graphite nanoplatelets (GNPs) and/or (MWCNTs)/LDPE and showed the synergistic role of CNTs (1D) and GNPs (2D) in improving the conductive properties of the materials.

Multiple studies regarding the properties of composites demonstrated that percolation phenomenon is very important in controlling electrical properties of these materials, considered as disordered systems [108]. Regarding polymer composites with conducting or semiconducting fillers, there is a critical volume/weight concentration of particles in the matrix, called percolation threshold, above which the electrical or thermal conductivity increases suddenly, as a result of a continuous conductive path formation [108].

In classical percolation, theory applied to composites a physical connection between the filler particles and the conductivity (σ) near the percolation threshold can be described by the power law:

$$\sigma \propto (\phi - \phi_c)^t \tag{3}$$

where ϕ is the volume fraction of filler, ϕ_c is the percolation threshold and t is a power law constant that depends on the geometry of the system [108,116,122]. ϕ_c is also a function of the filler geometry, dispersion and the type of connectivity between particles (*i.e.*, tunneling *versus* Schottky barrier) [62]. Typical values for three dimensional systems are $t = 2.0$ and $\phi_c = 0.17$ for spherical particles [108].

The model requires some modifications due to the filler geometry, dispersion and conduction in nanoparticles filled polymers. In the case of polymers nanocomposites, there can be a very thin polymer layer completely encasing the nanofillers that prevents direct particle-particle contact. In this case, electrical percolation occurs when particles are close enough for tunneling conduction through the interstitial layer (*i.e.*, carbon black filler polymers) [108]. In the case of spherical nanofillers that are not perfectly dispersed in the polymer matrix, there are resulting fractally and not necessarily spherical agglomerates during synthesis and processing.

This situation will shift the percolation threshold because the aspect ratio of nanofillers is greater than one or they effectively fill a larger volume because of the fractal shape. Thus, ϕ_c could be predicted by using the concept of an excluded volume, which is the volume around the filler that cannot be occupied by the center of another object [108]. Due to the fact that CNTs tend to bundle, their shape remaining cylindrical, a hard core model is the most appropriate to estimate the percolation threshold.

Thus, nano/microfillers offer the ability to tailor and optimize the electrical properties of polymers, but their commercial use meets challenges such as a poor dispersion performance during large scale processing and understanding the electrical and thermal conduction mechanisms.

6.1.3. Relative Permittivity and Loss Factor

Many research studies were performed on the relative permittivity and loss factor of micro/nanocomposites materials [123]. If several tens weight percentage of inorganic microfillers are introduced in polymers, usually the relative permittivity of the composite increases [33]. This is because fillers have a higher permittivity by nature compared to the base polymers and they cause Maxwell-Wagner interfacial polarization, which provide information about charge trapping associated with internal surfaces and relaxation processes associated with dipole reorientation [124]. This type of polarization will increase the values of loss tangent, too [33]. Increased values for microcomposites are usually explained in the terms of the Lichtenecker-Rother logarithmic law of mixing [33]. Conversely, the addition of nanoparticles causes major changes in the dielectric response and their permittivities were found to decrease in many cases, such as Figure 24a,b from Nelson *et al.* [22] experimental studies.

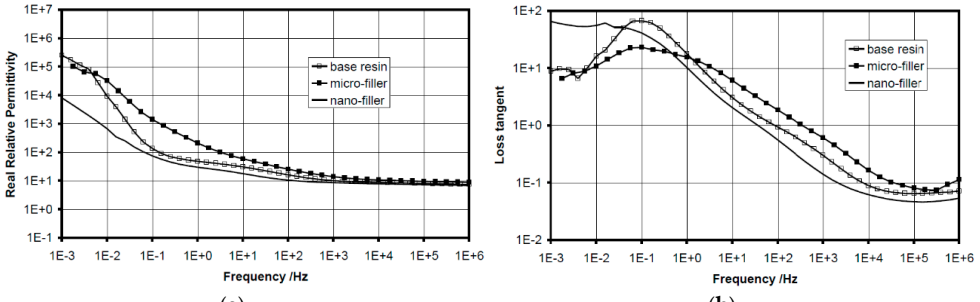

Figure 24. (**a**) Real part of relative permittivity and (**b**) loss tangent of unfilled epoxy resin and epoxy/ 10 wt % TiO_2 micro/nanocomposites materials at 393 K (© IOP Publishing. Reproduced with permission. All rights reserved [22]).

At high frequencies, the microcomposites showed a higher relative permittivity, probably, due to the higher permittivity of fillers incorporated in the base polymer ($\varepsilon_r(TiO_2) \approx 99$) [22]. For example at 1 kHz and 393 K, the measured relative permittivities were 9.99 for the base resin, 13.8 for microcomposites and 8.49 for nanocomposites, which is significantly less than the base polymer. This result suggests that the interaction zone, which surrounds the nanoparticles, has a profound effect on the dielectric behavior of nanocomposite and gives rise to limited cooperative movements of dipolar reorientation within them [22,124]. This behavior could be also due to the movement restriction of epoxy molecules end-chains of side-chains by the presence of nanoparticles [22].

In the mid-range of frequency between 0.1 and 100 Hz, the base resin and the nanocomposites show the same behavior with a small dielectric relaxation, probably due to the bound water [22,124]. The real permittivity of the microcomposite shows a significant increase with decreasing frequency associated with Maxwell-Wagner polarization [22].

At low frequencies, the nanocomposite materials show a different behavior. The slope of the real part changes from -2 to -1 in these Bode plots and the loss tangent is flat and independent of frequency and this can be explained by the "low-frequency dispersion" (LFD) proposed by Jonscher [125] or what Dissado and Hill [126] refer to as "quasi-DC" (QDC) behavior. This behavior is observed when charge carriers have some limited freedom of movement within the material and they may follow tortuous paths under the influence of the electric field, that do not allow complete transport through the material [22]. Since nanoparticles could cause morphological changes to the epoxy resin during the crosslinking process, a "dielectric interaction" layer surrounding these particles could be formed. Lewis [79] has considered the electrical (polarization and conduction) phenomena in the zones that are surrounding the nanoparticles and the formation of a charged layer (Stern layer) on the surface of the particles, encircled by a diffuse charged layer (Gouy-Champan layer) [76,127]. The Gouy-Champan layer is highly conductive compared to the polymer base and charge movement through it would be relative facile [22]. If these layers overlap between several nearby nanoparticles, charge movement over limited distances will be facilitated and the path-lengths of such carriers would form a distribution [22]. Dissado and Hill [126] modeled this field-enhanced percolation in the terms of fractal circuits. Therefore, the reduction of the fillers concentration from 10 to 1 wt % did not bring fundamental changes, but nanocomposite materials showed a low frequency response, more typical of the base polymer and microcomposites, suggesting that behavior changing requires filler concentrations higher than a few percent [22].

Singha *et al.* [128] analyzed the dielectric behavior of epoxy nanocomposites with single nanofillers of Al_2O_3 and TiO_2 at low filler concentrations (0.1/0.5/1/5 wt %) over a frequency range of 1 MHz–1 GHz. The experimental results obtained on these

nanocomposites samples showed very different dielectric characteristics compared to those for microcomposites. In the case of polymer microcomposites the permittivity was increasing by rising the filler concentration, but for a certain concentration of nanofillers into the polymer and depending on their permittivity value, the equivalent permittivity of the epoxy nanocomposite is smaller compared to the one of the base resin, for all the measured frequencies. These results suggest that there is a strong dependence of the filler permittivity and concentration on the equivalent permittivity of the nanocomposite material for all the analyzed frequencies. The loss tangent behavior was not affected by the filler concentrations, but in the case of epoxy/Al_2O_3 nanocomposites, loss tangent values were found to be marginally lower at all concentrations when compared to the values for unfilled polymer [128].

Kochetov *et al.* [129] realize a study on the dielectric spectroscopy of epoxy-based nanocomposites filled with different types of particles, such as Al_2O_3, AlN, MgO, SiO_2 and BN. The nanoparticles surfaces were modified with a silane-coupling agent, in order to realize the compatibility between the inorganic and organic components and to obtain a better dispersion of the nanofillers into the polymer matrix. The relative permittivity of nanocomposites shows an unusual behavior. It was observed that the introduction of a low percentage (below 5 wt %) of high permittivity filler results in a decrease of the bulk polymer permittivity. This can be explained by the presence of the interface layer of surface modified particles, which plays a more important role than the nature of the particles and also by the immobilization caused by the surface treatment of the nanoparticles [129]. It was observed that dielectric losses in the system do not change significantly with the addition of nanofillers up to 5 wt. % [129]. Similar studies on dielectric behavior of micro/nanocomposites systems based on epoxy resin and different types and concentrations of filler were performed by Mackersie *et al.* [123], Fothergill *et al.* [124,130], Tanaka *et al.* [4,33], Singha *et al.* [32,128], Smith *et al.* [104], Plesa *et al.* [131], Kozako *et al.* [132], Castellon *et al.* [26], Heid *et al.* [133], Mo *et al.* [134], *etc.*

Roy *et al.* [102,135] analyzed the dielectric behavior of different systems based on XLPE/SiO_2 functionalized with amino-silane, hexamethyl-disilazane (HMDS) and triethoxyvinylsilane agents. The dielectric spectroscopy analyses (see Figure 25a,b) provide considerable insight into the nature of the structure, which contributes to the polarization and loss. The results showed that the untreated nanocomposites exhibit a relative permittivity lower than the unfilled polymer, which suggests the presence of an interfacial zone around the particles with a smaller permittivity compared to the bulk polymer [102]. A marked dispersion was observed in the case of unfilled XLPE at the frequency of 1 Hz, but was eliminated for the cases of functionalized nanocomposites. With respect to the loss tangent, it is very significant that a QDC conduction region appears in the case of untreated nanoparticles, which suggests the presence of a conductive interface in their case [102]. Low frequency dispersion

can be observed in microcomposites which is absent in all nanocomposites. This behavior likely results from Maxwell-Wagner polarization, which is mitigated for the nanodielectrics [102]. Similar studies on dielectric behavior of micro/nanocomposites systems based on polyethylene and different types and concentrations of filler were performed by Ciuprina *et al.* [83,136–138], Tanaka *et al.* [24], Panaitescu *et al.* [139], Plesa [84], Hui *et al.* [140], Lau *et al.* [53], *etc.*

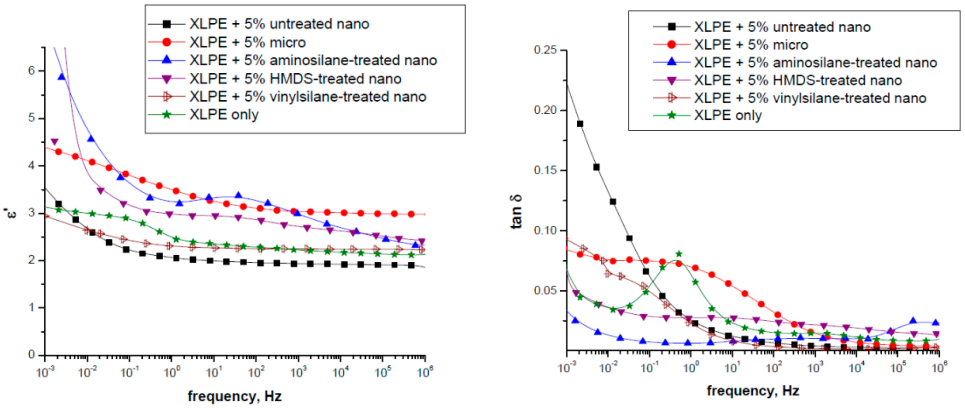

(**a**) (**b**)

Figure 25. (**a**) Real part of relative permittivity and (**b**) loss tangent of functionalized XLPE at 23 °C (© 2016 IEEE. Reprinted, with permission, from [102]).

In other systems such as PI/SiO_2 materials [141], loss tangent tends to decrease for pure PI, PI/SiO_2 microcomposites and PI/SiO_2 nanocomposites, at low frequency region, up to 200 Hz. Regarding PI/SiO_2 microcomposites, a peak appears in the middle frequency region (about 1 kHz) due to the Maxwell-Wagner interfacial polarization and is more much reduced in terms of PI/SiO_2 nanocomposites. This peak can be caused by the mitigation of the field around fillers due to their size differences [4,141]. Room temperature vulcanized (RTV) silicone rubber/LS nanocomposites exhibit a slight increase of loss tangent and a slight decrease of relative permittivity at the industrial frequency [4]. Evaluation of the dielectric behavior seems to be more complicated when comparing neat polymer, microcomposites and nanocomposites materials [4]. The most important aspect to be clarified is whether or not relative permittivity and loss tangent are reduced by nanomization at the industrial frequencies. In literature, some reported data indicate a certain reduction whilst other data did not, which creates confusions [4]. These results can depend on many factors, such as how inorganic and organic components are compatibilized, the dispersion of the fillers in the base polymer, fillers agglomerations, humidity, temperature, *etc.*

6.1.4. Partial Discharges and Erosion Resistance

The resistance of insulating materials to partial discharges (PD) is a very important property for high-voltage applications, such as the stator end windings of rotating machines or wires of randomly wound motors or HVDC XLPE cables, where PD will gradually erode the insulating materials and cause breakdown [25]. PD resistance of polymer insulation can be evaluated by using several configurations of electrode systems such as International Electrotechnical Commission (IEC) electrode and rod-to-plane electrode systems. The former gives surface roughness, while the latter allows evaluation of erosion depth and can be used for micro/nanocomposites materials characterization [142].

Krivda *et al.* [25] evaluated the resistance to erosion due to PD of the epoxy micro/nanocomposites mixtures, using a rod-to-plane electrode system (see Figure 26a,b). From the results showed in Figure 26a, it became clear that a combination of micro and nano-sized fillers in epoxy composites provided better protection against PD erosion than the base resin, composites containing either solely microfillers or solely nanofillers [25]. Due to the fact that results depend on the test conditions (Figure 26a) shows the results obtained at 4 kV/600 Hz and Figure 26b shows the results at 10 kV/250 Hz) it is impossible to identify the best combination of micro and nanofillers in the polymer matrix. Nevertheless, from the obtained results is clear that micro+nanocomposites had smaller erosion depths and longer times to failure compared to unfilled resin and micro/nanocomposite materials [25]. When the material is only filled with microparticles, there is a relatively large volume of neat epoxy that is exposed to PD and degrades much faster compared to inorganic fillers. Inorganic particles can easily withstand temperatures above 1000 K, whereas epoxy thermally decomposes at 600 K and gives rise to large erosion depths in microcomposite materials. When nanoparticles are added into the mixture, they are filling the space between microparticles, creating additional barriers to PD. In addition, when the epoxy resin layer from the top is degraded, nanoparticles are released, but remaining on the surface, provide an additional PD protection of the composite [25].

Many experiments were done to investigate PD resistance of epoxy micro/nanocomposite materials. Most of them demonstrated that the addition of nanoparticles could improve this electrical property, despite of using the epoxy without fillers [143].

Iizuka *et al.* [144] analyzed two types of epoxy/ SiO_2 nanocomposites, such as Aerosil (prepared by dispersing commercially available nanoSiO_2, termed Aerosil, in epoxy resin and by curing the whole mixture) and Nanopox (prepared by directly curing available mixture of epoxy and nanoSiO_2, termed Nanopox) in order to clarify the effect of nanofiller dispersion and coupling agents on the electric filed

endurance. It was found that partial discharges resistance was improved only by adding nanofillers and coupling agents [144].

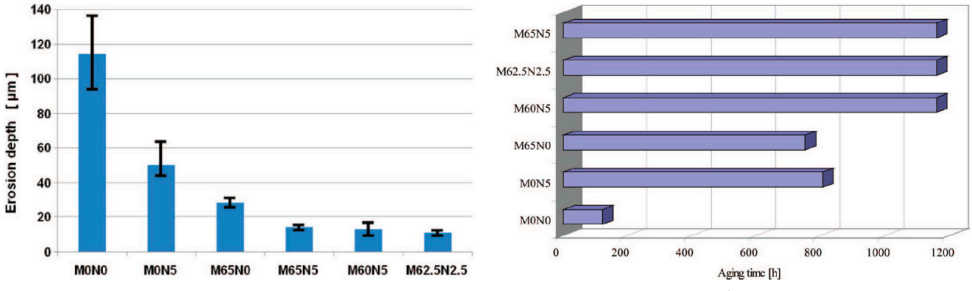

Figure 26. (**a**) Partial discharge erosion depths measured on neat epoxy resin (M0N0), 5 wt % nanoSiO_2 (M0N5), 65 wt % microSiO_2 (M65N0), 65 wt % microSiO_2 + 5 wt % nanoSiO_2 (M65N5), 60 wt % microSiO_2 + 5 wt % nanoSiO_2 (M60N5), 62.5 wt % microSiO_2 + 2.5 wt % nanoSiO_2 (M62.5N2.5) epoxy composites aged at 4 kV/600 Hz for 60 h; (**b**) time to failure of epoxy composites materials with 10 kV/250 Hz applied (© 2016 IEEE. Reprinted, with permission, from [25]).

Tanaka *et al.* [145] investigated PD endurance of epoxy and 1, 2, 3, 4, and 5 wt % SiC nanocomposites in comparison with that of epoxy/SiO_2 nanocomposites. It was remarked that epoxy resins could be improved in their PD erosion performance by replacing SiO_2 with SiC nano fillers, while the erosion profile was narrow in epoxy/SiO_2 nanocomposite. It can be concluded that SiO_2 fillers remain more stuck on the surface after exposure to PD than SiC fillers [145].

Preetha *et al.* [146] analyzed PD characteristics of epoxy nanocomposites samples with a good dispersion of Al_2O_3 particles (0.1, 1, 5, 10 and 15 wt %) into the polymer matrix. PD experiments were conducted at 10 kV for different durations using IEC type electrodes. The results were compared to unfilled epoxy and epoxy microcomposites. It was observed that even for a concentration of 0.1 wt % Al_2O_3 nanoparticles, the PD resistance of nanocomposite improved considerably. It was observed that the inter-particle distance has a significant effect on the discharge resistance to degradation and the improvements are attributed to the interactions between nanoparticles and the epoxy chains [146].

Kozako *et al.* [147,148] investigated PD for four types of epoxy nanocomposites with nanoTiO_2, two different sizes of SiO_2 and LS, unfilled epoxy and filled with microSiO_2 (see Figure 27a,b).

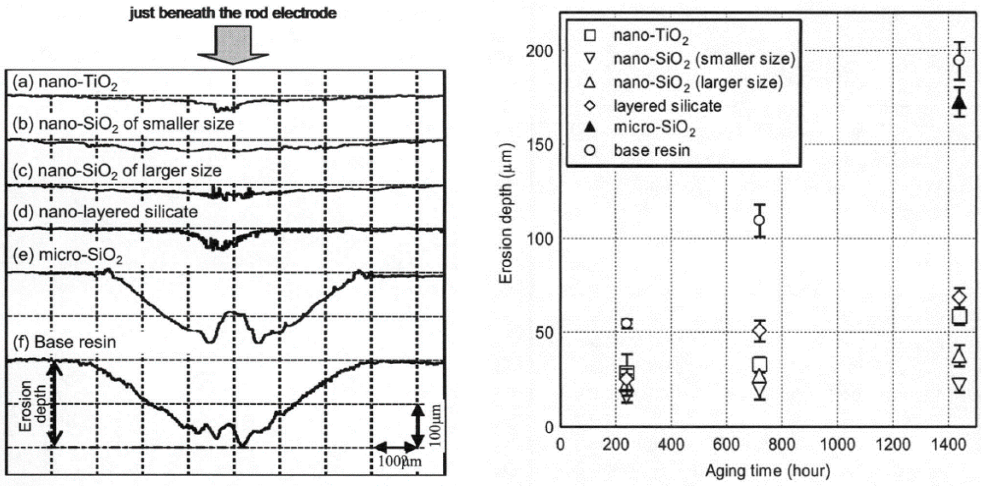

(**a**) (**b**)

Figure 27. (**a**) Surface profiles of erodated areas due to PDs in the samples containing different types of micro/nanofillers and without fillers after 120 h adding at 720 Hz; (**b**) Temporal change in erosion depth of area eroded by PDs at 4 kV of 720 Hz (© 2016 IEEE. Reprinted, with permission, from [148]).

Li *et al.* [149,150] analyzed PD erosion resistance of different kinds of insulation samples, such as neat epoxy, epoxy/5 wt % nanoAl_2O_3 composite, epoxy/60 wt % microAl_2O_3 composite, and combined epoxy/2 wt % nano- with 60 wt % micro-Al_2O_3 composite, using a rod-to-plane electrode system. It was observed that nanocomposites take the longest breakdown time (307 min) compared to neat epoxy (186 min), microcomposite (94 min), and micro/nanocomposite (275 min) [143]. From all these experimental results, it was concluded that by adding a low concentration of nanofillers into epoxy resin matrix, PD are significantly improved [143]. This is most likely due to the strong bonding between nanoparticles and epoxy resin chains at the interface zone, which causes a speed reduction of the material local degradation [32]. Addition of microfillers does not make any significant contribution to PD resistance compared to nanofillers, but they can increase the thermal conductivity, which is an advantage [149]. Similar results were obtained by Henk *et al.* [20], Li *et al.* [151], and Zhang *et al.* [152], Imai *et al.* [153].

The available results and data for XLPE polymer with nanofiller are limited in literature. Tanaka *et al.* [24] reported evidence of the enhanced of XLPE nanocomposite PD resistance values (see Figure 28a,b). The analyzed samples were based on standard commercial XLPE, in order to have more impact on improving the current insulation used for power-extruded cables.

Two methods of PD resistance evaluation were conducted in this investigation: the first by using a rod-to-plane electrode and the second similar to the IEC electrodes system. The first method showed that partial discharges endurance was significantly improved in the case of XLPE with 5 wt % SiO_2 nanofillers (chemically surface functionalized) compared to unfilled XLPE (see Figure 28a,b) [24].

On the other hand, with the second method, which uses an electrode similar to the IEC electrode system to test the three heat-treated samples (unfilled, filled nanoSiO_2 without and with surface-treated filler), no apparent improvement was observed by the addition of nanofillers (see Figure 29a,b). It was generally speculated that this is due to the effect of the filler treatment of the samples, but the test method and data analysis should be further investigated [24,143].

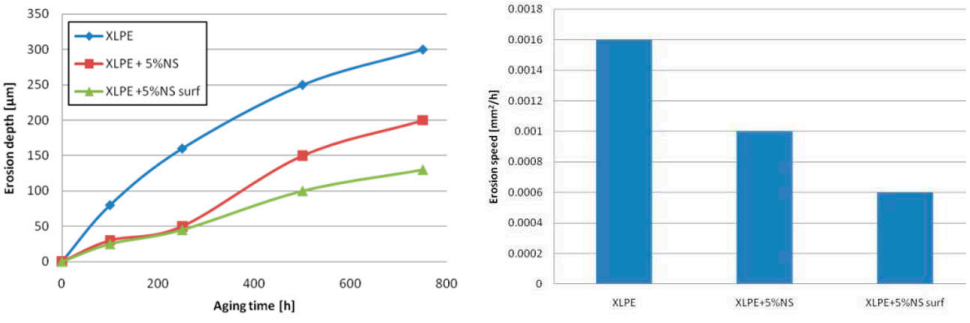

(**a**) (**b**)

Figure 28. (**a**) Evolution of PD erosion depth with aging time of unfilled XLPE, XLPE with 5 wt % unfunctionalized nanoSiO_2 and XLPE with 5 wt % chemical agent functionalized nanoSiO_2 and (**b**) erosion speed for these kinds of XLPE (© 2016 IEEE. Reprinted, with permission, from [24]).

Experimental studies were also performed on other type of systems. Ansorge *et al.* [154] analyzed the influence of various fillers (alumina trihydrate (ATH), Al_2O_3 and SiO_2 with different sizes (from 0.3 to 18 µm)) and their surface modifications (by the material supplier and *in situ* during compounding) on the erosion resistance of high temperature vulcanized (HTV) silicone rubber (SR) composites. It was found that with respect to ATH particles, larger particles showed slightly better results than smaller ones, due to the formation of boehmite [AlO(OH)], which causes a release of the bound water if the temperature exceeds certain values. The particles modifications with vinyltrimethoxysilane (VTMS) and methyltrimethoxsilane (MTMS) improved not significantly the erosion resistance of the composites, but reduced the water-uptake. It was concluded that to achieve a low erosion rate, high- filler loadings are necessary [154]. Heid *et al.* [133] found that incorporation of hexagonal boron nitride (h-BN) particles in epoxy resin resulted

in significant improvements of parameters such as resistance to PD. Other studies showed that PD resistance improves in PI by nanostructuration with LS [33] and PD resistance was larger in PI/SiO_2 nanocomposites than pure PI [4]. In summary, it is indicated that nanomization improves PD resistance of polymers, but depends also how nanofillers are dispersed in the polymer matrix and the compatibility between organic and inorganic components [4].

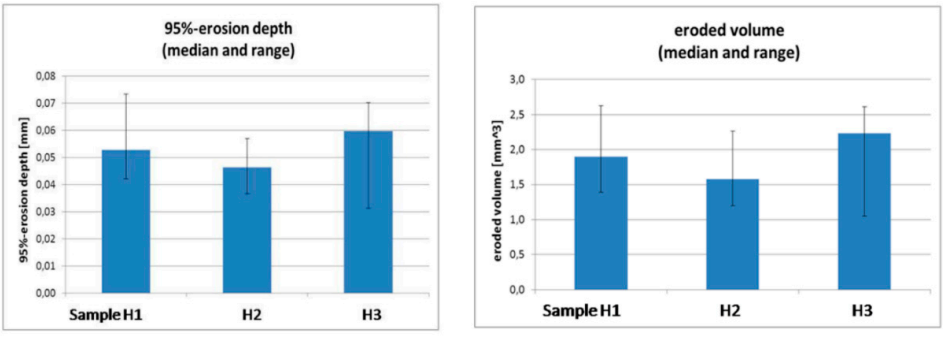

(**a**) (**b**)

Figure 29. (**a**) PD erosion depth and (**b**) PD erosion volume for unfilled XLPE (sample H1), XLPE/5 wt % unfunctionalized nanoSiO_2 (sample H2) and XLPE/5 wt % functionalized nanoSiO_2 (sample H3) (© 2016 IEEE. Reprinted, with permission, from [24]).

6.1.5. Space Charge Accumulation

Space charge occurs in a dielectric material when the rate of charge accumulation is different from the rate of removal and arises due to the moving or trapped internal charges, such as electrons, holes and ions [155]. It is generally undesirable since it causes a distortion in the electric field, increasing the internal field locally within the insulator, which will lead to a faster and premature failure of the material [124,155]. Thus, the homocharge (charge near an electrode of the same polarity as the electrode originally in contact with it) decreases the electric field in the electrode vicinity. As a result, a concomitant increase of the electric field elsewhere in the insulator volume is undesirable. This increase can lead to an intensification of partial discharges in the insulating system which results in an acceleration of the material electrical degradation process and a reduction on its lifetime [124]. Heterocharge increases the electric field next to the electrode, so a reduction of space charge accumulation is therefore an important goal [124]. Thus, the mechanisms of space charge formation are considered as a determination factor in establishing the overall dielectric properties of a polymeric insulation system and they are very complex in comparison to many other types of materials [155]. In semicrystalline PE, the interfaces between

the crystalline and amorphous phases are associated with the presence of charge trapping sites, which are likely to influence the charge accumulation. By the addition of nanofillers, the charge transport mechanism will become much more complicated because fillers will introduce numerous interfaces and interactions between the polymer and nanofillers. The presence of such interfaces will introduce/modify the distribution of the trapping sites within the system and the charge transport mechanisms will be affected [155]. Space charge is usually measured by different methods, such as piezoelectric induced pressure wave propagation (PIPWP) method, laser induced pressure propagation (LIPP) method, thermal step method (TSM) and pulsed electro-acoustic (PEA) method. Being aware of space charge density by different analytical and numerical methods, the electric field distribution and its maximum field values can be calculated [33]. The early experimental work regarding the space charge accumulation in nanocomposites was reported in comparison with microcomposites [22]. Nelson *et al.* were the first in reporting the reduction of space charge density through nanocomposites compared to microcomposites based on epoxy resin and TiO_2 [22]. Figure 30 demonstrate the difference between nanocomposites and microcomposites based on epoxy resin with 10 wt % of TiO_2, with the average diameter of 23 nm/1.5 μm and shows the maximum field intensity (at that point in the sample, where the electric field is highest) as a function of time for the two systems [22].

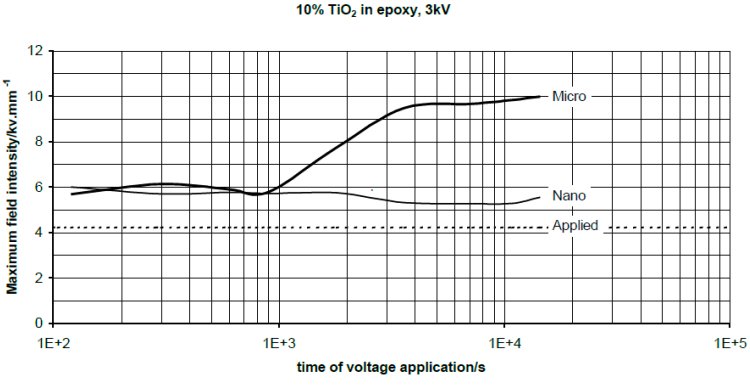

Figure 30. Maximum field intensity as a function of voltage time application on epoxy/TiO_2 micro/nanocomposites (© IOP Publishing. Reproduced with permission. All rights reserved [22]).

Accordingly to these analyses, it was observed that the maximum field in microcomposites builds up to over twice the average applied electric field, whereas nanocomposites stabilize at the field just a little bit higher than the average [33]. Trials were made in order to assign the polarity of charge formed in composites, but

they were not conclusive if the charge formed near the electrodes is homo or hetero, due to the complicated distribution and conditions that affect space change [33].

In literature, it was reported that space charge is mitigated by nanostructuration in different nanocomposites systems, such as epoxy/TiO_2, Al_2O_3 and ZnO, PP/EVA layer silicate and LDPE/TiO_2 [33]. Yin *et al.* [156] analyzed nanocomposites of LDPE with TiO_2, prepared via solution blending method. The space charge distribution of the samples with and without nanoTiO_2 was measured with PEA method. It was found that hetero-polar space charge near electrodes was much less in LDPE/TiO_2 nanocomposites compared with pure LDPE under lower DC stress, no more than 40 kV/mm [4,156]. The space charge inside the nanocomposites was much more uniform compared to the base polymer, which means that electrical stress concentration was improved under DC stress in nanocomposites [4,156]. Another observation was that the decay rate of the space charge remnant in LDPE/nanoTiO_2 increased by increasing TiO_2 concentration, when short-circuited after pre-stress at 50 kV/mm for 1 hour [4,156].

CIGRE Working Group D1.24 [24] realized a comprehensive experimental investigation of XLPE and its nanocomposites with fumed SiO_2. The research studies were carried out in different countries, but all the samples were prepared by only one source and evaluated by experts from several laboratories [24]. Three types of samples were analyzed involving unfilled XPLE (standard commercial material used for extruded power cables—sample 1), XLPE with 5 wt % unfunctionalized nanoSiO_2 (sample 2) and XLPE with 5 wt % functionalized nanoSiO_2 (sample 3). The samples were vacuum heat treated at different temperature values and time durations. Two types of measurements systems were applied to measure space charge in XLPE samples, such as PEA method and thermal step (TS) method at high/low field, by different research teams [24]. One of the results revealed that the lowest space charge amount is obtained when the nanofiller is surface treated (see Figure 31).

The overall results showed that heterocharge is generated for unfilled XLPE and is due to some cross-linking residues and natural impurities [24]. On the other hand, it was confirmed that nanofillers reduce this heterocharge since nanoparticles are characteristic for impurities absorbance. Concerning the charge injection, it was shown that homocharges are easier injected into filled than unfilled XLPE and when nanofillers are added, a charge compensation takes place. It was also highlighted that charge packets appeared for very high electric field values (near breakdown) [24]. This unstable and chaotic phenomenon consists of a slowly travel across the insulator of some waves of charges, with a rate of about 1 mm/hour and a magnitude that can double the local electric field. These charge packets are generally found to be reduced by the addition of nanoparticles [124]. Similar findings were obtained also by Lau *et al.* [155] on nanocomposites based on XLPE with 2 wt %/5 wt %/10 wt % treated and untreated nanoSiO_2.

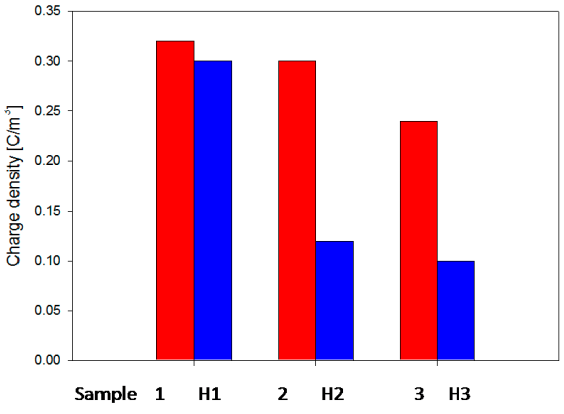

Figure 31. Space charge distribution at 20 kV/mm in unfilled and filled XLPE (samples 1, 2 and 3) before and after treatment (samples H1, H2 and H3) at 80 °C for five days (© 2016 IEEE. Reprinted, with permission, from [24]).

In other polymer systems, such as EVA and i-PP, charge accumulations were considerably large at the field value of 60 kV/mm, but tended to decrease by increasing the addition of nanofillers from 2 to 6 wt % [33]. A common behavior is the charge reducing at high electric field due to nanofillers introduction, while it is increasing at low field due to ionic impurities included in nanofillers. This charge can be swept away by the pretreatment of nanofiller purification [33].

In summary, the following findings are confirmed as effects of nanostructuration: space charge increases at low fields and decreases at high field; space charge inception field decreases; space charge is generated internally and charge decay time decreases [124].

6.1.6. Electrical Breakdown

Electrical breakdown of insulating materials is an important factor in high-voltage applications [59]. The incorporation of inorganic fillers into the base polymer can significantly modify the electrical breakdown of the composite material, depending on the filler concentration, their shape, size and surface modifications with different agents, materials homogeneity affected by the dispersion of the fillers into the base polymer, and the electrical properties of the fillers [59]. In order to obtain high electrical breakdown strength of composites is it necessary to choose fillers with similar electrical characteristic as the polymer matrix, since electric field distortion and enhancement can be caused by the differences in relative permittivity and electrical conductivity between inorganic fillers and organic polymers [59]. The dielectric strength of the polymers can be deteriorated by high-permittivity fillers ($BaTiO_3$, SiC, ZnO and AlN) and high electrical conductivity fillers (carbon black,

carbon fiber and nanotubes, graphite, metals), but they can be used in applications demanding high thermal conductivity materials [59]. Low permittivity and high electrical resistivity fillers can be used in polymer composites with high thermal conductivity and high breakdown strength for the insulation systems of electrical equipment. For example, combining BN nanofiller (70 nm, 10 wt %) with microfiller (500 nm, 1.5 µm, 5 µm, 10 wt %), Andritsch *et al.* [30] demonstrated an increase in the DC breakdown strength of an epoxy composite. From Figure 32a it can be observed that the increase coincides with the increase of the interfaces in the composite material [30]. It is suspected that one of the key parameters in improving the dielectric behavior of nanodielectrics refers to the strong interfaces between polymers and fillers, because of their surface modifications [30]. Even when the functionalization of nanoparticles was not performed, surprising results were obtained [30].

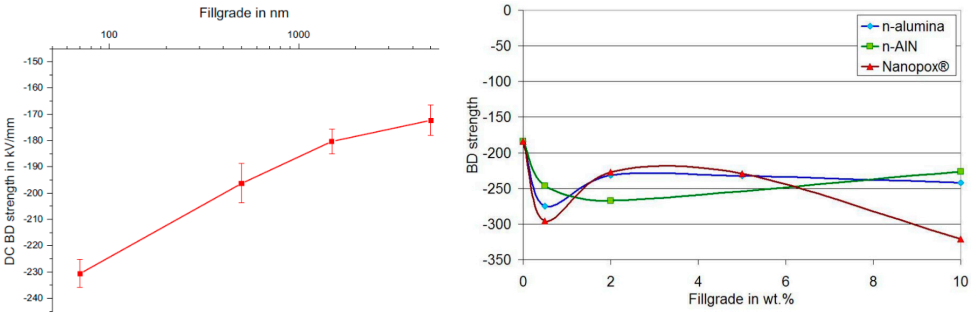

(**a**) (**b**)

Figure 32. (**a**) Short term DC breakdown strength for BN/epoxy resin composites as a function of filler size (© 2016 IEEE. Reprinted, with permission, from [30]) and (**b**) Weibull scale parameter, which shows the voltage for 63.2% failure probability of samples with two components (epoxy resin and nanofillers) (© 2016 IEEE. Reprinted, with permission, from [157]).

The electrical breakdown strength values were measured in the case of epoxy-nanocomposites with Al_2O_3, SiO_2 and AlN as-received/functionalized and plots for a Weibull scale parameter can be seen in Figure 32b, which shows the voltage for 63.2% failure probability of the samples [157].

Electrical breakdown results are frequently analyzed through Weibull statistics (Weibull plots) and represent the cumulative probability of breakdown, which would equate to the proportion of specimens failed for a large sample size [124]. Since these composites had their highest DC breakdown strength for 0.5 and 2 wt % fillers concentrations, it can be assumed that also epoxy resin/BN composites with surface functionalized particles of 70 nm on average would also have higher breakdown strength for fillers concentration between 0.5 and 2 wt % [30]. Other

studies [4] reported that electrical breakdown values remained almost the same up to 10 wt % nanoparticles concentration, while it decreased significantly for 10 wt % microparticles loading.

Roy *et al.* [135] observed that incorporation of SiO_2 nanoparticles into XLPE increased the dielectric strength significantly compared to the incorporation of microparticles and their values were compared with the base polymer in Figure 33.

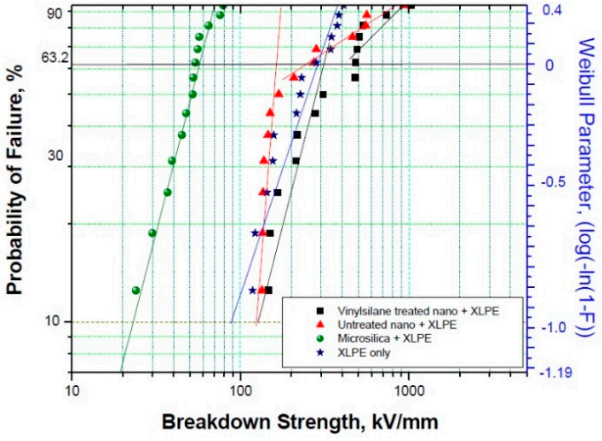

Figure 33. Weibull plot for the electrical breakdown strength of XLPE with 5 wt % micro-/untreated and vinylsilane-treated nanoSiO_2 at 25 °C (© 2016 IEEE. Reprinted, with permission, from [135]).

A dramatic increase in breakdown strength was observed in the case of untreated nanocomposites compared to microcomposites. However, the largest increase was observed for the vinylsilane treated SiO_2/XLPE composites at 25 °C that maintained to increase their values at elevated temperature of 80 °C. For all the analyzed samples, the Weibull shape parameter (β) increased at 80 °C due to an increase in free volume with temperature [135]. Electrical breakdown of polymer-based micro/nanocomposites is affected by several factors, such as degree of crystallinity, space charge accumulation, interfacial area, temperature, free volume and type of bonding [135]. In this study [135], the highest increase in electrical breakdown was achieved with nanoparticles compared to microparticles, where no significant change in crystallinity occurred. It has been postulated that nanoparticles prevent the space charge accumulation in the volume of nanocomposites, by generating local conducting paths. The existence of these paths through the overlapping of nanometric double layers, can explain the breakdown values [135]. Similar results were obtained by Lau *et al.* [155] in their experimental studies.

Li *et al.* observed in their review [151] that DC breakdown strength decreases for micro/ nanocomposites by increasing the filler loadings as illustrated in Figure 34a.

In order to effectively comment on these published experimental data in the review [151], the ratio k_2, between the breakdown voltage values of nanocomposites with different fillers concentration and the ones of the polymer matrix are employed. Below a certain content (about 10 wt %) nanofillers indicate a positive effect on improving DC electrical breakdown strength [151]. From Figure 34a it can be observed that microfillers have a negative effect on DC electrical breakdown [151].

Calebrese *et al.* [158] demonstrated that nanoparticles exhibit both increasing and decreasing of breakdown strength in different systems. In obtaining these variations, the effect of processing can also be a determining factor. For example, it was shown that both microfillers and size agglomeration of nanoparticles, lead to reductions in the breakdown strength [158]. Tanaka *et al.* [4] observed that DC breakdown strength was enhanced for nanocomposites based on PP, while it did not changed significantly in the case of EVA copolymers.

Electrical breakdown property of dielectrics depends also on the applied voltage [151]. It was observed that in the process of data compilation, electrical breakdown field stress presents a strong dependence on the applied voltage as depicted in Figure 34b [151]. This figure clearly reveals that nanofillers are beneficial to improve electrical breakdown strength of unidirectional voltage, which was affected by space charge [151].

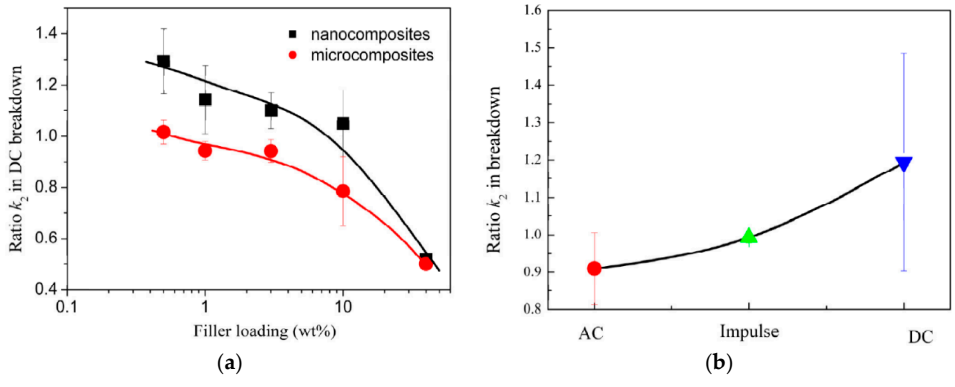

Figure 34. Ratio k_2 (**a**) in DC electrical breakdown *versus* micro/nanofillers concentration and (**b**) of nanocomposites in electrical breakdown depending on the AC and DC applied voltage (© 2016 IEEE. Reprinted, with permission, from [151]).

In other nanocomposites systems based on epoxy resin/ZnO and epoxy resin/layers silicate, better performance in AC breakdown strength were reported [33]. It was shown that the addition of a very small amount of ZnO nanoparticles (between 0.5 and 1 wt %) in epoxy resin, leads to a significant improvement in breakdown time [33].

Therefore, electrical breakdown strength might not be significantly affected by nanomization, under small concentrations of nanofillers and proper dispersion conditions. Favorable results were reported in the cases presented before in comparison to unfilled and micro-filled materials [4].

6.1.7. Tracking Resistance

In high-voltage applications, especially on outdoor polymeric insulators appear tracking phenomena, which means the formation of permanent conducting path across the insulator surface due to surface erosion under voltage stress. During the service, the outdoor polymeric insulators are coated with dust, moisture or environmentally impurities, leading to conducting path formation on their surface. When a voltage is applied, this path will start to conduct, resulting in heat generation and sparks occurrence, which damage the surface of the insulator. Due to the fact that polymers are organic materials, the carbonizes regions at the sparking places act as semiconducting or conducting channels resulting in an increased stress in these regions and over the rest of the material. Consequently, the temperature increases in the vicinity of the channels and a new region is carbonized. As the process is cumulative, the channels increase in time and the carbonized track bridges the entire distance resulting in a failure of the insulation [159].

One common approach for increasing the tracking resistance of polymeric insulators, corresponding to an increase of equipment lifetime, is the introduction of inorganic microfillers into the polymer matrix. In this direction, Piah *et al.* [160] analyzed the tracking resistance through experimental observations of leakage currents values and carbon track development of linear low density polyethylene and natural rubber (LLDPE/NR) blends with and without ATH fillers. The experimental results showed that the compound of 80% LLDPE mixed with 20% NR, without ATH seems to be the best compound based on the least damage and the lowest normalized degradation index [160]. Although the experimental results revealed favorable tracking resistance enhancement, for high-voltage applications, this property of polymeric insulators should be further improved to attain greater reliability [159] and nanocomposites materials could be the answer.

Tanaka [33] considers that silicone elastomers, which can be used for outdoor insulators are expected to have better tracking resistance performances by nanostructuration, but further investigations need to be accomplished in this direction. By addition of ATH nanoparticles in RTV silicone rubber, the tracking performances of the silicone rubber are improved [4]. El-Hag *et al.* [161] obtained experimental results on the erosion resistance of silicone rubber (SIR) filled with 12 nm size fumed nanoSiO_2 and filled with 5 μm size SiO_2 microfiller. It was concluded that the erosion resistance of SIR materials increased by increasing the percentage of fillers, and similar performances were observed for 10 wt %

nano-filled SIR and 50 wt % micro-filled SIR. Sarathi *el al.* [162] demonstrated that the tracking time is higher in terms of aged epoxy nanocomposites compared to pure epoxy. Ageing studies were carried out to understand the surface characteristic variation through contact angle measurements. Raetzke *et al.* [163] tested the resistance to tracking and erosion of silicone rubber with two different kinds of nanoscale SiO_2 filler particles. The results showed a high improvement of the resistance to both stresses for one type of untreated SiO_2 particles at very low filler contents. Later, in 2015, Ansorge *et al.* [154] analyzed the influence of various fillers, such as ATH, Al_2O_3 and SiO_2 with different sizes (from 0.3 µm to 18 µm) and surface modifications (unmodified, modified by the material supplier and *in situ* modified during compounding, using vinyltrimethoxysilane (VTMS) and methyltrimethoxsilane (MTMS)) on the erosion resistance of high temperature vulcanized (HTV) silicone rubber (SR) composites (see Figure 35). The main research focus was on ATH fillers as they have the ability to release water at elevated temperature.

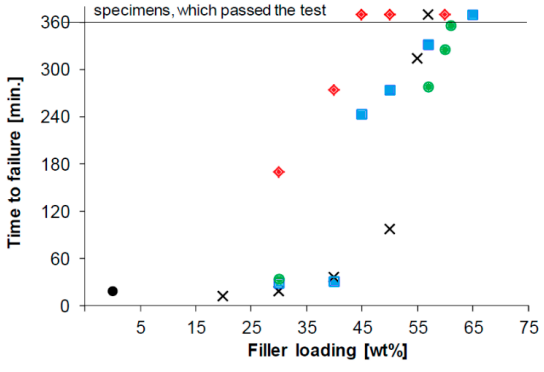

Figure 35. Average time to failure of composites material supplier (crosses), ground modified ATH of 3.5 µm (squares), ground modified ATH of 3.5 µm (diamonds) and surface modified ground SiO_2 particles (circles) in the inclined plane test (IPT) at 6 kV filled at different contents and compared with unfilled base rubber (black circle) (© 2016 IEEE. Reprinted, with permission, from [154]).

It was found that for very small filler contents, ATH was not favorable for the erosion performance of polymeric composite and by employing 20 wt % of filler, the performance is even worse compared to the base polymer. For a positive effect on this property, a sufficient amount of ATH filler must be added into the polymer matrix. The behavior of the surface modified ground SiO_2 particles is slightly worse in case of high filler loadings (> 50 wt %), while there was no substantial difference visible at filler loading of 30 wt %. The composite material filled with ground modified ATH of 3.5 µm shows the best performance. The

performance of ground modified ATH of 3.5 μm and material supplier filler was very similar [154]. Until the present time, literature on tracking performance of polymer nanocomposites is limited. Experimental investigation onto the tracking resistance of polymer nanocomposites would be of great importance, especially in confirming its performance with nanofillers [159].

6.1.8. Electrical Tree Resistance

The propagation of electrical trees represents one of the major causes for electrical breakdown of high-voltage equipment and power cables insulation [164]. In order to extend the lifetime of an insulation until breakdown, composite materials with barriers and surrounding polymer matrix are commonly used in power engineering. The influence of barriers on the electrical trees propagation were analyzed and many research studies were made on the micro/nanocomposites development for electrical breakdown resistance compared to the base polymer.

Ding *et al.* [165] analyzed the electrical tree growth on samples, such as unfilled Araldite epoxy resin and micro-sized $Al(OH)_3$ particle, in different concentrations ranging from 0 to 15 wt %, as reinforcement to enhance the time to breakdown of the composite material. It was concluded that the addition of filler particles in the epoxy resin could make considerable improvements in breakdown resistance by increasing the time of the electrical breakdown with the increase of filler concentrations [165]. Different models could explain the results. For unfilled polymers, it has been assumed that the propagation of electrical trees arises from the formation of a damage process zone (DPZ) which precedes and surrounds the tree tip during the tree growth process [165]. It was supposed that the submicroscopic trees are initiated and grow due to the submicroscopic voids created by thermal fluctuation within the DPZs from the vicinities of the tree tips [165]. With respect to composite materials, it is suggested that by introducing microfillers into the polymer matrix, more submicron-size voids are generated around ATH fillers due to the induced changes in local thermal and residual mechanical stress. Therefore, when a tree channel tip reaches this area, the immovable submicron-voids in the matrix will behave as submicron-trees near the primary tree tip. The DPZ size is then expanded and consequently may increase the resistance to electrical growth of dielectrics and hence increasing the electrical insulation lifetime.

Uehara *et al.* [166] analyzed the tree growth and breakdown characteristics of composites based on polymer barrier film layers molded in an EVA copolymer, using a needle – plan configuration and an AC voltage. The electric field was perpendicular to the EVA/barrier film interfaces. It was found that the barrier film retards the electrical tree development, which punctures the film, or develops along the edge of the film. It was also demonstrated that the pressure of the decomposing gas in the tree channels and the interface of the analyzed composite materials play an

important role in tree propagation [166]. Vogelsang *et al.* [164] analyzed the tree growth diagrams in composites structure of mica-epoxy winding insulations and their growth characteristic was optically analyzed (see Figure 36a). During the electrical tree propagation, electrical discharges take place in the small branches and their structure changes to hollow pipe-shaped channels (see Figure 36a) [164].

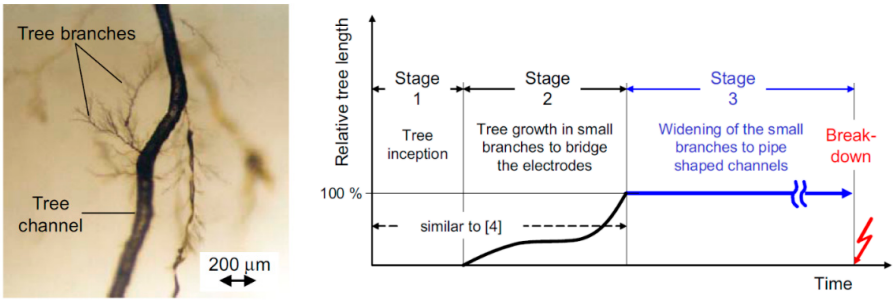

(**a**) (**b**)

Figure 36. (**a**) Optical micrographs of tree branches and channel and (**b**) stages of electrical tree propagation until the final breakdown (© 2016 IEEE. Reprinted, with permission, from [164]).

Experimental results showed that the electrical tree propagation could be slowed down when a barrier is introduced between the needle and the plane electrode. This barrier may cause significantly increased time of breakdown values. The enhancement depends on the barrier nature, their thickness and widths, and the dielectric strength of the surrounding polymer interface. When multiple barriers exists, their arrangement influence significantly the time to breakdown and when they are overlapped a much higher time until breakdown is obtained than impinged ones [164]. Based on these results, Vogelsang *et al.* [164] proposed a model that emphasizes the widening of the small branches to pipe-shaped channels. There are three stage in electrical tree propagation until the final breakdown of the composite material (Figure 36b). The first stage represents the tree inception and the second one is the growth of the first small branches to the opposite electrode. The third stage is the stage where the small branches are widened up to pipe shaped channels. It starts when the first branch has reached the opposite electrode and it ends with final electrical breakdown [164]. It can be concluded that the barrier materials and their processing play a major role concerning the time to breakdown of composite insulation materials [164].

Based on similar experimental results, Christantoni *et al.* [167] simulated with the aid of Cellular Automata (CA), the propagation of electrical trees in an insulating system consisted of epoxy resin and mica sheets, which is affected by

the applied voltage, the local dielectric strength and the relative permittivity of the involved material. The simulation results indicated that the mica barriers hinder the propagation of electrical trees [167]. Iizuka *et al.* [144] analyzed two types of epoxy/SiO_2 nanocomposites, Aerosil and Nanopox samples, respectively, in order to clarify the effect of nanofiller dispersion and of coupling agents on electrical tree resistances and voltage endurance. The study revealed that nanofillers and coupling agents could improve treeing resistance in both cases, but depend on the level of nanofiller dispersion [144].

6.1.9. Water Absorption

The presence of absorbed water can have undesired effects on the improvements of electrical properties of micro/nanocomposites and these influences were analyzed by many researchers [87]. Zhang *et al.* [168] analyzed the dielectric behavior in the presence of humidity and dried nanocomposites consisting of either epoxy resin or PE with different concentration of nanoAl_2O_3. With respect to the epoxy/Al_2O_3 nanocomposites, no difference in the dielectric properties compared to the unfilled polymer were detected under dry conditions. Nevertheless, their dielectric characteristics differed significantly when the adsorbed water amounted to 0.4% b.w. (body weight), which is the normal concentration that occurs under ambient exposure. It can be concluded that the sites for absorbed water in the epoxy nanocomposites increases compared to the unfilled polymer, which does not present interface regions [168]. Zou *et al.* [87] reported that epoxy/SiO_2 nanocomposites absorbed significantly more water than unfilled polymer due to the fact that extra water was located around the surface of nanoSiO_2. Epoxy microcomposites were found to absorb less water than the base resin due to the reduced proportion of the polymer in this composite. These hypotheses were confirmed by the measurements on the water uptake, swelling and density change, as a function of humidity. The water shell model, in which percolation of charge carriers occurred through overlapping water shells, explained the low frequency dielectric results [87]. It was observed that nanofillers with functionalized hydrophobic surfaces considerably reduced the amount of water absorbed in the same conditions of humidity.

Dodd *et al.* [169] analyzed the dielectric properties in the presence of humidity for two types of bisphenol-A epoxy resin systems, Araldite CY1301 and Araldite CY1311. It was found that frequency and magnitude parameters, for all the analyzed electrical conduction and dielectric process were dependent on the humidity. In particular, above the glass transition temperature of both epoxy systems, it was found that absorbed moisture was involved in the formation of a bulk quasi-DC dielectric response (QDC) consistent with cluster formation of the absorbed water molecules [169]. Lutz *et al.* [101] analyzed the water absorption behavior of disk-like mineral filled epoxy resin samples determined by charge of weight measurements

at different relative air humidity. A significant decrease of volume resistivity was achieved by increasing the water content. This dynamic degradation of the volume resistivity during humidity storage was simulated with a model based on Fick's diffusion law and the results were verified by periodic measurements of the volume resistivity on epoxy samples during storage at 99% relative humidity [101].

Calebrese *et al.* [158] accomplished a review study of the experimental literature regarding nanodielectrics, such as PAI/nanoAl_2O_3 and XLPE/SiO_2, which indicated numerous inconsistencies in the obtained results. It was concluded that if the processing parameters of the nanocomposites are not carefully selected, the addition of nanoparticles can alter the structure of the materials and can introduce water into the system, generating cavities and facilitating materials degradation [158].

Hui *et al.* [140] analyzed the dielectric behavior of XLPE/SiO_2 nanocomposites in the presence of humidity. Decreases in AC breakdown strength, increases on losses and space charge formation and significant reduction in water tree aging were obtained. It was also demonstrated that XLPE/SiO_2 nanocomposites have an increased moisture uptake compared to the base polymer, due to the addition of nano SiO_2 particles. The results were hypothetically explained by two major factors, which influence the dielectric behavior of XLPE/SiO_2 nanocomposites, as the concentric water shell around the particles and the charge from inter-particle distances. It was also concluded that a water layer thickness of nanometers tens could initiate percolation in the analyzed XLPE/SiO_2 nanocomposites [140].

In 2015, Lau *et al.* [53] prepared a review article with the most recent findings and issues concerning nanodielectrics research, highlighting the role of nanofiller/polymer interfaces. One important section referred to the water absorption in nanocomposite materials. It can be concluded that due to the hygroscopic character of nanoparticles, the presence of water on their surface lead to agglomerations. Taking into consideration this aspect, nanoparticles and matrix drying under vacuum conditions or nanoparticles surface functionalization, which replace surface hydroxyl groups and physically block water from getting to the surface of the particles, should be necessary steps. The presence of water can have additional effects on the behavior of nanocomposites, leading to changes in their dielectric behavior [158,170].

6.2. Thermal and Mechanical Properties

6.2.1. Thermal Properties

To improve the performance of high-voltage electrical equipment, new electrical insulating materials (with superior properties) are necessary [134]. One important issue is the necessity to use dielectric polymers, as micro/nanocomposites with higher thermal conductivities, which has also excellent processability and low costs.

Most of the used polymers are thermally insulating and have a thermal conductivity between 0.1 and 0.5 $W/m \cdot K$ [59]. One of the possibilities to reach this goal is to introduce high-conductivity fillers in polymers, such as Al_2O_3, AlN, BN, Si_3N_4, beryllium oxide (BeO) or diamond, such as it can be seen in Table 3 [59].

From the all high-thermal conductivity fillers listed in Table 3, only some of them are useful and attractive to be employed in high-voltage applications. Al_2O_3 has a relatively high value of λ and is often used as filler because of the low cost and high electrical resistivity. Nevertheless, the main disadvantage in high-voltage applications is its high relative permittivity ($\varepsilon_r \sim 9$) [59]. Crystalline SiO_2 and fumed SiO_2 are the most commonly material used in electronics and also as fillers to produce highly conductive composites, but their intrinsic thermal conductivity is a bottleneck for the thermal conductivity of their composites [59]. ZnO is a semiconductor and it has been widely exploited as an additive in the rubber industry. Its high thermal conductivity and nonlinear property make its composites useful for electric stress control in high-voltage applications. Another filler with non-linear electrical property and high thermal conductivity is SiC. Due to properties, such as high-saturated carrier drift velocity and high permittivity, its applications in dielectric materials, microelectronic packaging, and high-voltage insulation are limited [59]. Although BeO possesses a higher thermal conductivity than other non-metals and is corrosion resistant, with excellent electrical insulating properties, its toxicity and high cost makes it unattractive for commercial use. Due to the high intrinsic thermal conductivity, low thermal expansion coefficient and high electrical resistivity, AlN attracts much interest. Nevertheless, the low oxidation resistance and relatively high permittivity, limits its applications. Due to its high thermal conductivity and electrical resistivity, low permittivity and density and excellent high temperature resistance, BN is ideal for electronic packaging application. Despite its excellent properties, Si_3N_4 has been rarely used as filler for high-thermal-conductivity composites because of its moderate thermal conductivity. Diamond is used as filler for preparing highly conductive composites, but its high cost makes it unattractive for industrial applications. $BaTiO_3$ has relatively low thermal conductivity, very high permittivity and density, which makes it unattractive for preparing high-thermal-conductivity composites [59].

The effective thermal conductivity of a composite material composed of one type of filler introduced into a polymer matrix depends on the thermal conductivity of the components, the fillers shape, size and concentration, their dispersion into the polymer and the thermal interfacial resistance [59]. Taking into consideration all these aspects, many theoretical models for computing the thermal conductivity of a composite had been proposed until now, but due to the complex influences (inexact data intrinsic thermal conductivity, shape, size, distribution and orientation of the fillers), only few of them fit the experimental data very well [59]. It was observed

that as the intrinsic thermal conductivity of the fillers increases, appears a limit to the thermal conductivity of the composite, as in the theoretical prediction of Nielsen [171] for spherical particles (see Figure 37) with packing fraction 0.637 and the ratios of λ_p/λ_m = 10, 20, 50, 100, 500 and 1000 (λ_p is the intrinsic thermal conductivity of the filler and λ_m is the thermal conductivity of the composite) [59].

Table 3. Thermal conductivities and coefficient of thermal expansion of selected inorganic high-conductivity fillers (Adapted table from [59]).

High-conductivity fillers	Thermal conductivity (W/m· K)	Coefficient of thermal expansion (ppm/°C)
Fused SiO_2	1.5–1.6	0.4–0.5
Crystalline SiO_2	3	10
Al_2O_3	38–42	7
BeO	300	5.5
ZnO	60	2–3
Si_4N_3	86–120	2.7–3.1
BN	29–300	1.1–4.3
AlN	150–220	2.5–5
SiC	85	4.1–4.7
$BaTiO_3$	6.2	6
Diamond	2000	0.11–1.23

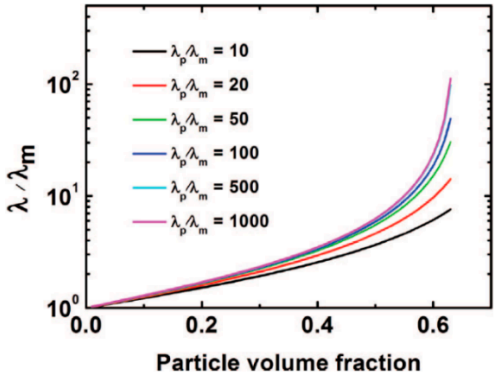

Figure 37. Theoretical prediction of the relative thermal conductivity (λ) of composites (© 2016 IEEE. Reprinted, with permission, from [59]).

Kochetov *et al.* [172] compared different theoretical models for predicting thermal conductivity of a two-phase system with experimental data of nanoAlN and nanoBN particles distributed in an epoxy resin matrix. From Figure 38 was concluded that the Agari&Uno model correlated best with the experimental data on the analyzed nanocomposites.

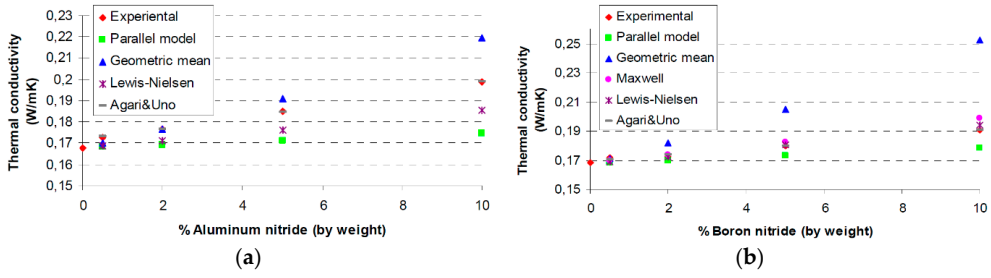

Figure 38. Experimental and predicted thermal conductivity data for (**a**) epoxy resin/AlN and (**b**) epoxy resin/BN composites at 18 °C (© 2016 IEEE. Reprinted, with permission, from [172]).

Heat conduction processes in polymer composites are based on phonons. Interfacial thermal resistance is due to the differences between phonon spectra of different phases of the composites and due to scatterings at the interface between these phases [59]. This means that a large interfacial area can cause large phonon scattering and low thermal conductance. Thus, it is expected that the thermal conductivity of polymer composites to increase by increasing the particle size for a given filler loading. Han *et al.* [173] showed in Figure 39 that the thermal conductivities of all analyzed composites increase by increasing BN concentration and that there is no distinctive difference between BN-Micro, BN-Meso and BN-Nano. These results suggest that the size of BN is not necessarily crucial for the thermal conductivity of the epoxy/hardener/filler composites at low to moderate concentrations as the sizes of these BNs are very different [173].

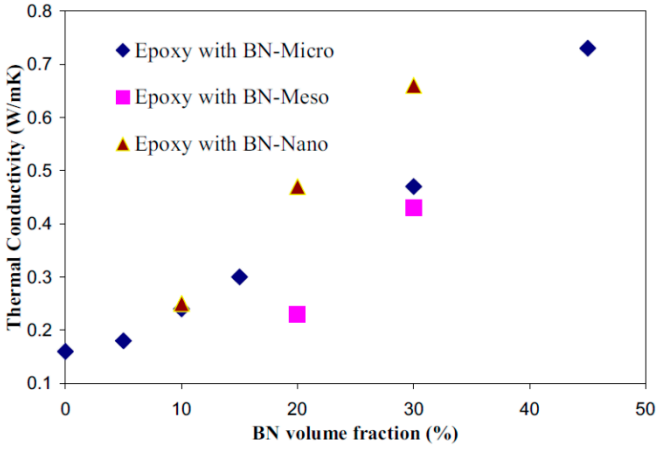

Figure 39. The thermal conductivities of the epoxy composites filled with BN-Micro, BN-Meso and BN-Nano (© 2016 IEEE. Reprinted, with permission, from [173]).

In general, the high thermal conductivity of a composite is achieved when thermally conductive pathways (percolating network) are formed in the material. A percolating network is obtained if either the filler particles are spherical and their concentration is high, or if the particles exceed a critical value. These requirements increase the material and processing costs and could deteriorate the mechanical and other properties of composite materials [59]. In this situation, there are two methods to ensure a low percolating threshold: (i) immiscible polymer blends can be used as matrix and (ii) composites can be prepared by molding the filler-coated polymer particles [59]. It was reported that the thermal conductivity was enhanced for PI nanocomposite filled with coated nanoparticles compared to pure PI and PI microcomposite (see Figure 40) [174].

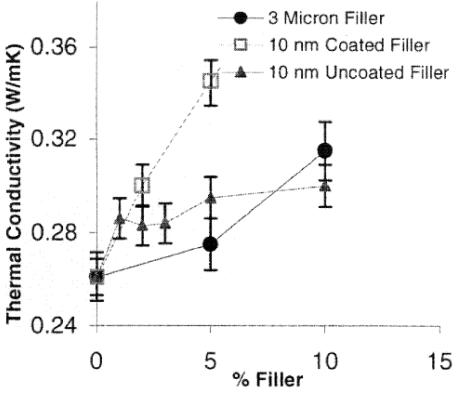

Figure 40. Thermal conductivity in function of the filler concentration characteristics for pure PI, PI microcomposites and PI nanocomposites (nanoparticles uncoated and coated) (© 2016 IEEE. Reprinted, with permission, from [174]).

The thermal conductivity of nanocomposites cannot be completely determined by size, concentration, dispersion, aspect ratio or particles orientation in the polymer matrix [59]. Xu *et al.* [175] showed in Figure 41 that the surface treatment of BN with acetone, silane, nitric acid (HNO_3) or sulfuric acid (H_2SO_4), resulted in epoxy composites with increased thermal conductivity. The greatest increase was given by silane modification and the least effective was obtained with acetone treated particles.

Thermal conduction in glassy and crystalline dielectrics is caused through elastic vibrations of the crystalline lattice. The use of high thermal conductivity fillers can enhance this process because of the rapidly heat transfer along the fillers [59].

Significant progress has been made during the last few years in the research for high thermal conductivity dielectric micro/nanocomposites. Based on the papers and discussions with numerous equipment manufacturers, there is a strong- interest in improved thermal conductivity with various goals such as: (i) lower operating

temperature; (ii) longer service life; (iii) increased operating stress without increasing hot spot temperature; (iv) reduced wall build, *etc.* Various methods have been proposed for improvements ranging from solventless resins to modification of the insulation with high thermal transfer modifiers [176].

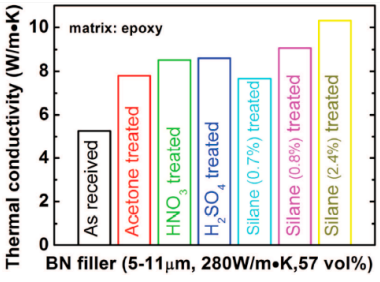

Figure 41. Effect of various surface treatments on the thermal conductivity of epoxy/BN composites (© 2016 IEEE. Reprinted, with permission, from [59]).

6.2.2. Mechanical Properties

Polymer composites used in the production of high-voltage insulating systems, applied in electrical machines, generators, electrical equipment, *etc.*, are often subjected to constant vibrations/abrasion by power frequency magnetic forces and high shear stress under rapid thermal loading conditions [177]. Nevertheless, composite insulation state of the art reports that these mechanical stresses lead to voids/crack initiation or delamination effects with subsequent electrical discharge and catastrophic failure. Many experimental studies were performed on the mechanical properties of composites filled with nano- and micro-fillers and compared with the base polymer.

Yasmin *et al.* [178] investigated composites based on epoxy resin (anhydride-cured diglycidyl ether of bisphenol A, DGEBA) reinforced with 2.5 to 5 wt % graphite. It was concluded that tensile strength and elastic modulus of the composites are increased by adding fillers, and an agglomeration of fillers occurred at 5 wt % fillers concentration. Yang *et al.* [179] studied the mechanical properties of composites based on PP filled with 10, 20, 30 and 40 wt % rice husk flour. They demonstrated that the tensile and impact strength of the composites decreased, while the tensile modulus increased by increasing the filler concentration. In 2005, Lam *et al.* [180] experimentally investigated the mechanical and thermal properties of nano-clay filled epoxy resin composites. The results evidenced that the hardness values of the nanocomposite were increasing by adding nano-clay fillers up to a limit and then were decreasing due to the clusters formed for a high filler concentration. The fracture surfaces observed by microscopic techniques revealed that the size of clusters varied with the nano-clay concentration in the nanocomposite materials. Ray *et al.* [181]

analyzed the mechanical properties of vinylester resin matrix composites prepared with 30, 40, 50 and 60 wt % of fly ash. It was found that fly ash enhanced the stiffness and rigidity of composite, but the mechanical strength was reduced at high filler content.

Later, in 2009, Gao *et al.* [182] characterized the mechanical performance of nanocomposites based on PS with nano$CaCO_3$. Tensile and compact tensile tests showed that the strength and toughness of PS were decreasing after the addition of nano$CaCO_3$ particles, which can be explained by the defects induced by interfacial debonding and nanofiller agglomerations. Asi [183] investigated the mechanical properties of Al_2O_3-filled glass fiber-reinforced epoxy composites. The results demonstrated that the tensile strength and the shear strength of the composites decreased by increasing Al_2O_3 particles content, while the bending strength increased up to 10 wt % filler ratio and decreased at higher ratios.

Panaitescu *et al.* [139] analyzed the influence of nanostructration and fillers dispersion on the mechanical and electrical properties of nanocomposites filled with inorganic fillers, such as SiO_2 and Al_2O_3. An increase of the tensile strength and elongation at break were observed for low nano-oxide concentration (2 wt %). These results were associated with a more favorable dispersion of nanoparticles as well as an increased adhesion at the interface. In 2012, Zaman *et al.* [184] studied the micro- and nano- ZnO-filled i-PP composites with filler concentrations between 2 and 8 wt %. Tensile tests showed that the tensile strength at yield and tensile modulus of the composites tended to increase by increasing contents of microZnO/nanoZnO particles. Nano-filled composites provided improved mechanical properties compared to micro-filled composites for the same filler concentration. It was concluded that the dispersion of particles was optimal at a filler content of 5 wt % since the morphology images and dispersion of nanofillers were better, which led to stronger interfacial adhesion between matrix and fillers. Ibrahim *et al.* [185] investigated composites based on oil palm ash (OPA) as filler in unsaturated polyester, in different concentrations between 10 and 30 vol %. The study revealed that the modulus increases by increasing the filler content, while tensile and flexural strength of UP/OPA composites decrease.

In 2013, Agubra *et al.* [186] analyzed the effects of nano-clay dispersion in glass fiber epoxy composites on the mechanical properties. It was concluded that the high viscosity of the composite generates homogeneity problems due to the agglomeration of the fillers. Chuhan *et al.* [187] investigated the filler size and loading effects on the mechanical and tribological performance of cenosphere-filled vinylester composites. The work revealed that the mechanical and tribological performance could be enhanced, and optimum values were obtained with 6 wt % filler content. Sayer [188] concluded that the elastic modulus and bulking load caring capability of composites based on glass reinforced epoxy resin composites

were increased by adding ceramic fillers, such as SiC, Al_2O_3, and boron carbide (B_4C). Sudheer *et al.* [189] studied the mechanical and tribological characteristics of potassium titanate whisker (PTW) reinforced epoxy composites. It was found that PTW additions present beneficiary effect on density, hardness, and stiffness properties of composites; however, mechanical strength and ductility were found to decrease with the increasing content of PTW. In 2015, Pakash *et al.* [190] studied flexural strength, compressive strength, vickers micro-hardness and density for different concentrations of ceria filler. As the content of ceria is increased, an enhancement of the mechanical properties was achieved until a maximum value was reached and then, these properties decreased again by increasing filler concentration.

Ozsoy *et al.* [191] studied the influence of microfiller (between 10 and 30 wt % Al_2O_3, TiO_2 and fly ash) and nanofillers (between 2.5 and 10 wt % Al_2O_3, TiO_2 and clay) on the mechanical behavior of epoxy based composites. Figure 42 shows the tensile strength *versus* filler content in epoxy resin based micro/nanocomposites. It was observed that the tensile strength of micro-filled composites decreased by increasing filler concentration. In the case of nanocomposite materials, an increase of strength values was observed for up to 2.5 wt % filler content, but beyond this concentration the strength of the composite depleted again.

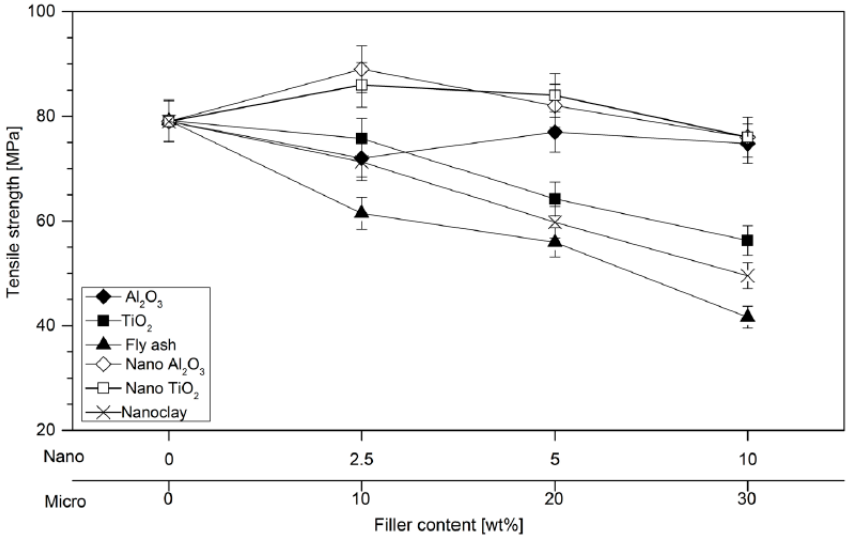

Figure 42. Tensile strength of epoxy resin based micro/nanocomposites *versus* filler content (Reprint with the permission of Strojniski vestnik–Journal of Mechanical Engineering [191]).

Figure 43 illustrates the tensile modulus in dependence on the filler content in epoxy resin based micro/nanocomposites. It was observed that the tensile modulus

of epoxy based composites increased with rising filler concentration, which was attributed to the fact that micro- and nanofillers increased the polymer stiffness [191]. Figure 44 describes the elongation at break *versus* the filler content in epoxy resin based micro/nanocomposites. It is clear that the elongation at break decreased by increasing filler concentration distributed into the base epoxy, due to the fact that fillers imposes to the matrix the brittle behavior [191].

Ozsoy *et al.* [191] attributed the decrease in the tensile strength of microcomposites at high filler concentration to the weak adhesion between epoxy matrix and particles. In terms of nanocomposites, the drop in mechanical strength was associated with the inhomogeneous distribution of fillers at higher concentrations, which led to agglomerations and caused stress concentration regions. When it comes to nano-clay-filled epoxy composite even at low filler contents the decrease in strength was related to agglomeration problems [191]. The drop in elongation at break due to the addition of inorganic filler was mainly attributed to the elastic properties of the composite, which depend on the polymer matrix properties. Nevertheless, in the presence of fillers that restrict the mobility of the polymer, epoxy resin shows brittle behavior and the higher the filler content is, the higher the brittleness of the composite is [191].

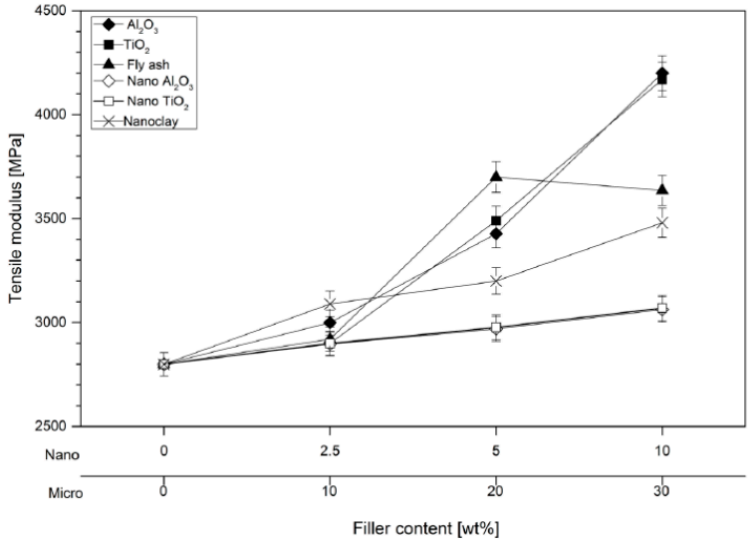

Figure 43. Tensile modulus of epoxy resin based micro/nanocomposites *versus* filler (Reprint with the permission of Strojniski vestnik–Journal of Mechanical Engineering [191]).

The attempt of improving the electrical, thermal and mechanical properties of an existing micro- or nanocomposite material or synthesizing a new material

can be based on an Edisonian approach. In the case of a new material, many testing samples are necessary to build reliable statistics [94]. The results presented in this review reveal that various nanodielectric systems have a promising future in high-voltage applications.

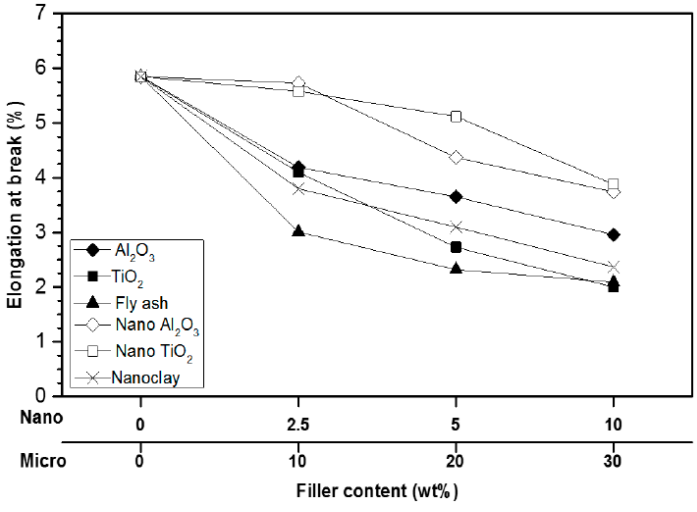

Figure 44. Elongation at break in epoxy resin based micro/nanocomposites *versus* filler content (Reprint with the permission of Strojniski vestnik—Journal of Mechanical Engineering [191]).

7. Future Trends

Future evolution of polymer based materials in electrical applications will mirror most recent advancements (i) in the preparation and application of new nano-scaled filler (*i.e.*, graphene); (ii) in the design of functional and stimuli-responsive polymer matrix materials (*i.e.*, self-healing concepts) and (iii) in new production techniques (*i.e.*, additive manufacturing). Whilst previous work on polymer based composites is strongly driven by the requirement for materials with enhanced electrical and thermo-mechanical properties that are cheap to produce, advanced material concepts and innovative processing techniques open up the window for completely new product and process designs (*i.e.*, flexible electronics, supercapacitors).

7.1. Graphene-Based Nanohybrid Materials

Since the pioneering work of Geim *et al.*, who have successfully identified single layers of graphene in 2004, the one-atom-thick planar sheet of sp^2-bonded carbon atoms have gained enormous attention [192]. Due to its high electrical conductivity, mechanical flexibility, optical transparency, thermal conductivity and low coefficient

of thermal expansion graphene has been recently employed in the preparation of polymer based nanocomposites. Several studies reveal that only a very low graphene content is required to enhance the material performance (*i.e.*, high strength and modulus) of polymer based nanocomposites [193–195]. The high intrinsic conductivity and 2D structure of graphene favors the formation of a percolation path at low filler loadings since the electrical conduction in a nanocomposite relies on the formation of a continuous conductive network formed by the fillers. Thus, aligned nano-scaled fillers with a high aspect ratio have a high probability to percolate at low filler concentrations in comparison to spherically shaped nanofillers [196].

Current trends in research on nanohybrid materials with graphene give an indication that graphene-based composites play a crucial role in the fabrication of flexible electronics, supercapacitors and energy storage devices [197–199]. Moreover, compared to pure graphene the electrochemical stability of graphene-based polymer composites is higher [200]. Sangermano *et al.* [199] have successfully demonstrated the preparation of UV curable epoxy based composites containing evenly distributed graphene platelets. The cured composites were characterized by high T_g values and improved storage modulus at high temperature [201]. Along with the manufacture of graphene based polymer coatings that comprised a high optical transparency and excellent flexibility, Sangermano *et al.* also developed graphene oxide containing inkjet inks for the fabrication of microelectronic devices [202,203].

Graphene oxide is often used as precursor for the synthesis of processable graphene and is obtained from natural graphite by different methods. The most prominent technique involves the modified Hummers method [204,205]. Graphene oxide surfaces are highly oxygenated and bear various oxygen functionalities (*i.e.*, hydroxyl, epoxide, ketone, and carboxylic groups). In dependence on the surface composition, the solubility of graphene oxide in water and organic solvents can be alterated [193,206,207]. In particular, carbonyl and carboxyl groups located at the edge of the sheets increase the hydrophilicity of graphene oxide and improve its dispersibility in water. For the preparation of graphene, graphene oxide is reduced in a subsequent step by exploiting (photo) chemical and thermal routes [200].

The preparation of epoxy/graphene nanocomposites is a rapidly growing research field, which is reflected by the strong increase in publications in this field [208]. Increased attention is on the preparation of epoxy based graphene composites that comprise improved mechanical performance, enhanced electrical conductivity as well as thermal conductivity. Numerous studies demonstrate that the dispersion of graphene plays an important part in the final properties of the nanocomposites [209].

To tailor the dispersion properties of graphene and graphene oxide in the polymer matrix, several surface modification routes have been established involving nucleophilic substitution reactions (*i.e.*, modification with alkyl amine and dopamine),

electrophilic substitution reactions (*i.e.*, functionalization with sulfanilic acid and 4-bromo aniline), condensation reactions (*i.e.*, modification with isocyanates and polyvinyl alcohol) and addition reactions (*i.e.*, functionalization with polyacetylene and aryne) [200]. Along with the chemical surface composition, the preparation procedure governs the dispersion of the graphene platelets in the matrix polymer (solvent mixing *vs*. epoxy impregnation).

Going from the employment of graphene as single filler, current research is geared towards the exploitation of synergistic effects of additional nanofillers in graphene based polymer composites. Particular interest is aimed at binary systems of graphene and carbon nanotubes, which lead to a significant increase in fracture toughness and thermal conductivity [210]. Chemical functionalization of graphene with gold nanoparticles leads to distinctive increase of the electrical conductivity whilst ceramic fillers (*i.e.*, zirconia, gibbsite and boehmite) are applied to improve the capacitive behavior of graphene based epoxy composites [211,212].

7.2. Self-Healable Polymer Composites

In recent years, the preparation self-healing polymers that recover their physical and mechanical properties after crack formation or other mechanical damages is also gaining increased attention in the design of functional polymer composites [213]. Healable polymers usually heal in response to a stimulus or an external trigger (*i.e.*, heat, light, and change in pH value) and in principle, two different healing mechanisms are exploited. In terms of autonomically healable polymers, the material properties are regained without an external stimulus whilst with respect to mendable or healable polymers an external stimulus is required to heal [214]. When it comes to the design of healable epoxy based materials, a prominent preparation route involves the application of microencapsulated repair agents. The mechanically rupture of the microcapsules triggers the healing process autonomically and healing of the crack is achieved by the subsequent release of the repair agent [215]. Different repair agents including monomers, hardeners (*i.e.*, polyfunctional thiols), catalysts (*i.e.*, a complex of copper (II) bromide ($CuBr_2$) with four 2-methyl imidazol units) are encapsulated to ensure a spatial separation of these reactive components from the bulk material [216–218]. These developments of self-healing polymeric materials present interest for electrical insulation systems, which could confer self-healing functionality in a large variety of electrical applications. Particular areas of interest refer to underground power cables and electrical insulation for high-voltage components since failures of the equipment being very costly and, in general, difficult to detect and prevent [219–221].

Although the microcapsule approach is characterized by a high versatility and an efficient healing of microscopic cracks, account has to be taken into the fact that both chemical as well as physical properties of the healed zone are not comparable to the bulk material. Moreover, the self-healing properties of the polymer matrix

are often limited due to the heterogeneous distribution of the healing agent [213]. To enable a repeated healing of the same damage zone, alternative strategies have been developed that aim at the introduction of reversible crosslinks into polymer materials. By exploiting non-covalent and supramolecular interactions using hydrogen bonds, metal-ligand complexation or self-assembly forces mechanically broken crosslinks can be reformed autonomically [222,223]. To obtain higher mechanical properties, covalent reversible crosslinks based on thermally reversible Diels-Alder/*retro* Diels-Alder chemistry are often used. Prominent examples are polymer materials that undergo concerted [4πs + 2πs] cycloadditions of furan (diene) and maleimide (dienophile) units. In addition, various cyclic dienes such as anthracene or dicyclopentadiene are applied to generate thermally reversible crosslinks with maleimide or bismaleimide moieties [224–227]. Healing of a crack is achieved by a reheating of the material at temperatures higher than 100 °C under pressure [228,229]. Along with thermally induced healing reactions, [4πs + 4πs] cycloadditions of anthracene and [2πs + 2πs] photocycloaddition reactions of cinnamoyl or coumarin groups are exploited to generate optically healable polymer matrices [230–234]. The ability to reversible bond formation and bond breakage simply by light exposure has gained increased interest since it allows a spatially resolved healing of cracks under ambient conditions.

7.3. New Production Routes

7.3.1. Laser Processing of Polymer Composites

Composite materials based on insulating polymeric matrices (*i.e.*, LDPE, high density polyethylene (HDPE), *etc.*) and conducting fillers (*i.e.*, metals, CNTs and nanofibers (CNFs), graphene) are very attractive to be used in numerous applications (*i.e.*, polymeric and flexible electronic, sensor applications, anti-static and electromagnetic interference shielding, *etc.*) due to their good electrical properties determined by the fillers characteristics [235,236]. For concentrations lower than 0.5–5 wt %, composites are characterized by a very low conductivity while it is increasing several orders of magnitude for composites with filler contents higher than the percolation threshold.

In current research, considerable efforts have been made on the fabrication of conducting tracks based on metals and/or carbon on insulating matrices (*i.e.*, thermal and laser treatment of low amount of CNTs and additives and immiscible polymer blends) and laser technique has proven also its utility for *in situ* localized reduction of graphite oxide [237,238]. Cesano *et al.* [235] described the formation of conductive paths obtained by CO_2-pulsed laser irradiation (laser writing) of MWCNTs in low concentrations and single polymer phase (LDPE, HDPE) composites. Using an investigation at the micro/nano level, conductive paths were successfully generated

by a laser induced percolation process. In the irradiated zones, the polymer melting and the formation of an accumulation layer could be clearly shown. In these regions, nanotubes percolation occurs, followed by an enhancement of electrical conductivity with several orders of magnitude. As the layer accumulation is strongly adhering to the undisturbed polymer zone, the obtained tracks are very stable and a control of electrical conductivity along the tracks of any selected pattern is possible. This result is very important in many applications, where the electric signal through the composite must be avoided [235].

7.3.2. 3D Printing

3D printing (3DP) technology is used for the rapid production of 3D objects directly from digital computer aided design (CAD) files [239]. In a 3D printer (3DP) the ink is deposited in thin layers to build up a solid object. A software takes a series of digital cross-sections through a computer aided design (CAD) which are then sent to the 3D printer to achieve different layers according to the 3D printer. After the first layer is complete, the build surface is moved few dozens of micrometers and the second layer is added [239]. The most popular technologies used in low-cost 3D printers are Fused Deposition Modeling (FDM) and Fused Filament Modeling (FFM). In terms of FFM, a thin filament of molten thermoplastic is extruded through a heated nozzle. The filaments cool down and adhere to the layers to build up a solid 3D object [239].

Traditionally, the technology has been used by large companies to produce "rapid prototypes" before production [239]. Nowadays, the technology has found greater appeal in more in the manufacture of final-product across different fields from medical implants to the artistic and creative industries. 3DPs (i.e., RepRap and Fab@Home) have facilitated the manufacturing of customized and producing objects by individualized and personalized approaches. Furthermore, the technology provides low-cost, low-volume and low-risk routes to market for entrepreneurs with novel products leading to a reduction in time to market for innovations [239]. Recent advances in nanotube chemistry enable the dissolution and dispersion of CNTs in various solvents. These developments and research results suggest new alternatives for fabricating CNTs patterns by simply dispersing/printing the dissolved/dispersed particles on substrates. Kordás *et al.* [240] presented a cost-effective and scalable deposition method for generating conductive MWCNTs patterns on paper and polymer surfaces. MWCNTs grown by chemical vapor deposition method (CCVD) were chemically modified to obtain CNTs dispersible in water and the aqueous dispersion was applied on various substrates using a commercial desktop inkjet printer. The electrical behavior of the printed patterns and the process limitations were analyzed. Using 3DP technology, in the last 10 years, groups of researchers and designers worked to create more complex products. One of the future trends in this

field involves the incorporation of functional elements (i.e. electronic sensors) into 3D printed macroscale structures. Of course, for this purpose, functional materials and 3D printing methodologies are necessary [240].

8. Conclusions

Research and development of composites and nanocomposites materials used in high-voltage applications are challenging. Although much effort has been put forth in the last two decades to investigate the potential electrical benefit of such newly emerging materials and numerous findings in the field were reported, many uncertainties remain unanswered, and much remains to be explored. The tendency in this evolution is towards a multidisciplinary collaboration of electrical, mechanical, thermal engineering, chemistry, material science, physics and other sciences, in order to clarify the fundamental relationship between structure and properties and to bring much more benefits to society with these materials. This close collaboration will hopefully lead to a better understanding of polymers micro/nanocomposites and of the most important component of these materials, respectively the interface region. When all the mechanisms will be identified and clarified, the desired materials with tailored properties proper for high-voltage application will be obtained.

Acknowledgments: The research work was performed within the K-Project "PolyComp" at the Polymer Competence Center Leoben GmbH (PCCL, Austria) within the framework of the COMET-program of the Federal Ministry for Transport, Innovation and Technology and Federal Ministry for Economy, Family and Youth. Funding is provided by the Austrian Government and the State Government of Styria.

Author Contributions: All authors have contributed to the co-writing of this manuscript. Ilona Pleșa elaborated the plan of the review, wrote the manuscript and designed the presentation of some figures in close collaboration with Petru V. Notingher. Sandra Schlögl was jointly responsible for the sections of the review related to chemistry and for the future trends chapter. Christof Sumereder provided the state of the art of nanocomposite materials involved in high-voltage applications, such as cables. Michael Muhr provided support for the high-voltage applications sections of the manuscript.

Conflicts of Interest: The authors declare no conflict of interest.

Abbreviations

The following abbreviations are frequently used in this manuscript:

AlN	Aluminum Nitride
Al_2O_3	Aluminum Oxide or Alumina
$Al(OH)_3$	Aluminum Trihydroxide
ATH	Alumina Trihydrate
BN	Boron Nitride
BeO	Beryllium Oxide

$BaTiO_3$	Barium Titanate
$CaCO_3$	Calcium Carbonate
LS	Layered Silicate
MgO	Magnesium Oxide
SiC	Silicon Carbide
SiO_2	Silicon Dioxide or Silica
TiO_2	Titanium Oxide or Titania
ZnO	Zinc Oxide
CNTs	Carbon Nanotubes
SWCNTs	Single Walled Carbon Nanotubes
MWCNTs	Multi-Walled Carbon Nanotubes
GNPs	Graphite Nanoplatelets
PE	Polyethylene
XLPE	Cross-linked polyethylene
LDPE	Low-density polyethylene
HDPE	High-density polyethylene
PP	Polypropylene
i-PP	Isotactic polypropylene
PVC	Polyvinyl chloride
PS	Polystyrene
PUR	Polyurethane
PC	Polycarbonate
PA	Polyamide
PI	Polyimide
PAI	Polyamide-imide (PAI)
EVA	Ethylene-vinyl-acetate
AC	Alternating Current
DC	Direct Current
HVDC	High-Voltage Direct Current
HVAC	High-Voltage Alternating Current
IEC	International Electrotechnical Commission
PD	Partial Discharges
VPI	Vacuum Pressure Impregnation

References

1. Han, J.; Garrett, R. Overview of polymer nanocomposites as dielectrics and electrical insulation materials for large high voltage rotating machines. *NSTI-Nanotech* **2008**, *2*, 727–732.
2. Matthews, F.L.; Rawlings, R.D. Overview. In *Composite Materials: Engineering and Science*, 2nd ed.; CRC Press, Woodhead Publishing Limited: Cambridge, UK, 1999; pp. 1–28.
3. Wikipedia—The Free Encyclopedia. Available online: https://en.wikipedia.org/wiki/Nanocomposite (accessed on 9 December 2015).
4. Tanaka, T.; Montanari, G.C.; Mülhaupt, R. Polymer nanocomposites as dielectrics and electrical insulation—Perspectives for processing technologies, material characterization and future applications. *IEEE Trans. Dielectr. Electr. Insul.* **2004**, *11*, 763–784.
5. Camargo, P.H.C.; Satyanarayana, K.G.; Wypych, F. Nanocomposites: Synthesis, structure, properties and new application opportunities. *Mater. Res.* **2009**, *12*, 1–39.
6. Nelson, J.K. Overview of nanodielectrics: Insulating materials of the future. In Proceedings of the Electrical Insulation Conference and Electrical Manufacturing Expo, Nashville, TN, USA, 22–24 October 2007; pp. 229–235.
7. Sheer, M.L. Advanced composites: The leading edge in high performance motor and transformer insulation. In Proceedings of the 20th Electrical Electronics Insulation Conference, Boston, MA, USA, 7–10 October 1991; pp. 181–185.
8. ATTAR Advanced Technology Testing and Research. Available online: http://www.attar.com.au/materials- engineering.aspx (accessed on 5 November 2015).
9. Stone, G.C.; Boulter, E.A.; Culbert, I.; Dhirani, H. Historical development of insulation materials and systems. In *Electrical Insulation for Rotating Machines—Design, Evaluation, Aging, Testing, and Repair*, 1st ed.; Kartalopoulos, S.V., Ed.; Wiley-IEEE Press: Piscataway, NJ, USA, 2004; pp. 73–94.
10. Pyrhönen, J.; Jokinen, T.; Hrabovcová, V. Insulation of electrical machines. In *Design of Rotating Electrical Machines*, 2nd ed.; John Wiley & Sons Ltd.: West Sussex, UK, 2014; pp. 429–455.
11. Notingher, P.V. Chapter 23. In *Materials for Electrotechnics*; Politechnica Press: Bucharest, Romania, 2005; Volume 2, pp. 157–170.
12. Park, J.J. AC Electrical breakdown characteristics of an epoxy/mica composite. *Trans. Electr. Electron. Mater.* **2012**, *13*, 200–203.
13. Lenko, D.; Schlögl, S.; Bichler, S.; Lemesch, G.; Ramsauer, F.; Ladstätter, W.; Kern, W. Flexible epoxy-silicone rubber laminates for high voltage insulations with enhanced delamination resistance. *Polym. Compos.* **2015**, *36*, 2238–2247.
14. Schlögl, S.; Lenko, D. High voltage insulations with enhanced delamination resistance. *Rubber Fibres Plast. Int.* **2015**, *10*, 260–261.
15. Kojima, Y.; Usuki, A.; Kawasumi, M.; Okada, A.; Kurauchi, T.; Kagimoto, O. One-pot synthesis of nylon 6-clay hybrid. *J. Polym. Sci. Pt. A* **1993**, *31*, 1755–1758.
16. Lewis, T.J. Nanometric Dielectrics. *IEEE Trans. Dielectr. Electr. Insul.* **1994**, *1*, 812–825.

17. Frechette, M.F.; Trudeau, M.; Alamdari, H.D.; Boily, S. Introductory remarks on nanodielectrics. In Conference on Electrical Insulation and Dielectric Phenomena, 2001 Annual Report, Kitchener, ON, Canada, 14–17 October 2001; pp. 92–99.
18. Cao, Y.; Irwin, P.C.; Younsi, K. The future of nanodielectrics in the electrical power industry. *IEEE Trans. Dielectr. Electr. Insul.* **2004**, *11*, 797–807.
19. Johnston, D.R.; Markovitz, M. Corona-Resistant Insulation, Electrical Conductors Covered Therewith and Dynamoelectric Machines and Transformers Incorporating Components of Such Insulated Conductors. US Patent 4760296 A, 26 July 1988.
20. Henk, P.O.; Kortsen, T.W.; Kvarts, T. Increasing the electrical discharge endurance of acid anhydride cured DGEBA epoxy resin by dispersion of nanoparticle silica. *High Perform. Polym.* **1999**, *11*, 281–296.
21. Fothergill, J.C.; Dissado, L.A.; Nelson, J.K. *Nanocomposite Materials for Dielectric Structures*; EPSRC: Swindon, UK, 2002; pp. 1–6.
22. Nelson, J.K.; Fothergill, J.C. Internal charge behaviour in nanocomposites. *Nanotechnology* **2004**, *15*, 586–595.
23. Tanaka, T.; Imai, T. Advances in nanodielectric materials over the past 50 years. *IEEE Electr. Insul. Mag.* **2013**, *29*, 10–23.
24. Tanaka, T.; Bulinski, A.; Castellon, J.; Frechette, M.; Gubanski, S.; Kindersberger, J.; Montanari, G.C.; Nagao, M.; Morshuis, P.; Tanaka, Y.; *et al.* Dielectric properties of XLPE/SiO_2 nanocomposites based on CIGRE WG D1.24 cooperative test results. *IEEE Trans. Dielectr. Electr. Insul.* **2011**, *18*, 1482–1517.
25. Krivda, A.; Tanaka, T.; Frechette, M.; Castellon, J.; Fabiani, D.; Montanari, G.C.; Gorur, R.; Morshuis, P.; Gubanski, S.; Kindersberger, J.; *et al.* Characterization of epoxy microcomposite and nanocomposite materials for power engineering applications. *IEEE Electr. Insul. Mag.* **2012**, *28*, 38–51.
26. Castellon, J.; Nguyen, H.N.; Agnel, S.; Toureille, A.; Frechette, M.; Savoie, S.; Krivda, A.; Schmidt, L.E. Electrical properties analysis of micro and nano composite epoxy resin materials. *IEEE Trans. Dielectr. Electr. Insul.* **2011**, *18*, 651–658.
27. Frechette, M.F.; Trudeau, M.L.; Alamdar, H.D.; Boily, S. Introductory remarks on nanodielectrics. *IEEE Trans. Dielectr. Electr. Insul.* **2004**, *11*, 808–818.
28. Reed, C.W. Self-assembly of polymer nanocomposites for dielectrics and HV insulation. In Proceedings of the IEEE International Conference on Solid Dielectrics, 2007. ICSD '07, Winchester, UK, 8–13 July 2007.
29. Nelson, J.K. Background, principles and promise of nanodielectrics. In *Dielectric Polymer Nanocomposites*; Nelson, J.K., Ed.; Springer: New York, NY, USA, 2010; pp. 1–30.
30. Andritsch, T.; Kochetov, R.; Gebrekiros, Y.T.; Morshuis, P.H.F.; Smit, J.J. Short term DC breakdown strength in epoxy based BN nano- and microcomposites. In Proceedings of the International Conference on Solid Dielectrics (ICSD), Postdam, Germany, 4–9 July 2010; pp. 1–4.
31. Wang, Q.; Chen, G. Effect of nanofillers on the dielectric properties of epoxy nanocomposites. *Adv. Mater. Res.* **2012**, *1*, 93–107.

32. Singha, S.; Thomas, M.J. Dielectric properties of epoxy nanocomposites. *IEEE Trans. Dielectr. Electr. Insul.* **2008**, *15*, 12–23.
33. Tanaka, T. Dielectric nanocomposites with insulating properties. *IEEE Trans. Dielectr. Electr. Insul.* **2005**, *12*, 914–928.
34. Singha, S.; Thomas, M.J. Reduction of permittivity in epoxy nanocomposites at low nano-filler loadings. In Proceedings of the Conference on Electrical Insulation and Dielectric Phenomena (CEIDP), Quebec, QC, Canada, 26–29 October 2008; pp. 726–729.
35. Kadhim, M.J.; Abdullah, A.K.; Al-Ajaj, I.A.; Khalil, A.S. Dielectric properties of epoxy/Al_2O_3 nanocomposites. *Int. J. Appl. Innov. Eng. Manag.* **2014**, *3*, 468–477.
36. Castellon, J.; Agnel, S.; Toureille, A.; Frechette, M. Space charge characterization of multi-stressed microcomposites nano-filled epoxy for electrotechnical applications. In Proceedings of the Conference on Electrical Insulation and Dielectric Phenomena (CEIDP), Quebec, QC, Canada, 26–29 October 2008; pp. 532–535.
37. Andritsch, T. Epoxy Based Nanodielectrics for High Voltage DC-Applications-Synthesis, Dielectric properties and Space Charge Dynamics. Ph.D. Thesis, Delft University of Technology, Delft, The Netherlands, 2010.
38. Magraner, F.; García-Bernabé, A.; Gil, M.; Llovera, P.; Dodd, S.J.; Dissado, L.A. Space charge measurements on different epoxy resin alumina nanocomposites. In Proceedings of the International Conference on Solid Dielectrics (ICSD), Potsdam, Germany, 4–9 July 2010; pp. 1–4.
39. Stancu, C.; Notingher, P.V.; Ciuprina, F.; Notingher, P., Jr.; Agnel, S.; Castellon, J.; Toureille, A. Computation of the electric field in cable insulation in the presence of water trees and space charge. *IEEE Trans. Ind. Appl.* **2009**, *45*, 30–43.
40. Dissado, L.A.; Mazzanti, G.; Montanari, G.C. The role of trapped space charges in the electrical aging of insulating materials. *IEEE Trans. Dielectr. Electr. Insul.* **1997**, *4*, 496–506.
41. Fabiani, D.; Montanari, G.C.; Dardano, A.; Guastavino, G.; Testa, L.; Sangermano, M. Space charge dynamics in nanostructured epoxy resin. In Proceedings of the Conference on Electrical Insulation and Dielectric Phenomena, CEIDP, Quebec, QC, Canada, 26–29 October 2008; pp. 710–713.
42. Gröpper, P.; Hildinger, T.; Pohlmann, F.; Weidner, J.R. Nanotechnology in High Voltage Insulation Systems for Large Electrical Machinery–First Results. *Water Energy Int.* **2013**, *70*, 65–66.
43. Gröpper, P.; Meichsner, C.; Ritberg, I. Insulation for Rotating Electrical Machines. Patent No. WO2012013439 A1, 2012.
44. Gröpper, P.; Gruebel, A.; Jablonski, V.; Ritberg, I. Insulation with Improved Resistance to Partial Discharge. Patent No. DE 10/2010/032949 A1, 2012.
45. Lee, G.W.; Park, M.; Kim, J.; Lee, J.I.; Yoon, H.G. Enhanced thermal conductivity of polymer composites filled with hybrid filler. *Compos. Part A* **2006**, *37*, 727–734.
46. Zweifel, P.; Fennessey, S.F. Thermal conductivity of reinforced composites for electrical application. In Proceedings of the IEEE International Symposium on Electrical Insulation (ISEI), San Diego, CA, USA, 6–9 June 2010; pp. 1–4.

47. Zhang, C.; Han, Z.; Stevens, C.G. Effects of micro and nano fillers on electrical and thermal properties of epoxy resin. In Proceedings of the 10th International Electrical Insulation Conference (INSUCON), Birmingham, England, 24–26 May 2006.
48. Kochetov, R.; Korobko, A.V.; Andritsch, T.; Morshuis, P.H.F.; Picken, S.J.; Smit, J.J. Three-phase Lewis-Nielsen model for the thermal conductivity of polymer nanocomposites. In Proceedings of the Conference on Electrical Insulation and Dielectric Phenomena (CEIDP), Cancun, Mexic, 16–19 October 2011; pp. 338–341.
49. Murata, Y.; Sakamaki, M.; Abe, K.; Inoue, Y.; Mashio, S.; Kashiyama, S.; Matsunaga, O.; Igi, T.; Watanabe, M.; Asai, S.; *et al.* Development of high voltage DC-XLPE cable system. *SEI Tech. Rev.* **2013**, 55–62.
50. Tanaka, T.; Frechette, M.; Agoris, D.P.; Campus, A.; Castellon, J.; Densley, J.; Gorur, R.S.; Gubanski, S.M.; Henriksen, M.; Hillborg, H.; *et al.* Emerging nanocomposite dielectrics. *Electra* **2006**, *226*, 24–32.
51. Lee, T.H.; Lee, S.B.; Nam, J.H.; Kim, Y.H.; Lee, S.K.; Lee, I.H.; Jeon, S.I.; Won, Y.J.; Kim, J.S.; Lee, J.H. Development status of DC XLPE cable in Korea. In Proceedings of CIGRE Session, Paris, France, 24–29 August 2014.
52. Zaccone, E. Chapter 2, Innovative Cables. In *Advanced Technologies for Future Transmission Grids*; Migliavacca, G., Ed.; Springer: London, UK, 2013; pp. 39–84.
53. Lau, K.Y.; Vaughan, A.S.; Chen, G. Nanodielectrics: Opportunities and challenges. *IEEE Electr. Insul. Mag.* **2015**, *31*, 45–54.
54. Xanthos, M. Chapter 1, Polymers and polymer composites. In *Functional Fillers for Plastics*, 2nd ed.; Xanthos, M., Ed.; Wiley-VCH Verlag GmbH & Co. KGaA: Weinheim, Germany, 2010; pp. 1–18.
55. Notingher, P.; Panaitescu, D.; Paven, H.; Chipara, M. Some characteristics of conductive polymer composites containing stainless steel fibers. *J. Optoelectron. Adv. Mater.* **2004**, *6*, 1081–1084.
56. Marquis, M.D.; Guillaume, E.; Chivas-Joly, C. Chapter 11, Properties of nanofillers in polymer. In *Nanocomposites and Polymers with Analytical Methods*; Cuppoletti, J., Ed.; InTech: Rijeka, Croatia, 2011; pp. 261–284.
57. Okutan, E.; Aydın, G.O.; Hacıvelioglu, F.; Kılıç, A.; Beyaz, S.K.; Yesilot, S. Synthesis and characterization of soluble multi-walled carbon nanotube/poly-(organophosphazene) composites. *Polymer* **2011**, *52*, 1241–1248.
58. Malwela, T.; Ray, S.S. Unique morphology of dispersed clay particles in a polymer nanocomposite. *Polymer* **2011**, *52*, 1297–1301.
59. Huang, X.; Jiang, P.; Tanaka, T. A review of dielectric polymer composites with high thermal conductivity. *IEEE Electr. Insul. Mag.* **2011**, *27*, 8–16.
60. Prato, M. Materials chemistry: Controlled nanotube reactions. *Nature* **2010**, *465*, 172–173.
61. Hong, R.Y.; Chen, Q. Dispersion of inorganic nanoparticles in polymer matrices: challenges and solutions. In *Organic-Inorganic Hybrid Nanomaterials*; Kalia, S., Haldorai, Y., Eds.; Springer International Publishing: Berlin Heidelberg, Germany, 2015; pp. 1–38.

62. Plesa, I.; Schlogl, S.; Radl, S.V.; Muhlbacher, I.; Schichler, U. The influence of surface modification on the electrical properties of silicon carbide flakes. In Proceedings of the 9th International Symposium on Advanced Topics in Electrical Engineering (ATEE), Bucharest, Romania, 7–9 May 2015; pp. 460–463.
63. Anyszka, R.; Bielinski, D.M.; Pedzich, Z.; Szumera, M. Influence of surface-modified montmorillonites on properties of silicone rubber-based ceramizable composites. *J. Therm. Anal. Calorim.* **2015**, *119*, 111–121.
64. Tayfun, U.; Kanbur, Y.; Abaci, U.; Guney, H.Y.; Bayramli, E. Mechanical, flow and electrical properties of thermoplastic polyurethane/fullerene composites: Effect of surface modification of fullerene. *Compos. Part B Eng.* **2015**, *80*, 101–107.
65. Xu, T.; Yang, J. Effects of surface modification of MWCNT on the mechanical and electrical properties of fluoro elastomer/MWCNT nanocomposites. *J. Nanomater.* **2012**, *2012*, 1–9.
66. Ma, D.; Hugener, T.A.; Siegel, R.W.; Christerson, A.; Mårtensson, E.; Önneby, C.; Schadler, L.S. Influence of nanoparticle surface modification on the electrical behaviour of polyethylene nanocomposites. *Nanotechnology* **2005**, *16*, 724.
67. Peng, S.; He, J.; Hu, J. Influence of surface modification on electrical properties of polyethylene SiO_2 nanocomposites. In Proceedings of the IEEE 11th International Conference on the Properties and Applications of Dielectric Materials (ICPADM), Sydney, Australia, 19–22 July 2015; pp. 372–375.
68. Jölly, I.; Schlögl, S.; Wolfahrt, M.; Pinter, G.; Fleischmann, M.; Kern, W. Chemical functionalization of composite surfaces for improved structural bonded repairs. *Compos. Part B Eng.* **2015**, *69*, 296–303.
69. Dalian Sibond Intl Trade Co., Ltd. Available online: http://www.sibond.com/silanes/coupling_agent.htm (accessed on 2 December 2015).
70. Rong, M.Z.; Zhang, M.Q.; Zheng, Y.X.; Zeng, H.M.; Walter, R.; Friedrich, K. Irradiation graft polymerization on nano-inorganic particles: An effective means to design polymer-based nanocomposites. *J. Mater. Sci. Lett.* **2000**, *19*, 1159–1161.
71. Rong, M.Z.; Zhang, M.Q.; Zheng, Y.X.; Zeng, H.M.; Walter, R.; Friedrich, K. Irradiation graft polymerization on nano-inorganic particles: An effective means to design polymer-based nanocomposites. *J. Mater. Sci. Lett.* **2000**, *19*, 1159–1161.
72. Uyama, Y.; Kato, K.; Ikada, Y. Surface modification of polymers by grafting. In grafting/characterization techniques/kinetic modeling. *Adv. Polym. Sci.* **1998**, *137*, 1–39.
73. Kickelbick, G. Chapter 1, Introduction to hybrid materials. In *Hybrid Materials, Synthesis, Characterization, and Applications*; Kickelbick, G., Ed.; Wiley-VCH Verlag GmbH & Co. KGaA: Weinheim, Germany, 2007; pp. 1–48.
74. O'Connor, K.A.; Curry, R.D. Three-dimensional electromagnetic modeling of composite dielectric materials. In Proceedings of the IEEE Pulsed Power Conference (PPC), Chicago, CA, USA, 19–23 June 2011; pp. 274–279.
75. Ciuprina, F.; Andrei, L.; Tomescu, F.M.G.; Plesa, I.; Zaharescu, T. Electrostatic model of LDPE-SiO_2 nanodielectrics. In Proceedings of the IEEE International Conference on Solid Dielectrics (ICSD), Bologna, Italy, 30 June–4 July 2013; pp. 876–879.

76. Tanaka, T.; Kozako, M.; Fuse, N.; Ohki, Y. Proposal of a multi-core model for polymer nanocomposite dielectrics. *IEEE Trans. Dielectr. Electr. Insul.* **2005**, *12*, 669–681.
77. Tsagaropoulos, G.; Eisenberg, A. Dynamic mechanical study of the factors affecting the two glass transition behavior of filled polymers. Similarities and differences with random ionomers. *Macromolecules* **1995**, *28*, 6067–6077.
78. Pitsa, D.; Danikas, M.G. Interfaces features in polymer nanocomposites: A review of proposed models. *Nano Brief Rep. Rev.* **2011**, *6*, 497–508.
79. Lewis, T.J. Interfaces: Nanometric dielectrics. *J. Phys. D Appl. Phys.* **2005**, *38*, 202–212.
80. Seiler, J.; Kindersberger, J. Insight into the interphase in polymer nanocomposites. *IEEE Trans. Dielectr. Electr. Insul.* **2014**, *21*, 537–547.
81. Danikas, M.G. On two nanocomposite models: Differences, similarities and interpretational possibilities regarding Tsagaropoulos' model and Tanaka's model. *J. Electr. Eng.* **2010**, *61*, 241–246.
82. Danikas, M.G.; Bairaktari, A.; Sarathi, R.; Basri Bin Abd Ghani, A. A review of two nanocomposite insulating materials models: Lewis' contribution in the development of the models, their differences, their similarities and future challenges. *Eng. Technol. Appl. Sci. Res.* **2014**, *4*, 636–643.
83. Ciuprina, F.; Plesa, I.; Notingher, P.V.; Tudorache, T.; Panaitescu, D. Dielectric Properties of nanodielectrics with inorganic fillers. In Proceedings of the Conference on Electrical Insulation and Dielectric Phenomena (CEIDP), Quebec, QC, Canada, 26–29 October 2008; pp. 682–685.
84. Plesa, I. Influence of Inorganic Fillers on the Dielectric Properties of Polymer Nanocomposites Based on Polyethylene. Ph.D. Thesis, Politehnica University of Bucharest, București, Romania, February 2012.
85. Raetzke, S.; Kindersberger, J. Role of interphase on the resistance to high-voltage arcing, on tracking and erosion of silicone/SiO_2 nanocomposites. *IEEE Trans. Dielectr. Electr. Insul.* **2010**, *17*, 607–614.
86. Andritsch, T.; Kochetov, R.; Morshuis, P.H.F.; Smit, J.J. Proposal of the polymer chain alignment model. In Proceedings of the Conference on Electrical Insulation and Dielectric Phenomena (CEIDP), Cancun, Mexic, 16–19 October 2011; pp. 624–627.
87. Zou, C.; Fothergill, J.C.; Rowe, S.W. The effect of water absorption on the dielectric properties of epoxy nanocomposites. *IEEE Trans. Dielectr. Electr. Insul.* **2008**, *15*, 106–117.
88. U.S. Congress, Office of Technology Assessment. Chapter 3, Polymer matrix composites. In *Advanced Materials by Design*; Gibbons, J.H., Ed.; U.S. Government Printing Office: Washington, DC, USA; June; 1988; pp. 73–95.
89. Li, S.; Lin, M.M.; Toprak, M.S.; Kim, D.K.; Muhammed, M. Nanocomposites of polymer and inorganic nanoparticles for optical and magnetic applications. *Nano Rev.* **2010**, *1*, 1–19.
90. Oliveira, M.; Machado, A.V. Preparation of Polymer-Based Nanocomposites by Different Routes. In *e-book Nanocomposites: Synthesis, Characterization and Applications*; Wang, X., Ed.; NOVA Publishers: New York, NY, USA, 2013; pp. 1–22.

91. Singh, N.B.; Rai, S.; Agarwal, S. Polymer nanocomposites and Cr(VI) removal from water. *Nanosci. Technol.* **2014**, *1*, 1–10.
92. Tanahashi, M. Development of fabrication methods of filler/polymer nanocomposites: With focus on simple melt-compounding-based approach without surface modification of nanofillers. *Materials* **2010**, *3*, 1593–1619.
93. Cui, Y.; Kumar, S.; Konac, B.R.; van Houckec, D. Gas barrier properties of polymer/clay nanocomposites. *RSC Adv.* **2015**, *5*, 63669–63690.
94. Tuncer, E.; Sauers, I. Industrial applications perspective of nanodielectrics. In *Dielectric Polymer Nanocomposites*; Nelson, J.K., Ed.; Springer: New York, NY, USA, 2010; pp. 321–338.
95. Lalankere, G. Opportunities and challenges of employing composite materials in switchgear industry. In Proceedings of the 20th International Conference on Electricity Distribution (CIRED), Prague, Czech Republic, 8–11 June 2009; pp. 1–4.
96. Boulter, E.A.; Stone, G.C. Historical development of rotor and stator winding insulation materials and systems. *IEEE Electr. Insul. Mag.* **2004**, *20*, 25–39.
97. Janssen, H.; Seifert, J.M.; Karner, H.C. Interfacial phenomena in composite high voltage insulation. *IEEE Trans. Dielectr. Electr. Insul.* **1999**, *6*, 651–659.
98. Nelson, J.K.; Fothergill, J.C.; Dissado, L.A.; Peasgood, W. Towards an understanding of nanometric dielectrics. In Proceedings of Conference on Electrical Insulation and Dielectric Phenomena (CEIDP), Cancun, Mexico, 20–24 October 2002; pp. 295–298.
99. Imai, T.; Sawa, F.; Nakano, T.; Ozaki, T.; Shimizu, T.; Kozako, M.; Tanaka, T. Effects of nano- and micro-filler mixture on electrical insulation properties of epoxy based composites. *IEEE Trans. Dielectr. Electr. Insul.* **2006**, *13*, 319–326.
100. Patel, R.R.; Gupta, N. Volume resistivity of epoxy containing nano-sized Al_2O_3 fillers. In Proceedings of the Fifteenth National Power Systems Conference (NPSC), Bombay, India, December 2008; pp. 361–365.
101. Lutz, B.; Kindersberger, J. Influence of absorbed water on volume resistivity of epoxy resin insulators. In Proceedings of the 10th IEEE International Conference on Solid Dielectrics (ICSD), Potsdam, Germany, 4–9 July 2010; pp. 1–4.
102. Roy, M.; Nelson, J.K.; Schadler, L.S.; Zou, C.; Fothergill, J.C. The influence of physical and chemical linkage on the properties of nanocomposites. In Proceedings of the Conference on Electrical Insulation and Dielectric Phenomena, (CEIDP), Nashville, TN, USA, 16–19 October 2005; pp. 183–186.
103. Smith, R.C.; Liang, C.; Landry, M.; Nelson, J.K.; Schadler, L.S. Studies to unravel some underlying mechanisms in nanodielectrics. In Proceedings of the Conference on Electrical Insulation and Dielectric Phenomena (CEIDP), Vancouver, BC, Canada, 14–17 October 2007; pp. 286–289.
104. Smith, R.C.; Liang, C.; Landry, M.; Nelson, J.K.; Schadler, L.S. The mechanisms leading to the useful electrical properties of polymer nanodielectrics. *IEEE Trans. Dielectr. Electr. Insul.* **2008**, *15*, 187–196.

105. Ciuprina, F.; Plesa, I. DC and AC conductivity of LDPE nanocomposites. In Proceedings of the 7th International Symposium on Advanced Topics in Electrical Engineering (ATEE), Bucharest, Romania, 12–14 May 2011; pp. 1–6.
106. Plesa, I.; Zaharescu, T. Effects of γ irradiation on resistivity and absorption currents in nanocomposites based on thermoplastic polymers. In Proceedings of the 8th International Symposium on Advanced Topics in Electrical Engineering (ATEE), Bucharest, Romania, 23–35 May, 2013; pp. 1–6.
107. Lau, K.Y.; Vaughan, A.S.; Chen, G.; Hosier, I.L.; Holt, A.F. Absorption current behaviour of polyethylene/silica nanocomposites. *J. Phys. Conf. Ser.* **2013**, *472*, 1–6.
108. Schadler, L.S.; Wang, X.; Nelson, J.K.; Hillborg, H. Non-linear field grading materials and carbon nanotube nanocomposites with controlled conductivity. In *Dielectric Polymer Nanocomposites*; Nelson, J.K., Ed.; Springer: New York, NY, USA, 2010; pp. 259–284.
109. Boggs, S.A. 500 Ω-m-low enough resistivity for a cable ground shield semicon? *IEEE Electr. Insul. Mag.* **2001**, *17*, 26–32.
110. Roberts, A. Stress grading for high voltage motor and generators. *IEEE Electr. Insul. Mag.* **1995**, *11*, 26–31.
111. Foulger, S.H. Electrical properties of composites in the vicinity of the percolation threshold. *J. Appl. Polym. Sci.* **1999**, *72*, 1573–1582.
112. Jager, K.M.; Lindbom, L. The continuing evolution of semiconductor materials for power cable applications. *IEEE Electr. Insul. Mag.* **2005**, *21*, 20–34.
113. Jäger, K.-M.; McQueen, D.H. Fractal agglomerates and electrical conductivity in carbon black polymer composites. *Polymer* **2001**, *42*, 9575–9581.
114. Hindermann-Bischoff, M.; Ehrburger-Dolle, F. Electrical conductivity of carbon black–polyethylene composites: Experimental evidence of the change of cluster connectivity in the PTC effect. *Carbon* **2001**, *39*, 375–382.
115. Nakamura, S.; Tomimura, T.; Sawa, G. Dielectric properties of carbon black—Polyethylene composites below the percolation threshold. In Proceedings of the Conference on Electrical Insulation and Dielectric Phenomena (CEIDP), Austin, TX, USA, 17–20 October 1999; pp. 293–296.
116. Stancu, C.; Notingher, P.V.; Panaitescu, D.; Marinescu, V. Electrical conductivity of polyethylene- neodymium composites. In Proceedings of 8th International Symposium on Advanced Topics in Electrical Engineering (ATEE), Bucharest, Romania, 23–25 May, 2013; pp. 1–6.
117. Chung, D.D.L. Materials for electromagnetic interference shielding. *J. Mater. Eng. Perform.* **2000**, *9*, 350–354.
118. Mamunya, Y.P.; Davydenko, V.V.; Pissis, P.; Lebedev, E.V. Electrical and thermal conductivity of polymers filled with metal powders. *Eur. Polym. J.* **2002**, *38*, 1887–1897.
119. Min, C.; Shen, X.; Shi, Z.; Chen, L.; Xu, Z. The electrical properties and conducting mechanisms of carbon nanotube/polymer nanocomposites: A review. *Polym. Plast. Technol. Eng.* **2010**, *49*, 1172–1181.

120. Pang, H.; Bao, Y.; Lei, J.; Tang, J.-H.; Ji, X.; Zhang, W.-Q.; Chen, C. Segregated conductive ultrahigh-molecular-weight polyethylene composites containing high-density polyethylene as carrier polymer of graphenenanosheets. *Polym. Plast. Technol. Eng.* **2012**, *51*, 1483–1486.
121. Cravanzola, S.; Haznedar, G.; Scarano, D.; Zecchina, A.; Cesano, F. Carbon-based piezoresistive polymer composites: Structure and electrical properties. *Carbon* **2013**, *62*, 270–277.
122. Haznedar, G.; Cravanzola, S.; Zanetti, M.; Scarano, D.; Zecchina, A.; Cesano, F. Graphite nanoplatelets and carbon nanotubes based polyethylene composites: Electrical conductivity and morphology. *Mater. Chem. Phys.* **2013**, *143*, 47–52.
123. Mackersie, J.W.; Given, M.J.; MacGregor, S.J.; Fouracre, R.A. The electrical properties of filled epoxy resin systems—A comparison. In Proceedings of the 2001 IEEE 7th International Conference on Solid Dielectrics (ICSD), Eindhoven, Nederland, 25–29 Jun 2001; pp. 125–128.
124. Fothergill, J.C. Electrical properties. In *Dielectric Polymer Nanocomposites*; Nelson, J.K., Ed.; Springer: New York, NY, USA, 2010; pp. 197–228.
125. Jonscher, A.K. *Dielectric Relaxation in Solids*, 1st ed.; Chelsea Dielectric Press: London, UK, 1983; pp. 1–400.
126. Dissado, J.A.; Hill, R.M. Anomalous low-frequency dispersion. Near direct current conductivity in disordered low-dimensional materials. *J. Chem. Soc. Faraday Trans.* **1984**, *80*, 291–319.
127. Chapman, D.L. A contribution to the theory of electrocapillarity. *Philos. Mag. Ser. 6* **1913**, *25*, 475–481.
128. Singha, S.; Thomas, M.J. Permittivity and tan delta characteristics of epoxy nanocomposites in the frequency range of 1 MHz-1 GHz. *IEEE Trans. Dielectr. Electr. Insul.* **2008**, *15*, 2–11.
129. Kochetov, R.; Andritsch, T.; Morshuis, P.H.F.; Smit, J.J. Anomalous behaviour of the dielectric spectroscopy response of nanocomposites. *IEEE Trans. Dielectr. Electr. Insul.* **2012**, *19*, 107–117.
130. Fothergill, J.C.; Nelson, J.K.; Fu, M. Dielectric properties of epoxy nanocomposites containing TiO_2, Al_2O_3 and ZnO fillers. In Proceedings of the Conference on Electrical Insulation and Dielectric Phenomena (CEIDP), Boulder, CO, USA, 17–20 October 2004; pp. 406–409.
131. Plesa, I.; Ciuprina, F.; Notingher, P.V. Dielectric spectroscopy of epoxy resin with and without inorganic nanofillers. *J. Adv. Res. Phys.* **2010**, *1*, 2069–7201.
132. Kozako, M.; Okazaki, Y.; Hikita, M.; Tanaka, T. Preparation and evaluation of epoxy composite insulating materials toward high thermal conductivity. In Proceedings of the 10th IEEE International Conference on Solid Dielectrics (ICSD), Postdam, Germny, 4–9 July 2010; pp. 1–4.
133. Heid, T.; Fréchette, M.; David, E. Epoxy/BN micro- and submicro-composites: Dielectric and thermal properties of enhanced materials for high voltage insulation systems. *IEEE Trans. Dielectr. Electr. Insul.* **2015**, *22*, 1176–1185.

134. Mo, H.; Huang, X.; Liu, F.; Yang, K.; Li, S.; Jiang, P. Nanostructured electrical insulating epoxy thermosets with high thermal conductivity, high thermal stability, high glass transition temperatures and excellent dielectric properties. *IEEE Trans. Dielectr. Electr. Insul.* **2015**, *22*, 906–915.
135. Roy, M.; Nelson, J.K.; MacCrone, R.K.; Schadler, L.S.; Reed, C.W.; Keefe, R. Polymer nanocomposite dielectrics-the role of the interface. *IEEE Trans. Dielectr. Electr. Insul.* **2005**, *12*, 629–643.
136. Ciuprina, F.; Plesa, I.; Notingher, P.V.; Zaharescu, T.; Rain, P.; Panaitescu, D. Dielectric properties of LDPE-SiO_2 nanocomposites. In Proceedings of the 10th IEEE International Conference on Solid Dielectrics (ICSD), Potsdam, Germany, 4–9 July 2010; pp. 1–4.
137. Ciuprina, F.; Zaharescu, T.; Pleşa, I. Effects of γ-radiation on dielectric properties of LDPE-Al_2O_3 nanocomposites. *Radiat. Phys. Chem.* **2013**, *84*, 145–150.
138. Ciuprina, F.; Zaharescu, T.; Jipa, S.; Pleşa, I.; Noţingher, P.V.; Panaitescu, D. Effects of ionizing radiation on the dielectric properties of LDPE-Al_2O_3 nanocomposites. *UPB Sci. Bull. Series C* **2010**, *72*, 259–268.
139. Panaitescu, D.; Ciuprina, F.; Iorga, M.; Frone, A.; Radovici, C.; Ghiurea, M.; Sever, S.; Plesa, I. Effects of SiO_2 and Al_2O_3 nanofillers on polyethylene properties. *J. Appl. Polym. Sci.* **2011**, *122*, 1921–1935.
140. Hui, L.; Schadler, L.S.; Nelson, J.K. The influence of moisture on the electrical properties of crosslinked polyethylene/silica nanocomposites. *IEEE Trans. Dielectr. Electr. Insul.* **2013**, *20*, 641–653.
141. Cao, Y.; Irwin, P.C. The electrical conduction in polyimide nanocomposites. In Proceedings of the Conference on Electrical Insulation and Dielectric Phenomena (CEIDP), Albuquerque, NW, USA, 19–22 October 2003; pp. 116–119.
142. Tanaka, T. Interface properties and surface erosion resiatnce. In *Dielectric Polymer Nanocomposites*; Nelson, J.K., Ed.; Springer: New York, NY, USA, 2010; pp. 229–258.
143. Izzati, W.A.; Arief, Y.Z.; Adzis, Z.; Shafanizam, M. Partial discharge characteristics of polymer nanocomposite materials in electrical insulation: A review of sample preparation techniques, analysis methods, potential applications, and future trends. *Sci. World J.* **2014**, *2014*, 1–14.
144. Iizuka, T.; Uchida, K.; Tanaka, T. Voltage endurance characteristics of epoxy/silica nanocomposites. *Electron. Commun. Jpn.* **2011**, *94*, 65–73.
145. Tanaka, T.; Matsuo, Y.; Uchida, K. Partial discharge endurance of epoxy/SiC nanocomposite. In Proceedings of the Conference on Electrical Insulation and Dielectric Phenomena (CEIDP), Quebec, QC, Canada, 26–29 October 2008; pp. 13–16.
146. Preetha, P.; Thomas, M.J. Partial discharge resistant characteristics of epoxy nanocomposites. *IEEE Trans. Dielectr. Electr. Insul.* **2011**, *18*, 264–274.
147. Kozako, M.; Yamano, S.; Kido, R.; Ohki, Y.; Kohtoh, M.; Okabe, S.; Tanaka, T. Preparation and preliminary characteristic evaluation of epoxy/alumina nanocomposites. In Proceedings of the 2005 International Symposium on Electrical Insulating Materials (ISEIM), Kitakyushu, Japan, 5–9 June 2005; pp. 231–234.

148. Kozako, M.; Kuge, S.; Imai, T.; Ozaki, T.; Shimizu, T.; Tanaka, T. Surface erosion due to partial discharges on several kinds of epoxy nanocomposites. In Proceedings of the Conference on Electrical Insulation and Dielectric Phenomena (CEIDP), Nashville, TN, USA, 16–19 October 2005; pp. 162–165.
149. Li, Z.; Okamoto, K.; Ohki, Y.; Tanaka, T. Effects of nano-filler addition on partial discharge resistance and dielectric breakdown strength of micro-Al_2O_3 epoxy composite. *IEEE Trans. Dielectr. Electr. Insul.* **2010**, *17*, 653–661.
150. Li, Z.; Okamoto, K.; Ohki, Y.; Tanaka, T. The role of nano and micro particles on partial discharge and breakdown strength in epoxy composites. *IEEE Trans. Dielectr. Electr. Insul.* **2011**, *18*, 675–681.
151. Li, S.; Yin, G.; Chen, G.; Li, J.; Bai, S.; Zhong, L.; Zhang, Y.; Lei, Q. Short-term breakdown and long-term failure in nanodielectrics: A review. *IEEE Trans. Dielectr. Electr. Insul.* **2010**, *17*, 1523–1535.
152. Zhang, Y.; Danikas, M.G.; Zhao, X.; Cheng, Y. Preliminary experimental work on nanocomposite polymers: small partial discharges at inception voltage, the existence of possible charging mechanisms below inception voltage and the problem of definitions. *J. Electr. Eng.* **2012**, *63*, 109–114.
153. Imai, T.; Sawa, F.; Nakano, T.; Ozaki, T.; Shimizu, T.; Kuge, S.; Kozako, M.; Tanaka, T. Insulation properties of nano- and micro-filler mixture composite. In Proceedings of the Conference on Electrical Insulation and Dielectric Phenomena (CEIDP), Nashville, TN, USA, 16–19 October 2005; pp. 171–174.
154. Ansorge, S.; Schmuck, F.; Papailiou, K. Impact of different fillers and filler treatments on the erosion suppression mechanism of silicone rubber for use as outdoor insulation material. *IEEE Trans. Dielectr. Electr. Insul.* **2015**, *22*, 979–988.
155. Lau, K.Y.; Vaughan, A.S.; Chen, G.; Hosier, I.L.; Holt, A.F.; Ching, K.Y. On the space charge and DC breakdown behavior of polyethylene/silica nanocomposites. *IEEE Trans. Dielectr. Electr. Insul.* **2014**, *21*, 340–351.
156. Yin, Y.; Chen, J.; Yang, J.; Xiao, D.; Tu, D.; Yin, R.; Qian, H. Effect of space charge in nanocomposite of LDPE/TiO_2. In Proceedings of the International Conference on Properties and Applications of Dielectric Materials, Nagoya, Japan, 1–5 June 2003; pp. 913–916.
157. Andritsch, T.; Kochetov, R.; Gebrekiros, Y.T.; Lafont, U.; Morshuis, P.H.F.; Smit, J.J. Synthesis and dielectric properties of epoxy based nanocomposites. In Proceedings of the IEEE Conference on Electrical Insulation and Dielectric Phenomena (CEIDP), Virginia Beach, VA, USA, 18–21 October 2009; pp. 523–526.
158. Calebrese, C.; Hui, L.; Schadler, L.S.; Nelson, J.K. A review on the importance of nanocomposite processing to enhance electrical insulation. *IEEE Trans. Dielectr. Electr. Insul.* **2011**, *18*, 938–945.
159. Lau, K.Y.; Piah, M.A.M. Polymer nanocomposites in high voltage electrical insulation perspective: A review. *Malays. Polym. J.* **2011**, *6*, 58–69.

160. Piah, M.A.M.; Darus, A.; Hassan, A. Electrical tracking performance of LLDPE-natural rubber blends by employing combination of leakage current level and rate of carbon track propagation. *IEEE Trans. Dielectr. Electr. Insul.* **2005**, *12*, 1259–1265.
161. El-Hag, A.H.; Simon, L.C.; Jayaram, S.H.; Cherney, E.A. Erosion resistance of nano-filled silicone rubber. *IEEE Trans. Dielectr. Electr. Insul.* **2006**, *13*, 122–128.
162. Sarathi, R.; Sahu, R.K.; Rajeshkumar, P. Understanding the thermal, mechanical and electrical properties of epoxy nanocomposites. *Mater. Sci. Eng. A* **2007**, *445–446*, 567–578.
163. Raetzke, S.; Kindersberger, J. Resistance to high voltage arcing and the resistance to tracking erosion for silicone/SiO_2 nanocomposites. In Proceedings of the 16th International Symposium on High Voltage Engineering, Cape Town, South Africa, 24–28 August 2009; pp. 1–6.
164. Vogelsang, R.; Farr, T.; Fröhlich, K. The effect of barriers on electrical tree propagation in composite insulation materials. *IEEE Trans. Dielectr. Electr. Insul.* **2006**, *13*, 373–382.
165. Ding, H.-Z.; Varlow, B.R. Filler volume fraction effects on the breakdown resistance of an epoxy microcomposite dielectric. In Proceedings of the IEEE International Conference on Solid Dielectrics (ICSD), Toulouse, France, 5–9 July 2004; pp. 816–820.
166. Uehara, H.; Kudo, K. Barrier effect of treeing in composite insulating materials with heat-adhesive interfaces of different polymers. *IEEE Trans. Dielectr. Electr. Insul.* **2005**, *12*, 1266–1271.
167. Christantoni, D.D.; Vardakis, G.E.; Danikas, M.G. Propagation of electrical tree growth in a composite solid insulation consisted of epoxy resin and mica sheets: Simulation with the aid of cellular automata. In Proceedings of the 10th IEEE International Conference on Solid Dielectrics (ICSD), Postdam, Germany, 4–9 July 2010; pp. 1–4.
168. Zhang, C.; Stevens, G.C. The dielectric response of polar and non-polar nanodielectrics. *IEEE Trans. Dielectr. Electr. Insul.* **2008**, *15*, 606–617.
169. Dodd, S.J.; Dissado, L.A.; Fothergill, J.C. Influence of absorbed moisture on the dielectric properties of epoxy resins. In Proceedings of the Conference on Electrical Insulation and Dielectric Phenomena (CEIDP), West Lafayette, IN, USA, 17–20 October 2010; pp. 1–4.
170. Tsekmes, I.A.; Morshuis, P.H.F.; Smit, J.J. The influence of interfaces and water uptake on the dielectric response of epoxy-cubic boron nitride composites. *J. Mater. Sci.* **2015**, *50*, 3929–3941.
171. Nielsen, L.E. The thermal and electrical conductivity of two-phase systems. *Ind. Eng. Chem. Fundamen.* **1974**, *13*, 17–20.
172. Kochetov, R.; Andritsch, T.; Lafont, U.; Morshuis, P.H.F.; Picken, S.J.; Smit, J.J. Thermal behaviour of epoxy resin filled with high thermal conductivity nanopowders. In Proceedings of the IEEE Electrical Insulation Conference (EIC), Montreal, QC, Canada, 31 May–3 June 2009; pp. 524–528.
173. Han, Z.; Wood, J.W.; Herman, H.; Zhang, C.; Stevens, G.C. Thermal properties of composites filled with different fillers. In Proceedings of the IEEE International Symposium on Electrical Insulation (ISEI), Vancouver, BC, Canada, 9–12 June 2008; pp. 497–501.

174. Irwin, P.C.; Cao, Y.; Bansal, A.; Schadler, L.S. Thermal and mechanical properties of polyimide nanocomposites. In Proceedings of the Conference on Electrical Insulation and Dielectric Phenomena (CEIDP), Albuquerque, NW, USA, 19–22 October 2003; pp. 120–123.
175. Xu, Y.S.; Chung, D.D.L. Increasing the thermal conductivity of boron nitride and aluminum nitride particle epoxy-matrix composites by particle surface treatments. Compos. *Interfaces* **2000**, *7*, 243–256.
176. Miller, G.H. Trends in insulation materials with processes for rotating machines. *IEEE Electr. Insul. Mag.* **1998**, *14*, 7–11.
177. Irwin, P.; Zhang, W.; Cao, Y.; Fang, X.; Tan, D.Q. Mechanical and thermal properties. In *Dielectric Polymer Nanocomposites*; Nelson, J.K., Ed.; Springer: New York, NY, USA, 2010; pp. 163–196.
178. Yasmin, A.; Daniel, I.C. Mechanical and thermal properties of graphite platelet/epoxy composites. *Polymer* **2004**, *45*, 8211–8219.
179. Yang, H.-S.; Kim, H.-J.; Son, J.; Park, H.-J.; Lee, B.-J.; Hwang, T.-S. Rice-husk flour filled polypropylene composites; mechanical and morphological study. *Compos. Struct.* **2004**, *63*, 305–312.
180. Lam, C.-K.; Cheung, H.-Y.; Lau, K.-T.; Zhou, L.-M.; Ho, M.-W.; Hui, D. Cluster size effect in hardness of nanoclay/epoxy composites. *Compos. Part B* **2005**, *36*, 263–269.
181. Ray, D.; Bhattacharya, D.; Mohanty, A.K.; Drzal, L.T.; Misra, M. Static and dynamic mechanical properties of vinylester resin matrix composites filled with fly ash. *Macromol. Mater. Eng.* **2006**, *291*, 784–792.
182. Gao, Y.; Liu, L.; Zhang, Z. Mechanical performance of nano-$CaCO_3$ filled polystyrene composites. *Acta Mech. Solida Sin.* **2009**, *22*, 555–562.
183. Asi, O. Mechanical properties of glass-fiber reinforced epoxy composites filled with Al_2O_3 particles. *J. Reinf. Plast. Compos.* **2009**, *28*, 2861–2867.
184. Zaman, H.U.; Hun, P.D.; Khan, R.A. Morphology, mechanical, and crystallization behaviors of micro- and nano-ZnO filled polypropylene composites. *J. Reinf. Plast.* **2012**, *31*, 323–329.
185. Ibrahim, M.S.; Sapuan, S.M.; Faieza, A.A. Mechanical and thermal properties of composites from unsaturated polyester filled with oil palm ash. *J. Mech. Eng. Sci.* **2012**, *2*, 133–147.
186. Agubra, V.A.; Owuor, P.S.; Hosur, M.V. Influence of nanoclay dispersion methods on the mechanical behavior of E-glass/epoxy nanocomposites. *Nanomaterials* **2013**, *3*, 550–563.
187. Chauhan, S.R.; Thakur, S. Effects of particle size, particle loading and sliding distance on the friction and wear properties of cenosphere particulate filled vinylester composites. *Mater. Des.* **2013**, *51*, 398–408.
188. Sayer, M. Elastic properties and buckling load evaluation of ceramic particles filled. *Compos. Part B* **2014**, *59*, 12–20.
189. Sudheer, M.; Prabhu, R.; Raju, K.; Bhat, T. Effect of filler content on the performance of epoxy/PTW composites. *Adv. Mater. Sci. Eng.* **2014**, *2014*, 1–11.

190. Prakash, M.A.; Kumar, G.S.; Sandeep, N.; Ravikumar, K. A review on ceria epoxy nanocomposites with a new research proposal. *IOSR J. Mech. Civil Eng.* **2015**, *12*, 1–3.
191. Ozsoy, I.; Demirkol, A.; Mimaroglu, A.; Unal, H.; Demir, Z. The influence of micro- and nano-filler content on the mechanical properties of epoxy composites. *Strojniški vestnik. J. Mech. Eng.* **2015**, *61*, 601–609.
192. Novoselov, K.S.; Geim, A.K.; Morozov, S.V.; Jiang, D.; Zhang, Y.; Dubonos, S.V.; Grigorieva, I.V.; Firsov, A.A. Electric field effect in atomically thin carbon films. *Science* **2004**, *306*, 666–669.
193. Stankovich, S.; Dikin, D.A.; Dommett, G.H.B.; Kohlhaas, K.M.; Zimney, E.J.; Stach, E.A.; Piner, R.D.; Nguyen, S.T.; Ruoff, R.S. Graphene-based composite materials. *Nature* **2006**, *442*, 282–286.
194. Kuila, T.; Bose, S.; Hong, C.E.; Uddin, M.E.; Khanra, P.; Kim, N.H.; Lee, J.H. Preparation of functionalized graphene/linear low density polyethylene composites by a solution mixing method. *Carbon* **2011**, *49*, 1033–1037.
195. Potts, J.R.; Dreyer, D.R.; Bielawski, C.W.; Ruoff, R.S. Graphene-based polymer nanocomposites. *Polymer* **2011**, *52*, 5–25.
196. Sandler, J.K.W.; Kirk, J.E.; Kinloch, I.A.; Shaffer, M.S.P.; Windle, A.H. Ultra-low electrical percolation threshold in carbon-nanotube-epoxy composites. *Polymer* **2003**, *44*, 5893–5899.
197. Wang, D.-W.; Li, F.; Zhao, J.; Ren, W.; Chen, Z.G.; Tan, J.; Wu, Z.-S.; Gentle, I.; Lu, G.Q.; Cheng, H.-M. Fabrication of graphene/polyaniline composite paper via *in situ* anodic electropolymerization for high-performance flexible electrode. *ACS Nano* **2009**, *3*, 1745–1752.
198. Murugan, A.V.; Muraliganth, T.; Manthiram, A. Rapid, facile microwave-solvothermal synthesis of graphene nanosheets and their polyaniline nanocomposites for energy strorage. *Chem. Mater.* **2009**, *21*, 5004–5006.
199. Sangermano, M.; Chiolerio, A.; Veronese, G.P.; Ortolani, L.; Rizzoli, R.; Mancarella, F.; Morandi, V. Graphene–epoxy flexible transparent capacitor obtained by graphene–polymer transfer and UV-induced bonding. *Macromol. Rapid Commun.* **2014**, *35*, 355–359.
200. Kuila, T.; Bose, S.; Mishra, A.K.; Khanra, P.; Kim, N.H.; Lee, J.H. Chemical functionalization of graphene and its applications. *Prog. Mater. Sci.* **2012**, *57*, 1061–1105.
201. Martín-Gallego, M.; Verdejo, R.; Lopez-Manchado, M.A.; Sangermano, M. Epoxy-graphene UV-cured nanocomposites. *Polymer* **2011**, *52*, 4664–4669.
202. Sangermano, M.; Marchi, S.; Valentini, L.; Bon, S.B.; Fabbri, P. Transparent and conductive graphene oxide/poly(ethylene glycol) diacrylate coatings obtained by photopolymerization. *Macromol. Mater. Eng.* **2011**, *296*, 401–407.
203. Giardi, R.; Porro, S.; Chiolerio, A.; Celasco, E.; Sangermano, M. Inkjet printed acrylic formulations based on UV-reduced graphene oxide nanocomposites. *J. Mater. Sci.* **2013**, *48*, 1249–1255.
204. Park, S.; Ruoff, R.S. Chemical methods for the production of graphenes. *Nat. Nanotechnol.* **2009**, *4*, 217–224.

205. Hummers, W.S.; Offeman, R.E. Preparation of graphitic oxide. *J. Am. Chem. Soc.* **1958**, *80*, 1339.
206. Dreyer, R.D.; Park, S.; Bielawski, C.W.; Ruoff, R.S. The chemistry of graphene oxide. *Chem. Rev. Soc.* **2010**.
207. Dikin, A.K.; Stankovich, S.; Zimney, E.J.; Piner, R.D.; Dommett, G.H.B.; Evmenenko, G.; Nguyen, S.T.; Ruoff, R.S. Preparation and characterization of graphene oxide paper. *Nature* **2007**, *448*, 457–460.
208. Wei, J.; Vo, T.; Inam, F. Epoxy/graphene nanocomposites–processing and properties: A review. *RSC Adv.* **2015**, *5*, 73510–73524.
209. Bai, S.; Shen, X. Graphene-inorganic nanocomposites. *RSC Adv.* **2012**, *2*, 64–98.
210. Chatterjee, S.; Nafezarefi, F.; Tai, N.H.; Schlagenhauf, L.; Nüesch, F.A.; Chu, B.T.T. Size and synergy effects of nanofiller hybrids including graphene nanoplatelets and carbon nanotubes in mechanical properties of epoxy composites. *Carbon* **2012**, *50*, 5380–5386.
211. Sangermano, M.; Buzzerio, G.; Rizzoli, R.; Ortolani, L.; Morandi, V.; Pirri, F.; Chiolerio, A. Enhanced performance of graphene-epoxy flexible capacitors by means of ceramic fillers. *Macromol. Chem. Phys.* **2015**, *216*, 707–713.
212. Martin-Gallego, M.; Lopez-Manchado, M.A.; Calza, P.; Roppolo, I.; Sangermano, M. Gold-functionalized graphene as conductive filler in UV-curable epoxy resin. *J. Mater. Sci.* **2015**, *50*, 605–610.
213. Guimard, N.K.; Oehlenschlaeger, K.K.; Zhou, J.; Hilf, S.; Schmidt, F.G.; Barner-Kowollik, C. Current trends in the field of self-healing materials. *Macromol. Chem. Phys.* **2012**, *213*, 131–143.
214. Burattini, S.; Greenland, B.W.; Chappell, D.; Colquhoun, H.M.; Hayes, W. Healable polymeric materials: A tutorial review. *Chem. Soc. Rev.* **2010**, *39*, 1973–1985.
215. Wu, D.Y.; Meure, S.; Solomon, D. Self-healing polymeric materials: A review of recent developments. *Prog. Polym. Sci.* **2008**, *33*, 479–522.
216. Billiet, S.; Hillewaere, X.K.D.; Teixeira, R.F.A.; Du Prez, F.E. Chemistry of crosslinking processes for self-healing polymers. *Macromol. Rapid Commun.* **2013**, *34*, 290–309.
217. Yuan, Y.C.; Rong, M.Z.; Zhang, M.Q. Preparation and characterization of microencapsulated polythiol. *Polymer* **2008**, *49*, 2531–2541.
218. Blaiszik, B.J.; Caruso, M.M.; McIlroy, D.A.; Moore, J.S.; White, S.R.; Sottos, N.R. Microcapsules filled with reactive solutions for self-healing materials. *Polymer* **2009**, *50*, 990–997.
219. German, I.; Rhodes, R.; Stevens, G.C.; Thomas, J. An investigation of self-repair systems for solid extruded polymeric and fluid filled cables. In Proceedings of the IEEE Electrical Insulation Conference (EIC), Seattle, DC, USA, 7–10 June 2015; pp. 301–304.
220. Lesaint, C.; Risinggård, V.; Hølto, J.; Sæternes, H.H.; Hestad, Ø.; Hvidsten, S.; Glomm, W.R. Self-healing high voltage electrical insulation materials. In Proceedings of the Electrical Insulation Conference (EIC), Philadelphia, PA, USA, 8–11 June 2014; pp. 241–244.

221. Rudi, K.; Andrew, D.H.; Managam, R.; Nawawi, Z.; Hozumi, N.; Nagao, M. The self-healing property of silicone rubber after degraded by treeing. In Proceedings of the International Conference on Condition Monitoring and Diagnosis (CMD), Bali, Indonesia, 23–27 September 2012; pp. 254–257.
222. Burattini, S.; Greenland, B.W.; Merino, D.H.; Weng, W.; Seppala, J.; Colquhoun, H.M.; Hayes, W.; Mackay, M.E.; Hamley, I.W.; Rowan, S.J. A healable supramolecular polymer blend based on aromatic pi-pi stacking and hydrogen-bonding interactions. *J. Am. Chem. Soc.* **2010**, *132*, 12051–12058.
223. Krauss, S.; Metzger, T.H.; Fratzl, P.; Harrington, M.J. Self-repair of a biological fiber guided by an ordered elastic framework. *Biomacromolecules* **2013**, *14*, 1520–1528.
224. Chen, X.; Dam, M.A.; Ono, K.; Mal, A.; Shen, H.; Nutt, S.R.; Sheran, K.; Wudl, F. A thermally re-mendable cross-linked polymeric material. *Science* **2002**, *295*, 1698–1702.
225. Liu, Y.; Hsieh, C.; Chen, Y. Thermally reversible cross-linked polyamides and thermo-responsive gels by means of Diels–Alder reaction. *Polymer* **2006**, *47*, 2581–2586.
226. Peterson, A.M.; Jensen, R.E.; Palmese, G.R. Room-temperature healing of a thermosetting polymer using the Diels-Alder reaction. *ACS Appl. Mater. Interfaces* **2010**, *2*, 1141–1149.
227. Chen, X.; Wudl, F.; Mal, A.K.; Shen, H.; Nutt, S.R. New thermally remendable highly cross-linked polymeric materials. *Macromolecules* **2003**, *36*, 1802–1807.
228. Syrett, J.A.; Mantovani, G.; Barton, W.R.S.; Price, D.; Haddleton, D.M. Self-healing polymers prepared via living radical polymerisation. *Polym. Chem.* **2010**, *1*, 102–106.
229. Yoshie, N.; Saito, S.; Oya, N. A thermally-stable self-mending polymer networked by Diels-Alder cycloaddition. *Polymer* **2011**, *52*, 6074–6079.
230. Ling, J.; Rong, M.Z.; Zhang, M.Q. Photo-stimulated self-healing polyurethane containing dihydroxyl coumarin derivatives. *Polymer* **2012**, *53*, 2691–2698.
231. Chung, C.; Roh, Y.; Cho, S.; Kim, J. Crack healing in polymeric materials via photochemical [2+2] cycloaddition. *Chem. Mater.* **2004**, *16*, 3982–3984.
232. Froimowicz, P.; Frey, H.; Landfester, K. Towards the generation of self-healing materials by means of a reversible photo-induced approach. *Macromol. Rapid Commun.* **2011**, *32*, 468–473.
233. Radl, S.; Kreimer, M.; Griesser, T.; Oesterreicher, A.; Moser, A.; Kern, W.; Schlögl, S. New strategies towards reversible and mendable epoxy based materials employing [4πs + 4πs] photocycloaddition and thermal cycloreversion of pendant anthracene groups. *Polymer* **2015**, *80*, 76–87.
234. Radl, S.; Kreimer, M.; Manhart, J.; Griesser, T.; Moser, A.; Pinter, G.; Kalinka, G.; Kern, W.; Schlögl, S. Photocleavable epoxy based materials. *Polymer* **2015**, *69*, 159–168.
235. Cesano, F.; Rattalino, I.; Demarchi, D.; Bardelli, F.; Sanginario, A.; Gianturco, A.; Veca, A.; Viazzi, C.; Castelli, P.; Scarano, D.; Zecchina, A. Structure and properties of metal-free conductive tracks on polyethylene/multiwalled carbon nanotube composites as obtained by laser stimulated percolation. *Carbon* **2013**, *61*, 63–71.
236. Kaiser, A.B.; Skakalova, V. Electronic conduction in polymers, carbon nanotubes and graphene. *Chem. Soc. Rev.* **2011**, *40*, 3786–3801.

237. Chun, K.-Y.; Oh, Y.; Rho, J.; Ahn, J.-H.; Kim, Y.-J.; Choi, H.R.; Baik, S. Highly conductive, printable and stretchable composite films of carbon nanotubes and silver. *Nat. Nanotechnol.* **2010**, *5*, 853–857.
238. Gao, W.; Singh, N.; Song, L.; Liu, Z.; Reddy, A.L.M.; Ci, L.; Vajtai, R.; Zhang, Q.; Wei, B.; Ajayan, P.M. Direct laser writing of micro-supercapacitors on hydrated graphite oxide films. *Nat. Nanotechnol.* **2011**, *6*, 496–500.
239. Leigh, S.J.; Bradley, R.J.; Purssell, C.P.; Billson, D.R.; Hutchins, D.A. A simple, low-cost conductive composite material for 3D printing of electronic sensors. *PLoS ONE* **2012**, *7*, e49365.
240. Kordás, K.; Mustonen, T.; Tóth, G.; Jantunen, H.; Lajunen, M.; Soldano, C.; Talapatra, S.; Kar, S.; Vajtai, R.; Ajayan, P.M. Inkjet printing of electrically conductive patterns of carbon nanotubes. *Small* **2006**, *2*, 1021–1025.

Mechanical Properties of Composites Used in High-Voltage Applications

Andreas Moser and Michael Feuchter

Abstract: Materials used in high voltage applications have to meet a lot of regulations for their safety and functional usage during their lifetime. For high voltage applications the electrical properties are the most relevant designing criteria. However, the mechanical properties of such materials have rarely been considered for application dimensioning over the last decades. This article gives an overview of composite materials used in high voltage applications and some basic mechanical and thermo-mechanical characterization methods of such materials, including a discussion of influences on practically used epoxy based thermosets.

Reprinted from *Polymers*. Cite as: Moser, A.; Feuchter, M. Mechanical Properties of Composites Used in High-Voltage Applications. *Polymers* **2016**, *8*, 260.

1. Introduction

For all electrical and electronic applications, the material's ability to insulate and protect the conductive circuit is of high importance for the safety and functional operation. Solid organic materials used in electrical engineering are paper, wood, wax, leather, as well as a number of natural and synthetic resins, rubbers, and polymers [1] (see electric resistivity chart in Figure 1). Since their introduction in the early 1970s, insulators built of polymer materials have been heavily used as suitable replacements for porcelain and glass insulators.

Thermosets are generally reported as having very good dimensional stability, which makes them usable in sheets and bulk molding compounds for encapsulates, coatings, and insulating applications. The processing of thermosets can be done with high precision to form very stable polymer films. For electrical insulating moldings, such as switch housings, connector shells, high voltage insulators, and equipment casings, thermosets are often chosen for their dimensional stability and mechanical performance when subjected to electrical, thermal and environmental stress over time [2]. In the case of electrical equipment, such as high voltage capacitors and printed circuit boards epoxy matrix materials—based on bisphenol A diglycidyl ether (DGEBA/BADGE)—are known to withstand high dielectric breakdown voltage and high temperatures [3]. However, in the construction process of electrical applications, mechanical stresses are not considered to have severe influences on the lifetime of a product, though it is known in polymer engineering that the slightest stress or defect in polymer materials could lead to a failure of the product. Therefore, mechanical,

fracture mechanical, and long-term characterization should be considered for the dimensioning of polymeric materials in electrical and electronic applications. In the following review, a brief overview on methods of mechanical and thermo-mechanical characterizations is given including representative examples found in literature. In addition, short background information of these characterization methods is presented.

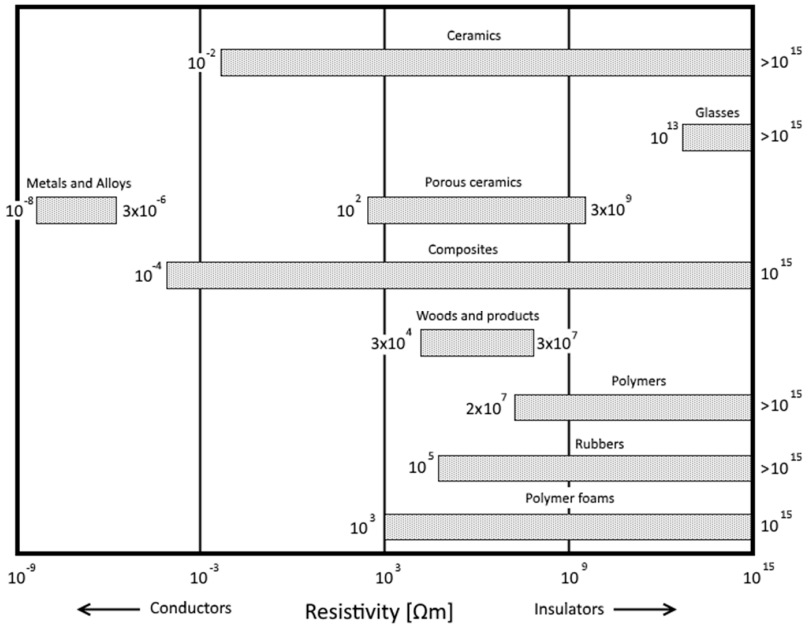

Figure 1. Electrical resistivity chart of various material classes.

2. Characterization of Thermo-Mechanical Properties of Thermosets

In the case of application requirements, the required temperature range is described as service temperature. For thermosets, the suitability is described as the glass transition temperature (T_g). If the thermoset is loaded during its lifespan it is of immense importance for the T_g to be well above the service temperature. Therefore, a good understanding of thermal and thermo-mechanical properties of thermosets is necessary. To characterize the thermo-mechanical behavior of polymeric materials, the use of dynamic mechanical analysis (DMA) provides precise information about the usable service region of a thermoset [1,2,4].

2.1. Dynamic Mechanical Analysis

The DMA is used to characterize the viscoelastic behavior of a polymeric material over a broad range of temperature and frequency. Viscoelastic behavior

covers changes in molecular dynamics, which is characterized by localized and cooperative motions in polymers. These motions are responsible for different relaxations processes, which are composed of energy dissipation and mechanical damping. The determination of this viscoelastic behavior is performed via small dynamically applied strain or stress (sinusoidal strain, stress). As a result of the viscoelastic behavior of polymeric materials, a phase lag is introduced between strain and stress. As a result of this dynamic problem, a complex solution is applied and results in a complex modulus: $E^* = E' + iE''$, which describes the mechanical property of the characterized material. This complex modulus breaks down into the storage modulus (E', elastic part) and the loss modulus (E'', non-elastic part). The quotient of these values is called the damping factor (tan δ) [5]. The dynamically applied strain or stress can be monitored as a function of frequency and temperature. A typical DMA curve for a thermoset resin is shown in Figure 2. For thermosets this curve can be divided into three characteristic regions. At low temperatures (below the glass transition region) the material is in the glassy state and exhibits a brittle and rigid behavior. In the glass transition region there is a loss in the storage modulus of many decades, and peaks in loss modulus and damping factor appears. The materials' behavior changes from brittle and rigid to soft and ductile. The width of the damping factor peak may describe the degree of homogeneity and crosslink density in thermoset polymers. Adjacent to the glass transition region is the rubbery state, where the material stiffness is very low and it retains its soft and ductile behavior [6].

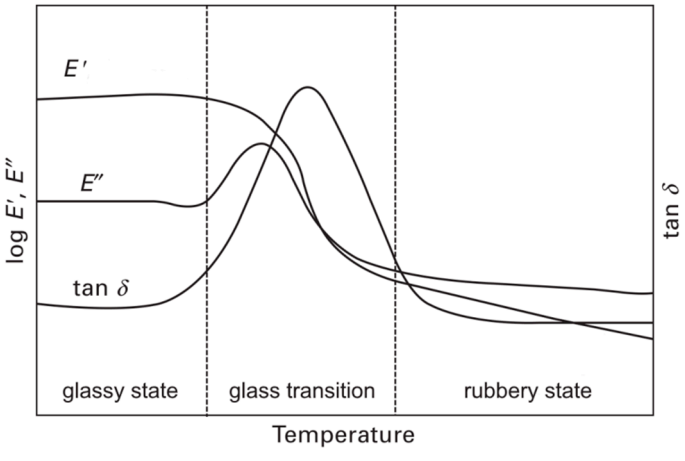

Figure 2. A typical dynamic mechanical analysis (DMA) curve of thermoset polymer.

2.2. Structure Property Relationships in the Glass Transition Region

Through the direct connection of network formation (crosslink density, conversion, etc.) and glass transition (T_g), relationships can be reasonably established on the basis of experimental data. In the case of network formation, mainly two cases (homogenous or inhomogeneous networks) can be distinguished [7].

2.3. Homogenous Network

Fully cured (homogenous network) can be represented by epoxy-amine systems in terms of stoichiometric mixing. These types of thermosets feature a high conversion rate. Due to the homogenous network, the relaxation process in the glass transition region is consistent. This is represented through an almost spontaneous drop in storage modulus and a sharp and symmetrical peak in damping factor (see Figure 3).

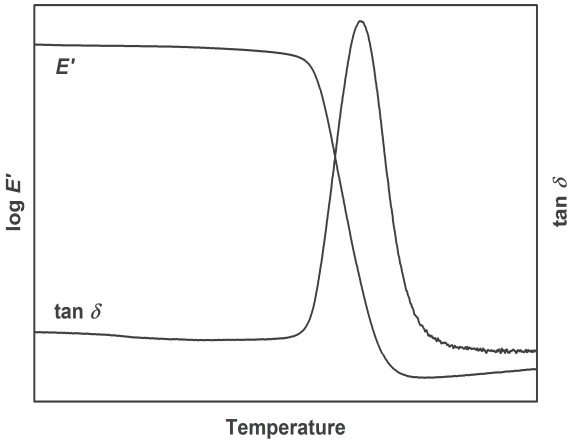

Figure 3. Representative DMA curve of a homogenous thermoset.

2.4. Inhomogeneous Network

As a result of insufficient curing or non-stoichiometric mixture of monomers, the resulting network of thermosets may be inhomogeneous. This leads to regions in the polymeric material, where crosslink density varies. As a result, these regions may differ in glass transition temperature. The use of dynamic mechanical analysis reveals these different relaxation regions occur by overlapping peaks in damping factor curves. In Figure 4, such a curve is presented. It shows an unsymmetrical peak of the damping factor in the region of glass transition. Furthermore, the peak can be separated into at least 3–4 individual peaks. As described, these individual peaks represent different fractions of the network with individual crosslink density.

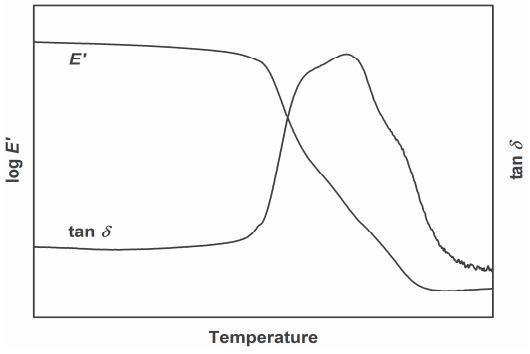

Figure 4. Representative DMA curve of an inhomogeneous thermoset.

2.5. Application of DMA Analysis on Epoxy Based Materials

Epoxy based thermosets are often used for insulating applications. One of the utilized epoxy matrix systems are epoxy-amine thermosets. The formation of a homogenous network of DGEBA based epoxy-amine systems only occurs on a stoichiometric mixture. Preparing non-stoichiometric mixtures with varying amine concentrations results in decreasing glass transition temperatures for hypo- and hyperstoichiometric amine content (see Table 1) [8,9]. Additionally, this leads to increasing network inhomogeneity (broader glass transition with more than one relaxation process). Also, blending of epoxy based thermosets with other polymeric materials may lead to network inhomogeneity [10]. However, this inhomogeneity depends on the polarity interactions between the two polymeric systems [11–13]. In addition to the influence of reaction stoichiometry, the incorporation of microscale or nanoscale fillers may also have an influence on the glass transition temperature of homogenous networks [14,15] as well as using different types of plasticizer [16].

Table 1. Glass transition values of epoxy based thermosets measured at maximum of tan δ.

Epoxy base	T_g measured at maximum tan δ (°C)	Reference
DGEBA	161	[8]
DGEBA + carbon black	169	[14]
Epoxidized allyl soyate	90	[17]
Epoxidized soybean oil	80	[18]

Due to the fact that DGEBA is based on bisphenol A, which seems to have severe impacts on animals' and human health [19,20], researchers have been trying to create substitutes for DGEBA based epoxy thermosets. In recent years, bio-based polymers derived from renewable resources have become increasingly important as sustainable

and eco-efficient products to replace the petrochemical-derived DGEBA. Until now numerous bio-based epoxy resins deriving from vegetable oils—such as soybean oil, linseed oil, and castor oil—have been studied [17,21–23]. These types of epoxy resins contain linear aliphatic chains and cannot lead to glass transition temperatures above 100 °C. However, these linear systems (if not blended with other monomers) easily form homogenous networks. Using epoxy monomers based on Isosorbide leads to glass transition temperatures above 100 °C [24]. Table 1 sums up some glass transition values found in literature for various epoxy based formulations.

3. Mechanical Properties of Thermosets

In electric and electronic applications, the mechanical properties are a subordinate factor to the electrical performance. However, for moldings used in connectors, housings, and cases, the mechanical properties like impact properties or tensile/bending strength and elongation to failure are important. In flexible printed circuits (FPC), brittle thermoset polymers are not desirable, as these circuits are often undergoing static or dynamic loading during their lifespan. In both cases flexibility is a requirement for the resins used in the adhesive and dielectric films.

In the following sections, a brief description of the basic principles of mechanical behavior of thermosets is given, including tensile, bending, and impact behavior. Since the temperature range in thermosets' applications lies mostly below the glass transition temperature [25], the majority of the discussions in this section will be focused on the mechanical behavior at glassy state.

3.1. Tensile tests on Thermosets

Among static and quasi-static testing and measuring methods, the tensile test is regarded as the most fundamental test in mechanical material testing. In contrast to the fact that pure tensile loading is rather uncommon in reality, this test ranks high in polymer testing. Various approaches to execute tensile tests are possible, requiring different specimens, loading conditions and/or clamping devices [26]. Due to the narrow elastic deformation range of plastics, the Young's modulus is determined as a secant modulus. It includes the elastic and linear-viscoelastic deformation range of the stress–strain diagram. Evaluation is limited to the deformation range between 0.05% and 0.25% of the strain.

$$E = \frac{\sigma_2 - \sigma_1}{\varepsilon_2 - \varepsilon_1} \tag{1}$$

The decrease of Young's modulus, with increasing test temperature, can be qualitatively represented by the storage modulus in Figure 2. Because the different regions of tensile behavior are associated with different magnitudes and amounts of molecular motions and relaxation effects, it is apparent that anything that alters the molecular motions also alters the regions of tensile behavior. Thus, molecular

structure, molecular weight (for thermoplastics), crosslink density (for thermosets), and test temperature can significantly influence these behaviors [5]. Tensile tests for determining strength and deformation properties of plastics are usually performed at a testing speed of 1–500 mm/min. Typical stress–strain diagrams for various plastics are shown in Figure 5. The parameters derivable from the curves correspond to characteristic points in the diagrams. Diagram (a) can be assigned to brittle material behavior with relatively high tensile strength (σ_M), whereby the tensile strain at break (ε_B) achieved can be as much as 10%. Typical examples for such material behavior include thermosets, as well as filled and reinforced plastics. Stress–strain diagrams of types (b) through (d) represent ductile deformation behavior with strains at break of several hundred percent, but relatively low tensile strengths. Some typical examples for such material behavior include polyolefines and polyamides. Particularly thermoplastics with type (b) and (c) stress–strain behavior exhibit a yield stress (σ_y), at which local necking followed by a constant stress plateau occurs, also called cold yielding. The stress plateau is the result of stretching with yield zone formation, whereby the material is stretched and pulls itself simultaneously out of the unstretched part of the specimen. The type (e) stress–strain diagram in Figure 5 corresponds to the typical curve of rubbery materials with very low strength and modulus, but very high tensile strains at break. This material group includes, for example, polyvinyl chloride, as well as natural and synthetic rubber [25,26].

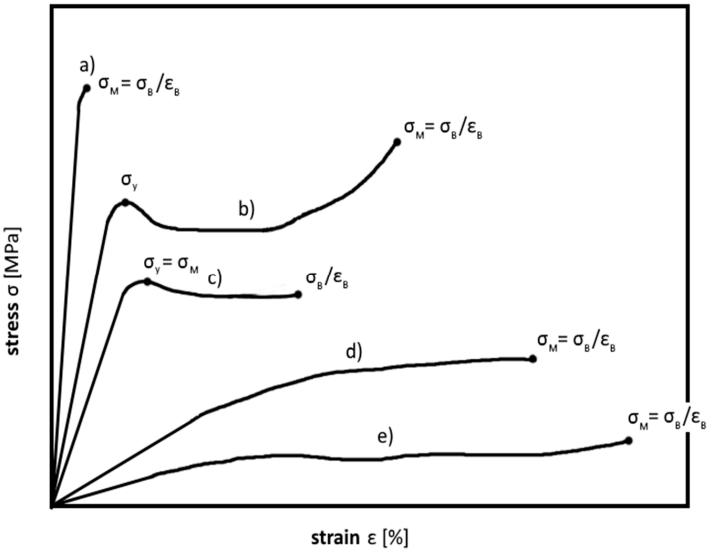

Figure 5. Stress–strain curves of various polymeric materials, (**a**) brittle materials; (**b**,**c**) tough materials with yield point; (**d**) tough material without yield point and (**e**) elastomeric materials.

3.2. Application of Tensile Tests on Epoxy Based Materials

The effects of crosslink density or conversion on Young's modulus, tensile strength, and elongation at break have been covered by various authors. With an increase in crosslink density or conversion, the Young's modulus and the tensile strength are increased—whereas the elongation is decreased. This is caused by the evolution from a very soft and ductile material (at low crosslink density or conversion) to a very hard and rigid material [27]. Blending the DGEBA based epoxy materials with aliphatic or cyclic epoxy-species results in a significant change in Young's modulus, tensile strength and elongation at break [28,29]. Through the growing hype of nanoparticles in the last centuries, various nanoparticle types like particles based on nanosilicates, carbon-nanotubes, fullerenes, etc., were incorporated into epoxy matrices to increase the material's properties. Some of them, like carbon-nanotubes, tend to increase Young's modulus and tensile strength at preservation of the elongation at break at filler contents below 1 w% [30]. An undoubted challenge when using layered nanoparticles is the exfoliation property of these particles, especially in the case of layered nanosilicates [18,31]. In the field of bio based DGEBA substitutes, tensile tests were also performed covering influences on tensile properties of a second reactive epoxy species, which increases Young's modulus and tensile strength but decreases elongation [18]. Also, the influence of nanoparticles on the tensile properties of bio based epoxies was studied, revealing increases for Young's modulus and tensile strength. However, at higher filler content the tensile strength is lower, due to the lack of particle exfoliation [32]. Table 2 illustrates values of Young's Modulus for different types of epoxy based materials.

Table 2. Young's Modulus values of epoxy based thermosets measured in tension mode.

Epoxy base	Young's modulus (MPa)	Reference
DGEBA	2,750	[15]
DGEBA + Carbon nanotubes	3,500	[30]
DGEBA + sisal fibers	15,000	[33]
Epoxidized soybean oil	648	[18]

3.3. Bending Test on Thermosets

Flexural loading is one of the most common types of load encountered in electric/electronic applications. Thus it is highly significant for determining characteristic values of polymers and composite materials [25]. The quasi-static bend test is used especially for testing brittle materials, like thermosets, whose failure behavior causes technical problems with tensile tests. In actual testing practice, three-point and four-point bend test equipment is available for performing such

tests. In view of the occurring loads, the four-point bend test is the fundamentally more suitable method, due to the constant bending moment and the freedom from transverse force [26]. The general differential equation of the elastic bending line, the elasticity modulus (E_f), is acquired under the same condition as the tensile test [25,26]:

$$E = \frac{\sigma_{f2} - \sigma_{f1}}{\varepsilon_{f2} - \varepsilon_{f1}} \quad (2)$$

Figure 6 shows typical flexural stress–strain diagrams of various polymers. For the characteristic points in the diagram see the tensile test section.

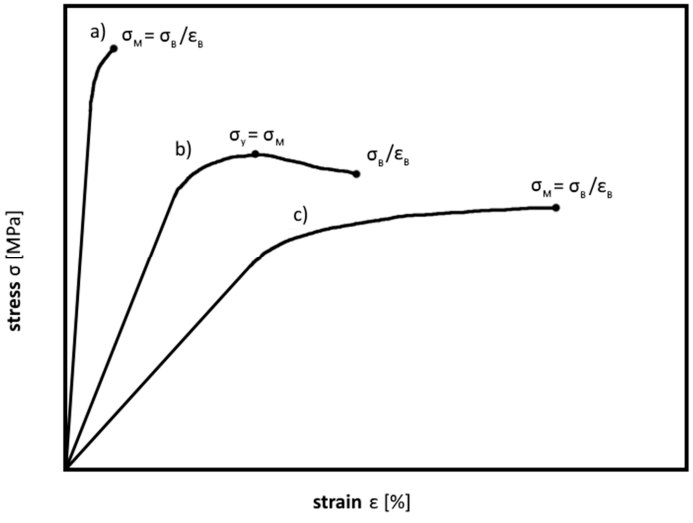

Figure 6. Flexural stress–strain curves of various polymeric materials, (**a**) brittle materials; (**b**,**c**) tough materials.

3.4. Application of Bending Tests on Epoxy Based Materials

Compared to the tensile testing method, the same structure-property relationships also hold for bending tests. That means that an increase in crosslink density raises the flexural modulus and the bending strength—whereas the maximum flexural strain is lowered [8]. Also, blending the resin with linear reaction species results in a softening of the material (modulus and strength decreases whereas the strain is increased) [16]. Besides the use of nanoparticles as fillers to modify the resulting properties of the composite [30,31], short or endless fibers can be used to drastically change the mechanical behavior of composites. Fiber types like glass or carbon fibers drastically increase modulus and strength but lower the flexibility dramatically [34,35]. In the field of bio based materials, the use of hemp, sisal, or jute fibers are common and the resulting property changes are well described in

literature [36,37]. Table 3 illustrates values of flexural modulus for different types of epoxy based materials.

Table 3. Flexural modulus values of epoxy based thermosets measured in 3 point bending mode.

Epoxy base	Flexural modulus (Mpa)	Reference
DGEBA	3,000	[24]
DGEBA + glass fibers	4,900	[36]
DGEBA + hemp fibers	2,900	[36]
Epoxidized soybean oil	775	[18]

3.5. Impact Behavior of Thermosets

In many applications thermosets have to withstand impact load due to environmental or application influences. Even a very small amount of impact energy could seriously reduce the static strength of materials, decreasing component reliability; any attempt to improve the tensile property would lead to a decrease of impact property at the same time. The impact toughness can be determined by measuring the needed energy to break a standard specimen, which is one of the most common methods to evaluate impact properties. Charpy (simple supported beam load; Figure 7a) and Izod (cantilever beam load; Figure 7b) impact tests were developed for isotropic materials [25]. To determine the Charpy impact strength of an unnotched specimen (a_{cU}), the energy (W_c) absorbed by breaking the specimen is related to the initial cross-section area of the specimen:

$$a_{cU} = \frac{W_c}{b * h} \tag{3}$$

Notched Charpy impact strength (a_{cN}) is calculated from the absorbed energy (W_c), related to the smallest initial cross-section of the specimen at notch base:

$$a_{cN} = \frac{W_c}{b_N * h} \tag{4}$$

The difference between Charpy impact strength a_{cU} and notched Charpy impact strength a_{cN} indicates how sensitive a material is to external notches, i.e., takes the problematic notch effect for the Charpy impact test into consideration and indicates how effective fillers are. Thus notch sensitivity can be calculated from the quotients of a_{cN} and a_{cU}:

$$k_Z = \frac{a_{cN}}{a_{cU}} * 100\% \tag{5}$$

In case of inhomogeneous materials or composites (especially fire reinforced composites), fracture mode and energy absorption are affected by various test

parameters, such as fiber orientation, the sample size, and the impact rate. Figure 8 illustrates the occurring failure modes in impact tests. Thermosets in the glassy state mostly feature a brittle failure mode [25,26].

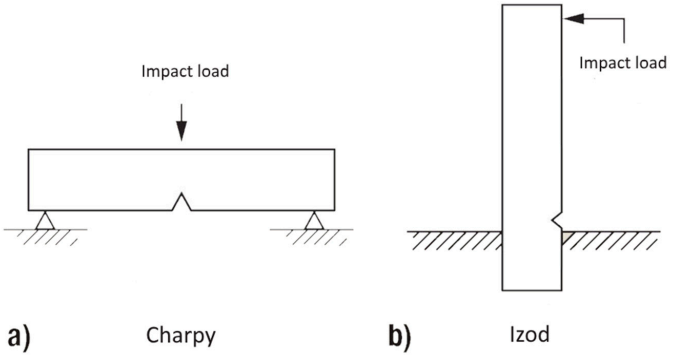

Figure 7. Impact loading in (**a**) Charpy and (**b**) Izod configuration.

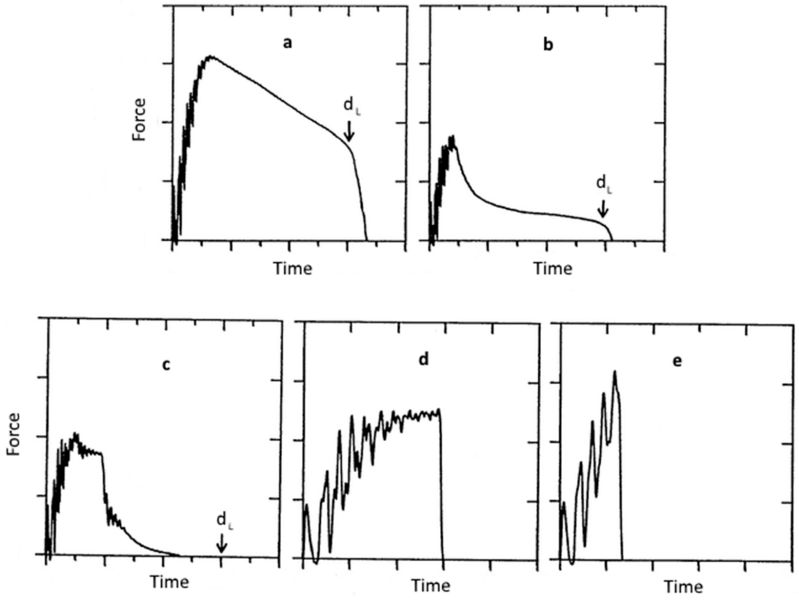

Figure 8. Types of failure modes in impact tests: (**a**) no break: yielding followed by plastic deformation till deflection limit d_L; (**b**) partial break: additional yielding and stable crack growth till deflection limit d_L; (**c**) tough break: yielding and stable crack growth till total failure; (**d**) brittle break: yielding followed by unstable crack growth; (**e**) splintering break: unstable cracking followed by yielding.

3.6. Application of Impact Tests on Epoxy Based Materials

Basically, epoxy based materials exhibit a brittle impact behavior. However, regarding an increase in crosslink density results in a shift in brittle-to-tough transition region [24,27]. This means that with increasing crosslink density the material characteristics change from soft and ductile to brittle and rigid. Whereas a soft material can easily transform impact energy to increase molecular mobility, a rigid material needs even more energy to reach the same amount of mobility. Adding filler types like non-interactive inorganic particles to the material results in a decrease in impact property. However, by changing the interaction through surface modification or adding fibers to the material, the impact property can be highly increased [33,38,39]. In case of fibers this enhancement is caused by the crack propagation inhibition property, if they are oriented right angular to the loading direction [40]. Characterizing bio based epoxy systems the impact properties at room temperature are significantly better compared to epoxy amine systems. This is caused by their lower glass transition values and therefore higher molecular mobility [18,22]. Through the use of natural fibers like hemp, sisal, or jute fibers, the impact properties can be further increased [37]. Table 4 illustrates values of impact properties for different types of epoxy based materials.

Table 4. Unnotched Charpy impact strength of epoxy based thermosets.

Epoxy base	Impact strength (kJ/m^2)	Reference
DGEBA	11.7	[39]
DGEBA + multi walled carbnon nanotubes	23.1	[39]
DGEBA + Epoxidized soybean oil	22	[41]

4. Conclusions

This article only represents a basic overview of applicable thermo-mechanical and mechanical tests, including literature data values of epoxy amine and bio based epoxy systems for the characterization of thermoset materials. However, in the construction process of electrical applications, mechanical stresses are not considered to have severe influences on the lifetime of a product, though it is known in polymer engineering that the slightest stress or defect in polymer materials could lead to a failure of the product. Therefore, mechanical, fracture mechanical, and long-term characterization should be considered for the dimensioning of polymeric materials in electrical and electronic applications.

Acknowledgments: The research work was performed within the K-Project "PolyComp" at the Polymer Competence Center Leoben GmbH (Leoben, Austria) within the framework of the COMET-program of the Federal Ministry for Transport, Innovation and Technology and

Federal Ministry for Economy, Family and Youth with contributions by Montanuniversitaet Leoben. Funding is provided by the Austrian Government and the State Government of Styria.

Conflicts of Interest: The authors declare no conflict of interest. The founding sponsors had no role in the design of the study; in the collection, analyses, or interpretation of data; in the writing of the manuscript, and in the decision to publish the results.

References

1. Ashby, M.; Shercliff, H.; Cebon, D. *Dynamic Materials Engineering, Science, Processing and Design*, 1st ed.; Butterworth-Heinemann: Oxford, UK, 2007.
2. Arora, R.; Mosch, W. *High Voltage and Electrical Insulation Engineering*, 1st ed.; John Wiley & Sons Inc.: Hoboken, NJ, USA, 2011.
3. Mohanty, A.; Srivastava, V.K. Dielectric breakdown performance of alumina/epoxy resin nanocomposites under high voltage application. *Mater. Des.* **2013**, *47*, 711–716.
4. Guo, Q. *Thermosets Structure, Properties and Application*, 1st ed.; Woodhead Publishing Limited: Cambridge, UK, 2012.
5. Menard, K.P. *Dynamic Mechanical Analysis a Practical Introduction*, 2nd ed.; CRC Press: New York, NY, USA, 2008.
6. Ehrenstein, G.W.; Riedel, G.; Trawiel, P. *Praxis der Thermischen Analyse*, 2nd ed.; Carl Hanser Verlag: München, Germany, 2003.
7. Pascault, J.P.; Sautereau, H.; Verdu, J.; Williams, R.J.J. *Thermosetting Polymers*, 1st ed.; Marcel Dekker Inc.: New York, NY, USA, 2002.
8. Vanalandingham, M.R.; Eduljee, R.F.; Gillespie, J.W. Relationships between stoichiometry, microstructure, and properties for amine-cured epoxies. *J. Appl. Polym. Sci.* **1999**, *71*, 699–712.
9. Palmese, G.R.; McCullough, R.L. Effect of epoxy-amine stoichiometry on cured resin material properties. *J. Appl. Polym. Sci.* **1992**, *46*, 1863–1873.
10. Guo, Q. Effect of curing agent on the phase behavior of epoxy resin/phenoxy blends. *Polymer* **1995**, *36*, 4753–4760.
11. Guo, Q.; Peng, X. The miscibility and morphology of epoxy resin/poly(ethylene oxide) blends. *Polymer* **1991**, *32*, 53–57.
12. Guo, Q.; Jinyu, H.; Liaohai, H.; Zhiliu, F. Phase separation in anhydride-cured epoxy resin containing phenolphthalein poly(ether ether ketone). *Eur. Polym. J.* **1992**, *28*, 405–409.
13. Clark, J.N.; Daly, J.H.; Garton, A. Hydrogen bonding in epoxy resin/poly(ϵ-caprolactone) blends. *J. Appl. Polym. Sci.* **1984**, *29*, 3381–3390.
14. Kosmidou, T.V.; Vatalis, A.S.; Delides, C.G.; Logakis, E.; Pissis, P.; Papanicolaou, G.C. Structural, mechanical and electrical characterization of epoxy-amine/carbon black nanocomposites. *eXPRESS Polym. Lett.* **2008**, *2*, 364–372.
15. Ma, J.; Mo, M.S.; Du, X.S.; Rosso, P.; Friedrich, K.; Kuan, H.C. Effect of inorganic nanoparticles on mechanical property, fracture toughness and toughening mechanism of two epoxy systems. *Polymer* **2008**, *49*, 3510–3523.
16. Rodriguez, M.T.; Garcia, S.J.; Cabello, R.; Suay, J.J.; Gracenea, J.J. Effect of plasticizer on the thermal, mechanical, and anticorrosion properties of an epoxy primer. *J. Coat. Technol. Res.* **2008**, *2*, 557–564.

17. Shabeer, A.; Sundararaman, S.; Chandrashekhara, K.; Dharani, L.R. Physicochemical properties and fracture behavior of soy-based resin. *J. Appl. Polym. Sci.* **2007**, *105*, 656–663.
18. Gupta, A.P.; Ahmad, S.; Dev, A. Modification of novel bio-based resin-epoxidized soybean oil by conventional epoxy resin. *Polym. Eng. Sci.* **2011**, *51*, 1087–1091.
19. Rochester, J.R. Bisphenol A and human health: A review of the literature. *Reprod. Toxicol.* **2013**, *42*, 132–155. PubMed]
20. Tsai, W.T. Human health risk on environmental exposure to bisphenol-A: A review. *J. Environ. Sci. Health* **2006**, *24*, 225–255. PubMed]
21. Park, S.J.; Jin, F.L.; Lee, J.R. Effect of biodegradable epoxidized castor oil on physicochemical and mechanical properties of epoxy resins. *Macromol. Chem. Phys.* **2004**, *205*, 2048–2054.
22. Miyagawa, H.; Misra, M.; Drzal, L.T. Fracture toughness and impact strength of anhydride-cured biobased epoxy. *Polym. Eng. Sci.* **2005**, *45*, 487–495.
23. Chrysanthos, M.; Galy, J.; Pascault, J.P. Preparation and properties of bio-based epoxy networks derived from isosorbide diglycidyl ether. *Polymer* **2011**, *52*, 3611–3620.
24. Bell, J.P. Mechanical properties of a glassy epoxide polymer: effect of molecular weight between crosslinks. *J. Appl. Polym. Sci.* **1970**, *14*, 1901–1906.
25. Grellmann, W.; Seidler, S. *Polymer Testing*, 2nd ed.; Hanser Gardner Publications Inc.: Cincinnaty, OH, USA, 2013.
26. Bonten, C. *Kunststofftechnik Einführung und Grundlagen*, 1st ed.; Carl Hanser Verlag: München, Germany, 2014.
27. Kim, S.L.; Skibo, M.D.; Manson, J.A.; Hertzberg, R.W.; Janiszewski, J. Tensile, impact and fatigue behavior of an amine-cured epoxy resin. *Polym. Eng. Sci.* **1978**, *18*, 1093–1100.
28. Urbaczewski-Espuche, E.; Galy, J.; Gerard, J.F.; Pascault, J.P.; Sautereau, H. Influence of chain flexibility and crosslink density on mechanical properties of epoxy/amine networks. *Polym. Eng. Sci.* **1991**, *32*, 1572–1580.
29. Daly, J.; Britten, A.; Garton, A.; McLean, P.D. An additive for increasing the strength and modulus of amine-cured epoxy resins. *J. Appl. Polym. Sci.* **1984**, *29*, 1403–1414.
30. Gojny, F.H.; Wichmann, M.H.G.; Köpke, U.; Fiedler, B.; Schulte, K. Carbon nanotube-reinforced epoxy-composites: Enhanced stiffness and fracture toughness at low nanotube content. *Compos. Sci. Technol.* **2004**, *64*, 2363–2371.
31. Kornmann, X.; Thomann, R.; Mülhaupt, R.; Finter, J.; Berglund, L. Synthesis of amine-cured, epoxy-layered silicate nanocomposites: The influence of the silicate surface modification on the properties. *J. Appl. Polym. Sci.* **2002**, *86*, 2643–2652.
32. Wang, R.; Schumann, T.; Vuppalapati, R.R.; Chandrashekhara, K. Fabrication of bio-based epoxy-clay nanocomposites. *Gr. Chem.* **2014**, *16*, 1871–1882.
33. Rong, M.Z.; Zhang, M.Q.; Ruan, W.H. Surface modification of nanoscale fillers for improving properties of polymer nanocomposites: A review. *Mater. Sci. Technol.* **2006**, *22*, 787–797.
34. Xu, Y.; Hoa, S.V. Mechanical properties of carbon fiber reinforced epoxy/clay nanocomposites. *Compos. Sci. Technol.* **2008**, *68*, 854–861.

35. Rong, M.Z.; Ming, M.Q.; Liu, Y.; Yang, G.C.; Zeng, H.M. The effect of fiber treatment on the mechanical properties of unidirectional sisal-reinforced epoxy composites. *Compos. Sci. Technol.* **2001**, *61*, 1437–1447.
36. Sgricca, N.; Hawley, M.C.; Misra, M. Characterization of natural fiber surfaces and natural fiber composites. *Compos. Part A* **2008**, *39*, 1632–1637.
37. Wambua, P.; Ivens, J.; Verpoest, I. Natural fibres: Can they replace glass in fibre reinforced plastics? *Compos. Sci. Technol.* **2003**, *63*, 1259–1264.
38. Tjong, S.C. Structural and mechanical properties of polymer nanocomposites. *Mater. Sci. Eng. Rep.* **2006**, *53*, 73–197.
39. Wang, J.; Fang, Z.; Gu, A.; Xu, L.; Liu, F. Effect of amino-functionalization of multi-walled carbon nanotubes on the dispersion with epoxy resin matrix. *J. Appl. Polym. Sci.* **2006**, *100*, 97–104.
40. Sharma, S.P.; Lakkad, S.C. Impact behavior and fractographic study of carbon nanotubes grafted carbon fiber-reinforced epoxy matrix multi-scale hybrid composites. *Compos. Part A* **2015**, *69*, 124–131.
41. Czub, P. Application of modified natural oils as reactive diluents for epoxy resins. *Macromol. Symp.* **2006**, *242*, 60–64.

Mica/Epoxy-Composites in the Electrical Industry: Applications, Composites for Insulation, and Investigations on Failure Mechanisms for Prospective Optimizations

Natascha Andraschek, Andrea Johanna Wanner, Catharina Ebner and Gisbert Riess

Abstract: The investigation of mica and mica/epoxy-composites has always been of high importance and has gained increased attention in recent years due to their significant role as insulation material in the electrical industry. Electrical insulation represents a key factor regarding the reliability and lifespan of high voltage rotating machines. As the demand for generating power plants is increasing, rotating machines are of intrinsic importance to the electrical energy supply. Therefore, impeccable functioning is of immense importance for both the producers of high voltage machines as well as the energy suppliers. Thus, cost reduction caused by shorter maintenance times and higher operational lifespan has become the focus of attention. Besides the electrical properties, composites should offer compatible chemical and mechanical, as well as thermal characteristics for their usage in insulating systems. Furthermore, knowledge of several occurring stresses leading to the final breakdown of the whole insulation is required. This review aims to give an overview of the properties of pure components, the composite, and the possible occurring failure mechanisms which can lead to a full understanding of insulation materials for high voltage rotating machines and therefore establish a basis for prospective optimizations.

Reprinted from *Polymers*. Cite as: Andraschek, N.; Wanner, A.J.; Ebner, C.; Riess, G. Mica/Epoxy-Composites in the Electrical Industry: Applications, Composites for Insulation, and Investigations on Failure Mechanisms for Prospective Optimizations. *Polymers* **2016**, *8*, 201.

1. Definition, Nomenclature, Composition, and Occurrence

Mica is a general term for a mineralogical group with common structural and chemical properties. From the mineralogical point of view, the term mica is not distinctly defined. Generally, it is assigned to the group of phylites, but according to the literature, it is referred to as its own group of so called hydro silicates [1–4].

The principle of classification of micas and therefore the nomenclature is based on chemical composition and generalized crystal-structure determination. Physical properties are discarded, since they do not offer the opportunity to distinctly

differentiate between the diverse mica types. Therefore, the classification is based on the chemical data [5].

Despite a huge number of varieties, micas build their own mineral family with similar characteristics, which is represented in the following formula (general formula of mica) [6]:

$$\mathbf{XY_2 \cdot (OH,\ F)_2 \cdot ZZ_3O_{10}} \tag{1}$$

This applies: **X** = K^+, Na^+, Rb^+ and Cs^+ in some cases as well; Ba^{2+} with a coordination number 12, **Y** = Al^{3+}, Fe^{3+}, Cr^{3+}, Mn^{3+}, V^{3+}, Ti^{3+}, FE^{2+}, Mn^{2+} and Li^+; rarely Zn^{2+} with a co-ordination number of 6, **Z′**= Al^{3+}, often Si^{4+}, as well as Fe^{3+}, Mn^{3+} and Ti^{3+}; with a co-ordination number 4 and **Z′′** = only Si^{4+} with a co-ordination number 4.

The crystallo-chemical formula should be composed of chemical data, density, and cell data. The procedure of the formula calculation is recommended as follows, presuming that only chemical data is available: (1) If a solid determination of H_2O is given, the formula should have regard to 12 O + F atoms; (2) In case no determination of H_2O took place, as in electron-microprobes analyses, the assumption of an idealized ion group is necessary, which includes the fact that the formula is based on 22 positive charges; (3) Based on no determination of H_2O and the presumption, that a later oxidation caused deprotonation of the anion group, the formula should consist of 22 + z positive charges, where z is defined as the quantity of trivalent iron [7–9].

Mica belongs to the monoclinic system. Formerly it was attributed to the hexagonal system due to its hexagonal crystal figurine. Accurate measurements however have shown that the angles are not exactly 120°. The hardness of mica is between 2.1 and 2.5 on the hardness scale which is based on the hardness of diamond with a value of 10 as a reference value; therefore it is harder than halite and gypsum, but softer than calcite.

Mica is widely spread in nature, but in hardly any provenance is it promoted in such an amount, respectively size, which is required for technical application. Among various amounts of mica types, only three types are of importance for electrical engineering, namely muscovite and phlogopite, and in small amounts biotite as well [10]. Muscovite, which is the most common and therefore the most important natural mica is represented in the following formula (muscovite) [6]:

$$\mathbf{K \cdot Al_2 \cdot AlSi_3 \cdot O_{10} \cdot (OH)_2} \tag{2}$$

The gaps in the formula expose the different parts which belong to each with regard to their ions. The most significant consideration from a chemical point of view is the fact that each 22 positive as well as negative charges occur. Within the scope of

crystallo-chemical laws, the charges can be exchanged to build the different types of mica groups [6].

Muscovite is classified as a potassium–aluminum–double–silicate. The staining is reddish, as well as white or green in different shades, sometimes brown, partly clear, in some cases with reddish or black spots [10]. Phlogopite or so called chalk mica differs from muscovite by two Al^{3+} which have been exchanged for three Mg^{2+}-ions and is represented by the formula (phlogopite) [6]:

$$\mathbf{K \cdot Mg_3 \cdot AlSi_3 \cdot O_{10} \cdot (OH)_2} \tag{3}$$

Phologite, which is also known as amber, is a chemically complex potassium-magnesium- aluminum-iron-double silicate and contains a slight amount of crystal- or constitution water compared to the previously mentioned muscovite. Hereby the crumbliness, which is characterized as softness, might be crucial and as well may be the reason for higher temperature stability. Compared to muscovite, which will calcinate between 600 and 650 °C, resulting in a loss of the solid crystal structure, phologite remains nearly undamaged in this temperature range. The calcination of the constitution water is the reason for blurring of the so far totally lucent crystal. The higher temperature stability (900 to 1000 °C) of phlogopite is the reason for its application in heaters. The color is amber to even reddish-amber [10].

Biotite or ferric mica (the ordinary black mica) is a phlogopite, which possesses iron ions in exchange for some of the magnesium (biotite) [6]:

$$\mathbf{K \cdot (Mg,\ Fe)_3 \cdot AlSi_3 \cdot O_{10} \cdot (OH)_2} \tag{4}$$

The chemical composition of biotite is very complicated and therefore does not really arouse the interest of electrical engineers. It occurs in huge crystals, its coloration is nearly always quite dark, mostly totally black. Due to the very dark staining, the occurring inclusions are hardly distinguishable, sometimes not at all. The application of biotite for electrochemical purposes is troublesome and met with failure due to its high surface conductivity within the layers. In addition the dielectric strength which is perpendicular to the crystal face is subjected to extraordinary fluctuations. The reasons for this are metallic, invisible inclusions and microscopic small cuts [10].

Besides the listed mica types there are further possibilities of substitution with relatively rare ions like Cr, V, Ta, Cs, and Rb [4,11].

2. Physical and Chemical Properties of Mica

The different physical and chemical properties of the commercially available mica types muscovite and phlogopite are summarized in Table 1.

Table 1. Summary of properties of muscovite and phlogopite [6].

Properties	Unit	Muscovite	Phlogopite
Thermal properties			
Melting temperature	°C	1,200 to 1300	1,200 to 1,300
Start of Calcination	°C	550 to 650	750 to 900
Long term thermal stability	°C	500	700
Thermal conductivity	W/m·K	0.25 to 0.75	*ca.* 1.7
Coefficient of thermal expansion	K^{-1}	90×10^{-7}	135×10^{-7}
Specific heat	J/g·K	0.06	0.26
Flammability		inflammable	inflammable
Mechanical properties			
Density	g/cm^3	2.6 to 3.1	2.6 to 3.2
Hardness (acc. to mobs)	N/mm^2	2.8 to 3.2	2.5 to 2.7
Compressive strength	N/mm^2	200 to 400	150 to 300
Shear strength	N/mm^2	250	110
E-module (d = 250 µm)	N/mm^2	180×10^{-3}	170×10^{-3}
Electrical properties			
Permittivity	ε	6 to 8	5 to 6
Dielectric loss factor (tan α)		3×10^{-4} (10^6 Hz)	10 to 100 $\times 10^{-4}$
Dielectric strength (20 °C, 50 Hz)	KV/mm	60 to 70 (up to 1 mm)	50 (up to 1 mm)
Resistance to tracking	KB-wert	>600	>600
Corona resistance		corona resistant	corona resistant
Other physical/chemical properties			
Refractive number		1.56 to 1.61	1.58 to 1.61
Radiation resistance		very good	very good
Resistance against organic solvents		resistant	resistant
Acid resistance		resistant (except hydrofluoric acid)	resistant (except hot acids)
Oil resistance		resistant	resistant
Color		reddish ,green, colorless, brown	amber, green
Physiological effect		no precautionary measures, harmless	
Amount of crystal bonded water %		4.5	3

These properties show that mica is an ideal material with a huge number of optimal properties covering many aspects. Especially for the purpose of electrical insulation mica exceeds all comparable materials due to its extremely high temperature resistance and low coefficient of thermal expansion.

The melting temperature of natural mica is around 1200–1300 °C. The high melting temperature, however, does not say anything about the temperature resistance. Since natural mica is a hydro silicate, it usually contains a certain amount of crystal-bound water. Depending on the chemical structure, calcination occurs at a particular temperature, which means, that the crystal bond breaks open, water becomes free, and some of the original properties undergo changes. Therefore, the calcination temperature is an important temperature for the quality evaluation of mica [6]. It is not flammable, has good dielectric properties and a very high dielectric strength. Furthermore, it is tracking resistant and corona stable and therefore the

only choice when it comes to application in high voltage insulations. Last but not least, mica also meets the requirements concerning radiation resistance.

3. Mica in Technical Application

The biggest deposits of mica are found in India (muscovite), in Canada (phlogopite), in Argentina and Brasilia (muscovite), in Madagascar (phlogopite), in Africa (muscovite) and in the USA (muscovite) [6].

As previously mentioned, mica is a natural product which is commercially available in huge pieces as so-called block mica. By cleaving the block mica into thin layers the split mica occurs [12].

The better quality mica variety, mostly in the form of mica splittings, is mainly used in the electrical industry. In the seventies mica splittings were largely used for the manufacturing of vacuum tubes and condensers [13]. Splittings mainly serve the production of so called built-up mica, which is also known as micanite and "Mikafolium". In this form it is used in the electrical industry and on the strength of its special properties it cannot be replaced by other materials [14–16].

The commercial value of mica depends on two main factors. The first is its size, which can be easily controlled by experienced producers. The second is its quality, whose diagnosis requires long term experts as its determination affords lots of experience. For the quality, three things are decisive: (1) the basic color; (2) the purity, and (3) the absence of errors in the crystal. The best mica should gleam in light-pink shades at a thickness of 0.1 mm, be free from inclusions, and be planar as well as free of cracks [10].

In addition, many experiments concerning the utilization of lower quality micas were performed [15–19].

Table 2 shows that the huge era of application of mica initially occurred due to the progress in the electrical engineering area.

In addition to this listing, the huge scope of application of several so-called "Mahlglimmer" as well as mica powder, used for attainment of particular effects, is the following (not only electro technical applications):

- Addition of colors (color industry)
- Filling material (rubber industry)
- Filling material (for molding compounds)
- Silky gloss (wallpaper production)
- Sheatings of welding rods
- Addition for exterior rendering (construction industry)

Mica powder exceeds other flake-shaped silica powders mainly because its flakes are quite thin, very elastic, smooth, and acid resistant. Furthermore it displays a high tear resistance [20,21].

Table 2. Application of mica [6].

Application/Devices	Example of usage
electrical devices	inductor of voltmeters, commutators, power inverters, high voltage commutators, rotating field coils, high voltage transformers, heat traps
radio receiver, TV, radar	solid state systems, condensers, tubes, microwave windows, transistor shielding
electrical light devices	arc lamps, huge incandescent lamps, bases for lampshades, neon lamps, dimmer counters, turn signal systems
mixed electric applications	fuse cover platelets, spark plugs for high compression engines, sealing shims, insulators
electrical household appliances	coffee machines, cigar lighters, hair roller, irons, immersion heaters, permanent wave devices, toasters, vibrators, space heaters, hair dryer, waffle iron
electrical monitoring systems	grid resistors, pyrometer, relays, electrical and thermal controller
mechanical applications	dials, membranes for acoustic instruments, heart-lung-machines, respirators, gaskets for high temperature measurement instruments, lantern windows, fireplaces, unbreakable safety goggles, quarter-wave-plates for optical instruments, vision panels in ovens, synthetic, optical crystals
industrial electrical applications	corrugated rolls, glue pots, lead baths, devices for local warming, several heating elements, soldering irons, thermostats

4. Mica as an Insulation Material

The merits of mica as an insulation material in electrical engineering are a high dielectric strength as well as the stability of the dielectric strength at all electro technical occurring, relevant, temperatures. Only at the calcination temperature of 650 °C might the dielectric strength sustain losses. Mica is of great value when it comes to insulation materials for technical properties as well as price [10].

Electrical insulation contains a composite material which provides resistance against corona discharge due to the inorganic components (mica) and additionally improves mechanical strength with glass fabrics. Furthermore, thermally curable epoxy-based resins which serve as an organic binder are essential to laminate the glass fabrics and the mica compartments and concurrently prevent air inclusions within the insulation [22].

The main wall insulation consists of about 65% mica paper, 25% resin and the glass fabric and other support materials compose 10% [23]. For the manufacturing of winding insulations of rotating machines, two technologies have been established.

The vacuum pressure impregnation (VPI) process works in the following way: The mica tape, which is strengthened with a glass fabric, is wrapped around a copper conductor and hence forms the main insulation (roebel bar). Filed grading tapes are wound around the main insulation to improve corona resistance. The essential construction of such an electrical insulation is presented in Figure 1.

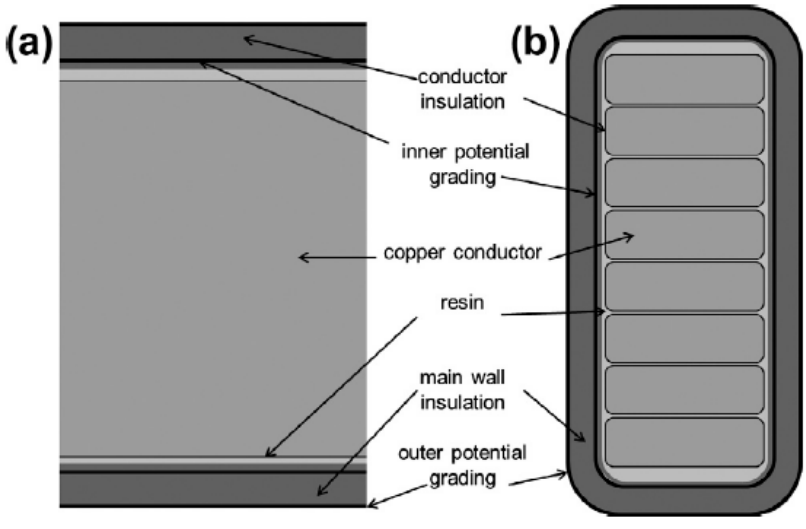

Figure 1. Construction of an electrical insulation. © copyright permission from Elsevier, 2014, Composites Part B: Engineering, New approaches towards the investigation on defects and failure mechanisms of insulating composites used in high voltage applications, License No. 3839281153636 [24].

The roebel bar is semi-cured in an oven to remove any moisture or volatile components and afterwards moved to the vacuum pressure impregnation tank. Using vacuum, almost all the air from the insulation is expelled. An epoxy resin is added to the tank while vacuum is still used to fully cover the roebel bar. After releasing the vacuum, the material is pressurized to force the resin completely into the insulation material. After removing the bar from the VPI tank it is placed in an oven to cure the resin and fully develop the properties of the insulation system [25]. Another well-known technology is the RR (resin rich) technology. In this process, the mica tapes of the main wall insulation are consolidated by a resin which is solid at ambient temperature. These tapes, the so-called prepags, are manually wrapped around the mechanically formed copper conductors. During the heating step of the RR process, the required temperature as well as the pressure is utilized in a tank with an asphalt bath. This leads to a curing of the resin within the tape and as a further consequence to a solid composite material. Both technologies are suitable to achieve

an inherent insulation quality with comparable properties providing that similar design and quality control are used [26,27].

The main difference between the two technologies is the setup and the manufacturing of the technical insulation system of the inductors. While the VPI system is only ready for use after impregnation and curing of the winding in an air circulated furnace, the "leg" of the resin rich inductor which is separately cured under temperature and pressure is already a functional and verifiable insulation system before the integration in the stator [28].

The advantage of the VPI inductor, respectively the VPI process, can be found in more cost-effective manufacturing in serial production. Furthermore, the hard inductor in the end winding is remarkably resistant against destruction by magnetic forces and the resulting movements causing subsequent failure of the insulation. Concerning the partial discharge resistance the extraordinary connection of the inductor to the iron core leads to a long-lasting operational life span. However, the investment for the VPI impregnation is quite high, therefore a high production number of the manufactured windings are necessary to achieve a final pay off. In contra-distinction, the manufacturing of resin-rich inductors is more sophisticated, which leads to an increase in costs for the single inductor. The resin-rich inductor offers a huge advantage though the validation of the inductors before integration in the stator implies higher guarantee during fabrication.

Both insulation systems are comparable concerning the product's quality for the respective production process. Nevertheless, the constructive fringe conditions avoid exchange between the two technologies, which are also presented in Table 3 [29].

Table 3. Comparison of vacuum pressure impregnation (VPI) and resin rich [30].

	VPI	Resin rich	
		With heated molds	**With asphalt pressure molding**
Strand insulation—dielectric strength	negligible difference between systems		
Insulation tape	mica paper with glass fabric carrier and without resin	mica paper with resin and glass carrier	mica paper with resin and glass carrier
Number of insulation layers	depending on rated voltage no appreciable difference between systems		
Internal potential grading for optimized field distribution in the main insulation	yes	multiturn coils—no Stator bars—yes	yes
Corona protection with tapes	yes	yes	yes
Vacuum impregnation with epoxy resin	yes	yes	yes—resin pre-loaded in tapes
Winding overhang section of bar	winding overhang and slot section—same materials	winding overhang and slot section—different material for coils only to improve windability	winding overhang and slot section—same materials
Composition of main insulation **Mica content** **Glass content** **Resin content**	approx. 65% approx. 10% approx. 25%	approx. 65% approx. 10% approx. 25%	
Main insulation dielectric strength	negligible difference between systems		
Partial Discharges within the insulation (PD level)	very low, no micro voids; PD/single bar lower than 2 nC	pressed—slightly higher due to lack of vacuum	very low, no micro voids; PD/single bar lower than 2 nC
Advantages	void-free insulation by removal of air through the vacuum process-penetration of impregnating resin into the insulation to fill the voids, minimization of corona activity, achieve very low levels of PD, high temperature capability	low viscosity resin during heating results in very few retained voids, insulation system results in very high dielectric strength, ow PD system, high temperature capability	void-free insulation by removal of air through the vacuum process, presence of pre-impregnated tapes ensures maximum void fill particularly near bare bar, achieve extremely low levels of PD, high temperature capability

5. Insulation Failure in Power Generators

Due to the increasing demand of generating plants, rotating machines will definitely be an important element in the electrical energy supply. Therefore their impeccable functioning is of extreme importance for both producers of high voltage machines as well as for energy suppliers. Cost reduction caused by shorter maintenance times and higher operational life span is therefore of high interest [31].

In the last years, the evaluation of the magnitude of aging of large generator insulations has been of huge interest for several researchers [32,33]. Some findings were published in recent years containing the main conclusions of the insulation sate process and aging validation [34–38].

Several studies deal with causes of failure of high voltage rotating machines in general as well as the failure mechanisms of power generators [39–44]. The investigation of 1199 hydro generators was carried out by the CIGRE study committee SC11, EG 11.02 shows an example of 69 break down scenes [45]. In 56% the break downs were caused by a failure of the insulation. Other reasons were found in mechanical, thermal, or bearing damages (Figure 2 left). The main causes of the mentioned damages are divided into seven distinct groups (Figure 2 right).

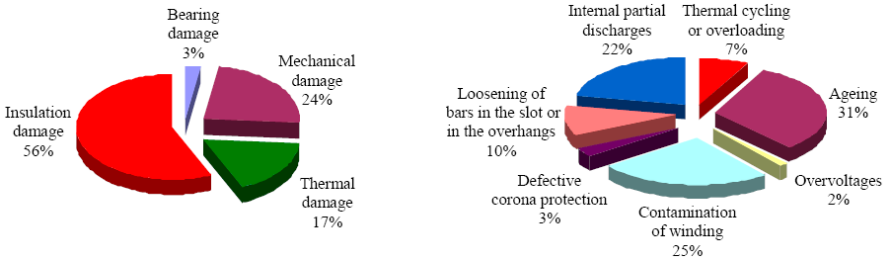

Figure 2. Percentage of the particular damages (**left**), damages divided into 7 distinct groups (**right**). © copyright permission from IEEE, 2008, IEEE Electrical Insulation Magazine, Insulation Failure Mechanisms of Power Generators, License No. 3844180528249 [46].

Therefore it may be assumed, that the failure of the insulation is crucial in the breakdown of high voltage rotating machines [46].

The published findings of failures range from contamination of the winding insulation during fabrication to several aging processes [22,47]. Since the insulation is suspended by stress of various kinds like mechanical, electrical, ambient, and thermal stress during operation, the insulation may incur a loss of its dielectric and mechanical strength [33,48].

The insulation stress may be short term, respectively, accidental as well, as long term usage may lead to permanent damage and is associated with the operating

regimes. Electrical stresses (normal, accidental) can cause partial discharges, electrical and water trees which might result in degradation and failure of the initial electrical characteristics of the insulation. Mechanical stresses (between two conductors or conductors and magnetic cores, *etc.*) induce abrasion and detachments of the insulation and might, as well, lead to cracks inside the material which ends in malfunction. Thermal stresses might determine weight loss, reduction of thickness, and insulation resistance to humidity and therefore change the required electrical and mechanical properties for the worse. The environmental stresses such as oxygen, humidity, radiation *etc.* might boost chemical reactivity and/or lead to new degradative reactions of the insulation [49].

The main difference between degradation and breakdown is the period of time. While degradation happens over a longer period, failure is a sudden event which is disastrous since the insulation is unable to support the nominal voltage after failure [50,51].

Fothergill published in 2006 an experimental study using samples of mica paper and epoxy resins which underwent simple and combined stresses with respect to the dependence of the capacity and the loss factor with regard to duration and strength of the stress situation [52].

Figure 3 represents the values of the electric field strength and duration of certain mechanisms which finally caused the insulation damage. Table 4 displays the process, respectively characteristic and the difference between breakdown, degradation and aging.

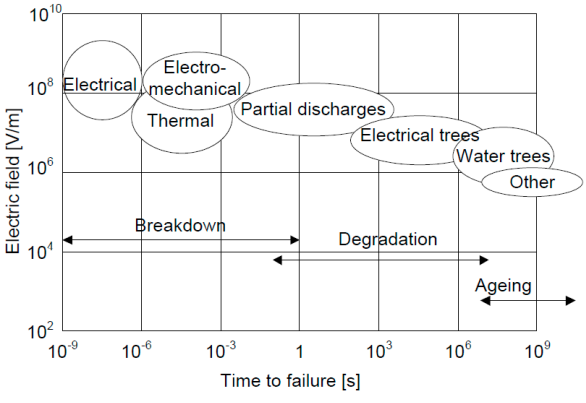

Figure 3. Values of electric field strength and the duration of certain mechanisms causing insulation damage. © copyright permission from the author(s), this is an open access article distributed under the terms of the Creative Commons Attribution License http://creativecommons.org/licenses/by/3.0/ [52].

Table 4. Process/characteristic and the difference between breakdown, degradation and aging [53].

Process/Characteristic	Breakdown	Degradation	Aging
Evidence	direct observation (normally by eye-hole through insulation)	observable directly (may require microscopic or chemical techniques)	difficult to observe (may even be difficult to prove existence)
Place	continuous filament	occurs in weak parts	assumed to occur throughout insulation
Size	< mm (dependent on energy of event)	<μm (may form larger structures)	<nm (molecular scale)
Speed	fast (occurs in <<1 s)	less than required service life (hours—years)	continuous process (whole service life)
Effect	catastrophic (insulation cannot be used afterwards)	leads to breakdown (reduces breakdown voltage)	may lead to degradation (may not reduce breakdown voltage)
Examples	thermal, electromechanical, mixed mode, avalanche, intrinsic	partial discharges, electrical trees, electrochemical trees	bond scissions, nano voids, trap formation, non-electrical changes (oxidation *etc.*)

Another, more recent study was published in 2013, which shows all root causes for each of the 111 failure mechanisms which were identified at that time classified by their category of stress.

Table 5 shows failures which occurred due to both thermal stress and electrical stress. Ambient stress caused 35 failure mechanisms and 60 can be attributed to mechanical stress.

Table 5. Process types and the distribution of the physical states [53].

Types of process	Number of physical states
Thermal (t)	9
Electrical (e)	22
Ambient (a)	14
Mechanical (m)	35

The number of intermediate physical states in these failure mechanisms is presented in Table 5 for each sort of stress category and the root causes per stress category are shown in Table 6 [53].

Table 6. Root causes per stress category and the distribution of failure mechanisms [53].

Root causes per stress category	Number of failure mechanisms
Thermal Stress (T)	8
T1 thermal aging (normal operation)	3
T2 accelerated aging (operation above specified rated temperatures)	3
T3 aging due to thermal cycling (frequent start/stop operation)	2
Electrical Stress (E)	8
E1 improper manufacturing or design of bars	2
E2 poor semiconducting coating on the straight part of the bars (slot discharges)	1
E3 poor design or manufacturing of end winding stress grading material (corona discharges)	1
E4 insufficient spacing between end windings (gap discharges)	1
E5 overvoltage transients	3
Ambient Stress (A)	35
A1 conducting contamination (carbon, steel or copper dust)	6
A2 non-conductive contamination (construction dust or oil)	9
A3 moisture in ambient air	7
A4 abrasive material attack	3
A5 water leakage (cooling system failure, fire protection and spills)	10
Mechanical Stress (M)	60
M1 loose windings	17
M2 bad connection	6
M3 presence of external objects or loose parts	5
M4 mechanical shocks	4
M5 Projectiles	4
M6 Rotor and/or stator deformation	24

According to Fothergill [52], most of the researchers employed nondestructive methods like insulation resistance, polarization index, dielectric dissipation factor, and phase resolved distributions of partial discharge to evaluate impairment of insulations.

Since these measurements are only eligible for certain insulations or test conditions, the development of proper test methods has still been a topic of discussion among several researchers. The main topic was to find an appropriate testing system to evaluate the impairment condition of the epoxy/mica insulation and define parameters that give indication of the actual condition of the insulation [54–56].

Several studies from different groups were performed to investigate the failure mechanisms of the mica insulation. Sample bars or other test specimen were used in the published surveys [57,58]. A list, respectively a comparison of insulation testing methods is presented by Vogelsang [37].

The main result of several of the above mentioned surveys led to the assumption, that electrical breakdown indeed causes the final collapse of the electrical insulation, but apparently electrical stress is not the decisive factor when it comes to the aging

of the insulation. In fact it is assumed, that thermal degradation of the binder resin controls the aging mechanisms, mechanical stress due to vibration, switching pulses and stress might be caused by decreased thermal expansion coefficients of the materials involved. The second main point of the studies is the temperature dependency. In the case when aging occurs under thermal, mechanical, and electrical stress at a moderate temperature of about 130 °C, it leads to an increase in the lifetime, whereas a temperature up to 180°C results in a rapid decrease in the lifetime.

The results are indicative of an increasing thermal degradation of organic matter on the one hand and a decrease of internal stress and crack formation of the binder resin at higher temperatures on the other hand [46].

6. Epoxy Resins as Binder for Insulation Composites

The most common resin systems are epoxy resins due to their excellent adhesion, permeability, corrosion resistance, and mechanical properties. Additionally, they distinguish themselves by an outstanding combination of physical and electrical properties compared to polyurethane-, silicone-, alkyd, unsaturated polyester-, and phenol-resins [59].

The majority of epoxy resins are used through polyaddition as a cold-hardening (room temperature) system, respectively as a hot-hardening system up to 200 °C. Besides the mainly used polyaddition reaction, several different polymerization mechanisms (cationic or coordinative mechanisms) are known for the cross linkage of epoxy resins [59,60].

For the winding of electrical machines (e.g., motors, generators) the diglycidylether of Bisphenol-A (DGEBA, Figure 4) in combination with different hardeners- and accelerator components is mainly deployed. For VPI resins anhydride hardening, e.g. 4-methylhexahydrophtalacid anhydride, (MHHPA, Figure 5) is preferred. Among other things, the properties can specifically be changed by the molar mass of the resin component as well as the processing conditions. The mostly used electro technical resin system DGEBA/MHHPA is easily applicable for use in the vacuum pressure impregnation process (VPI) by addition of different accelerators [12,61,62].

Referring to the literature, numerous distinct metal salts accelerators can be used for epoxy/anhydride systems, which can lead to a huge difference concerning the hardening temperatures (90–170 °C) as well as storage stabilities [63,64]. The usage of different accelerators can give rise to high levels of cross-linkage which leads to a shift of the glass transition temperature. Within the insulation composite of rotating electrical machines, zinc naphthenate (Figure 6) is mainly used as accelerator for the DGEBA/MHHPA system [65,66].

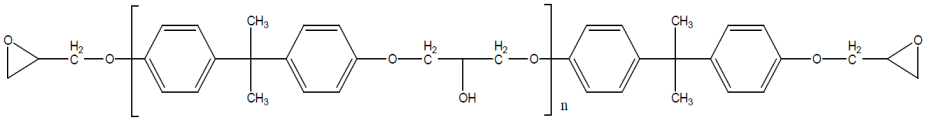

Figure 4. Diglycidylether of Bisphenol A (DGEBA) n = 0–1.

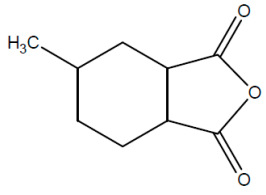

Figure 5. 4-Methylhexahydrophthalacid anhydride (MHHPA).

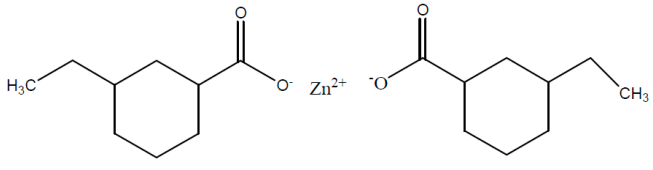

Figure 6. Zinc naphthenate (ZnNaph); structure example.

A cyclic anhydride like e.g., MHHPA however does not react directly with the epoxy group. The anhydride ring has to be opened by an active hydrogen atom, a hydroxyl group, or a Lewis base, as shown in Figure 7.

The resulting organic acid is then able to react with the epoxy group to form an ester, as shown in Figure 8.

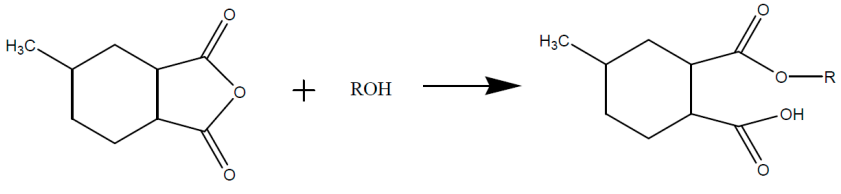

Figure 7. Opening of the anhydride ring due to reaction with an alcohol (R-OH).

Due to a further reaction step of the formed hydroxyl group with an anhydride the step reaction is continued. If di-epoxy-monomers (DGEBA) are used, a three dimensional network structure is formed, as represented in Figure 9 [67]. The molecular ratio between epoxy groups and anhydride groups therefore should be 1:1 to avoid rest monomers and ensure that all hydroxyl groups take part in the reaction.

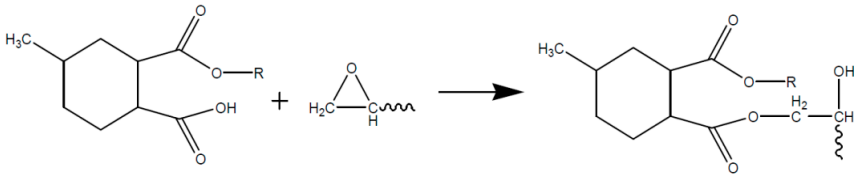

Figure 8. Reaction of the opened anhydride with an epoxy upon formation of an ester and a hydroxyl group.

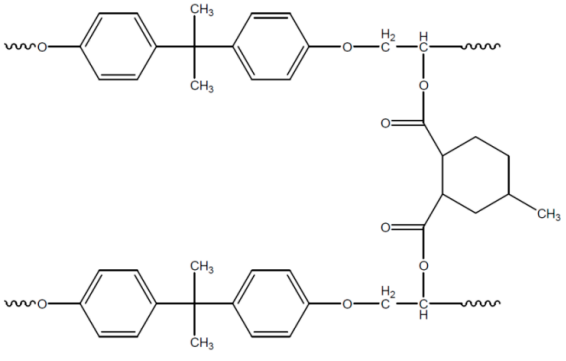

Figure 9. Network structure of an epoxy resin based on DGEBA/MHHPA.

For the anhydride-hardening, tertiary amines are mainly used as reaction accelerators. According to the literature, those amines do not function as typical catalysts since they do not revert back to their original structure (Figure 10) [68].

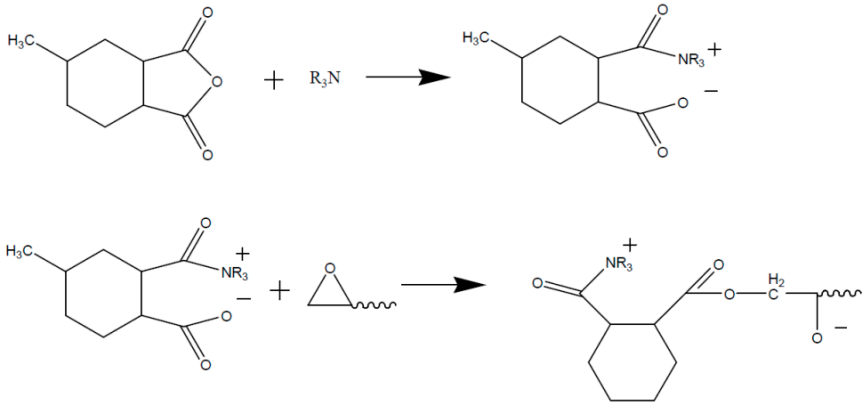

Figure 10. Amine-accelerated reaction of anhydride with an epoxy.

Another, essentially more complicated possibility represents the reaction of anhydrides with epoxy in the presence of metal salts (e.g., zinc naphthenate) as an accelerator. Since the epoxy/anhydride-system contains water in small amounts and furthermore aliphatic hydroxyl groups are found in DGEBA-structures at n =1, an opening of the anhydride ring to a carbon acid can be expected to a slight extent. Therefore the initiation of the hardening reaction of the presented carboxylic acid in Figure 11 in the presence of zinc-carboxylate as a catalyst can take place.

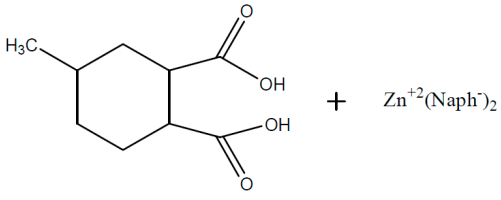

Figure 11. Opened anhydride and zinc naphthenate ($Naph^{-}$ = R–COO^{-}).

In respect of the reaction mechanism, Blank [69] and Han [70] assume that the reaction equilibrium between carboxylic acids and zinc naphthenate (Figure 12) at low temperatures is located on the left side. The reactivity is low and the epoxy/anhydride/ZnNaph system represents only a low increase of viscosity at room temperature.

If the temperature is increased, a faster exchange presented in Figure 12 of the reaction partners will occur and the equilibrium shifts to the right side. (Formation of free naphthenic acid, H–Naph). Due to the reaction of the free H–Naph with an epoxy group (Figure 13) the reaction equation of Figure 13 shifts further to the right side and leads to the formation of more $(R'COO)_2Zn$ [69,70].

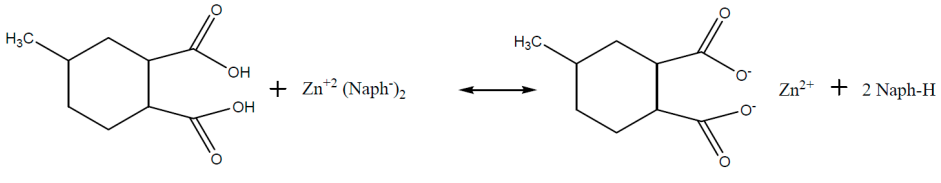

Figure 12. Zinc-naphthenate–MHHPA—dissociation at higher temperatures.

The formed naphthenic acid is able to react with an epoxy (Figure 13).

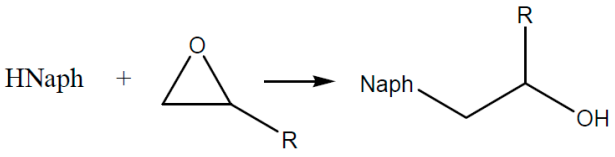

Figure 13. Epoxy-ring opening via free naphetenic acid H–Naph.

In Figure 14 the equilibrium between none-dissociated and dissociated zinc carboxylate $(R'COO)_2Zn$ is represented. The free carboxylate, which is formed of MHHPA, then reacts as a nucleophile and ring opening with the epoxy group and an ester group is formed (Figure 15) [69].

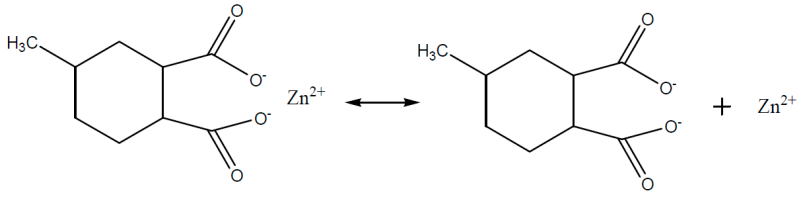

Figure 14. Equilibrium: non-dissociated and dissociated zinc salt of MHHPA.

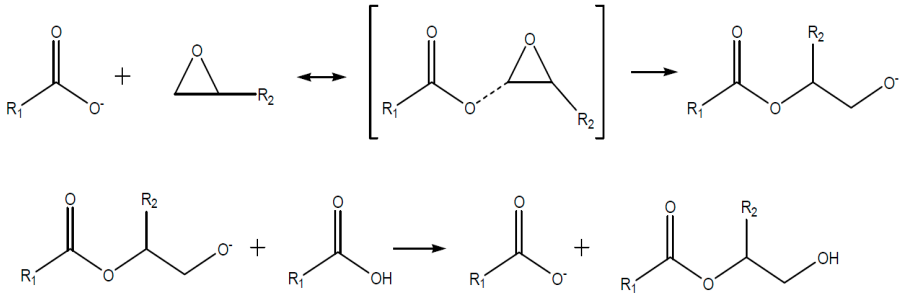

Figure 15. Carboxylate–epoxy reaction.

In the middle 1960s, Siemens AG developed the epoxy/anhydride system in combination with mica tapes and the therein immobilized zinc naphthenate as an accelerator for the VPI technology. This system is still used today [71,72]. Cycloaliphatic anhydrides like MHHPA react—on the contrary to aminic hardeners—at higher temperatures and reveal good storage stability. The combination of DGEBA with MHHPA exhibits a very slow reaction with the result that an accelerator is required [65,70].

7. Alternative Resins as Binder Materials (Cyanate Resins)

Cyanate resin systems represent another option for high voltage insulation. Compared to epoxy systems, cyanate resins exhibit a higher viscosity as well as higher glass transition temperatures. The advantages are excellent insulation properties and a very high temperature resistance [73–75].

Typical starting products for cyanate resins are bisphenol A, tetra methyl bisphenol F, bisphenol M or phenolic novolac. The reaction with cyan acids or gaseous cyan chloride leads to the reactive dicyanate ester Figure 16.

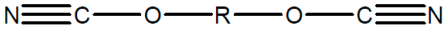

Figure 16. Structure of dicyanate ester.

The dicyanate esters, which are formed from the previously mentioned starting products are represented in Figures 17–20.

The hardening is achieved by a polycyclic trimerization of the dicyanate ester among the formation of triazin-ring (cyan urate) to a 3 dimensional network (Figure 21).

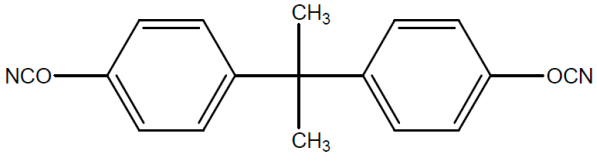

Figure 17. Structure of cyanate ester of bisphenol.

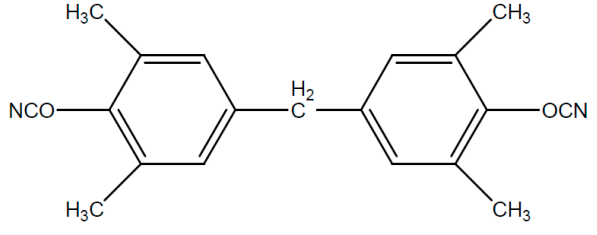

Figure 18. Structure of cyanate ester of tetra methyl bisphenol F.

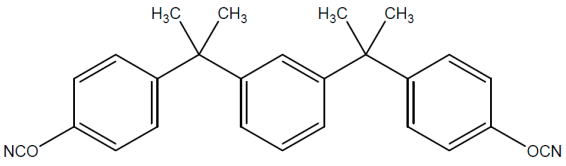

Figure 19. Structure of cyanate ester of bisphenol M.

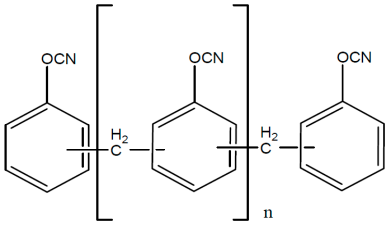

Figure 20. Structure of cyanate ester of phenol novolac resin.

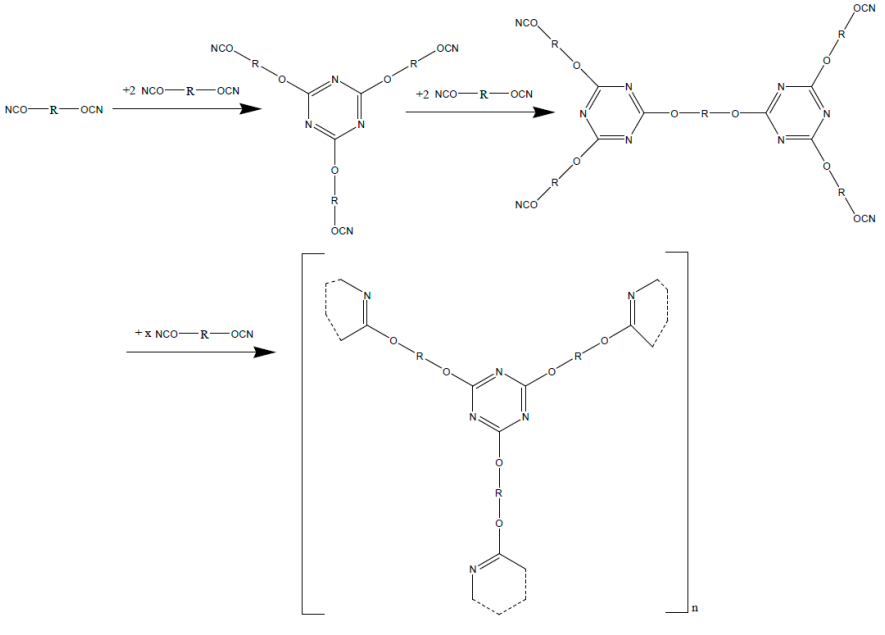

Figure 21. Polycyclic trimerization of di-cyanate ester to triazine-structures.

8. Temperature Resistance of Epoxy Resins

The different structures of the hardened epoxy resins lead to huge differences in the temperature resistance. Beside the different monomers, the chemistry of

hardening and the resulting structure of the polymer main chain are essential for the temperature resistance [76].

Basically, polymers with high aromatic content display a better thermal resistance compared to polymers with high aliphatic content in the main chain. The reason is the high stability of aromatic systems. The inertia concerning chemical reactions can be explained by the resonance stabilization of aromatic carbon hydrogens. Therefore, epoxy resin systems with epoxidized novolac (Figure 22) display higher, thermal resistance compared to epoxy resins systems based on diglycidylether or bisphenol A.

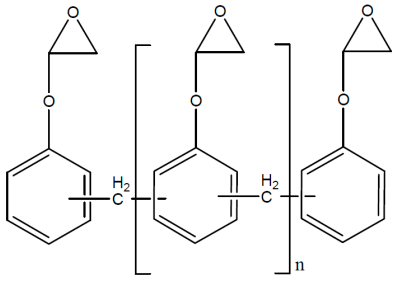

Figure 22. Epoxidized novolac.

Besides the deployed monomer, the hardening reaction determines the main chain structure and as a further consequence the thermal resistance. The polyester main chain, which originates from an epoxy/anhydride-hardening, (Figure 22) tends to hydrolytic cleavage and results in chain break. The hydrolysis of an ester group is represented in (Figure 23). In the case where the polyether main chain is achieved by homo-polymerization of the epoxy resin, represented in Figure 24, the thermal resistance is increased because the polyether main chain (Figure 25)—in comparison to ester—cannot be cleaved by hydrolysis. In a similar way, the amine-hardened epoxy systems are stable against hydrolysis [77].

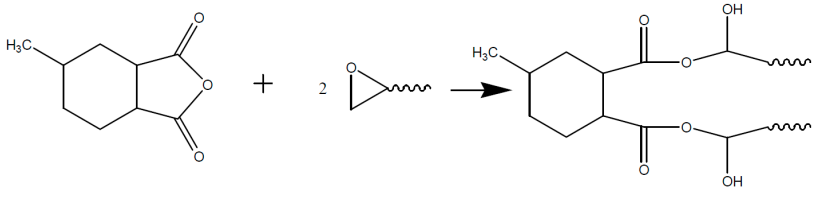

Figure 23. Hardening of epoxy/anhydride (simplified).

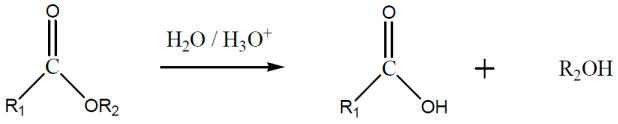

Figure 24. Hydrolysis of the ester structure.

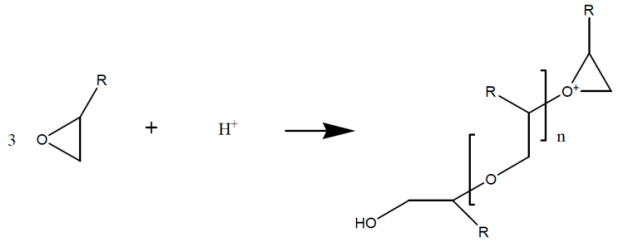

Figure 25. Polyether structure of the cationic hardened epoxy resins.

Concerning temperature resistance of epoxy resins the disruptive breakdown within the insulations composite occurs as a consequence of physical and chemical impairment. Besides thermal stress, strong potential occurs in the composite material due to different expansion coefficients of [57,77,78].

Thermosetting resins, particularly epoxy resins, have always played a significant role in certain applications such as the covering of surfaces, electronic components, and power moldings and they have served as matrix resins for advanced composites ever since. The adaptability of the formulation is another advantage of epoxy resins which allows their use as insulating materials [79,80].

The main insulation of high voltage electric machines is based on the VPI process. As previously mentioned, the conductors are swathed in a mica tape which contains an accelerator, zinc naphthenate, a resin, and the hardener. The tape itself is composed of a thin, non-calcinated muscovite tape, a glass fabric, a strengthened material, which links the glass fabric to the tape, as well as an accelerator [81].

This composite distinguished by a high specific stiffness and strength and in addition a high thermal stability. The molecular structure of the matrix is crucial for the required mechanical properties when used in high temperature ranges or at high levels of compressive stress at ambient temperatures, and therefore contributes considerably to the performance of the composite material itself [82].

A study published in 2011 shows an extensive characterization of the mica/epoxy-composite, its components as well as the thermo-analytical interactions between them. The thermal analysis was performed using the pure components and the results were consistent with those found in the literature [83].

A characterization of the pure components and the mixtures present in the composite has been performed using TG to gain information about thermal characteristics of each raw material.

Figure 26 displays the TG/DTG curves of the components. The results were compared to those found in the literature, which is presented in Table 7.

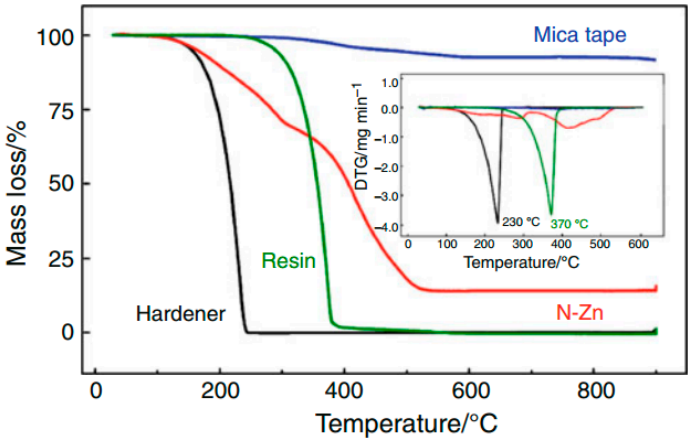

Figure 26. TG/DTG curves of components obtained under N_2 atmosphere (10 °C· min^{-1}), PT pan, and β of 10 °C· min^{-1}. © copyright permission Springer, 2011, Journal of Thermal Analysis and Calorimetry, Thermal characterization of mica–epoxy composite used as insulation material for high voltage, License No. 3837180507265 [83].

Table 7. Data of the single materials (experimental *vs.* literature) [83].

Component	Degradation temperature (°C)	
	Experimental	Literature
Resin	322	>300
Hardener	207	203
Mica tape	348	–
N–Zn	251	250

Comparing the TG/DTG curves of the components (Figure 26), the mixture of hardener with resin (1:1) (Figure 27) does not exhibit any detectable interference of the accelerator in the heating process relating to loss in mass. The pure hardener shows a mass loss at almost the same temperature. The mixture of resin/hardener (1:1) shows the same degradation pattern of both pure components, representing two events at onset 200 °C from the hardener and 320 °C, approximately from the resin. Moreover, it can be observed, that in the mixture of resin with zinc naphthenate

(1:0.03) there is a huge mass loss at 360 °C, which can be attributed to a thermal decomposition of the polymer. The polymerization takes place between 180 and 280°C as shown in the resin/N–Zn mixture DSC curve in Figure 28 represented by two exothermic events (T = 210 and 260 °C) in a temperature range where the TG-curve does not show any mass loss. Furthermore, the DSC curves (Figure 28) of the pure components do not show any exothermic reaction until 300 °C.

Therefore it can be assumed, that the accelerator is able to open the epoxy rings of the DGEBA and initiate a polymerization reaction with a small amount of N–Zn. The DSC curve of the mixture of the resin with the zinc naphthenate (resin/N–Zn) shows that at the end of the polymerization, the partial resin evaporation is evidenced by an endothermic event occurring at a temperature of 344 °C.

Figure 29 shows the TG and DTG curves of the resin and the hardener with and without the mica tape. As can be seen from Figure 27, the hardener does not show any interaction with the tape, representing the same shape and profile in pure form as also with the tape. Referring to the physical obstacle of evaporation and decomposition, the substance with the tape shows a slight shift of the degradation temperature. Moreover, the interaction of resin and hardener with the tape shows an exothermic reaction at 426 °C which can be seen as well using DTG. This leads to the assumption, that between these two components, the epoxy ring might open up and the molecules can react. The polymerization then shows a decomposition event at this higher temperature.

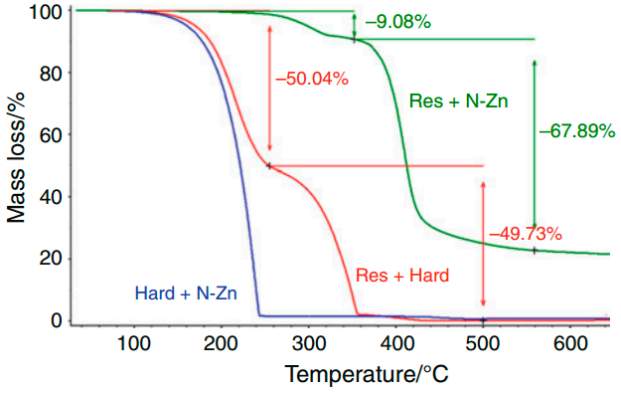

Figure 27. TG curves of mixtures: resin/hardener, hardener/N–Zn, and resin/N–Zn under N_2 atmosphere (10 mL·min^{-1}), Al_2O_3 pan, and β of 10 °C mL·min^{-1}. © copyright permission Springer, 2011, Journal of Thermal Analysis and Calorimetry, Thermal characterization of mica–epoxy composite used as insulation material for high voltage, License No. 3837180507265 [83].

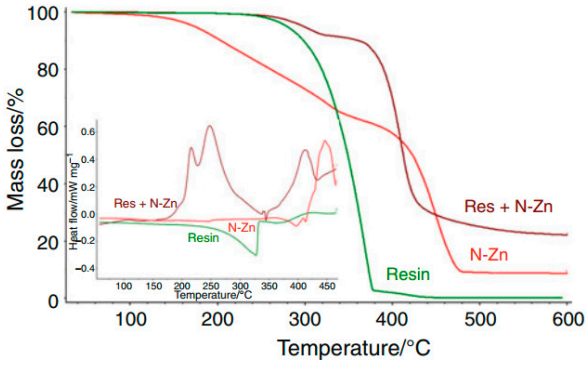

Figure 28. TG curves of resin, N–Zn and resin/N–Zn under N_2 atmosphere (10 mL· min^{-1}), Al_2O_3 pan, and β of 10 °C mL· min^{-1} and DSC curves under N_2 atmosphere (50 mL mL· min^{-1}), Al pan, and β of 10 °C min^{-1}. © copyright permission Springer, 2011, Journal of Thermal Analysis and Calorimetry, Thermal characterization of mica–epoxy composite used as insulation material for high voltage, License No. 3837180507265 [83].

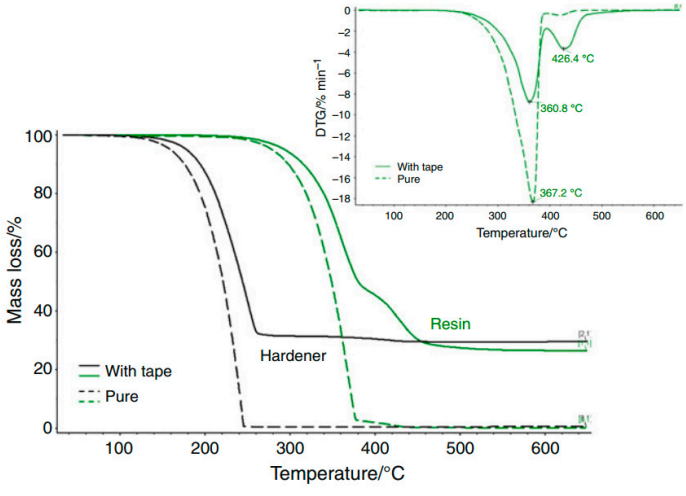

Figure 29. TG/DTG curves of resin and hardener with and without mice tape under N_2 atmosphere (10 mL· min^{-1}), Al_2O_3, pan, and β of 10 °C· min^{-1} .© copyright permission Springer, 2011, Journal of Thermal Analysis and Calorimetry, Thermal characterization of mica–epoxy composite used as insulation material for high voltage, License No. 3837180507265 [83].

All in all, the published thermal analysis allows a detailed study of curing processes and thermal decomposition and therefore allows the prediction and

suggestion of mechanisms as well as further optimization of the system. The glass transition (T_g) of the composite showed a value of $T_g = 138 \pm 2\ ^{\circ}C$ which finally characterizes the mica–epoxy composite material [83].

9. Final Review

Mica is widely spread in nature and has been known for many years, but gained increasing importance due to the developments in the electrical industry. Due to its unique properties in many respects, mica represents the optimal material for many applications. Especially for the purpose of electrical insulation, mica is superior to all comparable materials because of its extraordinary performance and is therefore widely deployed in high voltage rotating machines.

A typical, electrical insulation contains a composite material which consists of a mica tape and a glass fabric. An epoxy-based resin serves as an organic binder and laminates the two components. The main wall insulations in high voltage applications consists of about 65% mica, 25% resin, and 10% other support materials.

Due to the increasing demand of power plants, rotating machines definitely demonstrate an important element when it comes to electrical energy supply. Therefore, impeccable functioning is of immense importance. In the last years, the evaluation of the magnitude of aging of large generator insulations has been of huge interest for several researchers. Various test methods have been developed to gain more information about insulation failure mechanisms.

Due to these intense studies and comparison of mica-epoxy-composites, the properties of the pure components as well as the composite and its failure mechanisms, a better understanding and therefore a prospective optimization of high voltage insulations might be enabled.

Acknowledgments: I would like to show my gratitude to Michael Fuchs, KF University Graz, for sharing his wisdom with me during the course of this research. I am immensely grateful for the comments on an earlier version of the manuscript, although any errors are my own and should not tarnish the reputations of the esteemed person. The research work was performed at the Polymer Competence Center Leoben GmbH (PCCL, Austria) within the framework of the COMET-program of the Federal Ministry for Transport, Innovation and Technology and the Federal Ministry of Economy, Family and Youth with contributions by academic and commercial partners. The PCCL is funded by the Austrian Government and the State Governments of Styria and Upper Austria.

Conflicts of Interest: The authors declare no conflict of interest.

References

1. Brauns, R. *Das Mineralreich*; Fritz Lehmann-Verlag: Karlsruhe, Germany, 1903.
2. Romdohr, P. *Klockmanns Lehrbuch für Mineralogie*; Ramdohr, P., Enke, H.S., Eds.; Verlag Thieme: Stutgart, Germany, 1978.

3. Von Maegdefrau, E.; Hofmann, U.U. Glimmerartige Mineralien als Tonsubstanzen. Available online: http://www.degruyter.com/dg/viewarticle.fullcontentlink:pdfeventlink/$002fj$002fzkri.1938.98.issue-1-6 $002fzkri.1938.98.1.31$002fzkri.1938.98.1.31.pdf?t:ac=j$002fzkri.1938.98.issue-1-6$002fzkri.1938.98.1.31$002 fzkri.1938.98.1.31.xml (accessed on 31 March 2016).
4. Hartmann, M. *Über die Bauwürdigkeit von Pegmatitvorkommen auf Glimmer*; Montan-Verlag: Düsseldorf, Germany, 1954; pp. 84–86.
5. Rieder, M.; Cavazzini, G.; D'Yakonov, Y.S.; Frank-Kamenetskii, V.A.; Gottardi, G.; Guggenheim, S.; Koval, P.V.; Müller, G.; Neiva, A.M.R.; Radoslovich, E.W.; *et al. Nomenclature of the Micas*; The Canadian Mineralogist: Vancouver, BC, Canada, 1998; Volume 36.
6. Rotter, H.-W. *Glimmer & Glimmererzeugnisse: Eigenschaften, Entwicklungen, Anwendungen*; Siemens Aktiengesellschaft: Berlin, Germany, 1985; ISBN: 3-8009-1451-4.
7. Stevens, R.E. A system for calculatin analyses of micas and related minerals to end members. *U.S. Geol. Surv. Bull.* **1946**, *950*, 101–119.
8. Foster, M.D. Interpretation of the compostition of trioctahedral micas. *U.S. Geol. Surv. Prof. Pap.* **1960**, *354*, 11–49.
9. Rimsaite, J. Structural formulae of oxidized and hydroxyl-deficient micas and decompostition of the hydroxyl group. *Contrib. Mineral. Petrol.* **1970**, *25*, 225–240.
10. Schroeder, R. Glimmer und Glimmerprodukte. In *Sonderausdruck Aus "Die Isolierstoffe der Elektrotechnik"*; Schering, H., Ed.; Verlag von Julius Springer: Berlin, Germany, 1924.
11. Mutschke, H. *Glimmereigenschaften, Silikattechnik 19*; Verlag von Julius Springer: Berlin, Germany, 1968.
12. Helles, F. *Wicklungen Elektrischer Maschinen*; Verlag von Julius Springer: Berlin, Germany, 1936.
13. Espe, W. *Glimmer als Werkstoff der Hochvakuumtechnik*; Veb Deutscher Verlag der Wissenschaften: Berlin, Germany, 1959.
14. Mamdal, S.S.; Mahanti, P.C. Electrical properties of Indian mica. *Indian J. Phys. Proc. Indian Assoc. Cultiv. Sci.* **1953**, *XXVII*, 294–304.
15. Burmeister, H.C. *Glimmerm, ein Werkstoff der Elektrotechnik, in Elektrotechnik Nr. 10*; Montan-Verlag: Düsseldorf, Germany, 1985; pp. 64–68.
16. Liebscher, F.; Held, W. *Glimmer und Glimmererzeugnisse*; Springer: Berlin, Germany, 1955.
17. Rotter, H.W. *Dauerverhalten von Isolierstoffen und Isoliersystemen*; VDE-Verlag: Berlin, Germany, 1977; p. 757.
18. Rotter, H.W. Thermidur, ein Isoliersystem für Extrem Hohe Temperaturen. In *Siemens-Zeitschrift*; VDE-Verlag: Berlin, Germany, 1929; pp. 299–301.
19. Dawes, C.L.; Mansfield, W.R. Built-up mica plate for high-temperature applications. *Electr. Eng.* **1953**, *72*, 145–150.
20. R.I.S. Limited. *Mica*, 2nd ed.; R.I.S. Limited: London, UK, 1977.
21. British Paint Research Association. *Hochresistente Epoxy-Teerfarben mit Glimmerzusatz*; Micafine Ltd.: Melton Mowbray, UK, 1962; p. 653.

22. Schaumburg, H. *Polymere: Mit 127 Tabellen und 328 formeln*; Verlag-Teubner: Stuttgart, Germany, 1997.
23. Brütsch, J.A.R. Selection and application of insulating materials: Their importance in VPI insulation for rotating machines. In Proceedings of the Coil Winding, Insulation & Electrical Manufacturing Conference, Berlin, Germany, 12–14 May 1998; pp. 137–144.
24. Lenko, D.; Schlogl, S.; Bichler, S.; Lemesch, G.; Ramsauer, F.; Ladstätter, W.; Rosc, J.; Kern, W. New approaches towards the investigation on defects and failure mechanisms of insulating somposites used in high voltage applications. *Compos. Part B* **2013**, *58*, 83–90.
25. Hyundai Ideal Electric. Vacuum Pressure Impregnation (VPI) System. Available online: http://www.hyundaiideal.com/about/VPIPDF1.htm (accessed on 31 March 2016).
26. Stone, G.C.; Culbert, E.B.; Dhirani, I.H. *Stator Failure Mechanisms and Repair*; Wiley-IEEE Press: Hoboken, NJ, USA, 2003.
27. Stone, G.C.; Culbert, E.B.; Dhirani, I.H. *Dhirani Electrical Insulation for Rotating Machines—Design, Evaluation, Aging, Testing and Repair*; Wiley-IEEE Press: Hoboken, NJ, USA, 2003.
28. Elektromotoren, V. Hochspannungsspulenfertigung Nach Dem resin-rich/VPI-Verfahren bei Vogelsang Elektromotoren. Available online: http://www.vogelsang.com/news/newsdetail/article/hochspannungsspulenfertigung-nach-dem-resin-rich-vpi-verfahren-bei-vogelsang-elektromotoren-in-boc.html (accessed on 31 March 2016).
29. Vogelsang Elektromotoren. *Drehmomente*; Vogelsang Elektromotoren: Bochum, Germany, 2007.
30. Schwab, A. HydroNews. In *Magazin der Andritz Hydro*; Andritz Hydro GmBH: Vienna, Austria, 2009.
31. Vogelsang, R. *Time to Breakdown of High Voltage Winding Insulations with Respect to Microscopic Properties and Manufacturing Qualities*; Hartung-Gorre Verlag: Konstanz, Germany, 2004.
32. Kimura, K. Progress of insulation aging and diagnostics of high voltage rotating machine windings in Japan. *IEEE Electr. Insul. Mag.* **1993**, *3*, 13–20.
33. Kimura, K.; Kaneda, Y. The role of microscopic defects in multistress aging of micaceous insulation. *IEEE Trans. Dielect. Electr. Insul.* **1995**, *2*, 426–432.
34. Stone, G.C.; Gupta, B.K.; Lyles, J.F.; Sedding, H.G. Experience with accelerating aging tests on stator bars and coils. In Proceedings of the Conference Record of the 1990 IEEE International Symposium on Electrical Insulation, Toronto, ON, USA, 3–6 June 1990; pp. 356–360.
35. Kheirmand, A.; Leijon, M.; Gubanski, S.M. New practices for partial discharge detection and localization in large rotating machines. *IEEE Trans. Dielectr. Electr. Insul.* **2003**, *10*, 1042–1052.
36. Anders, G.J.; E, J.; Ford, G.L.; Stone, G.C. A probabilistic model for evcaluating the remaingin life of evaluating the remaining life of electrical insulation in rotating machines. *IEEE Trans. Energy Convers.* **1990**, *5*, 761–767.

37. Vogelsang, R.; Fruth, B.; Ducry, O. Performance testing of high voltage generator- and motor insulation systems. In Proceedings of the WSEAS International Conferences, Tenerife, Spain, 16–18 December 2005.
38. Cheng, X.; Cheng, Y.; Yue, B.; Xie, H. Study of epoxy/Mica insulation deterioration in generator stator using ultra-wide band partial discharge testing technique. *Polym. Test* **2006**, *2006*, 724–730.
39. Van Breen, H.J.; Gulski, E.; Smit, J.J. Several aspects of stator insulation condition based maintenance. In Proceedings of the Conference record of the 2004 IEEE International Sypmosium on Electrical Insulation, Indianapolis, IN, USA, 19–22 September 2004; pp. 446–449.
40. North American Electric Reliability Council (NERC). Available online: https://www.eeh.ee.ethz.ch/ uploads/tx_ethpublications/Froehlich_Insulation_Failure_Mechanism_of_Power_Generators__IEEE_El ectrical_Insulation_Magazine.pdf (accessed on 31 March 2016).
41. Evans, D.L. *IEEE Trans. on Power Apparatus and Systems PAS-100*; IEEE: Piscataway, NJ, USA, 1981; pp. 3284–3293.
42. Zwicknagl, W. Oesterreichischer verband der elektrotechnik. *J. Elektrotech. Masch.* **1998**, *98*, 221.
43. Bomba, R.; Gross, U.; Kaiser, J. VGB data base generator damage cases. *VGB PowerTech.* **2005**, *11*, 87–92.
44. Greg, C.; Stone, E.B.; Culbert, I.; Dhirani, H. Electrical insulation for rotating machines—Design, evaluation, aging, testing, and repair—Book review. *IEEE Electr. Insul. Mag.* **2004**, *20*, 65.
45. CIGRE Study Committee SC11. *Hydronenerator Failures—Results of the Survey*; CIGRE Study Committee SC11: Paris, France, 2003.
46. Bruetsch, R.; Tari, M.; Froehlich, K.; Weiers, T.; Vogelsang, R. Insulation failure mechanisms of power generators. *IEEE Electr. Insul. Mag.* **2008**, *24*, 17–25.
47. Zhidong, J.; Hao, Y.; Hengkun, X. The degradation assessment of epoxy/mica insulation under multi-stresses aging. *IEEE Trans. Dielect. Eletr. Insul.* **2006**, *13*, 415–422.
48. Srinivas, M.B.; Ramu, T.S. Multifactor aging of HV generator stator insulation including mechanical vibrations. *IEEE Trans. Elect. Insul.* **1992**, *27*, 1009–1021.
49. Rusu-Zagar, C.; Notingher, P.V.; Stancu, C. Aging and degradation of electrical machines insulation. *J. Int. Sci. Publ. Mater. Methods Technol.* **2014**, *8*, 526–546.
50. Nothinger, P.V. *Insulation Systems*; PRINTECH House Ltd.: Bucharest, Romania, 2002.
51. Nothinger, P.P. Accelerated development of electrical trees. Part I: Initiation of trees. *Electr. Eng. Electron. Autom.* **2009**, *57*, 1–19.
52. Fothergill, J.C. Ageing, Space Charge and Nanodielectrics: Ten Things We Don't Know About Dielectrics. In Proceedings of the International Conference on Solid Dielechtrics, Winchester, UK, July 8–13 2007; pp. 1–10.
53. Amyot, N.; Lévesque, M.; Bélec, M.; Brabant, F.; Frenette, F.X. A new prognostic approach for hydrogenerator stator windings. In Proceedings of the Annual Conference of the Prognostics and Health Management Society, Gaithersburg, MD, USA, 24–27 June 2013.

54. Yue, B.; Zhelei, Z.; Xiaolin, C.; Xie, H. Study on the characteristic parameters used to assess the insulation condition of stator windings. In Proceedings of the Seventh International Conference on Properties and Applications of Dielectric Materials, Rome, Italy, 1–5 June 2003.
55. Yue, B.; Jian, L.; Zhang, X.; Yonghong, C. Using AC current parameters to assess aging condition of epoxy/mica insulaion. In Proceedings of the International Symposium on Electrical Insulation Materials, Himeji, Japan, 19–22 November 2001.
56. Stone, G.C.; Sedding, H.G.; Lloyd, B.A.; Gupta, B.K. The ability of diagnostic tests to estimate the remaining life of stator insulation. *IEEE Trans. Energy Convers.* **1988**, *3*, 833–841.
57. Wichmann, A.; Grunewald, P.; Weidner, J. *Betriebliche Einflussgrössen auf die elektrische Lebensdauer von Hochspannungsisolierungen in Turbogeneratoren*; ETG Fachberichte: Hannover, Germany, 1985; Volume 16, pp. 44–48.
58. Kimura, K.; Kaneda, Y. Breakdown voltage and observation on mica insulation systems after thermal aging and mechanical fatigue. In Proceedings of the 7th Intnational Symposium on High voltage Engineering, Dresden, Germany, 26–30 August 1991.
59. Lee, S.M. *Electrical and Electronic Applications*; Marcel Dekker Inc: New York, NY, USA, 1988; pp. 783–884.
60. May, C.A. *Epoxy Resins, Chemistry and Technology*; Marcel Dekker: New York, NY, USA, 1988.
61. Boey, F.Y.C.; Qiang, W. Experimental modeling of the cure kinetics of an epoxyhexahydro-4- methylphtalicanhydride (MHHPA) system. *Polymer* **2000**, *41*, 2081–2094.
62. Liu, Y.; Du, Z.; Zhang, C.; Li, C.; Li, H. Curing behavior and thermal properties of multifunctional epoxy resin with methylhexahydrophtalic anhydride. *J. Appl. Polym. Sci.* **2007**, *103*, 2041–2048.
63. Hamerton, L.; Howlin, B.J.; Jepson, P. Metals and coordination compounds as modifiers for epoxy resins. *Coord. Chem. Rev.* **2002**, *224*, 67–85.
64. Smith, J.D.B. Metal acetylacetonates as latent accelerators for anhydride-cured epoxyresins. *J. Appl. Poly. Sci.* **1981**, *26*, 979–986.
65. Schmidlin, B. Verfahren zur Herstelluing von Imprägnierbaren Feinglimmerbänder mit Eingebautem Beschleuniger. Europa Patent O 194974, 27 April 2000.
66. Neville, L.J.; Neville, K. *Industrial Motors Users Handbook of Insulation for Rewinds*; Elsevier Science Ltd: Amsterdam, The Netherlands, 1977.
67. Grimsley, B.W.; Pascal, H.; Song, X.; Cano, R.J.; Loos, A.C.; Pipes, R.B. *Effects of amine and anhydride curing agents on the VARTM matrix processing properties*; The National Aeronautics and Space Administration (NASA): Washington, DC, USA, 2002.
68. Shen, S.; Li, Y.; Gao, J.; Sun, H. Curing kinetics and mechanism of bisphenol S epoxy resin with 4,4′-diaminodiphenyl ether or phthalic anhydride. *Int. J. Chem. Kinet.* **2001**, *33*, 558–563.
69. Blank, W.J.; Hu, Z.A.; Picci, M. *Catalysis of the Epoxy-Carboxyl Reaktion, I*; Waterborne: New Orleans, LA, USA, 2001.

70. Han, J.; Wood, B.; Herman, H.; Stevens, G.C. Cure kinetics for bisphenol A resin with zinc naphthanate accelerator. In Proceedings of the Conference Record of the 2010 IEEE International Symposium on Electrical Insulation (ISEI), San Diego, CA, USA, 6–9 June 2010.
71. Stabile, S.J. Extension of the post impregnation concept to high voltage windings. In Proceedings of the 11th Electrical Insulation Conference, New York, NY, USA, 30 September 1973.
72. Mertens, W.; Meyer, H.; Wichmann, A. Micalastic-insulation experience and progress. In Proceedings of the Seventh Electrical Insulation Conference, Chicago, IL, USA, 16 October 1967.
73. Kimura, H.; Ohtsuka, K.; Matsumoto, A. Curing reaction of bisphenol-A based benzoxazine with cyanate ester adn the properties of the cured thermosetting resin. *eXPRESS Polym. Lett.* **2011**, *5*, 1113–1122.
74. Prokopec, R.; Humer, K.; Fillunger, H.; Maix, R.K.; Weber, H. Mechanical behaiviour of cyanate ester/epoxy blends after reactor irradiation to high neutron fluences. In *Advanced in Cryogenic Engineering*; American Institute of Physics: Melville, NY, USA, 2008; pp. 182–189.
75. Hamerton, I. *Chemistry and Technology of Cyanate Ester Resins*; Chapman and Hall: London, UK, 1994.
76. Ehrenstein, G.W.; Pongratz, S. *Beständigkeit von Kunststoffen*; Carl Hanser Verlag GmbH & Co. KG: Munich, Germany, 2007.
77. Führer, R. Weiterentwicklung und Impementierung eines Isolationssystems der Temperaturklasse H für Hochspannungs-Anwendungen. In *Lehrstuhl für Chemie der Kunststoffe*; Montan Universität Leoben: Leoben, Austria, 2013.
78. Brütsch, T.H. *High Voltage Stator Insulation*; European Electrical Insulation Manufacturers: Reutlingen, Germany, 2005.
79. Jain, R.; Choudhary, V.; NArula, A.K. Curing and thermal behavior of DGEBA in presence of dianhydrides and aromatic diamine. *J. Appl. Polym. Sci.* **2007**, *105*, 3802–3808.
80. Boulter, E.A.; Stone, G.C. Historical development of rotor and stator winding insulation materials and systems. *IEEE Electr. Insul. Mag.* **2007**, *105*, 25–39.
81. Mertens, W. Method of Producing an Insulating Sleeve of Mica Tape Impregnated with Thermosetting Epoxide Impregnating Resin Mixtureand Product Thereof. US 3556925 A, 19 January 1971.
82. Chian, W. Chemical/mechanical analyses of anhydride-cured thermosetting epoxys: DGEBA/NMA/BDMA. *Macromolecules* **2004**, *37*, 8098–9109.
83. Koreeda, T.; Matos, J. *T*hermal characterization of mica-epoxy composite used as insulation material for high voltage machines. *J. Therm. Anal. Calorim.* **2001**, *106*, 619–623.

The Effects of *in Situ*-Formed Silver Nanoparticles on the Electrical Properties of Epoxy Resin Filled with Silver Nanowires

Gwang-Seok Song, Dai Soo Lee and Ilho Kang

Abstract: A novel method for preparing epoxy/silver nanocomposites was developed via the *in situ* formation of silver nanoparticles (AgNPs) within the epoxy resin matrix while using silver nanowires (AgNWs) as a conductive filler. The silver–imidazole complex was synthesized from silver acetate (AgAc) and 1-(2-cyanoethyl)-2-ethyl-4-methylimidazole (imidazole). AgNPs were generated *in situ* during the curing of the epoxy resin through the thermal decomposition of the AgAc–imidazole complex, which was capable of reducing Ag^+ to Ag by itself. The released imidazole acted as a catalyst to cure the epoxy. Additionally, after the curing process, the *in situ*-generated AgNPs were stabilized by the formed epoxy network. Therefore, by using the thermal decomposition method, uniformly dispersed AgNPs of approximately 100 nm were formed *in situ* in the epoxy matrix filled with AgNWs. It was observed that the nanocomposites containing *in situ*-formed AgNPs exhibited isotropic electrical properties in the epoxy resins in the presence of AgNWs.

Reprinted from *Polymers*. Cite as: Song, G.-S.; Lee, D.S.; Kang, I. The Effects of *in Situ*-Formed Silver Nanoparticles on the Electrical Properties of Epoxy Resin Filled with Silver Nanowires. *Polymers* **2016**, *8*, 157.

1. Introduction

Nanocomposite materials containing metal nanoparticles, graphenes, or organoclays dispersed into a polymer matrix exhibit significant absorbing properties because of their novel physical and chemical properties [1–3]. Specifically, epoxy/metal nanocomposites were used in the field of microelectronic packaging for applications in embedded capacitors and lead-free interconnecting materials [4–7]. One-dimensional nanostructured particles such as nanowires, nanotubes, nanorods, or nanofibers are expected to play an important role in fabricating nanoscale devices and nanocomposites. Metal nanowires such as silver nanowires (AgNWs) were employed as conductive fillers [8–16]. AgNWs have very low electrical resistivity and high thermal conductivity. Consequently, AgNWs have been primarily used as conductive fillers in conductive adhesive materials. An appropriate distribution of AgNWs within the epoxy network is very important for these applications. However, AgNWs are thermodynamically unstable and tend to form agglomerates because of their surface activity. Agglomeration occurs, and the anisotropic performance

of AgNWs by the aspect ratio is a significant problem when NWs are used to fabricate composites with high performance. Polymeric stabilizing agents, such as poly(vinylpyrrolidone), poly(ethyleneglycol), and other long-chain acids or amines, are usually introduced in the chemical syntheses of AgNWs to prevent agglomerate formation [17–25]. However, these stabilizing agents are seldom removed from the AgNW surfaces because of the strong interaction between them. These residues of organic molecules on NW surfaces are harmful, as they reduce electrical resistivity. Therefore, their application in electronic packaging is limited [26].

A uniform dispersion of AgNWs in nanocomposites is required as clumps of wires inside the polymer matrix lead to undesirable electrical, dielectric, and thermal properties. However, it is difficult to achieve uniformly dispersed ultrafine NWs in a polymer matrix by incorporating pre-added AgNWs into a polymer. This is because of the easy agglomeration of NWs and high viscosity of polymer systems with AgNWs. Conversely, the *in situ* formation of silver nanoparticles (AgNPs) in a polymer matrix could facilitate a more uniform dispersion of AgNWs in polymers. Further, *in situ* reduction can result in much smaller particle sizes than the commercially available micron or nano size silver particles. This, in turn, can help achieve electrical conductivity for the encapsulants and adhesives.

In this study, a novel method for preparing epoxy/silver nanocomposites was investigated. The method involved forming *in situ* AgNPs via the decomposition of a silver–imidazole complex with AgNWs and the curing of an epoxy resin. At a suitable curing temperature, the AgNP was formed *in situ* in the nanocomposites of the epoxy resin and in the AgNW by the decomposition of the silver–imidazole complex, which was capable of reducing Ag^+ to Ag by itself. Imidazole was immediately released from the silver–imidazole complex and could act as an epoxy resin catalyst. Specifically, the anisotropic properties of the nanocomposites due to the high aspect ratio of AgNWs disappeared because of the *in situ*-formed AgNP.

2. Materials and Methods

2.1. Materials

Silver nitrate ($AgNO_3$), chloroplatinic acid ($H_2PtCl_6 \cdot 6H_2O$), poly(vinylpyrrolidone) (PVP), anhydrous ethylene glycol (EG), and sodium chloride (NaCl) were purchased from Sigma Aldrich Chemical (Yongin, Kyeonggi-do, Korea) for the syntheses of AgNWs. A cycloaliphatic-type epoxy resin was purchased from Daicel Chemical Industry (Minato-ku, Tokyo, Japan). The anhydride-type curing agent, hexahydro-4-methylphthalic anhydride, and silver acetate (AgAc) were purchased from Sigma Aldrich Chemical. An imidazole-type catalyst, 1-(2-cyanoethyl)-2-ethyl-4-methylimidazole (imidazole), was purchased from TCI Chemical (Chuo-ku, Tokyo, Japan). The synthesized AgNW was purified using the washing method.

Isopropyl alcohol (IPA), purchased from SK Chemical (Seongnam-si, Kyeonggi-do, Korea), was chosen as the solvent because of its low boiling point and capacity as a good stabilizer for AgNWs.

2.2. Synthesis of Silver Nanowires (AgNWs) Using a Microwave Process

The microwave polyol process used in this study was the same as that in the literature [27]. The solution containing $AgNO_3$, $H_2PtCl_6 \cdot 6H_2O$, PVP (average molecular weight: 55,000 g/mol), and NaCl in EG was irradiated using a microwave oven (LG electronics, Yeongdeungpo-gu, Seoul, Korea) in continuous wave mode at 700 W. The solution was rapidly heated within 2 min, and an AgNW was formed. The AgNW was washed with acetone and dispersed in IPA.

2.3. Preparation of Silver–Imidazole Complex

Silver acetate (AgAc, 3 mmol) was added to imidazole (6 mmol). A paste mixer was used to dissolve the mixture until all the solid AgAc had dissolved. The liquid product had a yellow color and was viscous at 25 °C.

2.4. Preparation of Epoxy/Silver Nanocomposites with AgNWs

The 10 wt % of silver–imidazole complex was dispersed in the epoxy resin. The molar ratio of AgAc to imidazole was maintained at 1:2. A purified AgNW in IPA was added to the above mixture and was mixed until a light-yellow solution was formed. The solvent was evaporated under reduced pressure at 40 °C. Finally, the mix was cured at 110 °C for 30 min, 150 °C for 2.5 h, and 180 °C for 1 h to obtain epoxy/silver nanocomposites. The thermal decomposition of silver–imidazole complex realized the formation of AgNPs. The silver–imidazole complex was capable of reducing Ag^+ to Ag under the stepwise curing condition of the epoxy. Scheme 1 shows the synthesis process of AgNPs via the decomposition of the silver–imidazole complex [28]. This was confirmed using thermogravimetric analysis (TGA), field electron scanning electron microscopy (FE-SEM), and energy-dispersive X-ray spectroscopy (EDX) analysis. This study investigated various epoxy/silver nanocomposites with different AgNW loading levels.

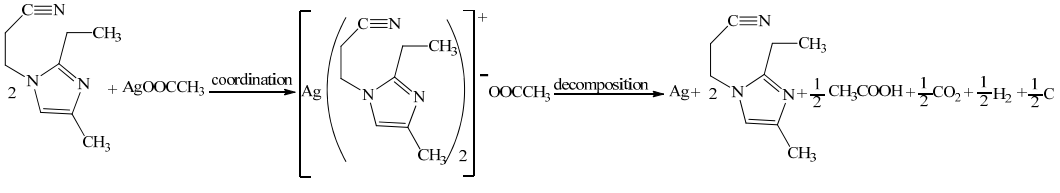

Scheme 1. Scheme for the silver nanoparticles (AgNPs) formed by *in situ* thermal decomposition of silver–imidazole complex.

The released imidazole in Scheme 1 acted as a catalyst for the curing of the epoxy resin. It was confirmed in DSC that the scanning of the epoxy resin containing anhydride-type curing agent and the silver–imidazole complex accompanied an exotherm due to the cure reaction, while the epoxy resin with only the anhydride-type curing agent without the silver–imidazole complex did not, as shown in Figure S1 in Supplementary Materials.

2.5. Characterization

The morphology of AgNWs was recorded using a transmission electron microscope (JEM-2010, JEOL, Akishima, Tokyo, Japan) and scanning electron microscope (JSM-5900, JEOL). The standard copper grid for the TEM image was dipped in the dispersion of a 0.1% AgNW in IPA for transmission electron microscopy (TEM) imaging. The fracture surfaces of the nanocomposite samples were observed under a field emission scanning electron microscope (S-4800, HITACHI, Minato-ku, Tokyo, Japan) after cryogenic fracture. The electrical properties of the nanocomposites were studied by measuring the surface resistivity of the composite sheets with a resistivity meter (ST-4, SIMCO JAPAN, Inc., Chuo-ku, Kobe, Japan) at room temperature. The TGA samples (Q50, TA Instruments, New Castle, DE, USA) were heated at a rate of 10 °C/min up to 800 °C under a nitrogen atmosphere to measure the amount of *in situ*-formed AgNPs.

3. Results and Discussion

Figure 1 displays a TEM micrograph and a histogram for the diameter of the AgNWs synthesized via the microwave process. The average diameter of the NWs was 80 nm. Figure 2 shows the SEM image and a histogram for the length of AgNWs after purification for removing the AgNPs from the synthesized sample. The average length of the NWs was 12.5 μm. Table 1 shows the EDX data for the cured epoxy/silver nanocomposite with a 10 wt % silver–imidazole complex. The epoxy/silver nanocomposite cured with the silver–imidazole complex had 3.29 wt % silver particles. The silver–imidazole-cured epoxy nanocomposite contained silver atoms. In contrast, the imidazole-cured nanocomposite did not contain silver atoms. Figure 3 shows the TGA thermograms of the imidazole, AgAc, and the silver–imidazole complex. It should be noted that 26 wt % silver was formed by the decomposition of the silver–imidazole complex. It was assumed that the AgNPs were formed *in situ* via the decomposition of the silver–imidazole complex during the curing of the epoxy resin. It is of interest to note that the silver content measured by EDX for the epoxy resin cured with the 10 wt % silver–imidazole complex was 3.29 wt %, which was higher than that expected, *i.e.*, 2.6 wt %, considering that 26 wt % silver was formed by the decomposition of the silver–imidazole complex in TGA. It is speculated that the silver content measured by EDX reflects silver atoms

in the surface of protruded silver nanoparticles in the fracture surface and can be higher than the silver content based on the TGA thermogram.

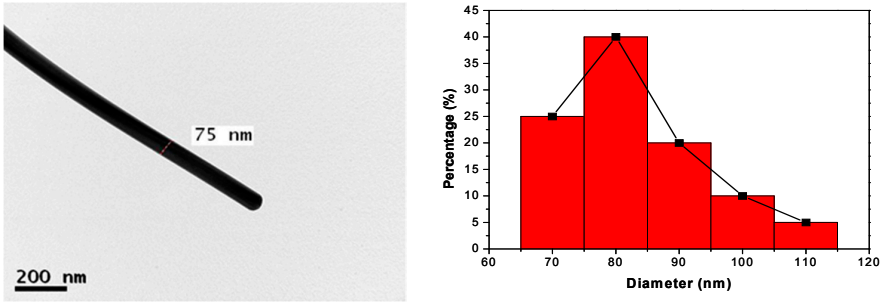

(**a**) (**b**)

Figure 1. Synthesized silver nanowires (AgNWs): (**a**) transmission electron microscopy image; (**b**) diameter distribution of the purified AgNW.

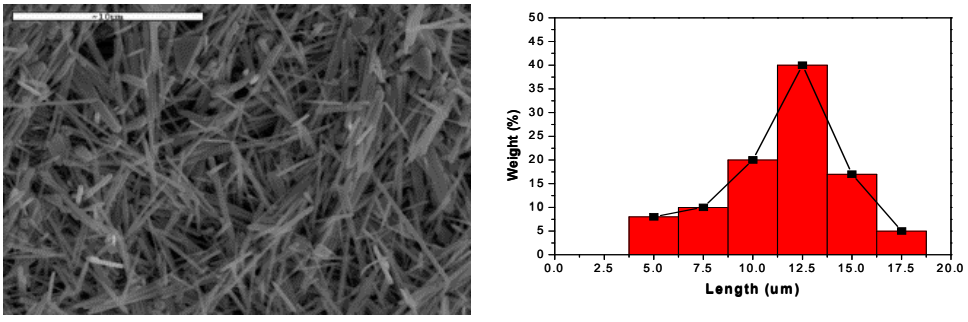

(**a**) (**b**)

Figure 2. Purified silver nanowires (AgNWs): (**a**) scanning electron microscopy image; (**b**) length distribution of a purified AgNW.

Table 1. Energy-dispersive X-ray spectroscopy data for epoxy/silver nanocomposites cured with the 10 wt % silver–imidazole complex and the epoxy resin cured with imidazole.

Element	Epoxy Resin Cured with the Silver–Imidazole Complex		Epoxy Resin Cured with Imidazole	
	Wt %	At %	Wt %	At %
C	67.86	75.50	69.48	75.62
O	28.85	24.09	30.52	24.38
Ag	3.29	00.41	0.00	0.00

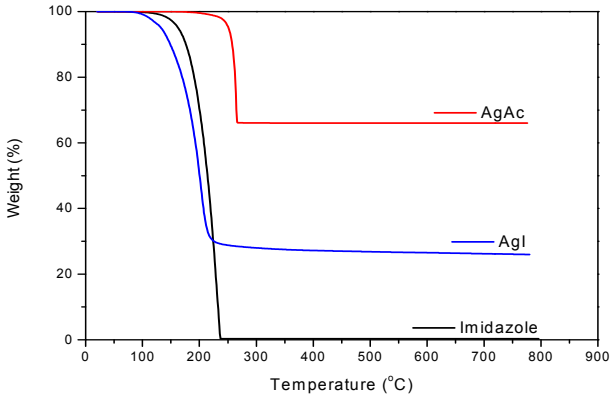

Figure 3. Thermogravimetric analysis thermograms of imidazole, silver–imidazole complex (AgI), and silver acetate (AgAc).

Figure 4 shows the surface electrical resistivities of the nanocomposites containing AgNWs at various concentrations with the imidazole and silver–imidazole complexes. Generally, the silver–imidazole-cured samples had lower surface electrical resistivities when compared with those of the imidazole-cured samples. Corcione and Maffezzoli measured transport properties of graphite/epoxy composites and characterized them with various theoretical models [29]. As the electrical resistivity of the nanocomposites in Figure 4 showed threshold decrease with increasing AgNW contents, the statistical percolation model was employed in this study. Thus, surface electrical resistivity (σ) can be expressed as follows:

$$\sigma = k(P - P_c)^{-t} \quad (1)$$

where P is the volume concentration of AgNW, P_c the critical volume concentration for the percolation threshold of AgNW, and t the exponent related to the dimensionality of the system. Fittings to Equation (1) were carried out as shown in Figure S2 of Supplementary Materials. Parameters obtained by the fitting are given in Table 2. It was observed that P_c values of the epoxy/AgNW nanocomposite with *in situ*-formed silver nanoparticles was lower than that of the epoxy/AgNW nanocomposite without the *in situ*-formed silver nanoparticles. It may be noted that the *in situ*-formed AgNP exerted a beneficial effect on the epoxy/silver nanocomposites in terms of electrical properties. The *in situ*-formed AgNPs between AgNWs decreased the interparticle distance, which facilitated the transfer of electrons between the AgNWs and AgNPs. The imidazole-cured samples had higher surface electrical resistivity when compared with those of the silver–imidazole-cured samples with the same AgNW volume fraction. This was due to the absence of silver nanoparticles formed by the *in situ* process. The anisotropic property, resulting

from the characteristic high aspect ratio of the AgNW, was confirmed by the surface electrical resistivity in the imidazole-cured samples. This phenomenon was especially observed in AgNWs at the loading of 6 to 10 vol %. However, it was not observed in AgNWs below 6 vol % or over 10 vol %. However, the silver–imidazole-cured nanocomposite did not exhibit the anisotropic phenomenon because of the presence of the silver nanoparticles formed by the *in situ* process. This is an important advantage of the nanocomposites composed of the *in situ*-formed silver nanoparticles as well as the AgNW. This allows the potential applications of these nanocomposites in devices requiring isotropic electrical properties.

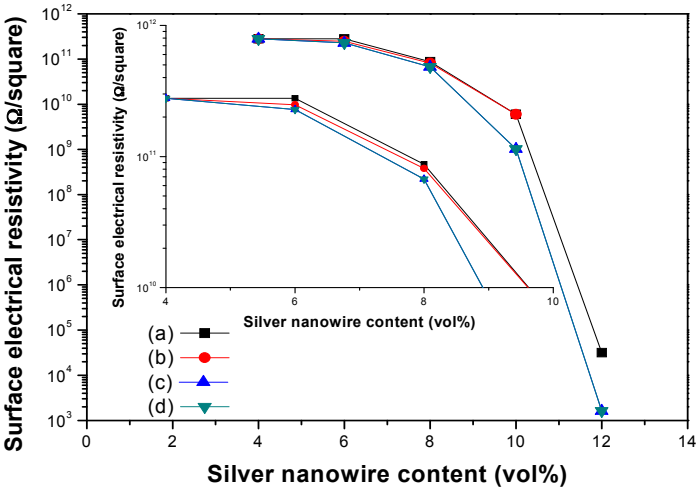

Figure 4. Surface electrical resistivity of the cured epoxy resin containing AgNWs of various concentrations: (**a**) sample cured with imidazole in the direction of the highest resistivity; (**b**) sample cured with imidazole in the direction perpendicular to that of (**a**); (**c**) sample cured with silver–imidazole complex in the direction of the highest resistivity; (**d**) sample cured with silver–imidazole complex in the direction perpendicular to that of (**c**).

Table 2. Parameter values of the percolation model for samples shown in Figure 4.

Sample	(a)	(b)	(c)	(d)
P_c (vol %)	12.60	12.80	12.50	12.50
t	4.29	4.57	4.49	4.49

Figure 5 shows the interwire distance in AgNW systems obtained from a geometrical model as described below. The interwire distance is defined as the distance between the two NW surfaces and is useful, as it can be used in conjunction

with potential energy curves to determine whether attractive or repulsive energy dominates in a NW particulate system. This information is useful in inferring the stability of NW systems and other surface-related phenomena. Interwire distance has been used as an important parameter for the viscosity estimation of suspensions such as in metallic filler/epoxy resin systems [30]. It also provides useful insights into problems related to formulating suspensions with high filler loadings. At the maximum filler loading, the interwire distance tends to approach a minimum value. Thus, it is useful to understand how the interwire distance affects the physical characteristics of the NW particulates. The model assumes that a parallel piped cell surrounds each NW. It also assumes that the NW volume fraction in a cell is equal to the NW volume fraction throughout the system. Given that the NW is cylindrical, the NW diameter is d_{w}, and the interwire distance of each NW is d_{i}. The volume fraction of the NWs is Φ_{w}, as given by:

$$\Phi_{\mathrm{w}} = V_{\mathrm{w}}/V_{\mathrm{u}} \tag{2}$$

where V_{w} is volume of NWs in the nanocomposite volume of which is V_{u}, and can be computed as:

$$V_{\mathrm{w}} = n\pi(d_{\mathrm{w}}/2)^2 L \tag{3}$$

$$V_{\mathrm{u}} = n(d_{\mathrm{i}} + d_{\mathrm{w}})^2 L \tag{4}$$

Equations (2)–(4) are combined to yield d_i as a function of Φ_{w} as follows:

$$d_{\mathrm{i}} = d_{\mathrm{w}}[\{\pi/(4\Phi_{\mathrm{w}})\}^{1/2} - 1] \tag{5}$$

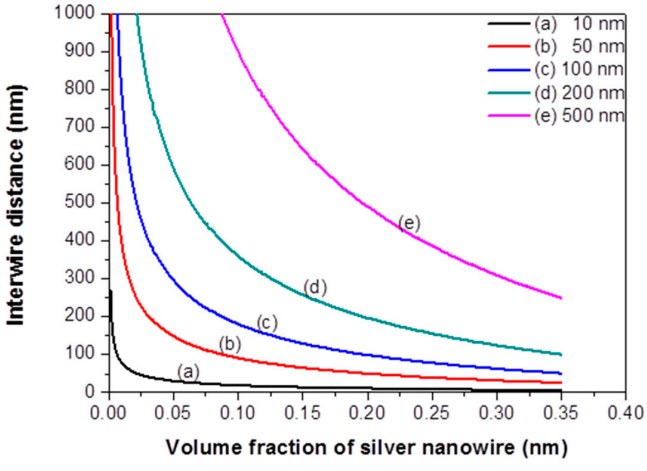

Figure 5. Interwire distances of AgNWs of different diameters: (**a**) 10 nm; (**b**) 50 nm; (**c**) 100 nm; (**d**) 200 nm; and (**e**) 500 nm.

The interwire distance for a AgNW of diameter 20 nm and volume fraction of 10 vol % was similar to that of the AgNW system with a NW diameter of 200 nm and a NW volume fraction of 20 vol %. This clearly indicated that an increase in the AgNW diameter increased the amount of AgNW dispersed into a medium and formed a high solid loading suspension. However, as the AgNW diameter decreased, the suspension was reduced to clumps. As the interwire distance is very small, it does not allow any more AgNWs to be dispersed into the system, even at a very low AgNW volume fraction. This may be the reason why it is extremely difficult to obtain a high solid loading suspension when the AgNW diameter size is in the nanometer range. The interwire distance in both the 10 vol % of the AgNW imidazole-cured sample and the silver–imidazole-cured sample in this study should be 144 nm.

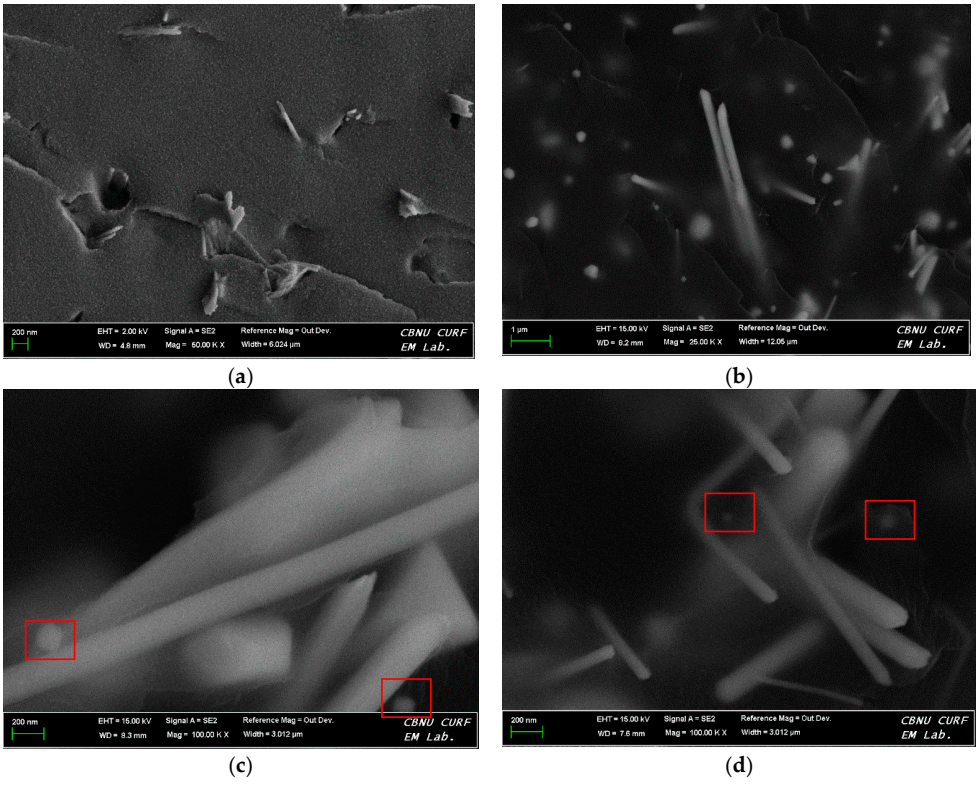

Figure 6. TEM images of the cured epoxy resin/silver nanocomposites: (**a**) sample cured with imidazole (scale bar, 200 nm); (**b**) sample cured with 10.0 wt % of the silver–imidazole complex with 6 vol % of AgNWs (scale bar, 1 µm); (**c**) magnified version of the sample in (**b**) (scale bar, 200 nm); (**d**) sample cured with 10.0 wt % of silver–imidazole with 8 vol % of AgNWs (scale bar, 200 nm).

The morphology of the cured systems was investigated using SEM. Figure 6a shows the SEM images of the films cured with imidazole with 8 vol % of AgNWs. No particles are observed in Figure 6a. Figure 6b,c show the SEM images of the films cured using 10.0 wt % of the silver–imidazole complex with 6 vol % of AgNWs. The *in situ*-formed nanoparticles were well dispersed in the epoxy resin with AgNWs, and no macroscopic agglomerates were formed. The average particle diameter was ~100 nm. The quality of the AgNW dispersion in the polymer matrix was directly correlated with its effectiveness in improving the properties of the nanocomposites. It is believed that a uniform distribution of the *in situ*-formed AgNPs in the polymer matrix with AgNWs leads to a relatively high electrical conductivity. The addition of AgNWs in conjunction with the *in situ* formation of AgNPs facilitated a more uniform dispersion of the NPs in the polymers, thereby reducing anisotropic properties.

4. Conclusions

Epoxy/silver nanocomposites were successfully prepared by the dispersion of AgNWs and the *in situ* formation of AgNPs via the thermal decomposition of a silver–imidazole complex. The simultaneously released imidazole acted as a catalyst to help cure the epoxy resin. The molar ratio of AgAc to imidazole in the silver–imidazole complex was 1:2. AgNPs were formed *in situ* during the curing process. The average particle diameter was ~100 nm. The *in situ*-formed AgNPs in the nanocomposites altered the electrical properties of the nanocomposites from anisotropic to isotropic. The nanocomposites of epoxy resin and the AgNWs with isotropic electrical properties caused by the *in situ* formation of AgNPs are useful as electronic materials in various applications.

Supplementary Materials: The following are available online at www.mdpi.com/2073-4360/8/4/157/s1. Figure S1: DSC thermograms obtained by scanning at heating rate of 10 °C/min in N_2 gas environment for the epoxy resins containing anhydride type curing agent: (**a**) without silver-imidazole complex; (**b**) with 10 wt % of the silver-imidazole complex. Exothermic heat of cure in (**b**) was 321.3 J/g, Figure S2: Fittings to the percolation model Equation (1) for surface electrical resistivity of the samples shown in Figure 4: (**a**) sample cured with imidazole in direction of the highest resistivity; (**b**) sample cured with imidazole in the direction perpendicular to that of (**a**); (**c**) sample cured with silver-imidazole complex in direction of the highest resistivity; (**d**) sample cured with silver-imidazole complex in the direction perpendicular to that of (**c**).

Acknowledgments: It is acknowledged that this work was supported by the Advanced Technical Center (ATC) project of Korea Evaluation Institute of Industrial Technology (KEIT funded by Ministry of Trade, Industry, and Energy (Project No: ATC-10048672) in Korea.

Author Contributions: Gwang-Seok Song and Dai-Soo Lee designed and performed the experiments; Ilho Kang contributed reagents/materials and analyzed the data. Dai-Soo Lee wrote the paper.

Conflicts of Interest: The authors declare no conflict of interest.

References

1. Yagci, Y.; Sangermano, M.; Rizza, G. Synthesis and Characterization of Gold-Epoxy Nanocomposites by Visible Light Photoinduced Electron Transfer and Cationic Polymerization Processes. *Macromolecules* **2008**, *41*, 7268–7270.
2. Maruo, M.; Acocella, M.R.; Corcione, C.S.; Maffezzoli, A.; Guera, G. Catalytic activity of graphite-based nanofillers on cure reaction of epoxy resins. *Polymer* **2014**, *55*, 5612–5615.
3. Greco, A.; Corcione, C.S.; Maffezzoli, A. Effect of multi-scale diffusion on the permeability behavior of intercalated nanocomposites. *J. Membr. Sci.* **2016**, *505*, 92–99.
4. Lee, H.; Chou, K.; Shih, Z. Effect of nano-sized silver particles on the resistivity of polymeric conductive adhesives. *Int. J. Adhes. Adhes.* **2005**, *25*, 437–441.
5. Jiang, H.; Moon, K.; Li, Y.; Wong, C.P. Surface functionalized silver nanoparticles for ultrahigh conductive polymer composites. *Chem. Mater.* **2006**, *18*, 2969–2973.
6. Lu, J.; Moon, K.; Wong, C.P. Silver/polymer nanocomposite as a high-k polymer matrix for dielectric composites with improved dielectric performance. *J. Mater. Chem.* **2008**, *18*, 4821–4826.
7. Konghua, L.; Lan, L.; Yuanfang, L.; Demin, J. One-step synthesis of metal nanoparticle decorated graphene by liquid phase exfoliation. *J. Mater. Chem.* **2012**, *22*, 20342–20352.
8. Ghosh, K.; Maiti, S.N. Mechanical properties of silver-powder-filled polypropylene composites. *J. Appl. Polym. Sci.* **1996**, *60*, 323–331.
9. Sastry, M.; Mayya, K.S.; Bandyopadhyay, K. pH dependent changes in the optical properties of carboxylic acid derivatized silver colloidal particles. *Colloids Surf. A Physicochem. Eng. Asp.* **1997**, *127*, 221–228.
10. Shipway, A.; Lahav, M.; Gabai, R.; Willner, I. Investigations into the Electrostatically Induced Aggregation of Au Nanoparticles. *Langmuir* **2000**, *16*, 8789–8795.
11. Huang, Y.; Duan, X.; Cui, Y.; Lauhon, L.; Kim, K.; Lieber, C. Logic gates and computation from assembled nanowire building blocks. *Science* **2001**, *294*, 1313–1317.
12. Mandal, S.; Gole, A.; Lala, L.; Gonnade, R.; Ganvir, V.; Sastry, M. Studies on the Reversible Aggregation of Cysteine-Capped Colloidal Silver Particles Interconnected via Hydrogen Bonds. *Langmuir* **2001**, *17*, 6262–6268.
13. Gudiksen, M.S.; Lauhon, L.J.; Wang, J.; Smith, D.C.; Lieber, C.M. Growth of nanowire superlattice structures for nanoscale photonics and electronics. *Nature* **2002**, *415*, 617–620.
14. Sauer, G.; Brehm, G.; Schneider, S. Highly ordered monocrystalline silver nanowire arrays. *J. Appl. Phys.* **2002**, *91*, 3243–3247.
15. Dang, M.; Shen, Y.; Nan, C.W. Dielectric behavior of three-phase percolative Ni–$BaTiO_3$/polyvinylidene fluoride composites. *Appl. Phys. Lett.* **2002**, *81*, 4814–4816.
16. Tao, A.; Kim, F.; Hess, C.; Goldberger, J.; He, R.; Sun, Y.; Xia, Y.; Yang, P. Langmuir-Blodgett silver nanowire monolayers for molecular sensing using surface-enhanced Raman spectroscopy. *Nano Lett.* **2003**, *3*, 1229–1233.
17. Sun, Y.; Xia, Y. Langmuir-Blodgett silver nanowire monolayers for molecular sensing using surface-enhanced Raman spectroscopy. *Science* **2002**, *298*, 2176–2179.

18. Sun, Y.; Yin, Y.; Mayers, B.; Herricks, T.; Xia, Y. Uniform Silver Nanowires Synthesis by Reducing $AgNO_3$ with Ethylene Glycol in the Presence of Seeds and Poly(Vinyl Pyrrolidone). *Chem. Mater.* **2002**, *14*, 4736–4745.
19. Yamamoto, M.; Nakamoto, M. Novel preparation of monodispersed silver nanoparticles via amine adducts derived from insoluble silver myristate in tertiary alkylamine. *J. Mater. Chem.* **2003**, *13*, 2064–2065.
20. Sun, Y.; Mayers, B.; Herricks, T.; Xia, Y. Polyol Synthesis of Uniform Silver Nanowires: A Plausible Growth Mechanism and the Supporting Evidence. *Nano Lett.* **2003**, *3*, 955–960.
21. Pothukuchi, S.; Li, Y.; Wong, C.P. Development of a novel polymer–metal nanocomposite obtained through the route of *in situ* reduction for integral capacitor application. *J. Appl. Polym. Sci.* **2004**, *93*, 1531–1538.
22. Wiley, B.; Herricks, T.; Sun, Y.; Xia, Y. Polyol Synthesis of Silver Nanoparticles: Use of Chloride and Oxygen to Promote the Formation of Single-Crystal, Truncated Cubes and Tetrahedrons. *Nano Lett.* **2004**, *4*, 1733–1739.
23. Luo, C.; Zhang, Y.; Zeng, X.; Zeng, Y.; Wang, Y. The role of poly(ethylene glycol) in the formation of silver nanoparticles. *J. Colloid Interface Sci.* **2005**, *288*, 444–448.
24. Wiley, B.; Xiong, Y.; Li, Z.; Yin, Y.; Xia, Y. Right Bipyramids of Silver: A New Shape Derived from Single Twinned Seeds. *Nano Lett.* **2006**, *6*, 765–768.
25. Sangermano, M.; Yagci, Y.; Rizza, G. *In Situ* Synthesis of Silver-Epoxy Nanocomposites by Photoinduced Electron Transfer and Cationic Polymerization Processes. *Macromolecules* **2007**, *40*, 8827–8829.
26. Zhang, R.; Moon, K.; Lin, W.; Wong, C.P. Preparation of highly conductive polymer nanocomposites by low temperature sintering of silver nanoparticles. *J. Mater. Chem.* **2010**, *20*, 2018–2023.
27. Tsuji, M.; Hashimoto, M.; Nishizawa, Y.; Tsuji, T. Synthesis of gold nanorods and nanowires by a microwave–polyol method. *Mater. Lett.* **2004**, *58*, 2326–2330.
28. Judd, M.D.; Plunkett, B.A.; Pope, M.I. The thermal decomposition of calcium, sodium, silver and copper(II) acetate. *J. Therm. Anal. Calorim.* **1974**, *6*, 555–563.
29. Corcione, C.E.; Maffezzoli, A. Transport properties of graphite/epoxy composites: Thermal, permeability and dielectric characterization. *Polym. Test.* **2013**, *32*, 880–888.
30. Hao, T.; Riman, R.E. Calculation of interparticle spacing in colloidal systems. *J. Colloid Interface Sci.* **2006**, *297*, 374–377.

On the Effect of Nanoparticle Surface Chemistry on the Electrical Characteristics of Epoxy-Based Nanocomposites

Celia Yeung and Alun S. Vaughan

Abstract: The effect of nanosilica surface chemistry on the electrical behavior of epoxy-based nanocomposites is described. The nanosilica was reacted with different volumes of (3-glycidyloxypropyl)trimethoxysilane and the efficacy of the process was demonstrated by infrared spectroscopy and combustion analysis. Nanocomposites containing 2 wt % of nanosilica were prepared and characterized by scanning electron microscopy (SEM), AC ramp electrical breakdown testing, differential scanning calorimetry (DSC) and dielectric spectroscopy. SEM examination indicated that, although the nanoparticle dispersion improved somewhat as the degree of surface functionalization increased, all samples nevertheless contained agglomerates. Despite the non-ideal nature of the samples, major improvements in breakdown strength (from 182 $\pm$ 5 kV$\cdot$mm^{-1} to 268 $\pm$ 12 kV$\cdot$mm^{-1}) were observed in systems formulated from optimally treated nanosilicas. DSC studies of the glass transition revealed no evidence for any modified interphase regions between the nanosilica and the matrix, but interfacial effects were evident in the dielectric spectra. In particular, changes in the magnitude of the real part of the permittivity and variations in the interfacial α'-relaxation suggest that the observed changes in breakdown performance stem from variations in the polar character of the nanosilica surface, which may affect the local density of trapping states and, thereby, charge transport dynamics.

Reprinted from *Polymers*. Cite as: Yeung, C.; Vaughan, A.S. On the Effect of Nanoparticle Surface Chemistry on the Electrical Characteristics of Epoxy-Based Nanocomposites. *Polymers* **2016**, *8*, 126.

1. Introduction

Composites have long been used in a wide range of different applications since, by combining two or more components, it is possible to generate material systems with improved properties. Nevertheless, the need for new materials with increased functionality has led to increasing interest in a new generation of composite materials, namely nanocomposites, since these have the potential to deliver combinations of properties that are not accessible through other routes [1,2]. These filled systems differ from conventional composite materials as the filling phase measures a maximum of 100 nm in at least one dimension and, consequently, the specific interfacial area

between the matrix and the filler is large. Indeed, it has been suggested that many aspects of nanocomposite behavior are dominated by interfacial effects related to the presence of interphases, which constitute a significant volume fraction of the system [3].

Although considerable initial effort was focused on generating nanocomposites with tailored thermomechanical properties, the concept of "nanodielectrics" was introduced by Lewis in 1994 [3] and quickly gathered momentum in the field of electrical insulation. As the demands on electrical power equipment grow, so do those imposed on their insulation, and may include: improved electrical breakdown strength, reduced dielectric loss, increased thermal conductivity, modified charge transport dynamics, *etc*. In the case of nanodielectrics, many beneficial effects have been attributed to the introduction of nanoparticles [4–6], but, as a consequence of their nanometric size, nanofillers tend to aggregate prior to and during nanocomposite production, which can impair properties. In particular, the use of polar fillers in non-polar dielectric media can be problematical, as typical mixing techniques are in constant competition with high surface energies and electrostatic forces that can adversely affect the homogeneity of the nanofiller dispersion within the matrix.

To address such compatibility issues, many studies have employed the use of coupling agents, where organofunctional surface reactants are used to modify the mineral substrate surface in order to improve interactions between the nanofiller and the matrix polymer. One of the most commonly employed coupling strategies exploits organosilanes and a number of publications have shown how the use of such compounds can lead to improved filler dispersion in nanodielectrics, thereby enhancing the resulting electrical properties of the system [7,8]. Determining the optimum quantity of coupling agent for functionalization is, however, of great importance. If insufficient coupling agent is used, the interactions at the nanofiller-matrix interface will not be optimal and weaker matrix bonding may result while, if excess coupling agent is used, self-condensation may prove disadvantageous [7]. Methods for estimating the optimum quantity of coupling agent have therefore been proposed in a number of studies. Some authors have attempted to calculate the required quantity of coupling agent based on the number of active sites on the surface of the nanofiller that is available for chemical bonding [9], while others have used the size of the nanoparticles and the thickness of a monolayer of coupling agent [7] to evaluate the required volume of reagent. Another approach has involved calculations based on the surface area of the filling phase and the specific wetting surface of the silane coupling agent [10]. Despite this, there have been few detailed studies in which the degree of functionalization has been treated as a variable parameter in studies of nanocomposite systems [11,12].

This study set out with the objective of systematically varying the functionalization conditions of nanosilica (SiO_2), with the aim of determining its effect on the structure and dielectric properties of a series of epoxy-based nanodielectrics. Specifically, the intention of the work was to test the generally accepted notion that, in nanodielectrics, surface interactions determine nanoparticle dispersion and that nanoparticle dispersion determines macroscopic properties through the formation of consequent interphases. Two functionalization methodologies have been considered, which involved hydrous and anhydrous conditions; only the former is reported here.

2. Materials and Methods

2.1. Materials

The epoxy resin used in this study was a diglycidyl ether of bisphenol A with an epoxide equivalent molar mass of 172–176 $g \cdot mol^{-1}$; D.E.R.™ 332, obtained from Sigma Aldrich, St. Louis, MO, USA. This was cured using a polyetheramine curing agent with an amine hydrogen equivalent molar mass of 60 $g \cdot mol^{-1}$; Jeffamine D-230, obtained from Huntsman Corporation, The Woodlands, TX, USA. The nanosilica was purchased from Sigma Aldrich and is characterized by a quote filler size of 10–20 nm; this was pre-treated with (3-glycidyloxypropyl)trimethoxysilane (GLYMO—Z-6040 from Dow Corning, Auburn, MI, USA) using the procedure described below.

Samples of nanosilica were modified to varying degrees by treating the nanoparticles with different quantities of coupling agent. Simplistic calculations suggest that, to functionalize 100 mg of spherical nanosilica particles 10–20 nm in diameter with a monolayer of GLYMO, ~20 mg of the coupling agent would be required; that is, a ratio of 5 parts nanosilica to 1 part GLYMO by mass. However, due to the uncertainties inherent in this calculation, seven samples were prepared using various ratios of nanosilica to GLYMO that span the above estimate (see Table 1). For this, the appropriate quantity of coupling agent was added to a pre-sonicated suspension composed of 800 mg of nanosilica in 25 mL of methanol and shaken vigorously. To inhibit GLYMO self-condensation reactions, the above reaction was conducted under acidic conditions; acetic acid was added according to the procedure specified by Ash *et al.* [13]. After 46 h, the nanosilica was recovered by first centrifuging and then washing with fresh methanol; this procedure was repeated five times to ensure that all excess coupling agent and all acid residues were removed from the system. Finally, the nanosilica was dried thoroughly at 40 °C under vacuum, to remove any residual solvent.

Table 1. Degree of nanosilica functionalization and designated codes for each sample. All nanocomposites contain 2 wt % of the appropriate nanosilica.

Nanocomposite	Nanosilica Filler	Ratio of Nanosilica to GLYMO
EPX	–	–
NCU	NSU	1:0
NC0	NS0	1:0
NC1	NS1	8:1
NC2	NS2	4:1
NC4	NS4	2:1
NC8	NS8	1:1
NC16	NS16	1:2
NC20	NS20	2:5

2.2. Nanocomposite Preparation

Nanocomposite samples were prepared from the above starting materials using the following procedure. First, 150 mg of the required nanosilica was introduced, with stirring, to 5.58 g of the D.E.R.™ 332 and sonicated for 1 h using a UP200s probe sonicator, Hielscher Ultrasonics, Teltow, Germany (110 W; 55% amplitude; pulsed mode with 0.7 s on, 0.3 s off). In order to prevent any excessive increase in temperature, the specimen was placed in a water bath throughout the sonication process and the water was replaced every 15 min. After sonication was complete, 1.92 g of hardener was added, as required to produce the optimum stoichiometric ratio of 1000:344 (epoxy:hardener), and the resulting mixture was thoroughly stirred with a magnetic stirrer for 15 min before being degassed under dynamic vacuum for 15 min. The resulting resin was then poured into a steel mold (pre-heated to 50 °C) containing a spacer, nominally 70 μm in thickness; all mold components were lightly coated with QZ-13 release agent, Huntsman Corporation, to aid removal of the resulting film specimen. All samples were cured at 100 °C for 4 h before, finally, being dried under vacuum at 40 °C for two weeks prior to testing.

2.3. Material Characterisation

To evaluate the effect of the surface functionalization treatment described above, specimens of the as-supplied nanosilica (*i.e.*, nanosilica NSU), NS0, NS4 and NS20 were subjected to combustion/CHN analysis (MEDAC Ltd., Woking, UK.), which, in this context, provides an indicative measure of the carbon content of each material. In addition, FTIR spectra were obtained from all nanosilicas, using a Thermo Nicolet 380 FTIR spectrometer (Thermo Scientific, Waltham, MA, USA) fitted with a Golden Gate single reflection diamond attenuated total reflectance (ATR) attachment. Spectra were collected with the spectrometer set in reflectance mode for wavenumbers ranging from 4000 cm^{-1} to 400 cm^{-1}, using 32 scans at a resolution of 4 cm^{-1}. All spectra

were finally normalized with respect to the peak at 1100 cm^{-1}, which, being related to the silica phase, provides a convenient reference.

The dispersion state of the nanofiller within each nanocomposite was examined using a field emission gun scanning electron microscope (FEG-SEM) 6500F SEM (JEOL Ltd., Tokyo, Japan). For this, film samples prepared as above were immersed in liquid nitrogen before being fractured to expose an internal surface. Images were obtained from gold sputter-coated specimens using an accelerating voltage of 15 kV and a working distance of 10 mm.

2.4. Nanocomposite Properties

AC electrical breakdown tests were conducted at room temperature on nominally 70 μm thick film specimens, in line with the ASTM D149 standard. Twenty random sites on each nanocomposite film were sequentially positioned between two 6.3 mm spherical ball bearing electrodes, whilst immersed in silicone oil and subjected to a 50 Hz AC ramp voltage that was increased at a rate of 50 $V \cdot s^{-1}$ (RMS) until failure. The ball bearing electrodes were routinely replaced after eight tests, to eliminate the possibility of surface pitting affecting the derived data. The sample thickness at each breakdown site was subsequently measured, such that the associated field at breakdown could be determined from the breakdown voltage. The resulting AC breakdown field data were processed using Weibull 7++ software (Reliasoft Corporation, Tucson, AZ, USA), assuming a two parameter Weibull distribution. The Weibull scale parameter, α, and shape parameter, β, were determined for each data set, together with 90% maximum likelihood confidence bounds.

The glass transition of each specimen was evaluated using a Perkin Elmer, Waltham, MA, USA, DSC 7 differential scanning calorimeter (DSC), after calibration with high purity indium. Samples weighing 5.0 ± 0.5 mg were enclosed in aluminum cans and held at 50 °C for 1 min, before the specimen temperature was raised from 50 to 120 °C at a rate of 10 $°C \cdot min^{-1}$ and then reduced rapidly to a nominal 30 °C. This procedure was executed twice in succession to erase the thermal history of the sample. Data for baseline correction were acquired from an unfilled DSC can and subtracted from the sample material second scan. The resulting baseline corrected data were finally normalized with respect to sample mass and the glass transition temperature, T_g, of each nanocomposite was determined by taking the mid-point of the step-change in the DSC heat flow data. The associated change in specific heat capacity, ΔC_p, and the width of the glass transition, ΔT_g, were also routinely evaluated.

The dielectric response of the various epoxy systems was recorded using a Schlumberger, Houston, TX, USA, SI 1260 impedance/phase gain analyzer, in conjunction with a Solatron, Farnborough, UK, 1296 dielectric interface and a purpose

built test cell with heating capability. Samples were prepared by sputter coating opposing circular gold electrodes measuring 32 mm in diameter onto each surface of the epoxy film. Dielectric spectra were obtained from each sample upon the application of a sinusoidal AC voltage of amplitude 1 V. Data were obtained at 20 °C intervals from 20 to 100 °C, over the frequency range 0.1 Hz to 0.1 MHz.

3. Results

3.1. Nanosilica Functionalization

The objective of surface treatment with an organosilane is to provide an amphiphilic bridge to promote desirable interactions between the filler and the surrounding matrix. The formulation used to produce each of the nanosilicas is listed in Table 1; each nanocomposite contained 2 wt % of the indicated nanosilica. The hydrolysis of the methoxy functional groups on the organosilane results in the formation of organosilane moieties with reactive silanol groups that can: (a) undergo self-condensation; or (b) react with hydroxyl groups on the surface of the nanosilica. Hydrogen bonds formed at the filler surface are replaced by covalent bonds upon drying, resulting in the functionalization of the nanofiller [7,14]. Figure 1 compares the weight percentages of carbon in untreated and treated samples of nanosilica. These data indicate that the carbon content in NSU and NS0 is equivalent; neither has been processed with GLYMO. This result also indicates that exposure to the acidic methanolic solvent does not lead to the adsorption of appreciable organic residues. The increasing levels of carbon detected in NS4 and NS20, although within the measurement uncertainties, are suggestive of successful surface modification.

Figure 2 contains Fourier transform infrared (FTIR) spectra obtained from all the nanocomposite systems listed in Table 1. All spectra show absorption bands from 1200 to 1000 cm^{-1}, at 805 cm^{-1} and at 471 cm^{-1}, which are characteristic of asymmetric Si–O–Si stretching, deformation of SiO_4 tetrahedra and O–Si–O deformation respectively [15]. Data acquired from the GLYMO contain a strong absorption peak at 1250 cm^{-1}, which is a consequence of the presence of the terminal epoxide ring, while the absorption in the range 2850 to 3000 cm^{-1} is representative of the CH_2 groups that are associated with the GLYMO organic backbone [12,16]. Despite the lack of clear epoxide features in the spectra obtained from the surface-modified nanosilicas, there are observable differences in the region 3000 to 3700 cm^{-1}, which is primarily associated with hydroxyl groups. As NSU and NS0 have not been chemically modified, they can be considered chemically equivalent as far as the GLYMO is concerned. Nevertheless, the strength of the hydroxyl band is rather less in the NS0 specimen; a decrease in the hydroxyl band is observed in processed silicas and is attributable to the removal of moisture from the surface during vacuum drying. There is also evidence of a minor additional peak

at 2944 cm^{-1} for all the samples that had been functionalized with the GLYMO, as highlighted in Figure 2b, which increases in intensity with the volume of GLYMO used in processing. This feature correlates with the GLYMO CH_2 absorption band indicated by the dotted lines in Figure 2 and therefore provides further evidence in support of the successful functionalization of the nanosilica.

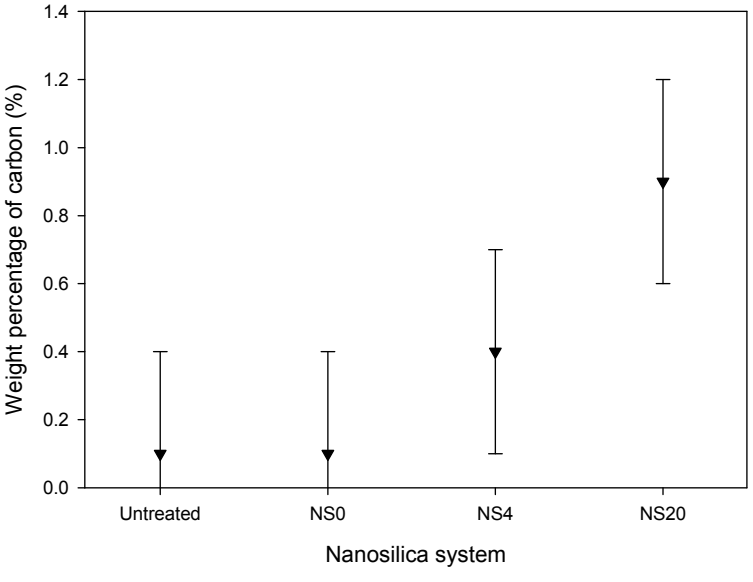

Figure 1. Combustion analysis data indicating an increase in nanosilica carbon content with increasing degree of surface modification. The error bars correspond to the accuracy of $\pm$0.30% absolute quoted by MEDAC Ltd., Woking, UK.

Published accounts of organosilane chemistry describe the chemical pathways in terms of hydrolysis and condensation [14,17], before hydrogen bonds are formed with the surface of the substrate. However, such an idealized outcome constitutes an unlikely extreme, with other conformations being possible. In such cases, unreacted hydroxyl (silanol) groups will be retained within a disordered organosilica surface layer and, consequently, even in the case of NS20, where it would seem that a vast excess of GLYMO has been used, residual hydroxyl groups still exist near the particle surface, as evinced by Figure 2.

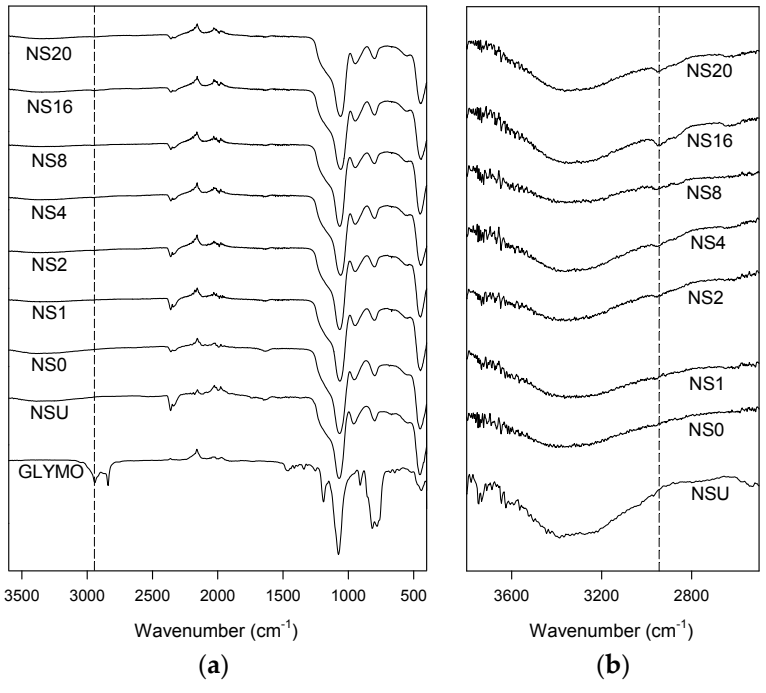

Figure 2. FTIR spectra obtained from all the nanosilica systems used in this study; the vertical dashed line indicates 2944 cm^{-1}. (**a**) full spectral range; (**b**) detail showing the hydroxyl region.

3.2. Nanocomposite Morphology

Although it is generally accepted that appropriate functionalization of nanoparticles leads to enhanced dispersion, we are not aware of any previous attempts to investigate how varying the degree of functionalization affects this. Figure 3a contains a typical scanning electron microscope (SEM) image of a cryofracture surface in an unfilled epoxy, which reveals a smooth texture in accordance with its amorphous structure. This image is in line with published work [18]. The surface striations indicated by the arrow are fractography features and lie orthogonal to the local crack propagation direction. In comparison, all nanocomposites were found to be characterized by much rougher surface textures that, locally, provide evidence of significant degrees of agglomeration, as shown in Figure 3b–d. Figure 3b shows an agglomerated region in sample NC0 that contains, in addition, bow-like fractography features associated with crack pinning [19]. Increasing the quantity of GLYMO used in functionalization results in a less agglomerated structure and in rather finer matrix surface textures.

While the presence of agglomerates in nanocomposites is not uncommon [20], the overall quality of the specimens shown above are markedly inferior to those reported by Nguyen *et al.* [18] in a recent study of epoxy/silica nanocomposites. In the work of Nguyen *et al.* [18], the nanosilica was introduced using a proprietary masterbatch system, Nanopox E 470 (supplied by Nanoresins), where the nanosilica is described as consisting of an agglomerate-free colloidal dispersion of surface-modified synthetic SiO_2 with an average particle diameter of 20 nm. It is evident from the study of Nguyen *et al.* [18] that it is possible to produce agglomerate-free materials through the use of systems such as Nanopox E 470, albeit that this comes at the cost of neither knowing the nanofiller surface chemistry nor being able to modify it as required.

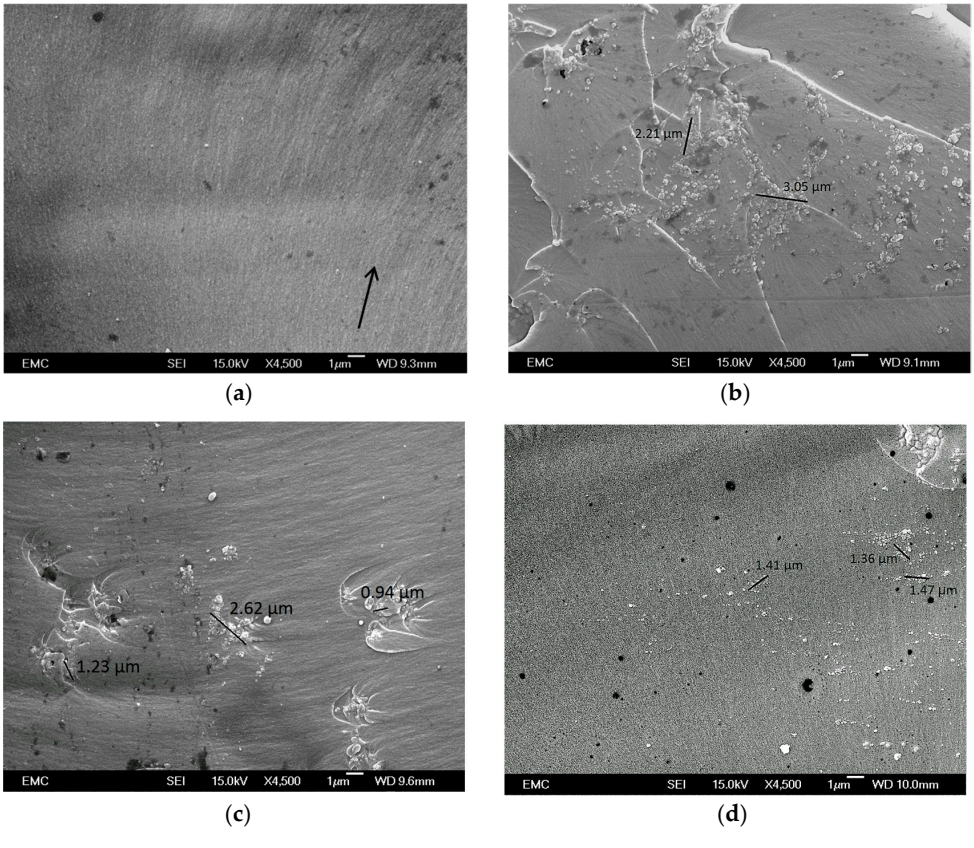

Figure 3. SEM micrographs showing representative fracture surfaces through a range of the materials considered here: (**a**) the unfilled epoxy specimen (EPX); (**b**) NC0; (**c**) NC4; and (**d**) NC16.

3.3. Dielectric Breakdown Strength

Table 2 contains breakdown parameters obtained from all the samples considered here, assuming two parameter Weibull statistics. From this, the breakdown strength, E_b, of the unfilled resin, which in line with convention we equate to the Weibull α parameter, is given by 182 ± 5 kV$\cdot$mm^{-1}. This constitutes a reference point for all the other systems. Adding nanosilica directly without surface modification or solvent processing results in a decrease in breakdown strength to 173 ± 6 kV$\cdot$mm^{-1}. Reductions in breakdown strength on the inclusion of a nanofiller have been seen in many studies and have been ascribed to a number of effects, notably nanoparticle agglomeration [21,22]. Alternatively, a reduction in breakdown strength may stem from the existence of adsorbed moisture on the filler used to formulate this system (*i.e.*, NSU), as deduced from the infrared data. The presence of hydroxyl groups on unfunctionalized nanosilica will promote adsorption of water molecules, which has previously been linked to reduced breakdown strength [23,24] and described by Zou's water model [25]. Indeed, the breakdown strength of the system containing the NC0 nanosilica, which has been subjected to both sonication and thorough drying, is increased by some 50 kV$\cdot$mm^{-1} compared with NSU, where neither process was used. Increasing the mass of GLYMO used in the functionalization process results in a further increase in breakdown strength; the highest α value of 268 ± 12 kV$\cdot$mm^{-1} being obtained from the system containing 2 wt % of NC8.

Table 2. Weibull parameters that characterize the breakdown behavior of the unfilled and filled epoxy systems.

Sample	E_b (kV$\cdot$mm^{-1})	β
EPX	182 ± 5	14 ± 4
NCU	173 ± 6	13 ± 5
NC0	238 ± 10	9 ± 3
NC1	242 ± 7	13 ± 4
NC2	257 ± 19	5 ± 1
NC4	258 ± 11	9 ± 2
NC8	268 ± 12	8 ± 2
NC16	265 ± 16	6 ± 2
NC20	244 ± 13	7 ± 4

In view of the effect on breakdown strength of varying the chemical treatment and, by implication, nanoparticle/matrix interactions and resulting interphase regions [26–29], the effect of varying the nanoparticle surface chemistry on molecular dynamics [27–29] was examined thermally (*i.e.*, through DSC) and electrically (*i.e.*, through dielectric spectroscopy).

3.4. The Glass Transition

All of the samples considered in this study exhibit a classical DSC glass transition, namely a singular step-change in heat capacity. The width of the transition, ΔT_g, did not vary systematically with material formulation and always fell in the range 13.3 $\pm$ 1.5 °C; comparable results have been reported elsewhere [18]. Figure 4a shows the effect on T_g of varying the surface chemistry of the nanosilica. From this it is evident that introducing the unfunctionalized nanofiller (NC0) results in a small increase in T_g (0.8 °C), compared with the unfilled epoxy (EPX). Although this variation is less than the uncertainty in these data, a similar increase was reported by Couderc *et al.* [30], who observed a 0.5 °C increase in T_g for the same epoxy system on adding 2.5 wt % of nanosilica. For samples containing functionalized nanosilicas, the mean value of T_g initially decreases before increasing slightly again. Comparing EPX (T_g = 80.7 $\pm$ 2 °C) with NC4 (T_g = 74.2 $\pm$ 2 °C), for example, the difference in T_g between these two systems exceeds the uncertainties in the measurements and therefore, although the error bars overlap when considering any adjacent pair of points in Figure 4a, we suggest that the general trend indicated by the dashed line is real. To test this assertion, the change in the heat capacity, ΔC_p, across the glass transition was determined for all samples and the effect of surface functionalization on this quantity is shown in Figure 4b. Where T_g is high in Figure 4a, generally, ΔC_p is low in Figure 4b; this anti-correlation is consistent with effects seen elsewhere in comparable systems [18], suggesting that the associated variations in T_g are indeed significant. Significant variations in the parameter ΔC_p have been seen in polyurethane-based nanocomposites containing organically modified montmorillonite (MMT), where a monotonic reduction in ΔC_p was seen as the volume of MMT in the system increased (0–5.7 vol %) [31]. This was interpreted in terms of an increasing rigid amorphous fraction, where reduced segmental mobility occurs as a consequence of immobilization within MMT tactoids. A comparable analysis is not possible here, since Figure 4b shows that ΔC_p both increased and decreased relative to the case of the unfilled system. Previously, it has been suggested that suitably modifying the surface chemistry of nanoparticles will restrict the overall mobility of the polymer chains within a nanocomposite, thereby increasing T_g [32–34]; in the case of nanocomposites containing graphitic nanofillers, the observed marked increase in T_g has been associated with a catalytic action of the nanofiller on the epoxy crosslinking reaction [35]. Elsewhere, it has been claimed that a reduction in T_g may be a consequence of poor interactions between the two phases [36]. However, the effects seen in Figure 4 are difficult to rationalize in either way. In the case of anhydride cured resins it has been demonstrated [18] that a change in the stoichiometric ratio of epoxy: anhydride results in a systematic variation in T_g and, since the various nanosilica systems discussed above may be expected to differ with respect to the number of epoxide groups adjacent to the surface, it is pertinent

to consider the extent to which this may influence the overall stoichiometry of the cure reaction. Even taking the extreme case of NS20 and, unreasonably, assuming that all of the added GLYMO became bonded to the nanoparticles, this would only equate to an increase in epoxide content of ~3 mol %. The variations in T_g seen above cannot therefore be explained by gross stoichiometry effects and the invariance in the width of the glass transition indicates that no extensive interphase regions exist where local interactions affect main-chain dynamics.

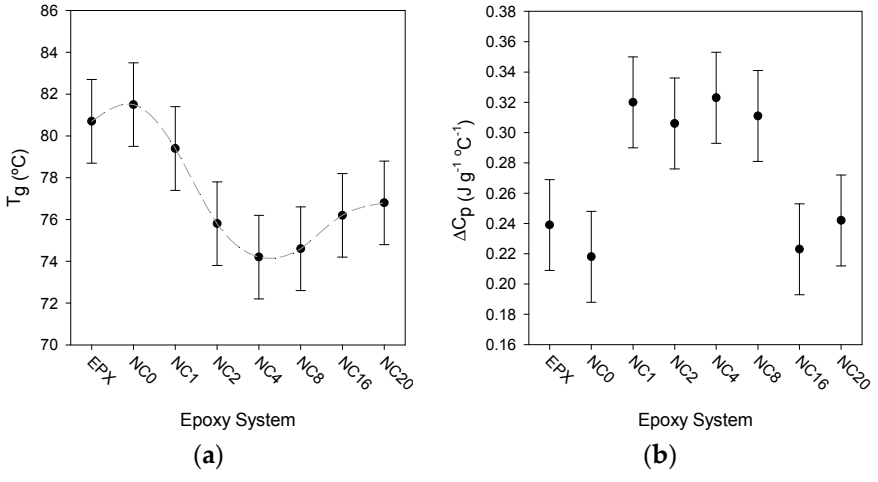

Figure 4. Effect of nanosilica surface chemistry on the observed DSC glass transition: (**a**) variation in the glass transition temperature with material system; and (**b**) variation in the change in the heat capacity, ΔC_p, across the glass transition with material system.

3.5. Dielectric Spectroscopy

Dielectric spectroscopy constitutes a powerful means of probing molecular dynamics in systems such as the nanocomposite samples considered here. Figure 5 presents data obtained from EPX, which reveal features that are typical of an unfilled epoxy [7,9,30]. At temperatures below T_g, a slight reduction in the real part of the relative permittivity, ε_r', can be seen to occur in the frequency range 10^4–10^5 Hz. This is associated with the β relaxation, which has been ascribed to the rotation of the hydroxyether groups [$CH_2CH(OH)CH_2O$] in the backbone that results from crosslinking reactions between the epoxy and the hardener [37]. Being associated with segmental mobility, the β relaxation has been shown to be related to the mechanical yield behavior of network systems [38]. Data collected from the unfilled EPX at 80 °C and above are significantly different due to the glass transition which, in the DSC, is observed at ~80 °C. In the data acquired at 100 °C, the α relaxation is

clearly visible in both the real and imaginary parts of the relative permittivity in the region 100–1000 Hz. Below this frequency range, the imaginary part of the relative permittivity, ε_r'', increases with decreasing frequency and, since $(d\log\varepsilon_r'')/(d\log\omega) \approx -1$, we primarily associate this with a conduction process, presumably, as a consequence of the presence of residual chloride ions in the D.E.R.™ 332 epoxy resin [39]. However, in addition, there is an observable increase in the real part of the relative permittivity below 0.2 Hz, which may be associated with some degree of interfacial polarization, as a consequence of the accumulation of charge carriers at the electrodes [40,41].

Figure 6 shows equivalent dielectric data obtained from NC0, from which it is evident that the introduction of 2 wt % of nanofiller has a marked effect on the dielectric response. At temperatures below the DSC T_g, the β relaxation is still evident, particularly in the 20 °C trace but, otherwise, the value of the real permittivity is increased at all frequencies and at all temperatures. This effect is particularly evident below 10 Hz. Although such effects are not uncommon when adding an inorganic filler to a polymer, in the case of a system based upon 2 wt % of silica (silica real relative permittivity ~3.9 [42]) in an epoxy (epoxy real relative permittivity ~4.0 from Figure 5a), simple effective medium approaches would not predict such a result. As such, this increase in ε_r' would appear to be a consequence of the presence of nanoparticle/matrix interfaces. At temperatures below T_g, (T_g = 82 °C in this system from DSC) the imaginary permittivity data contain a relaxation peak that moves from ~10^{-1} Hz at 20 °C to ~10 Hz at 60 °C; since no equivalent feature can be seen in Figure 5b, we suggest that this is again a direct consequence of introducing the nanoparticles. Indeed, Couderc *et al.* [30] have described an α′ relaxation that they associated with adsorbed water molecules at the interface between the silica and the epoxy, which is also consistent with the increase in the magnitude of ε_r' described above. Although NC0 was thoroughly dried prior to these measurements, this suggests that some residual bound water remains. At temperatures above the DSC T_g, the additional internal boundaries between the nanofiller and the matrix lead to a pronounced low frequency polarization effect, which manifests itself as a steep increase in the real part of the relative permittivity below ~1 Hz at 100 °C. As in the case of the unfilled sample, the imaginary part of the relative permittivity increases markedly once the temperature approaches T_g and, at 100 °C, the low frequency variation of this quantity is close to $(d\log\varepsilon_r'')/(d\log\omega) = -1$, indicating that conduction processes within the epoxy matrix are again important.

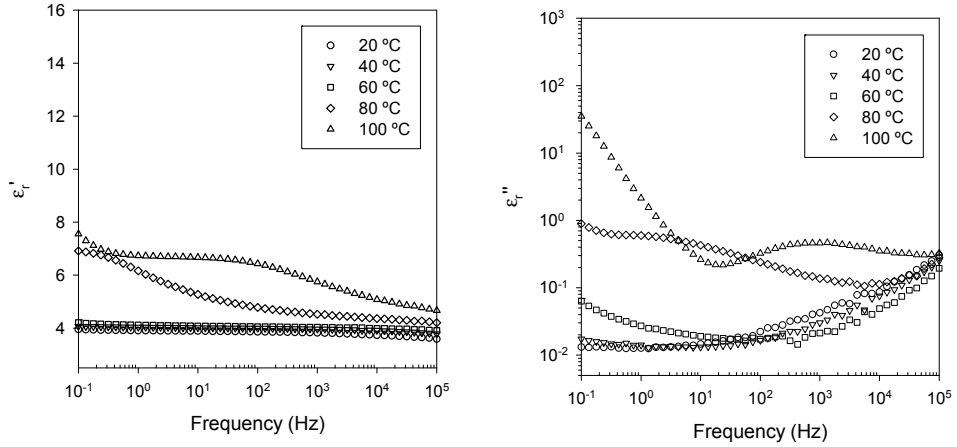

Figure 5. Dielectric data acquired from the unfilled epoxy (EPX): (**a**) real part of the relative permittivity; and (**b**) imaginary part of the relative permittivity.

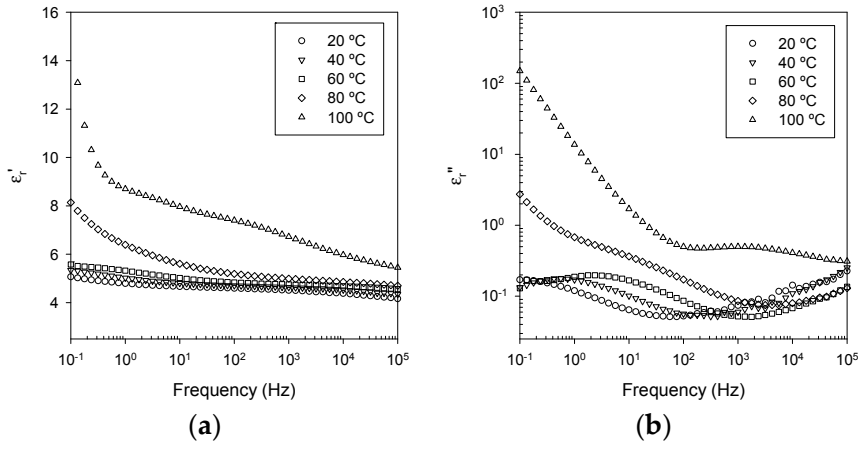

Figure 6. Dielectric data acquired from NC0, containing untreated nanosilica (NS0): (**a**) real part of the relative permittivity; and (**b**) imaginary part of the relative permittivity.

In summary, the data discussed above can be interpreted in terms of three major processes, in addition to the glass transition:

1. Ionic conduction, which becomes significant in all systems at temperatures above the DSC T_g.

2. Nanoparticle/matrix interfacial relaxation effects, that: (a) manifest themselves as an α' relaxation peak in the imaginary permittivity; and (b) underlie the overall increase in ε_r' seen in the nanocomposite.
3. Maxwell Wagner low frequency interfacial polarization at temperatures above the DSC T_g, which appears as a marked increase in the real part of the permittivity at frequencies <1 Hz at high temperatures (*i.e.*, 100 °C in this work).

To demonstrate the effect of surface chemistry on these features, spectra acquired from four different material formulations are compared, for the sake of brevity, at just 60 °C (*i.e.*, ~20 °C below the DSC T_g) and at 100 °C (*i.e.*, ~20 °C above the DSC T_g) in Figures 7 and 8 respectively. From Figure 7, it is evident that below the DSC T_g, surface functionalization has a pronounced effect on both the real and imaginary parts of the relative permittivity. In the case of ε_r' (see Figure 7a), increasing the degree of functionalization progressively reduces this parameter until, in the case of NC16, its value is below that of the unfilled epoxy. The effect of filler loading level on the permittivity of nanocomposites has been considered by many workers and, in some cases, it has been reported that the addition of a low volume fraction of a high permittivity nanofiller can result in a reduction in the real relative permittivity [43,44]. While it is commonly proposed that the origin of this effect is related in some way to the existence of nanoparticle/matrix interactions, this assertion has not been fully justified. In this case, a supplementary factor can also be introduced, namely the availability of polar interfacial sites that are available for hydrogen bonding with water. If the overall increase in ε_r' and the α' relaxation are indeed associated with adsorbed water molecules at the epoxy/silica interface then, presumably, reacting the hydroxyl groups on NC0 with increasing quantities of silane will reduce the sites available to bind water, in addition to modifying the local molecular structure. Indeed, from the imaginary relative permittivity data shown in Figure 7b, it is evident that the α' relaxation is much less apparent in all the GLYMO-treated systems, which reinforces this general concept. To conclude, the data shown in Figure 7 demonstrate that the overall dielectric response of a nanocomposite is determined not just by the components and the composition, but also by the nanoparticle surface chemistry and the consequent way in which the components interact. Specifically, the degree of polar character seems to be of considerable importance and not just in terms of matrix compatibility.

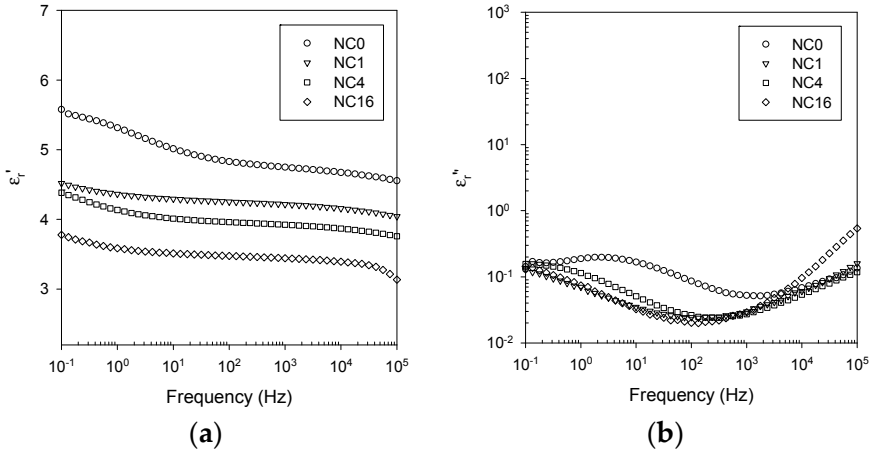

Figure 7. Dielectric data obtained at 60 °C comparing the response of nanocomposites NC0, NC1, NC4 and NC16: (**a**) real part of the relative permittivity; and (**b**) imaginary part of the relative permittivity.

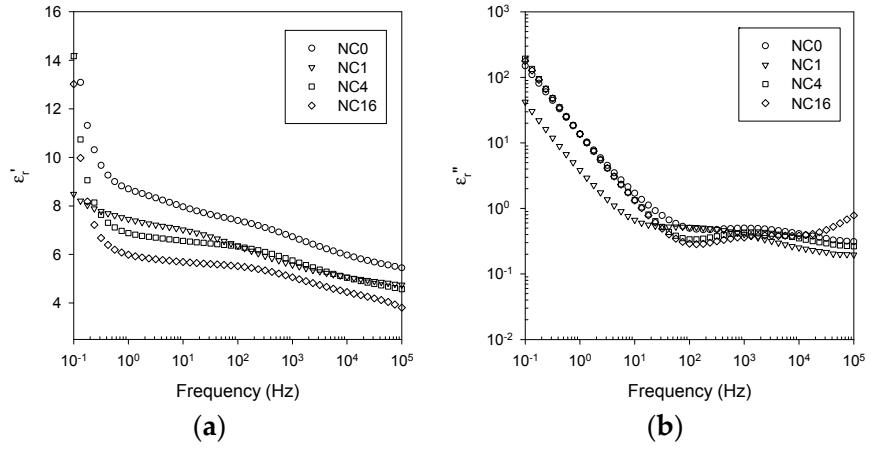

Figure 8. Dielectric data obtained at 100 °C comparing the response of nanocomposites NC0, NC1, NC4 and NC16: (**a**) real part of the relative permittivity; and (**b**) imaginary part of the relative permittivity.

Figure 8 shows dielectric data acquired at 100 °C from the same samples previously shown in Figure 7. The spectra recorded at 100 °C are, however, significantly different from those collected at 60 °C, being dominated by conductivity and polarization effects, particularly at frequencies below 10^2 Hz. Nevertheless, the magnitude of the real part of the relative permittivity again falls progressively with

increasing surface functionalization, such that ε_r' is again less in NC16 than in the unfilled EPX.

To permit further analysis, all data supporting this study are openly available from the University of Southampton repository at http://dx.doi.org/10.5258/SOTON/385542.

4. Discussion

A key paradigm that underpins the nanodielectric concept is that macroscopic properties are strongly affected by the presence of interphase regions, since: (a) the interphase constitutes a significant volume fraction of the system as a result of the high specific surface area of nanoparticles; and (b) that this fraction of the system is characterized by properties that are different from the bulk—perturbed molecular dynamics is commonly proposed [27–29]. The dielectric results presented above provide evidence of clear differences between the unfilled epoxy resin and those materials that contain nanosilica, which we ascribe to interfacial effects, in line with published work. Notably, the nanofilled systems all exhibit an α'-relaxation, which is strongly affected by the GLYMO treatment. While the DSC data demonstrate that the addition of nanosilica affects the glass transition and that the nature of this is dependent upon the nanofiller surface chemistry, the invariance of the width of the glass transition implies that the addition of nanoparticles does not, however, result in the development of a distinct interphase that differs significantly from the unperturbed matrix in terms of main-chain dynamics. In the case of controlled pore glasses, where interfacial interactions and confinement effects have been studied in detail, complex forms of behavior have been reported, which include two glass transitions, one below and one above the T_g measured for the equivalent bulk system [31] and a retardation and broadening of the glass transition [45]. In nanofilled polymers, Tsagaropoulos and Eisenberg [46] and Arrighi [47], for example, have both reported the existence of twin glass transitions, one corresponding to that of the unperturbed polymer and one related to polymer chains where interactions with the nanofiller result in reduced mobility. To rationalize the dielectric and DSC data, we suggest that the addition of the nanosilica affects the epoxy matrix in two ways, which can broadly be thought of in terms of the local behavior of small dipolar species and gross main-chain dynamics. For example, the data shown in Figure 7a equate to a progressive reduction in the polarizability of the system in going from NC0 to NC16 at a temperature below the DSC T_g, where variations in the α' relaxation are also apparent. We ascribe both of these effects to polar species at nanoparticle interfaces. Conversely, the glass transition, as revealed by DSC, implies that the whole of the matrix is being affected somewhat by the addition of the nanoparticles; this global effect does not, however, markedly influence the polarizability of the system (*i.e.*, ε_r') under conditions (temperature/frequency) where main chain mobility is negligible.

In many electrical applications, dielectric breakdown strength is an important technological parameter and, therefore, the effect of nanoparticles on this has attracted considerable attention. Andritsch *et al.* [48], for example, considered the effect of particle size on the breakdown strength of an epoxy resin containing hexagonal boron nitride and reported a monotonic increase in strength as the filler size was reduced at the constant loading level of 10 wt %. However, the effect of nano-structuring on breakdown is not always beneficial. In a recent study, the effect of surface chemistry on the AC breakdown strength of nanocomposites based upon nanosilica and a polyethylene blend has been described [49], in which this parameter was found to be independent of nanofiller loading level up to the point where nanofiller agglomeration became significant (5–10 wt % in the case of unfunctionalized nanosilica; >10% in the case of propyl-functionalized nanosilica), whereupon, inferior performance resulted. A similar dependence of breakdown strength on nanofiller loading level was also reported by Nguyen *et al.* [18] for epoxy/silica systems although, in this case, agglomeration of the nanofiller did not appear to be a significant factor. In the chemically treated and dried systems considered here, E_b increases for samples NC1 to NC8, before decreasing somewhat for more highly functionalized samples. Although changing the surface chemistry of the nanosilica does appear to have some effect on the dispersion state of the nanofiller, the SEM data indicate that this is relatively minor. That is, the pronounced improvement in breakdown strength that is evident in all functionalized systems is not related to improved dispersion. Indeed, in all the systems considered here, the nanoparticles are far from ideally dispersed and much more agglomerated than in the work of Nguyen *et al.* [18] where, despite the lack of agglomerated nanosilica, no significant increase in breakdown strength was seen.

The addition of epoxide functionality to a nanoparticle surface, as imposed here, may affect macroscopic properties in many ways. Covalent bonds will be formed with the curing resin, which will change the nature of the nanoparticle/matrix interface—mechanical integrity will be increased, for example [50]. In addition, electrically, the local density of states will change, thereby affecting charge transport through the system [41,51]. The process of functionalization additionally results in the replacement of hydroxyl surface groups with organic moieties, which can reduce adsorption of water molecules at nanoparticle surfaces [20]; adsorbed water has detrimental consequences. However, the silane will react with both the nanosilica surface and itself, such that residual silanol groups and epoxide functionality may be retained within the surface layer. It would appear that if this is too extensive, then the breakdown response becomes degraded.

In summary, the nature of the interactions that occur between nanoparticles and a matrix polymer are subtle and can manifest themselves in forms of behavior that can appear complex or even anomalous. In the study reported here, the consequence

is an improvement in breakdown strength approaching 50% when the nanosilica was suitably functionalized. Since this cannot be related to nanoparticle dispersion effects and the DSC data provide no evidence of distinct interphase structures, we suggest that the origin of this improved performance is related to changes in interface characteristics and, in the absence of evidence for any major changes in the local structure, we suggest that variations in local trapping states/charge transport dynamics constitute a more likely explanation for the pronounced increase in breakdown strength reported.

5. Conclusions

A range of nanosilicas has been produced in which the surface chemistry has been systematically varied. The efficacy of the chosen organosilane chemistry has been demonstrated both by combustion analysis and FTIR spectroscopy. SEM examination of fracture surfaces indicates that the reaction of the nanosilica with increasing amounts of (3-glycidyloxypropyl)trimethoxysilane results in some improvement in nanoparticle dispersion, presumable, as a result of the presence of the introduced epoxy functionality. Nevertheless, in all cases, significant agglomerates remain and the systems described are, from a structural perspective, considerably less ideal than those that have been reported elsewhere [18]. However, despite this, significantly increased breakdown strength values have nevertheless been observed; this cannot be related to nanoparticle dispersion effects. In the absence of any direct evidence for distinct interphase regions between the nanosilica and the matrix polymer, which have been reported to result in multiple/broadened glass transitions, we suggest that the property enhancements we see stem from changes in the local chemistry, which result in changes in the local density of charge trapping sites and affect charge transport dynamics through the system. In particular, the substitution of hydroxyl surface character with organic moieties will markedly affect adsorption of water molecules onto nanoparticle surfaces, which manifests itself in the so-called dielectric α' relaxation. However, the use of excess silane results in residual silanol groups (*i.e.*, polar groups) being incorporated into the organic-rich surface layer, which has negative consequences for macroscopic electrical properties, even if it leads to marginally improved nanoparticle dispersion.

Acknowledgments: Celia Yeung acknowledges the receipt of an Engineering and Physical Sciences Research Council Ph.D. studentship. No funds were received to cover the costs of publishing in open access.

Author Contributions: Alun S. Vaughan conceived the experiments; Celia Yeung designed and performed the experiments; and Alun S. Vaughan and Celia Yeung analyzed the data and wrote the paper.

Conflicts of Interest: The authors declare no conflict of interest.

Abbreviations

The following abbreviations are used in this manuscript:

GLYMO	(3-glycidyloxypropyl)trimethoxysilane
FTIR	Fourier transform infrared
SEM	scanning electron microscope
DSC	differential scanning calorimeter

References

1. Greco, A.; Corcione, C.E.; Maffezzoli, A. Effect of multi-scale diffusion on the permeability behaviour of intercalated nanocomposites. *J. Membr. Sci.* **2016**, *505*, 92–99.
2. Corcione, C.E.; Maffezzoli, A. Transport properties of graphite/epoxy composites: Thermal, permeability and dielectric characterization. *Polym. Test.* **2013**, *32*, 880–888.
3. Lewis, T.J. Nanometric dielectrics. *IEEE Trans. Dielectr. Electr. Insul.* **1994**, *5*, 812–825.
4. Henk, P.O.; Korsten, T.W.; Kvarts, T. Increasing the electrical discharge endurance of acid anhydride cured DGEBA epoxy resin by dispersion of nanoparticle silica. *High Perform Polym.* **1999**, *11*, 281–296.
5. Kozako, M.; Fuse, N.; Ohki, Y.; Okamoto, T.; Tanaka, T. Surface degradation of polyamide nanocomposites caused by partial discharges using IEC(b) electrodes. *IEEE Trans. Dielectr. Electr. Insul.* **2004**, *5*, 833–839.
6. Fuse, N.; Kozako, M.; Tanaka, T.; Murase, S.; Ohki, Y. Possible mechanisms and superior partial discharge resistance of polyamide nanocomposites. In Proceedings of the Annual Report Conference on Electrical Insulation and Dielectric Phenomena, Boulder, CO, USA, 17–20 October 2004; IEEE: Piscataway, NJ, USA, 2004; pp. 322–325.
7. Andritch, T. Epoxy Based Nanocomposite for High Voltage DC Applications. Ph.D. Thesis, Delft University of Technology, Delft, The Netherlands, 2010.
8. Wang, Z.; Iizuka, T.; Kozako, M.; Ohki, Y.; Tanaka, T. Development of epoxy/BN composites with high thermal conductivity and sufficient dielectric breakdown strength part I—Sample preparations and thermal conductivity. *IEEE Trans. Dielectr. Electr. Insul.* **2001**, *18*, 1963–1972.
9. Kochetov, R. Thermal and Electrical Properties of Nanocomposites, Including Nanomaterial Processing. Ph.D. Thesis, Delft University of Technology, Delft, The Netherlands, 2012.
10. Vassileva, E.; Friedrich, K. Epoxy/alumina nanoparticle composites. I. Dynamic mechanical behaviour. *J. Appl. Polym. Sci.* **2003**, *89*, 3774–3785.
11. Guo, Y.; Wang, M.; Zhang, H.; Liu, G.; Zhang, L.; Qu, X. The surface modification of nanosilica, preparation of nanosilica/acrylic core-shell composite latex, and its application in toughening PVC matrix. *J. Appl. Polym. Sci.* **2008**, *107*, 2671–2680.
12. Chen, S.; You, B.; Zhou, S.; Wu, L. Preparation and characterisation of scratch and mar resistant waterborne epoxy/silica nanocomposite clearcoat. *J. Appl. Polym. Sci.* **2009**, *112*, 3634–3639.

13. Ash, B.; Schadler, L.; Siegel, R. Glass transition behaviour of alumina/ polymethylmethacrylate nanocomposites. *Mater. Lett.* **2002**, *55*, 83–87.
14. Gelest Inc. Silane Coupling Agents. 2006. Available online: http://www.gelest.com/ goods/pdf/ couplingagents.pdf (accessed on 30 December 2015).
15. Chen, H.; Zou, S.; Gu, G.; Wu, L. Modification and dispersion of nanosilica. *J. Dispers. Sci. Technol.* **2005**, *25*, 837–848.
16. Rahimi, A.; Gharazi, S.; Ershad-Langroudi, A.; Ghasemi, D. Synthesis and characterization of hydrophilic nanocomposite coating on glass substrate. *J. Appl. Polym. Sci.* **2006**, *102*, 5322–5329.
17. Witucki, G.L. A silane primer: Chemistry and applications of alkoxy silanes. *J. Coat. Technol.* **1993**, *65*, 57–60.
18. Nguyen, V.T.; Vaughan, A.S.; Lewin, P.L.; Krivda, A. The effect of resin stoichiometry and nanoparticle addition on epoxy/silica nanodielectrics. *IEEE Trans. Dielectr. Electr. Insul.* **2015**, *22*, 895–905.
19. Lange, F.F.; Radford, K.C. Fracture energy of an epoxy composite system. *J. Mater. Sci.* **1971**, *6*, 1197–1203.
20. Lau, K.Y.; Vaughan, A.S.; Chen, G.; Hosier, I.L.; Holt, A.F. On the dielectric response of silica-based polyethylene nanocomposites. *J. Phys. D Appl. Phys.* **2013**, *46*, 1–9.
21. Singha, S.; Thomas, M.J. Dielectric properties of epoxy nanocomposites. *IEEE Trans. Dielectr. Electr. Insul.* **2008**, *15*, 12–23.
22. Vaughan, A.S.; Swingler, S.G.; Zhang, Y. Polyethylene nanodielectrics: The influence of nanoclays on structure formation and dielectric breakdown. *IEEJ Trans.* **2006**, *126*, 1057–1063.
23. Fabiani, D.; Montanari, G.C.; Testa, L.; Schifani, R.; Guastavino, F.; Bellucci, F.; Deorsola, F. Effect of water adsorption on the dielectric properties of polymer nanocomposites. In Proceedings of the Conference Record of the 2008 IEEE International Symposium on Electrical Insulating Materials, Vancouver, BC, Canada, 9–12 June 2008; IEEE: Piscataway, NJ, USA, 2008; pp. 510–513.
24. Hui, L.; Nelson, J.K.; Schadler, L.S. The influence of moisture on the electrical performance of XLPE/silica nanocomposites. In Proceedings of the 10th IEEE International Conference on Solid Dielectrics, Potsdam, Germany, 4–9 July 2010; IEEE: Piscataway, NJ, USA, 2010.
25. Zou, C.; Fothergill, J.C.; Rowe, S.W. A "water shell" model for the dielectric properties of hydrated silica-filled epoxy nano-composites. In Proceedings of the 9th IEEE International Conference on Solid Dielectrics, Winchester, UK, 8–13 July 2007; IEEE: Piscataway, NJ, USA, 2007; pp. 389–392.
26. Lewis, T.J. Interfaces are the dominant feature of dielectrics at the nanometric level. *IEEE Trans. Dielectr. Electr. Insul.* **2004**, *11*, 739–753.
27. Tanaka, T.; Kozako, M.; Fuse, N.; Ohki, Y. Proposal of a multi-core model for polymer nanocomposite dielectrics. *IEEE Trans. Dielectr. Electr. Insul.* **2005**, *12*, 669–681.
28. Arantes, T.M.; Leão, K.V.; Tavares, M.I.B.; Ferreira, A.G.; Longo, E.; Camargo, E.R. NMR study of styrene-butadiene rubber (SBR) and TiO_2 nanocomposites. *Polym. Test.* **2009**, *28*, 490–494.

29. Miwa, Y.; Drews, A.R.; Schlick, S. Detection of the direct effect of clay on polymer dynamics: The case of spin-labeled poly(methyl acrylate)/clay nanocomposites studied by ESR, XRD, and DSC. *Macromolecules* **2006**, *39*, 3304–3311.
30. Couderc, H.; Frechette, M.F.; Savoie, S.; Reading, M.; Vaughan, A.S. Dielectric and thermal properties of boron nitride and silica epoxy composites. In Proceedings of the Conference Record of the 2012 IEEE International Symposium on Electrical Insulating Materials, San Juan, Puerto Rico, 10–13 June 2012; IEEE: Piscataway, NJ, USA, 2012; pp. 64–68.
31. Corcione, C.E.; Maffezzoli, A. Glass transition in thermosetting clay-nanocomposite polyurethanes. *Thermochim. Acta* **2009**, *485*, 43–48.
32. Shang, X.Y.; Zhu, Z.K.; Yin, J.; Ma, X.D. Compatibility of soluble polyimide/silica hybrids induced by a coupling agent. *Chem. Mater.* **2002**, *14*, 1–77.
33. Kang, S.; Hong, S.; Choe, C. Compatibility of soluble polyimide/silica hybrids induced by a coupling agent. *Polymer* **2001**, *42*, 879–887.
34. Park, J.Y.; McKenna, G.B. Size and confinement effects on the glass transition behaviour of polystyrene/*o*-terphenyl polymer solutions. *Phys. Rev. B* **1999**, *61*, 6667–6676.
35. Mauro, M.; Acocella, M.R.; Corcione, C.E.; Maffezzoli, A.; Guerra, G. Catalytic activity of graphite-based nanofillers on cure reaction of epoxy resins. *Polymer* **2014**, *55*, 5612–5615.
36. Preghenella, M.; Pegoretti, A.; Miglairesi, C. Thermo-mechanical characterisation of fumed silica-epoxy nanocomposites. *Polymer* **2005**, *46*, 12065–12072.
37. Kosmidou, T.V.; Vatalis, A.S.; Delides, C.G.; Logakis, E.; Pissis, P.; Papanicolaou, G.C. Structural, mechanical and electrical characterization of epoxy-amine/carbon black nanocomposites. *Express Polym. Lett.* **2012**, *2*, 364–372.
38. Rana, D.; Sauvant, V.; Halary, J.L. Molecular analysis of yielding in pure and antiplasticized epoxy-amine thermosets. *J. Mater. Sci.* **2002**, *37*, 5267–5274.
39. Hammerton, I. *Recent Developments in Epoxy Resins (Rapra Review Reports)*; Smithers Rapra Technology: Shrewsbury, UK, 1997.
40. Schönhals, A.; Kremer, F. Analysis of dielectric spectra. In *Broadband Dielectric Spectroscopy*; Kremer, F., Schönhals, A., Eds.; Springer-Verlag: Berlin, Germany; Heidelberg, Germany, 2003; pp. 59–98.
41. Nelson, J.K. *Dielectric Polymer Nanocomposites*; Springer US: New York, NY, USA, 2010.
42. Kasprazak, W.; Nadolny, Z.; Walczak, K.; Siodla, K.; Sikorski, W.; Kozwiak, K.; Pasciak, D.; Moron, L. The influence of barium titanate as a filler in impregnating epoxy resin on chosen electrical parameters of obtained material. *Mater. Sci.* **2009**, *27*, 1219–1227.
43. Wang, Q.; Chen, G. Effect of nanofillers on the dielectric properties of epoxy nanocomposites. *IEEE Trans. Dielectr. Electr. Insul.* **2014**, *21*, 1809–1816.
44. Singha, S.; Thomas, M.J. Permittivity and tan delta characteristics of epoxy nanocomposites in the frequency range of 1 MHz-1 GHz. *IEEE Trans. Dielectr. Electr. Insul.* **2008**, *15*, 2–11.
45. Schüller, J.; Melnichenko, Y.B.; Yu, B.; Richert, R.; Ficher, E.W. Dielectric studies of the glass transition in porous media. *Phys. Rev. Lett.* **1994**, *73*, 2224–2227.

46. Tsagaropoulos, G.; Eisenberg, A. Dynamic mechanical study of the factors affecting the two glass transition behaviour of filled polymers: Similarities and differences with random ionomers. *Macromolecules* **1995**, *28*, 6067–6077.
47. Arrighi, V.; McEwen, I.J.; Qian, H.; Serrano Prieto, M.B. The glass transition and interfacial layer in styrene-butadiene rubber containing silica nanofiller. *Polymer* **2003**, *44*, 6259–6266.
48. Andritsch, T.; Kochetov, R.; Gebrekiros, Y.T.; Morshuis, P.H.F.; Smit, J.J. Short term DC breakdown strength in epoxy based BN nano- and microcomposites. In Proceedings of the 10th IEEE International Conference on Solid Dielectrics, Potsdam, Germany, 4–9 July 2010; IEEE: Piscataway, NJ, USA, 2010.
49. Lau, K.Y.; Vaughan, A.S.; Chen, G.; Hosier, I.L. Polyethylene nanodielectrics: The effect of nanosilica and its surface treatment on electrical breakdown strength. In Proceedings of the Annual Report Conference on Electrical Insulation and Dielectric Phenomena, Montreal, QC, Canada, 14–17 October 2012; IEEE: Piscataway, NJ, USA, 2012; pp. 21–24.
50. Choi, Y.Y.; Lee, S.H.; Ryu, S.H. Effect of silane functionalization of montmorillonite on epoxy/ montmorillonite nanocomposite. *Polym. Bull.* **2009**, *63*, 47–55.
51. Geng, Y.; Liu, M.Y.; Li, J.; Shi, X.M.; Kim, J.K. Effects of surface treatment on mechanical and electrical properties of CNT/epoxy nanocomposites. *Compos. A* **2008**, *39*, 1876–1863.

Charge Transport in LDPE Nanocomposites Part I—Experimental Approach

Anh T. Hoang, Love Pallon, Dongming Liu, Yuriy V. Serdyuk, Stanislaw M. Gubanski and Ulf W. Gedde

Abstract: This work presents results of bulk conductivity and surface potential decay measurements on low-density polyethylene and its nanocomposites filled with uncoated MgO and Al_2O_3, with the aim to highlight the effect of the nanofillers on charge transport processes. Material samples at various filler contents, up to 9 wt %, were prepared in the form of thin films. The performed measurements show a significant impact of the nanofillers on reduction of material's direct current (dc) conductivity. The investigations thus focused on the nanocomposites having the lowest dc conductivity. Various mechanisms of charge generation and transport in solids, including space charge limited current, Poole-Frenkel effect and Schottky injection, were utilized for examining the experimental results. The mobilities of charge carriers were deduced from the measured surface potential decay characteristics and were found to be at least two times lower for the nanocomposites. The temperature dependencies of the mobilities were compared for different materials.

Reprinted from *Polymers*. Cite as: Hoang, A.T.; Pallon, L.; Liu, D.; Serdyuk, Y.V.; Gubanski, S.M.; Gedde, U.W. Charge Transport in LDPE Nanocomposites Part I—Experimental Approach. *Polymers* **2016**, *8*, 87.

1. Introduction

Polyethylene (PE) has been widely used as cable insulation material thanks to its low electrical conductivity. Despite the successful application of this material for high voltage alternating current (HVAC) cables, a number of challenges has been encountered in its use in high voltage direct current (HVDC) counterparts [1]. Unlike the case of ac stress, the electric field distribution under dc stress is governed by material's dc conductivity. This parameter is dependent on both electric field and temperature. As cable insulation usually operates at a temperature gradient, electric field distribution inside the insulation bulk is a complex function of material properties and radial position [2]. Space charge accumulation and, hence, local field enhancements are usually observed inside HVDC insulation, which may stimulate accelerated ageing process [3].

The forecasted growth in worldwide demand for electrical power energy and the requirement of longer transmission distances are the incentives for designing extruded HVDC cables that should reliably work at high rated voltage, e.g., up

to 1 megavolt (MV), and have high power transmission capability, up to several gigawatts (GW). For such HVDC cables, the problem of field enhancement and space charge accumulation must be effectively solved and the most important requirement should be an extremely low dc conductivity of its insulation. A promising approach for dealing with this task is the application of nanotechnology, which allows for creating new materials with superior properties by adding a small amount of nanoparticles [4]. In case of insulation for HVDC cables, even though the semi-crystallized PE can be considered itself as a natural nanometric dielectric [5], the introduction of nanoparticles brings about a variety of advantages. In particular, significant reduction in dc conductivity, negligible space charge accumulation in the bulk as well as an increased dielectric strength have been observed in PE nanocomposites in comparison to unfilled counterpart [6–10]. The improvements in properties of nanomaterials have been attributed to the formation of interfacial regions between nanofillers and base polymer which are characterized by enormously high ratio of surface area to volume [6,11].

Although many investigations on PE nanocomposites have been reported recently, the transport of charge carriers contributing to their dc conductivity is not fully understood yet. In this context, a model describing transport of charge carriers in PE with and without nanofillers is highly desirable for analyzing the role of nanofillers in conduction processes. To formulate such a model, consistent input parameters need to be provided, in particular, mobilities of charge carriers in the materials. The latter have been studied extensively for pure PE for which it has been found to be dependent on both electric field and temperature [12–15], while information is very limited in case of PE-based nanocomposites.

In the present investigation, we attempt to address several aspects in the above defined gap of knowledge. Both experimental and simulation techniques are utilized and the obtained results are reported in two articles. In the first one here, we present measured charging currents and surface potential decay (SPD) characteristics obtained at various temperatures on two types of low-density polyethylene (LDPE) nanocomposites as well as on unfilled material. The most important parameters governing the conduction processes in the materials are deduced, namely the mobilities of charge carriers and energy distributions of traps. In the second paper, a model of charge transport is developed for LDPE with and without nanofillers. Materials' parameters attained from the measured data are used as input for the model whereas the measured current characteristics are utilized for validation of the simulated results.

2. Materials and Methods

2.1. Samples

Nanocomposites were manufactured using two types of uncoated metal-oxide nanofillers, namely alumina (Al_2O_3) and magnesia (MgO). The Al_2O_3 particles had spherical shape with an average diameter of 40 nm, whereas the MgO nanoparticles were in rounded hexagonal shape with an average size of 66 nm and a thickness of 10–20 nm. The nanoparticles used are characterized by narrow size distributions and high purity [16,17]. For preparing nanocomposites, a certain amount of nanoparticles and Irganox 1076 (used as antioxidant) were dispersed in heptane solvent and the suspension was added into LDPE powder. The obtained mixture was then shaken for 1 h and dried in an oven at 80 °C to evaporate all the solvent. Finally, the dry mixture powder was compounded by thermal extrusion at 150 °C in 6 min. The obtained materials were later on pressed to form 80 μm thick films that have square shape with a side of 65 mm. The prepared samples were then kept in a desiccator for preventing the intake of moisture from laboratory air.

To study the influence of filler content on material properties, two nanocomposites filled with Al_2O_3 at 1 and 3 wt % as well as five types of MgO-filled materials with filler content of 0.1, 1, 3, 6, and 9 wt % were prepared. All the materials contained the antioxidant at 0.02 wt % for avoiding degradation by oxidation. Both nanofillers are evenly distributed in LDPE matrix, as presented in [16] for LDPE/Al_2O_3. In case of LDPE/MgO at high filler contents (6 and 9 wt %), clustered and agglomerated particles were observed. While the clusters only consist of a couple of nanoparticles and are less than a micrometer in cross-section, the agglomerates can be several micrometers large and built up of thousands of nanoparticles. Detailed information on the particle distance and the degree and size of agglomerates is presented in a separate publication [17].

2.2. Conductivity Measurements

Measurements of dc conductivity were carried out at applied electrical field of ~30 kV/mm. The test setup is shown in Figure 1. The dc test voltage was generated by a Glassman power supply (model FJ60R2) and the current was measured using an electrometer Keithley 6517A (Tektronix Inc., Beaverton, OR, USA). The experiments followed a standard procedure [18] by using a three-electrode system, of which the high voltage electrode was a stainless steel cylinder with a diameter of 45 mm, the current measuring electrode was 30 mm in diameter, whereas the guard ring allowed for eliminating surface currents. A good contact of the high voltage electrode to the sample was provided by placing between them a layer of conducting silicon rubber (SIR) (Elastosil 570/70 from Wacker Chemie AG, Munich, Germany; dc conductivity

of 28 S/m). The use of the SIR electrode in the measurements resembles the operating conditions of cable insulation that is always in contact with a semiconducting layer.

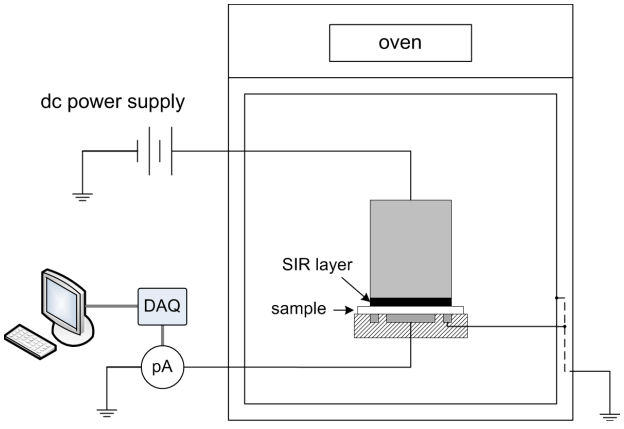

Figure 1. Schematic illustration of the test setup for conductivity measurements. DAQ, denotes data acquisition card and pA, picoammeter.

The measurements were conducted at isothermal conditions (room temperature ~20–22 °C, 40 °C, and 60 °C). The latter two temperature levels were reached by placing the electrode system with inserted sample inside an oven. In this case, the metallic walls of the oven were grounded constituting a shielding box for avoiding electromagnetic disturbances. Thermal equilibrium at a predefined elevated temperature was attained by keeping the setup inside the oven for ~2 h prior to each test. Thereafter, a dc voltage of 2.6 kV was applied to the high voltage electrode for 4×10^4 s (*i.e.*, ~11 h) and the current was recorded. Each test was repeated 2–3 times for checking the reproducibility of the results. The measured data were collected and stored in a personal computer via a data acquisition card (DAQ).

2.3. SPD Measurements

The experimental setup for SPD measurements is schematically illustrated in Figure 2. During the experiment one side of the film samples remains in contact with a grounded copper plate, while the other side is initially exposed to corona charging in air for 10 s. The corona is generated in a triode electrode system [19], which consists of a needle and a grid electrodes connected to dc voltage sources. The use of the grid electrode allows for improving uniformity of the deposited charges as well as for controlling the level of surface potential on the charged surface. The magnitude of the voltage applied to the grid was selected so that the initial electric field induced in the samples by the deposited charges was close to the electric field applied during the conductivity measurements. The potential induced by deposited surface charges

was measured by means of a non-contact technique [20] using a Kelvin probe placed above the sample surface. The probe was connected to an electrostatic voltmeter (Trek model 347B). The positions of the corona triode and the probe were controlled by a positioning system. Surface potential was continuously monitored at the center of the sample and potential distribution was regularly checked by scanning the surface through the center position. The data were stored for further analyses by using LabVIEW software (National Instruments, Austin, TX, USA).

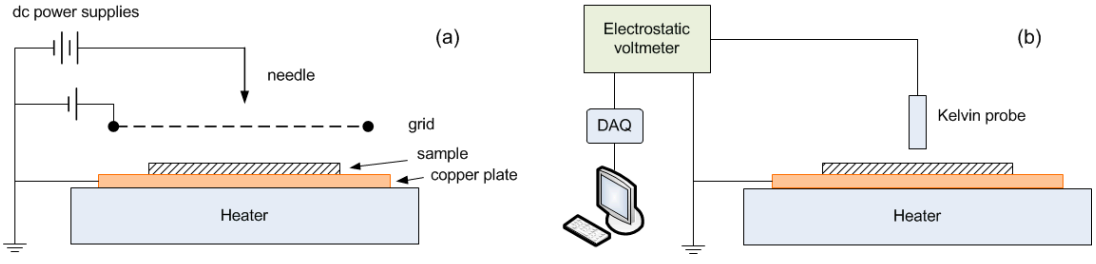

Figure 2. Schematic illustration of the setup for corona charging (**a**); and surface potential decay measurements (**b**).

The SPD measurements were conducted for two nanocomposites filled with 3 wt % of nanoparticles as well as on the reference material at three temperatures, as for the conductivity measurements. The sample heating was realized by means of a hot plate on which the grounded copper plate rested. Prior to each test at elevated temperatures, the sample was preconditioned at a targeted temperature for ~4 h, thus assuring that homogeneous temperature distribution is achieved in the tested thin film.

The SPD measurements were also conducted on multilayered sample structures. For this, three specimen configurations were used (NC/NC, Ref/NC(G), NC/Ref(G)), as illustrated in Figure 3. The initial electric field induced inside the insulation was kept at the same level as for the measurements on single-layered samples by increasing the voltage applied to the grid electrode. Since surface potential exceeding 3 kV should be detected, a Trek electrostatic voltmeter model 341B was utilized which allowed for measurements up to 20 kV. The tests were conducted at room temperature only by following the same experimental procedure as described earlier. Each SPD measurement was performed 2–3 times for checking the repeatability of the results.

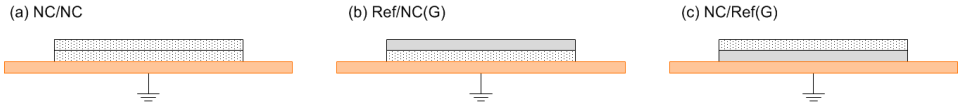

Figure 3. Multilayered sample structures used in SPD measurements: (**a**) NC/NC; (**b**) Ref/NC(G); and (**c**) NC/Ref(G). Ref and NC denote respectively the reference LDPE and LDPE/Al_2O_3 3 wt % nanocomposite whereas index (G) indicates the layer in contact with the grounded copper plate during the test.

3. Results and Discussion

3.1. Material DC Conductivity

Preliminary measurements showed that the addition of a small amount (0.02 wt %) of antioxidant into LDPE did not cause noticeable variation in material dc conductivity. LDPE doped with antioxidant is therefore utilized as a reference material throughout this study.

Figure 4 illustrates time variations of the density of the measured currents at 60 °C, which can be represented by power functions with various values of factor n

$$j(t) \propto t^{-n} \tag{1}$$

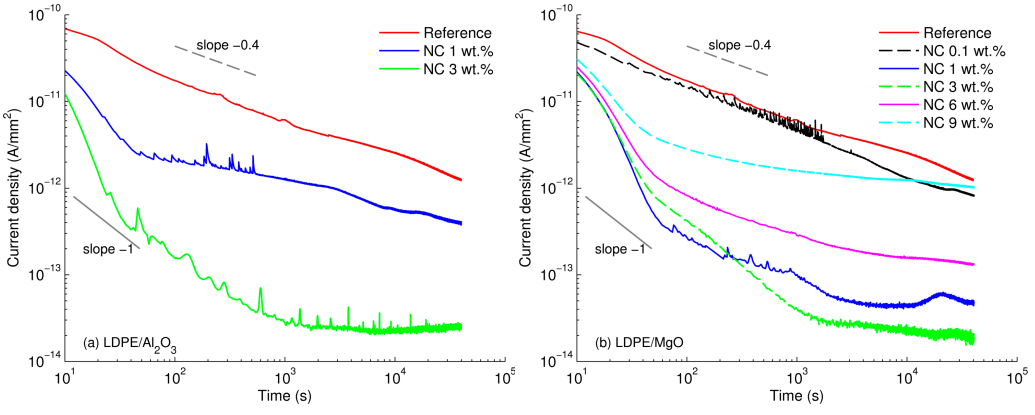

Figure 4. Densities of charging currents as functions of time measured at 60 °C for reference LDPE and both nanocomposites (Al_2O_3 (**a**) and MgO (**b**)).

As seen, the currents through the reference LDPE and LDPE/MgO 0.1 wt % materials decreased gradually and their time dependences exhibit a straight line (in the log-log scale) with a single slope $n \approx 0.4$. It is notable that these currents do not reach a steady state during the measuring time (~11 h) used in the present study.

Adamec and Calderwood [21] suggested that such slowly decaying currents can be attributed to the effect of space charge build-up in the bulk rather than to slow dipole orientation. Their hypothesis has been supported by the fact that the discharging current was remarkably lower than the charging counterpart, which indicated insignificant dipole depolarization [21]. Note that even though PE is well-known as a non-polar polymer, dipolar moieties such as impurities or by-products of oxidation may still exist in the material, resulting in the apparent polarization.

The shape of the recorded current traces changes significantly in cases of nanocomposites with filler content of 1 wt % or higher. A knee point at ~50–70 s after the voltage application can be seen in the characteristics of these materials. Within the initial 50–70 s, the current decayed rapidly with the slope n exceeding 1 that is more likely due to the slow polarization as suggested in [21]. Thereafter, as the polarization process ceases, the conduction current becomes prevailing and the power factor n in Equation (1) is getting closer to zero that corresponds to a steady state, *i.e.*, dc conduction mode. In the following, the quasi-steady state conduction current observed at ~4×10^4 s is used for comparisons. Overall, the measured currents are commonly lower for the nanocomposites as compared to the reference material, indicating a weakening of the charge transport. Thus, for LDPE/Al_2O_3 nanocomposite at the nanofiller content of 3 wt % the current is reduced by almost two orders of magnitude. A less pronounced reduction is found in case of 1 wt % of nanofiller load. For LDPE/MgO nanocomposite, a significant drop is also exhibited at filler loading of 3 wt %, whereas lower (0.1 wt %) or higher (9 wt %) amounts of this nanofiller do not result in a noticeable change of the property.

The materials' dc conductivities calculated by utilizing the charging currents at 4×10^4 s are shown in Figure 5. For LDPE, the outcome is in good agreement with data reported in literature, e.g., [8]. For the LDPE/Al_2O_3 nanocomposite, the reduction in dc conductivity seems to be proportional to the filler content up to 3 wt %. For the LDPE/MgO nanocomposite, a threshold-like behavior can be noticed at ~3 wt %. As seen from the plot, after reaching this point, further addition of nanoparticles causes a negative effect, *i.e.*, the dc conductivity increases remarkably with higher filler loading that can be explained by a formation of agglomerations of nanoparticles in the base material [10]. The obtained results for the LDPE/MgO nanocomposite are in line with earlier reported investigations [9,10] where a decrease in electrical conductivity in more than one order of magnitude and a threshold of filler loading at ~2 wt % were observed.

Further investigations focused on analyzing the temperature dependence of dc conductivity. The study was carried out on the nanocomposites showing the greatest reduction in dc conductivity, *i.e.*, the materials with filler loading of 3 wt %. Since the results obtained for the two nanocomposites were quite similar, only the current densities measured for LDPE/Al_2O_3 are presented in Figure 6 and are

compared with those for unfilled LDPE. Results for LDPE/MgO nanocomposite can be found in Figure S1 of the supplementary materials. It is noteworthy to mention that the time dependence of the current density measured at room temperature on the reference LDPE was in good agreement with the corresponding result reported in [22]. As it is seen in Figure 6, the reduction in the current density associated with the introduction of nanofillers is the most remarkable at 60 °C, whereas it is lower at room temperature.

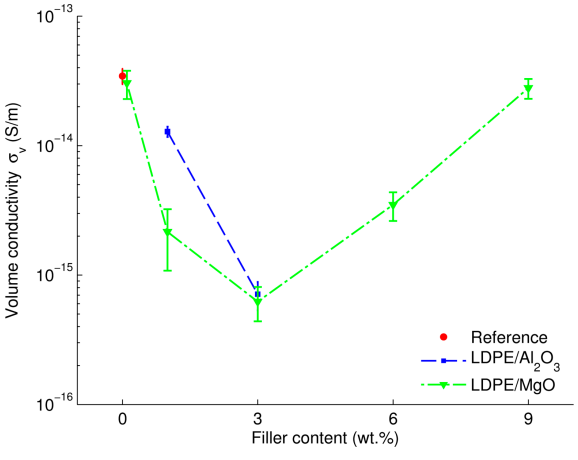

Figure 5. Dependence of dc conductivity (at 60 °C) of the studied nanocomposites on filler content.

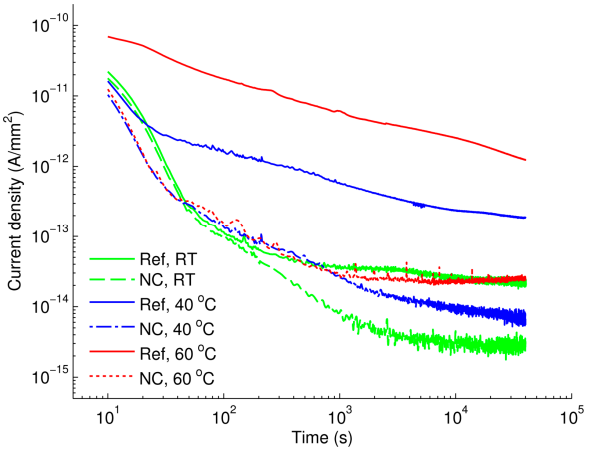

Figure 6. Densities of charging currents as functions of time measured at room temperature (RT) ~20–22 °C, 40 °C, and 60 °C for the reference LDPE (Ref) and 3 wt % LDPE/Al_2O_3 nanocomposite (NC).

The current densities obtained at 4×10^4 s as functions of the reciprocal of the absolute temperature are shown in Figure 7. The activation energies W_a for the studied materials can be derived by assuming Arrhenius type of temperature dependence

$$J_C(T) = J_0 \exp\left(-\frac{W_a}{kT}\right) \quad (2)$$

where $J_C(T)$ are measured current densities at various temperatures, J_0 is a constant value, k is the Boltzmann constant, and T is absolute temperature. The calculated values are indicated in the figure. The activation energy is higher for the reference LDPE as compared to both the nanocomposites. The outcome therefore suggests that at temperatures higher than 60 °C, the reduction in dc conductivity due to the introduced nanoparticles would be even more pronounced and the associated charge transport is much more suppressed.

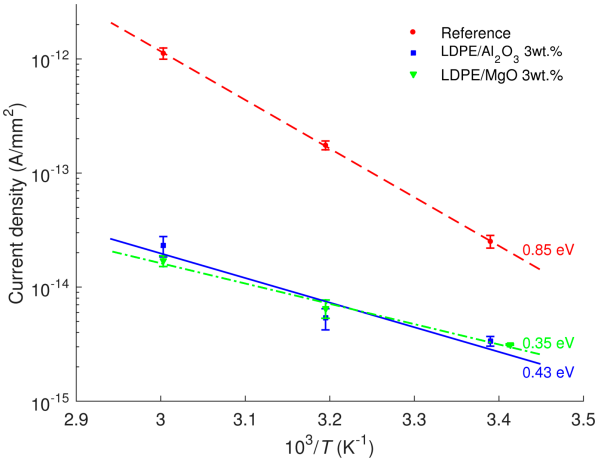

Figure 7. Temperature dependences of current densities at 4×10^4 s of LDPE and its nanocomposites. The calculated activation energies are indicated.

3.2. SPD on Single-layered Insulation

A distribution of surface potential measured on LDPE/Al_2O_3 nanocomposite is illustrated in Figure 8, which is typical results obtained at all considered temperatures on both materials. The initial surface potential distribution is relatively homogeneous in the center of the sample and the profile remains generally preserved during the measurements. A lateral spreading of the surface potential/charge is not noticed, indicating a negligible contribution of surface conduction to the decay process. As the Kelvin probe was always kept above the center of sample surface, zero electric field was maintained in the air gap between the surface center and the probe. Thus, neutralization by ionic species from air was to great extend prevented [23].

As a consequence, the decay is believed to be mainly caused by processes in the insulation bulk.

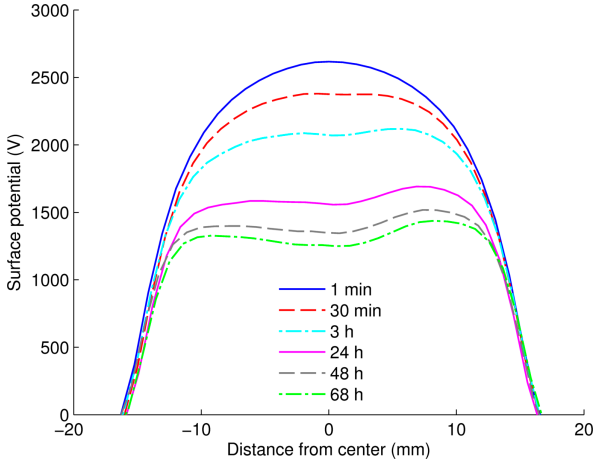

Figure 8. Distribution of surface potential during potential decay measurement on LDPE/Al_2O_3 3 wt % nanocomposite at 60 °C.

The decays of surface potentials on Al_2O_3-nanofilled and reference LDPE are compared in Figure 9a, where zero time corresponds to the end of corona charging. The initial potentials were recorded at ~4–5 s afterwards and they are close to the value of grid potential, except for reference LDPE at 60 °C. The decay appears to be considerably slower for the nanofilled LDPE as compared to the reference LDPE, especially at higher temperatures. Since SPD is attributed to the conduction through the bulk, *i.e.*, the transport of charge carriers within the material driven by the field of deposited surface charges, the experimental data imply significant limitation of charge transport due to the introduced nanoparticles.

The decay rates of the surface potentials (Figure 9b) can be represented as power-law functions of time. As temperature increases, a remarkable distinction in decay rates is observed at the initial stage, for the reference LDPE within the first 100 s of the decay. Note the initial drop of the potential was so high at 60 °C that the first measured potential point was ~200 V lower than the grid potential. However, after 10^3 s, the decay rates became similar for the samples exposed to different temperatures. This observation should not be misinterpreted as indicating a similarity in charge transport process. It is due to the difference in the magnitude of electric field induced in the material at certain time, in particular, the highest field strength presented in the sample subjected to the lowest temperature, so that the apparent decay rates are comparable. As the main features in the SPD

characteristics are similar for both nanofilled LDPE, measured results on LDPE/MgO nanocomposite are presented in Figures S2,S3 in the supplementary materials.

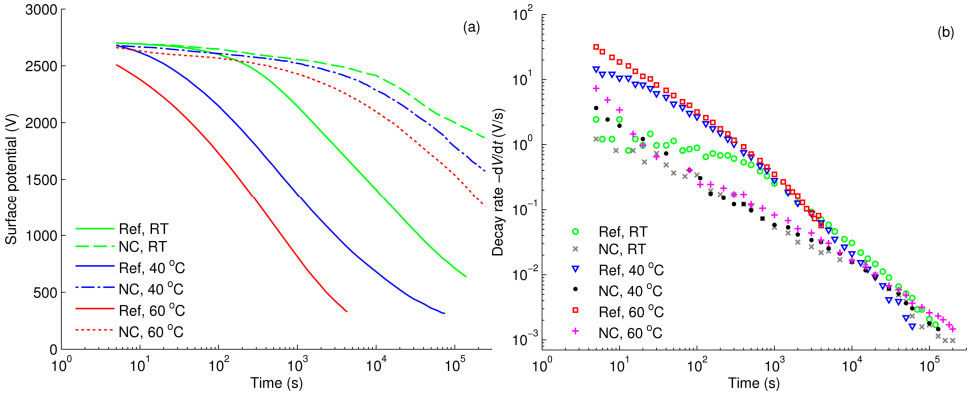

Figure 9. Measured surface potentials (**a**); and calculated decay rates (**b**) for reference LDPE (Ref) and LDPE/Al_2O_3 3 wt % nanocomposite (NC) at different temperatures.

3.3. SPD on Multilayered Samples

Measurements of surface potential decay on multilayered samples were conducted with the aim of revealing contributions of different processes to the decay in the considered conditions. Before presenting and discussing experimental results, we would like to provide a brief summary of physical processes that may take place during SPD measurements in the bulk and at interfaces of the flat samples depicted in Figures 2 and 3. First of all, high electric field induced by ionic charges created by corona and deposited on sample surface may stimulate charge generation processes in insulation bulk according to, for example, Poole-Frenkel mechanism. Secondly, electronic charges can be injected into the bulk from the metal-insulation interface [24]. Furthermore, other processes may occur at the air-insulation interface. A commonly used assumption is that deposited charges are trapped in deep surface traps and their release yields the decay of measured surface potential [25]. This surface controlled potential decay process is referred to as surface de-trapping mechanism. On the other hand, Baum *et al.* [26] suggested an electron transfer process between the deposited ionic charges and the surface states that results in the appearance of either holes or electrons in the latter, depending on the polarity of corona source. In other words, charges are apparently injected into insulation at the air-insulation interface. These injected charge carriers participate in the transport driven by the induced electric field that is reflected in the decaying surface potential. This hypothesis is commonly referred as the charge injection and transport model and has been used to explain results of SPD measurements in a variety of works, e.g., [13,14,27]. Even though an

electric field exceeding 10^7 V/m may be considered as sufficient enough for charge injection, a threshold value corresponding to its onset is not clearly indicated in literature. It is noteworthy to mention that in general both the surface de-trapping and charge injection mechanisms may take place during SPD. The former seems to be dominating on thin dielectric layers of a few μm [25,28] in which extremely deep surface traps exist, whereas the latter is considered to be prevailing on relatively thicker samples, usually of a few tens of μm [13,14,26], provided that the induced field is strong enough.

Results of SPD measurements on multilayered samples are presented in Figure 10. They exhibit a resemblance in potentials measured within the first 200 s. Thereafter, the fastest decay can be observed on Ref/NC(G) sample, whereas the slowest one—on NC/NC sample. If charge generation in the bulk, e.g., by Poole-Frenkel mechanism, is assumed to be the sole contributor to the decay, the same amount of electrons and/or holes would arise in conduction and/or valence bands due to excitation from donors and acceptors in samples Ref/NC(G) and NC/Ref(G). This eventually leads to similar potential decay on these specimens. As the latter is contradictory to the experimental results, this assumption can be ruled out. Combination of charge generation in the bulk and charge injection at the metal-insulation interface is also unlikely the dominating processes as this would lead to a faster decay on NC/Ref(G) sample than on Ref/NC(G).

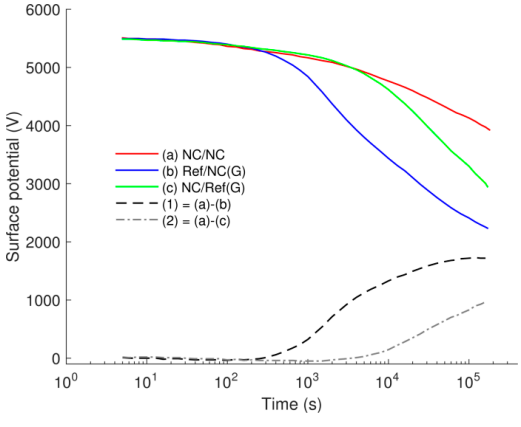

Figure 10. Surface potential decay on multilayered samples. Decay curves (a)–(c) are respectively obtained on samples (a)–(c) illustrated in Figure 3. Curve (1) is a difference in surface potential measured on samples (a) and (b), whereas curve (2)—is the difference for samples (a) and (c).

By comparing decay curves (a) and (c), one can observe that the reference LDPE as the bottom layer in NC/Ref(G) sample slightly alleviates the decay as compared

to the NC bottom counterpart in NC/NC sample. The difference in the decay is thus most likely due to an enhanced charge injection from the grounded copper plate into the LDPE layer. This can be related to the difference in dc conductivity measured on these materials. In contrast, significant difference in potential decays was obtained on samples NC/NC and Ref/NC(G) (the decay curves (a) and (b) in Figure 10). Since charges injected from the grounded copper plate were strongly prevented in both structures by the highly resistive NC bottom layer, the observed difference should mainly be attributed to the intensity of charge (hole) injection into the top layers of either NC or LDPE.

The possibility of injection at the air-insulation interface can be supported by appearance of return voltage [29] obtained in our experiments after short-circuiting the multilayered samples at the end of the SPD tests. The short-circuiting was done by placing a metallic electrode that was connected to ground on the sample surface for 10 s. The return voltage is understood here as a potential build-up after temporarily short-circuiting the previously charged object. In the measurements, the return voltages were built up on all the three considered samples (Figure 11), but it was most considerable on Ref/NC(G) sample. According to a simplified model proposed in [30], the appearance of return voltage can be explained by movement of charge carriers back to the surface. A schematic distribution of charges on the surface and in the bulk of Ref/NC(G) sample is proposed in Figure 12. Holes that are initially injected into the top layer and transported in the bulk accumulate at the interface between reference LDPE and nanocomposite as well as in the insulation bulk (Figure 12a). The proposed charge distribution resembles the results of space charge measurements reported in [31]. It is thus postulated that the injection of electrons into the bottom layer is strongly impeded due to its low dc conductivity and presence of these electrons is not shown in the figure. After neutralization, ionic charges on insulation surface cease and the electric field within the top layer is mainly created by the hole space charges. This corresponding induced field should be strongly reduced as compared to that before neutralization and its direction is altered (Figure 12b). The charge transport driven by this weak field requires more time to reach equilibrium distribution inside the considered sample. As an illustration, the measured return voltage did not reach a steady state level even after 18 h. Removal of the top LDPE layer led thereafter to an abrupt increase of the measured return voltage from ~570 V to ~660 V, as shown in the inset in Figure 11. This implies that the measured return voltage would increase further if the top layer was not removed. In contrast, the return voltage build-up for NC/NC sample was very small (~10 V), which can be explained by the reduced charge transport in the nanocomposite. For NC/Ref(G), the return voltage was ~100 V, which is most likely associated with the transport of negative space charges in the bottom layer of LDPE.

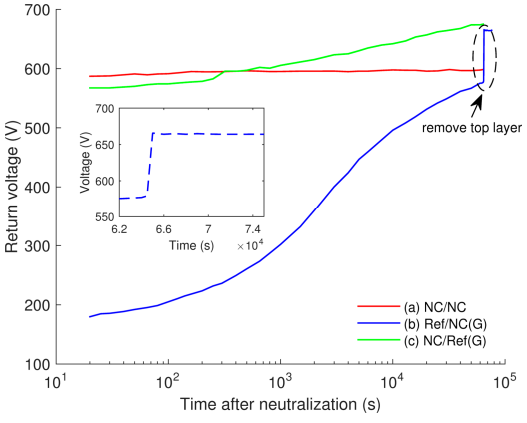

Figure 11. Return voltages measured after short-circuiting multilayered samples for 10 s at the end of SPD measurement. The inset shows the measured potential before and after removal of the top layer of sample Ref/NC(G).

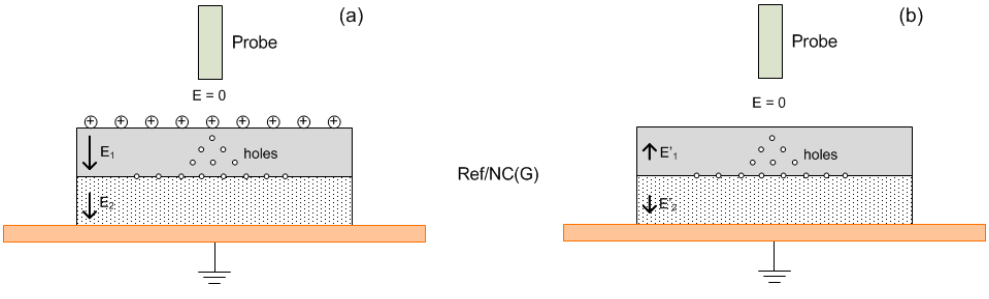

Figure 12. Schematic illustration of charge distribution and electric field (**a**) prior to; and (**b**) immediately after short-circuiting the Ref/NC(G) sample.

By comparing the results of SPD measurements on samples Ref/NC(G) and NC/Ref(G), see decay curves (b) and (c) in Figure 10, one can claim that the contribution of injected positive charges to the decay outweighed by far that of the injected negative charges. The experimental results are also consistent with the hypothesis that positive holes dominate the charge transport in LDPE [32]. In complementary, it can be suggested that this feature is preserved in LDPE nanocomposites, even though the introduction of nanofillers strongly weakens the transport of both the injected holes and electrons.

An additional interesting outcome from the study is presented in Figure 13, where the decay rates of surface potential measured on single-layered reference LDPE sample and on multilayered Ref/NC(G) are compared. As can be seen, the results for both cases are very similar and show a knee point at ~10^3 s, where the slope of the decay rate characteristic changes. The knee point can be attributed to the

arrival of the charge carriers injected at the air-insulation interface [29] to the counter electrode or to the materials' interface. Consequently, the corresponding time ~10^3 s may be treated as a transit time of injected holes in the single-layered LDPE sample or that in the top layer of the Ref/NC(G) sample.

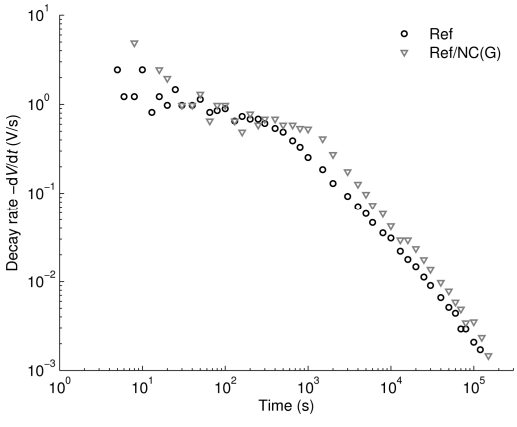

Figure 13. Decay rate of surface potential on reference LDPE and Ref/NC(G).

In summary, the results of SPD measurements on multilayered samples provide convincing evidence that bipolar charge injection takes place under the experimental conditions of this study, though the positive charge carriers (holes) dominate the transport in reference LDPE. This conclusion can also be extended to the case of single-layered sample, as a similar magnitude of the initial field strength is induced inside the material bulk.

3.4. Mobility of Charge Carriers Deduced from SPD Measurements

Dated back to the 60 and 70 s of the last century, the main interest of SPD measurements was related to explanation of the crossover phenomenon that was first reported by Ieda *et al.* [33]. The crossover phenomenon is referred to a faster decay process recorded on dielectric materials being charged to a higher surface potential, so that decay curves cross over each other if their initial surface potentials are different. The crossover phenomenon can be attributed to the non-linear behavior of the dielectric exposed to high electrical field. One of the models that provides a reasonable explanation for this was developed by Sonnonstine and Perlman in 1975 [27]. It accounts for injection of charge carriers from the air-insulation interface and their transport in the bulk of dielectric. By using the model, the authors

derived effective mobility of charge carriers [34] which is proportional to the initial decay rate and inversely proportional to the square of the initial field:

$$-\left(\frac{dV}{dt}\right)_{t=0} = \frac{\mu}{2}\left(\frac{V}{L}\right)^2_{t=0} \tag{3}$$

Thus, this method can be applied to attain mobility of holes in reference LDPE where they are injected from the air-insulation interface and dominate in charge transport as discussed in Section 3.3 (the same seems to be also valid for the studied LDPE nanocomposites). An alternative way relies on the observation of the knee point in the decay rate characteristics, being attributed to the transit time of charges through the bulk [29]. However, since a knee point is only discernible for reference LDPE at room temperature (Figure 9b), this method is solely applicable in this particular case.

Values of the effective mobility of holes in LDPE at room temperature calculated by the two described methods are respectively 4.2×10^{-15} and 2.4×10^{-15} $m^2/(Vs)$, which can already be considered as fairly agreeing with each other. The hole mobility in PE within a range $(1-5) \times 10^{-15}$ $m^2/(Vs)$ at electrical field strength of $(2-4) \times 10^7$ V/m was obtained in numerous investigations of surface charge decay [13,14,26,35], space charge measurements [32] as well as measurements of transient current [36]. Either slightly lower [15] or marginally higher [34] values of mobility can also be found in literature. As for electron mobility, it has been reported to be few times up to one order of magnitude higher than for the holes [13,32].

The results obtained by the procedure proposed by Sonnonstine and Perlman are illustrated in Figure 14. As seen, the effective mobility of holes is lower for the nanocomposites, and this difference exaggerates at higher temperatures. The reduction in charge mobility in nanofilled materials has also been reported in [7,10]. Lewis [37] has recently explained the reduced mobility of charge carriers in nanocomposites by modifications introduced by nanoparticles to the energy structure of the amorphous phase in semi-crystalline PE. The author attributes the hole transitions in unfilled PE to tunneling between donor and acceptor sites in the interfacial regions of the amorphous phase [38]. Thereby, the presence of nanoparticles modifies the height of the energy barrier for tunneling as well as the tunneling distance. As a consequence, the time for hole transitions is lengthened and charge carrier mobility decreases [37].

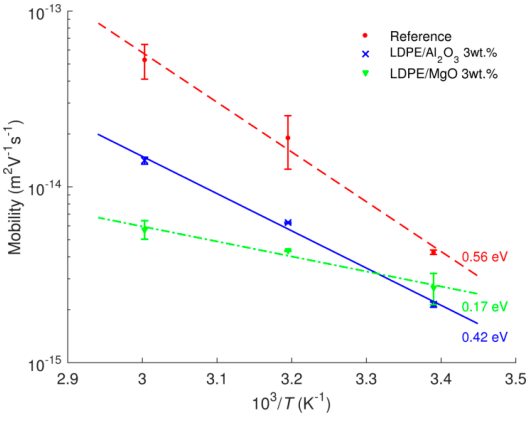

Figure 14. Temperature dependences of charge carrier (hole) mobility derived based on Sonnonstine and Perlman model.

The activation energy for carrier mobility $W_{a\mu}$ can be obtained by using Arrhenius dependence similar to Equation (2):

$$\mu(T) = \mu_0 \exp\left(-\frac{W_{a\mu}}{kT}\right) \tag{4}$$

where $\mu(T)$ represents charge mobility at temperature T and μ_0 is a constant. The respective calculated activation energies are indicated in Figure 14 and provided Table 1. The latter also provides activation energies derived earlier from the dc conductivity measurements. It is noteworthy to observe that the values of activation energies for LDPE/Al_2O_3 nanocomposite obtained by both methods are close to each other. However, this is not the case for reference LDPE and LDPE/MgO nanocomposite. By recalling the expression for the current density j

$$j = qE\sum_i n_i\mu_i \tag{5}$$

where q is elementary charge ($q = 1.6 \times 10^{-19}$ C), it is suggested that for the latter two materials, the density n_i of mobile charge carriers may also increase with temperature.

Table 1. Activation energies (in eV) of dc current density and carrier mobility for reference LDPE and its nanocomposites.

Materials	Derived from Current Density	Derived from Charge Mobility
LDPE	0.85	0.56
LDPE/Al_2O_3 3 wt %	0.43	0.42
LDPE/MgO 3 wt %	0.35	0.17

Conduction in PE has been discussed in a variety of works. A short summary provided in [39] shows that different conduction mechanisms may dominate in the material, depending on experimental conditions. Although the presented values of activation energy vary broadly, a range of 0.84–1.2 eV appears commonly and the activation energy gained in this study is close to the lower limit of the indicated interval. On the other hand, not much information can be found on the activation energy level for conduction in PE nanocomposites. The lower values of activation energy for the nanofilled LDPE presented here indicate that the conduction processes are less temperature-dependent, which would lead to less pronounced field enhancement and space charge accumulation in HVDC cable insulation, which is a positive aspect brought about by the nanofillers.

3.5. Plot of $-t\mathrm{d}V/\mathrm{d}t$ vs. log(t)

The plot of $-t\mathrm{d}V/\mathrm{d}t$ *vs.* $\log(t)$ has been widely employed for representing data of SPD measurements as it may reveal information about charge trapping and transport in disordered solids. As pointed out in [28], for the case of exponential potential decay $V = V_0\exp(-t/\tau)$, the peak in this plot corresponds to the characteristic time τ. The exponential potential decay is however rarely observed in reality. The peak of the curve $-t\mathrm{d}V/\mathrm{d}t$ *vs.* $\log(t)$ for a general decay shape can be related either to an average transit time of charge carriers, provided that charge injection takes place, or to an average residence time of charges in trapping sites in the case the surface de-trapping dominates [28]. The later hypothesis has been linked to the demarcation energy model [25], according to which the release of charges from traps at particular time t yields potential decay $\mathrm{d}V/\mathrm{d}t$, and hence, the plot of $-t\mathrm{d}V/\mathrm{d}t$ *vs.* $\log(t)$ shows a dynamic border between the filled (deeper) and the emptied (shallower) localized states. Thus, the energy depth of traps E_t is determined by time t that charges spend in them:

$$E_t = kT\ln(\nu_0 t) \tag{6}$$

where ν_0 is the attempt-to-escape frequency. Since $-t\mathrm{d}V/\mathrm{d}t$ is proportional to the trap density and time t is related to the trap depth, the characteristic $-t\mathrm{d}V/\mathrm{d}t$ *vs.* $\log(t)$ provides the image of trap energy distribution in considered materials.

The plots of $-t\mathrm{d}V/\mathrm{d}t$ *vs.* $\log(t)$ for reference LDPE obtained at different temperatures are presented in Figure 15a. At room temperature, the characteristic shows a broad peak with a shoulder. The time corresponding to the shoulder (~10^3 s) is close to the transit time of charge carriers, whereas the peak time (~10^4 s) is longer and appears to be the average dwelling time of charges in deep traps. As temperature rises, the peaks become narrower and the shoulder less pronounced. One can derive the value of the attempt-to-escape frequency ν_0 by using the characteristics of $-t\mathrm{d}V/\mathrm{d}t$ *vs.* $\log(t)$ obtained at different temperatures with an assumption of

temperature-invariant distribution of trap energy [25]. The calculation provides a value $\nu_0 \approx 4 \times 10^8$ s^{-1} and the trap depth at maximum density is $E_t \approx 0.72$ eV (Figure 15b). Both the derived values appear to be much lower than the commonly accepted parameters (ν_0 in order of 10^{12} s^{-1} and $E_t \approx 1.0$ eV). This discrepancy might be attributed to the fact that the decay is controlled by more than a single mechanism. It should be noted that by using the same procedure [25] low levels of the attempt-to-escape frequency ($\nu_0 = 2 \times 10^5$ s^{-1}) and the trap depth ($E_t \approx 0.36$ eV) have also been found for polypropylene [28].

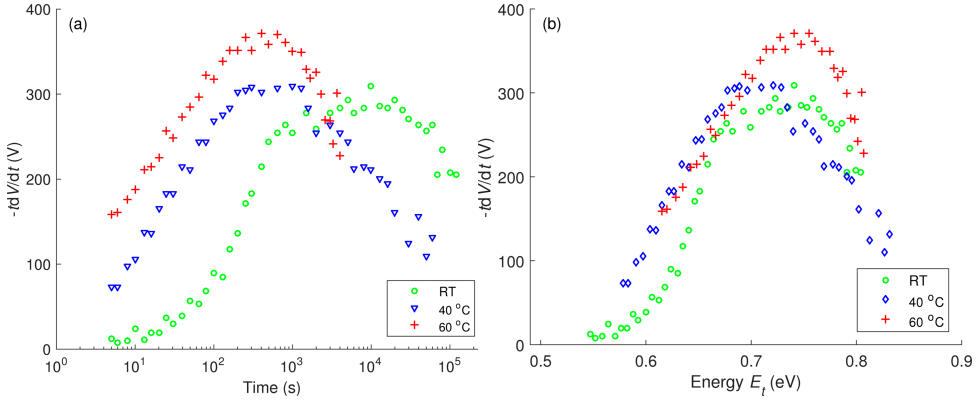

Figure 15. Plots $-t\mathrm{d}V/\mathrm{d}t$ *vs.* $\log(t)$ (**a**); and $-t\mathrm{d}V/\mathrm{d}t$ *vs.* E_t (**b**) obtained at different temperatures for reference LDPE.

In Figure 16, the energy distributions of traps are compared for the reference LDPE and LDPE/Al_2O_3 nanocomposite by assuming the attempt-to-escape frequency $\nu_0 \approx 6 \times 10^{12}$ s^{-1}. For the reference material, the distribution is characterized by a peak at ~1 eV, which may be associated with trapping centra revealed by measurements of thermally stimulated currents (TSC) and attributed to physical defects in amorphous-crystalline interfaces and in crystalline region of PE [40]. For the nanofilled material, the image of trap distribution shifts to deeper trap energy. A shoulder is also found at ~1 eV, suggesting an identical origin as in reference LDPE. In addition, the trap energy distribution of the nanocomposite implies a peak arising outside of the measurement window (at time exceeding 4.2×10^5 s) that can be associated with a deeper trap level ($E_t > 1.1$ eV). The appearance of this trapping level is most likely caused by the presence of nanofillers in the material; in particular in the interfacial region between nanofiller particles and the polymer. The energy depth of the trap may be as high as 2 eV, as revealed by TSC measurements on LDPE/MgO nanocomposite [41].

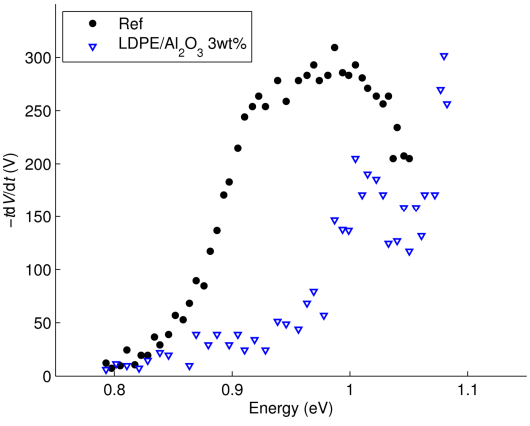

Figure 16. Trap energy distributions in reference LDPE and its nanocomposite.

3.6. Current Density Deduced from SPD Measurements

During SPD measurement under open circuit configuration, the total current density in elementary volume of dielectric is zero

$$j(x,t) + \frac{\partial\left(\varepsilon E\left(x,t\right)\right)}{\partial t} = 0 \tag{7}$$

where $j(x,t)$ is space- and time-dependent conduction current density and the second term represents displacement current, ε being the real part of material permittivity, E stands for electric field. The externally measurable conduction current density through the insulation can be defined as

$$J(t) = \frac{1}{L}\int_0^L j(x,t)dx \tag{8}$$

where L is sample thickness. By substituting Equation (7) into Equation (8) and noting the flat response of ε on frequency for LDPE and its nanocomposites [10], one obtains

$$J(t) = -\frac{\varepsilon}{L}\int_0^L \frac{\partial E\left(x,t\right)}{\partial t}dx = -\frac{\varepsilon}{L}\frac{dV(t)}{dt} \tag{9}$$

Equation (9) establishes a relationship between the conduction current density in SPD experiments and the decay rate of the measured potential. The current density is thus calculated and its dependence on electric field is examined in this section. Here the average magnitude of the electric field induced in the insulation $E = V/L$ is used.

A log-log plot of the current density *versus* electric field in reference LDPE presented in Figure 17a indicates that factor m in the dependency $J \propto E^m$ decreases with temperature. Since $m > 2$, the conduction current in reference LDPE is most likely governed by the space charge limited current (SCLC) mechanism for materials with traps, see Equation (10) [42], rather than the SCLC in trap-free materials described by the Mott-Gurney square law, see Equation (11) [43]:

$$J \propto \frac{V^{l+1}}{L^{2l+1}} \tag{10}$$

$$J = \frac{9}{8}\varepsilon\mu\frac{V^2}{L^3} \tag{11}$$

In Equation (10), factor $l = T_C/T$, where T_C is the characteristic temperature of the proposed exponential distribution of trap density [42]. Further, Schottky and Poole-Frenkel plots for reference LDPE are illustrated in Figures 18a and 19a, respectively. As seen, the magnitudes of the relative permittivity used to get best fit (provided in the curves) are quite different from the value 2.3 commonly reported for PE. This fact indicates that neither Schottky injection mechanism nor Poole-Frenkel mechanism satisfactorily explain the behavior of the conduction current density J at all considered temperatures. The change of the mechanism governing the conduction in LDPE with temperature has been noted in [44], where Schottky injection has been found to dominate at room temperature, but not at elevated ones.

The field dependencies of current density in LDPE/Al_2O_3 nanocomposite are illustrated in Figures 17b, 18b and 19b, whereas the calculated results for LDPE/MgO nanocomposite are provided in supplementary materials (Figures S4–S6). The derived parameters m and ε_r of these dependencies are provided in Table 2 for comparison. For both nanocomposites, the current density curves show a knee point at which the slopes change, and hence, the characteristics can be divided into two regions as indicated in the figures. It is noteworthy that the time corresponding to the observed knee point is close to the transit time calculated by using the hole mobility deduced in Section 3.4. Thus, the rapid decrease of current densities within the first region can be explained by a transient process followed the charge injection at the air-insulation surface. As the injected charges reach the counter electrode, the field dependence of current densities become less pronounced, as shown in the second region. Parameters m and ε_r are thus calculated only in the latter region for avoiding the effect of the transient process at the initial stage. As seen, the power factor m in the dependency $J \propto E^m$ is significantly higher for both nanocomposites as compared to that of reference LDPE. SCLC mechanism followed Equation (10) appears to be the dominating conduction mechanism in the nanocomposites. In contrast, both Schottky injection mechanism and Poole-Frenkel mechanism cannot fully explain

the experimental data of the nanofilled materials under consideration. This topic therefore requires further investigation.

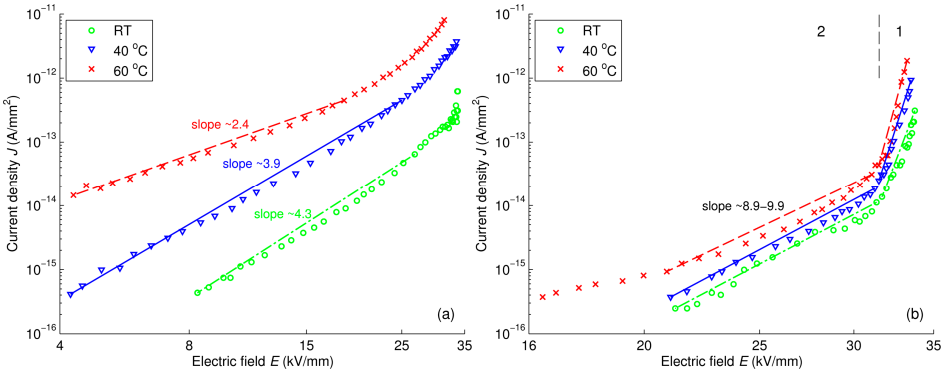

Figure 17. Log-log plot of *J vs. E* for reference LDPE (**a**); and LDPE/Al_2O_3 3 wt % nanocomposite (**b**) at various temperatures. Regions 1 and 2 in figure (**b**) are featured by different slopes of the dependencies.

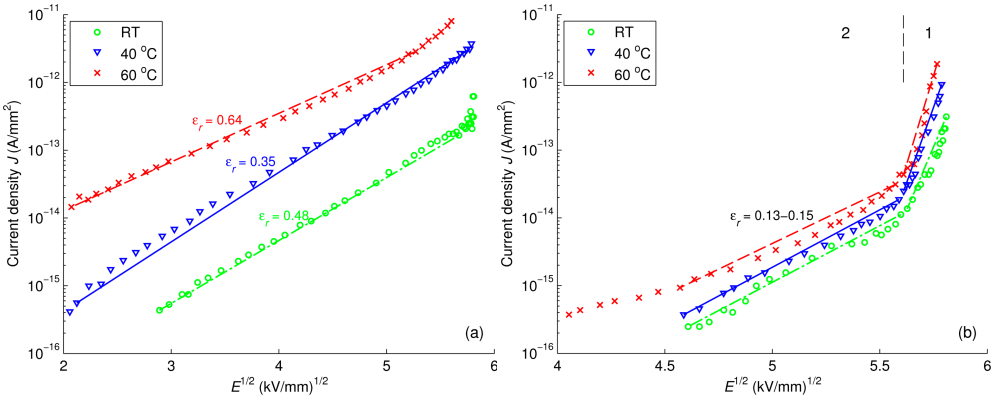

Figure 18. Schottky plot for reference LDPE (**a**); and LDPE/Al_2O_3 3 wt % nanocomposite (**b**) at various temperatures. Regions 1 and 2 in figure (**b**) are featured by different slopes of the dependencies.

Table 2. Calculated parameters in characteristics of *J vs. E*. Note that the obtained values of ε_r below 1 do not have physical significance.

Characteristics	Calculated Parameters	LDPE			LDPE/Al_2O_3 NC			LDPE/MgO NC		
		RT	40 °C	60 °C	RT	40 °C	60 °C	RT	40 °C	60 °C
$J \propto E^m$	m	4.3	3.9	2.4	9.8	9.9	8.9	11.5	9.6	5.6
Schottky	ε_r	0.48	0.35	0.64	0.15	0.13	0.14	0.12	0.14	0.30
Poole-Frenkel	ε_r	3.2	2.4	6.8	0.74	0.64	0.72	0.56	0.67	1.76

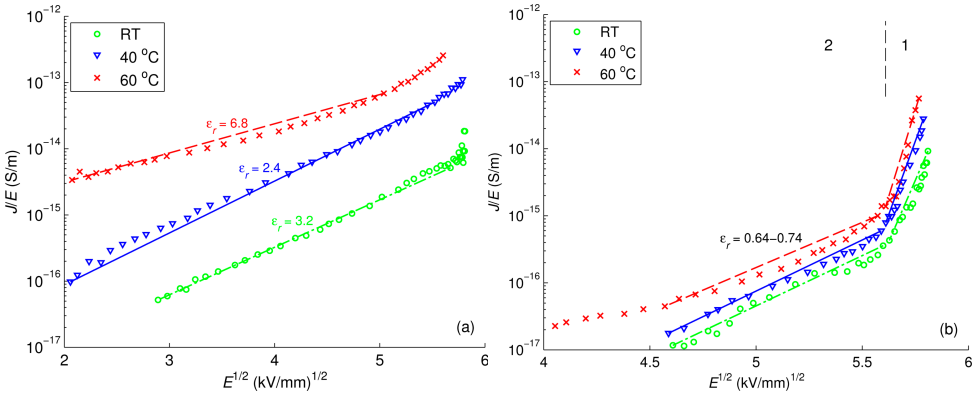

Figure 19. Poole-Frenkel plot for reference LDPE (**a**); and LDPE/Al_2O_3 3 wt % nanocomposite (**b**) at various temperatures. Regions 1 and 2 in figure (**b**) are featured by different slopes of the dependencies.

4. Conclusions

Charge transport in low-density polyethylene (LDPE) filled with nanoparticles of alumina (Al_2O_3) and magnesia (MgO) as well as the unfilled counterpart was investigated by means of conductivity and surface potential decay (SPD) measurements. As compared to the pure polymer case, a remarkable reduction in dc conductivity was found for both LDPE nanocomposites at filler content of 3 wt %. Results of SPD measurements on multilayered samples strongly suggest that (a) charge injection at the air-insulation interface and the transport of injected charges are dominating in decay process; and (b) positive charges are prevailing in LDPE. Based on these, mobility of holes in the considered materials has been deduced by using measured data on single-layered samples. The reduced mobility of charge carriers and the increased trap depth obtained in nanocomposites are closely correlated with the weakened charge transport, and hence, decreased dc conductivity of the nanofilled materials. Additionally, by using the measured current density and the calculated charge mobility, lower activation energies were obtained for nanocomposites compared to unfilled LDPE, indicating weaker temperature dependencies of the studied properties in nanofilled dielectrics. The field dependency of the current density derived from SPD measurements was analyzed, showing that the conduction mechanisms in studied materials are strongly affected by presence of nanofillers and temperature. The obtained experimental results are further utilized for computer simulations of charge transport in LDPE and its nanocomposites which are presented in the second part of the work.

Supplementary Materials: The supplementary materials can be found at www.mdpi.com/2073-4360/8/3/87/s1.

Acknowledgments: The financial support provided by Chalmers Area of Advance in Energy and Swedish Foundation for Strategic Research is gratefully acknowledged.

Author Contributions: Anh T. Hoang conducted measurements, performed analysis and systematization of the results, prepared the manuscript. Yuriy V. Serdyuk contributed to the analysis and interpretation of the experimental data as well as to the preparation of the manuscript. Stanislaw M. Gubanski coordinated the work, supported the interpretation of the results and contributed to the preparation of the manuscript. Love Pallon and Dongming Liu manufactured materials' samples for testing, while Ulf W. Gedde provided support in materials' sample fabrication.

Conflicts of Interest: The authors declare no conflict of interest.

References and Notes

1. Hanley, T.L.; Burford, R.P.; Fleming, R.J.; Barber, K.W. A general review of polymeric insulation for use in HVDC cables. *IEEE Electr. Insul. Mag.* **2003**, *19*, 13–24.
2. Reddy, C.C.; Ramu, T.S. On the computation of electric field and temperature distribution in HVDC cable insulation. *IEEE Trans. Dielectr. Electr. Insul.* **2006**, *13*, 1236–1244.
3. Dissado, L.A.; Mazzanti, G.; Montanari, G.C. The role of trapped space charges in the electrical aging of insulating materials. *IEEE Trans. Dielectr. Electr. Insul.* **1997**, *4*, 496–506.
4. Tanaka, T.; Imai, T. Advances in nanodielectric materials over the past 50 years. *IEEE Electr. Insul. Mag.* **2013**, *29*, 10–23.
5. Lewis, T.J. Nanometric dielectrics. *IEEE Trans. Dielectr. Electr. Insul.* **1994**, *1*, 812–825.
6. Roy, M.; Nelson, J.K.; MacCrone, R.K.; Schadler, L.S.; Reed, C.W.; Keefe, R. Polymer nanocomposite dielectrics-the role of the interface. *IEEE Trans. Dielectr. Electr. Insul.* **2005**, *12*, 629–643.
7. Roy, M.; Nelson, J.K.; MacCrone, R.K.; Schadler, L.S. Candidate mechanisms controlling the electrical characteristics of silica/XLPE nanodielectrics. *J. Mater. Sci.* **2007**, *42*, 3789–3799.
8. Fleming, R.J.; Ammala, A.; Lang, S.B.; Casey, P.S. Conductivity and space charge in LDPE containing nano- and micro-sized ZnO particles. *IEEE Trans. Dielectr. Electr. Insul.* **2008**, *15*, 118–126.
9. Murakami, Y.; Nemoto, M.; Okuzumi, S.; Masuda, S.; Nagao, M.; Hozumi, N.; Sekiguchi, Y. DC conduction and electrical breakdown of MgO/LDPE nanocomposite. *IEEE Trans. Dielectr. Electr. Insul.* **2008**, *15*, 33–39.
10. Ishimoto, K.; Kanegae, E.; Ohki, Y.; Tanaka, T.; Sekiguchi, Y.; Murata, Y.; Reddy, C.C. Superiority of dielectric properties of LDPE/MgO nanocomposites over microcomposites. *IEEE Trans. Dielectr. Electr. Insul.* **2009**, *16*, 1735–1742.
11. Tanaka, T.; Kozako, M.; Fuse, N.; Ohki, Y. Proposal of a multi-core model for polymer nanocomposite dielectrics. *IEEE Trans. Dielectr. Electr. Insul.* **2005**, *12*, 669–681.
12. Mizutani, T.; Ieda, M. Carrier transport in high-density polyethylene. *J. Phys. D: Appl. Phys.* **1979**, *12*, 291–296.
13. Toomer, R.; Lewis, T.J. Charge trapping in corona-charge polyethylene films. *J. Phys. D: Appl. Phys.* **1980**, *13*, 1343–1356.

14. Von Berlepsch, H. Interpretation of surface potential kinetics in HDPE by a trapping model. *J. Phys. D: Appl. Phys.* **1985**, *18*, 1155–1170.
15. Fischer, P.; Röhl, P. Transient currents in oxidized low-density polyethylene. In *Mehrphasige Polymersysteme*; Fischer, E.W., Horst Müller, F., Kausch, H.H., Eds.; Steinkopff: Dresden, Germany, 1977; Volume 62, pp. 149–153.
16. Liu, D.; Pourrahimi, A.M.; Olsson, R.T.; Hedenqvist, M.S.; Gedde, U.W. Influence of nanoparticle surface treatment on particle dispersion and interfacial adhesion in low-density polyethylene/aluminium oxide nanocomposites. *Eur. Polym. J.* **2015**, *66*, 67–77.
17. Pallon, L.K.H.; Hoang, A.T.; Pourrahimi, A.M.; Hedenqvist, M.S.; Nilsson, F.; Gubanski, S.M.; Gedde, U.W.; Olsson, R.T. The impact of MgO nanoparticle interface in ultra insulating polyethylene nanocomposites for high voltage DC cables. *J. Mater. Chem. A* **2016**. (under review).
18. IEC Standard 60093. Methods of test for volume resistivity and surface resistivity of solid electrical insulating materials, 1980.
19. Giacometti, J.A.; Oliveira, O.N. Corona charging of polymers. *IEEE Trans. Electr. Insul.* **1992**, *27*, 924–943.
20. Noras, M.A. *Non-Contact Surface Charge/Voltage Measurements: Fieldmeter and Voltmeter Methods*; Trek Inc.: Lockport, NY, USA, 2002.
21. Adamec, V.; Calderwood, J.H. On the determination of electrical conductivity in polyethylene. *J. Phys. D: Appl. Phys.* **1981**, *14*, 1487–1494.
22. Le Roy, S.; Teyssedre, G.; Laurent, C.; Montanari, G.C.; Palmieri, F. Description of charge transport in polyethylene using a fluid model with a constant mobility: Fitting model and experiments. *J. Phys. D: Appl. Phys.* **2006**, *39*, 1427–1436.
23. Kumara, S.; Serdyuk, Y.V.; Gubanski, S.M. Surface charge decay on polymeric materials under different neutralization modes in air. *IEEE Trans. Dielectr. Electr. Insul.* **2011**, *18*, 1779–1788.
24. Xu, Z.; Zhang, L.; Chen, G. Decay of electric charge on corona charged polyethylene. *J. Phys. D: Appl. Phys.* **2007**, *40*, 7085–7089.
25. Watson, P.K. The energy distribution of localized states in polystyrene, based on isothermal discharge measurements. *J. Phys. D: Appl. Phys.* **1990**, *23*, 1479–1484.
26. Baum, E.A.; Lewis, T.J.; Toomer, R. Decay of electrical charge on polyethylene films. *J. Phys. D: Appl. Phys.* **1977**, *10*, 487–497.
27. Sonnonstine, T.J.; Perlman, M.M. Surface-potential decay in insulators with field-dependent mobility and injection efficiency. *J. Appl. Phys.* **1975**, *46*, 3975–3981.
28. Llovera, P.; Molinié, P. New methodology for surface potential decay measurements: Application to study charge injection dynamics on polypropylene films. *IEEE Trans. Dielectr. Electr. Insul.* **2004**, *11*, 1049–1056.
29. Molinié, P. Measuring and modeling transient insulator response to charging: The contribution of surface potential studies. *IEEE Trans. Dielectr. Electr. Insul.* **2005**, *12*, 939–950.

30. Coelho, R.; Jestin, P.; Levy, L.; Sarrail, D. On the return-voltage buildup in insulating materials. *IEEE Trans. Electr. Insul.* **1987**, *22*, 683–690.
31. Kanegae, E.; Ohki, Y.; Tanaka, T.; Sekiguchi, Y.; Murata, Y.; Reddy, C.C. Space charge behavior in multi-layered dielectrics with LDPE and LDPE/MgO nanocomposites. In Proceedings of the 10th IEEE International Conference on Solid Dielectrics (ICSD), Potsdam, Germany, 4–9 July 2010; pp. 1–4.
32. Chen, G.; Tay, T.Y.G.; Davies, A.E.; Tanaka, Y.; Takada, T. Electrodes and charge injection in low-density polyethylene using the pulsed electroacoustic technique. *IEEE Trans. Dielectr. Electr. Insul.* **2001**, *8*, 867–873.
33. Ieda, M.; Sawa, G.; Shinohara, U. A decay process of surface electric charges across polyethylene film. *Jpn. J. Appl. Phys.* **1967**, *6*, 793–794.
34. Perlman, M.M.; Sonnonstine, T.J.; St.Pierre, J.A. Drift mobility determinations using surface potential decay in insulators. *J. Appl. Phys.* **1976**, *47*, 5016–5021.
35. Wintle, H.J. Decay of static electrification by conduction processes in polyethylene. *J. Appl. Phys.* **1970**, *41*, 4004–4007.
36. Pelissou, S.; St-Onge, H.; Wertheimer, M.R. Electrical conduction of polyethylene below and above its melting point. *IEEE Trans. Electr. Insul.* **1988**, *23*, 325–333.
37. Lewis, T.J. Charge transport in polyethylene nano dielectrics. *IEEE Trans. Dielectr. Electr. Insul.* **2014**, *21*, 497–502.
38. Lewis, T.J.; Llewellyn, J.P. Electrical conduction in polyethylene: The role of positive charge and the formation of positive packets. *J. Appl. Phys.* **2013**, *113*, 223705.
39. Raju, G.G. *Chapter 7—Field Enhanced Conduction. Dielectrics in Electric Fields*; Marcel Dekker: New York, NY, USA, 2003.
40. Mizutani, T.; Suzuoki, Y.; Ieda, M. Thermally stimulated currents in polyethylene and ethylene-vinyl-acetate copolymers. *J. Appl. Phys.* **1977**, *48*, 2408–2413.
41. Ishimoto, K.; Tanaka, T.; Ohki, Y.; Sekiguchi, Y.; Murata, Y. Thermally stimulated current in low-density polyethylene/MgO nanocomposite. On the mechanism of its superior dielectric properties. *Electr. Eng. Jpn.* **2011**, *176*, 1–7.
42. Mark, P.; Helfrich, W. Space-charge-limited currents in organic crystals. *J. Appl. Phys.* **1962**, *33*, 205–215.
43. Mott, N.F.; Gurney, R.W. *Electronic Processes in Ionic Crystals*; Clarendon Press: Oxford, England, 1948.
44. Boudou, L.; Guastavino, J. Influence of temperature on low-density polyethylene films through conduction measurement. *J. Phys. D: Appl. Phys.* **2002**, *35*, 1555–1561.

Charge Transport in LDPE Nanocomposites Part II—Computational Approach

Anh T. Hoang, Yuriy V. Serdyuk and Stanislaw M. Gubanski

Abstract: A bipolar charge transport model is employed to investigate the remarkable reduction in dc conductivity of low-density polyethylene (LDPE) based material filled with uncoated nanofillers (reported in the first part of this work). The effect of temperature on charge transport is considered and the model outcomes are compared with measured conduction currents. The simulations reveal that the contribution of charge carrier recombination to the total transport process becomes more significant at elevated temperatures. Among the effects caused by the presence of nanoparticles, a reduced charge injection at electrodes has been found as the most essential one. Possible mechanisms for charge injection at different temperatures are therefore discussed.

Reprinted from *Polymers*. Cite as: Hoang, A.T.; Serdyuk, Y.V.; Gubanski, S.M. Charge Transport in LDPE Nanocomposites Part II—Computational Approach. *Polymers* **2016**, *8*, 103.

1. Introduction

Accumulation of space charges in polymeric insulation is the main concern during the operation of high voltage direct current (HVDC) cables. It may greatly enhance the electric field inside the insulation bulk that eventually has a detrimental effect on the life expectancy of cables. Thus, knowledge of the generation and transport of charge carriers plays an important role in designing reliable insulation systems of HVDC cable working at high electric field strength. Nowadays, various experimental techniques are used to assess charge dynamics in insulating materials. Apart from that, computer simulations have become popular since they offer great flexibility in investigating effects of different factors and in conducting parametric studies.

A pioneering computer model considering transient processes of charge generation and transport in cable insulation exposed to dc stresses was published in 1994 by Alison and Hill [1] with the aim of reproducing space charge accumulation attained experimentally [2] on a 2.5 mm thick sample of cross-linked polyethylene (XLPE). The model incorporated charge generation due to injection at insulation-electrode interfaces and its transport through material bulk associated with trapping and recombination. Since that time, a variety of models [3–11] were developed for studying different physical processes taking place in polyethylene (PE) under a high dc electric field. Le Roy *et al.* [6] proposed a model accounting

for de-trapping of charges from deep trapping sites (in contrast to earlier works [1,3,4]) that yielded consistent prediction of experimental results on space charge distribution, conduction currents, and electroluminescence in low-density polyethylene (LDPE). Furthermore, Boufayed *et al.* [7] introduced more realistic exponential distribution of traps instead of two single trap levels (shallow and deep traps) utilized in other models [1,3,5,6]. Most recently, a contribution of surface states at the interfaces between dielectric and electrodes to the dynamics of space charges in LDPE films has been considered [10]. Additionally, formation of charge packets in PE arising as the applied electric field exceeds 100 kV/mm has been studied in [4,11].

It is worth noting that most of the reported simulations were performed for ambient temperatures ~20 °C, which is not the working condition of cable insulation in reality. The actual operating temperatures may reach ~70–80 °C. Moreover, a temperature gradient across the insulation may exist, which affects local characteristics of the material relevant to charge transport. These facts raise questions on the applicability of the existing models for predicting the behavior of insulation in practical situations. This difficulty, in fact, has been dealt with in [9], where the distribution of the electric field and space charges in a cable working under isothermal and temperature gradient conditions were modelled by assuming dependencies of charge carriers' mobility on temperature and electric field while setting all other model parameters the same as in [6]. The simulated results, however, have not been confirmed by respective experimental data yet.

As for simulations of charge transport in nanocomposites, information about such studies is rather limited. To formulate a consistent model for this case, the basic model of charge transport in pure polymers needs to be extended to account for formation of traps associated with nanofiller particles. These trapping sites may stimulate specific processes which are not present in pure materials. In particular, formation of deep traps that capture mobile carriers injected from electrodes, thus preventing further generation of charges at electrode-material interfaces has been introduced in [12]. Computer simulations utilizing parametric studies to examine the hypotheses as well as to compare contributions of different processes have been reported in [13,14]. The general requirement to such models is that they should be capable to explain the facts that the addition of nanofillers into polymers leads to greatly reduced material dc conductivity [15–17] and significantly limited accumulation of space charges [16,18,19] (that actually make, e.g., PE nanocomposites favorable materials for HVDC cable insulation). As for today, such a consistent model of charge transport in nanocomposites that can reproduce experimental results is still lacking and, hence, it needs to be developed.

In the present paper, we study charge transport in LDPE with and without nanofillers at different temperatures by computer simulations using COMSOL Multiphysics (COMSOL AB: Stockholm, Sweden). As a number of processes,

i.e., charge generation and transport as well as charge trapping, de-trapping, and recombination have to be accounted for, numerous parameters are involved in the model. It is a common practice to derive these parameters by using fitting procedures that result in additional uncertainties in the model. For avoiding this, we use values of parameters, in particular, the mobility of charges derived from experimental data presented in the first part of this work [17]. The validation of the developed model is examined by comparing the simulated results with conduction currents measured for unfilled LDPE and LDPE/Al_2O_3 nanocomposite.

2. Model of Charge Transport in Insulating Polymers

2.1. The Model

Following the experimental conditions of [17], we consider a flat sample of insulating material of thickness L that is sandwiched between a semiconducting anode and a stainless steel cathode. A positive dc voltage V_0 is applied to the anode at zero time, while the cathode is grounded. Since the radii of the electrodes are much larger than the thickness of material sample, the edge effect can be neglected. Thus, the study of charge transport in the flat sample can be reduced to a one-dimensional domain. In such a case, most of the parameters described below are functions of coordinate x along insulation thickness and time t (note that these dependencies are usually omitted in mathematical expressions below).

To describe conduction process under given conditions, bipolar charge transport model [1,6] is employed. In the model, charge carriers in the material appear due to injection of holes at the anode and electrons at the cathode. The injected charge carriers drift through the material bulk due to the electric field and their transfer is affected by two types of localized states, namely, shallow and deep traps. The former trap type is attributed to structural defects in materials, such as folds, kinks, or ends of polymeric chains. The latter trap type has chemical origin due to the presence of reactive groups such as carbonyl (–C=O), carboxyl (–COOH), *etc.* Charge carriers transported between shallow traps (by hopping) are referred as mobile electrons and holes, whereas the ones being captured in the deep trapping centers are referred as trapped electrons and holes. The trapped carriers occupy traps for a certain residence time, which is considerably longer than that the mobile carriers spend in shallow traps. Charged species captured in deep traps can be released back to the transport state through a de-trapping process. Furthermore, the drift of charge carriers through the material is also associated with their irreversible losses due to various types of recombination. The mathematical description of the model is provided below. Note that model parameters and other quantities in the following equations related to mobile electrons and holes and trapped electrons and holes are denoted by subscripts e and h, etr and htr, respectively.

As mentioned, charge carriers can be injected into the insulation through both electrodes as a high dc electrical field is applied. By assuming Schottky's mechanism, the densities of injected currents can be expressed as:

$$j_e(0,t) = AT^2 \exp\left(-\frac{q(\phi_K - \Delta\phi_K)}{kT}\right) \tag{1}$$

$$j_h(L,t) = AT^2 \exp\left(-\frac{q(\phi_A - \Delta\phi_A)}{kT}\right) \tag{2}$$

Here, the coordinates of the cathode and anode are respectively 0 and L, m; A is Richardson's constant (A = 1.2 × 10^6 A·m^{-2}·K^{-2}); T being absolute temperature, K; q is elementary charge (q = 1.6 × 10^{-19} C); ϕ_A and ϕ_K are respectively the barrier heights for charge injection from the anode and cathode, eV; k stands for Boltzmann's constant (k = 1.38 × 10^{-23} J·K^{-1}). In Equations (1) and (2), $\Delta\phi_{A,K}$ denote the field-lowered barrier heights for charge injection due to electric field $E_{A,K}$ at corresponding electrodes:

$$\Delta\phi_{A,K} = \sqrt{\frac{qE_{A,K}}{4\pi\varepsilon_0\varepsilon_r}} \tag{3}$$

where ε_0 = 8.854 × 10^{-12} F·m^{-1} is the permittivity of vacuum and ε_r being material relative permittivity.

Transport of injected charge carriers through insulating materials is governed by a system constituting transport equation (4), current continuity equation (5), differential equation (6), and Poisson's equation (7):

$$j_{e,h}(x,t) = q\mu_{e,h} n_{e,h}(x,t) E(x,t) \tag{4}$$

$$\frac{\partial n_{e,h}(x,t)}{\partial t} + \frac{1}{q}\frac{\partial}{\partial x}\left(j_{e,h}(x,t)\right) = S_{e,h}(x,t) \tag{5}$$

$$\frac{\mathrm{d}n_{etr,htr}(x,t)}{\mathrm{d}t} = S_{etr,htr}(x,t) \tag{6}$$

$$\nabla\left(\varepsilon_0\varepsilon_r E\left(x,t\right)\right) = \rho\left(x,t\right) \tag{7}$$

Note that in the transport equation (4) only the drift current is presented, whereas the diffusion current caused by a non-zero gradient of charge densities is neglected. The contribution of diffusion to conduction process has been revealed to be insignificant through additional simulations performed in models with and without considering it. For sake of clarity, the results obtained in these calculations are not presented here. The source terms on the right hand sides of Equations (5) and (6) are introduced

below. The term $\rho(x,t)$ on the right hand side of Equation (7) denotes the total space charge density:

$$\rho = q\left(n_h + n_{htr} - n_e - n_{etr}\right) \tag{8}$$

As mentioned, the conduction current through the material bulk is due to drift of the injected carriers associated with hopping between shallow traps. To introduce this mechanism, the apparent effective mobilities $\mu_{e,h}$ in Equation (4) are defined by the depth of shallow traps $\phi_{e,h}$:

$$\mu_{e,h} = \mu_{b(e,h)} \exp\left(-\frac{\phi_{e,h}}{kT}\right) \tag{9}$$

where $\mu_{b(e,h)}$ are band mobilities of the respective carriers.

The intensity of trapping process is characterized by trapping coefficients $t_{e,h}$ which reflect the probability of capturing of charged species per unit of time. The total trapping rates are quantified as:

$$T_{e,h} = t_{e,h} n_{e,h}\left(1 - \frac{n_{etr,htr}}{N_{etr,htr}}\right) \tag{10}$$

where $n_{e,h}$ and $n_{etr,htr}$ are the number densities of the charge carriers, $N_{etr,htr}$ are the total densities of deep traps in the insulating material.

The rates of de-trapping from deep traps, which are considered as potential wells with barrier heights $\phi_{etr,htr}$, are introduced as:

$$DT_{e,h} = \nu n_{etr,htr} \exp\left(-\frac{\phi_{etr,htr}}{kT}\right) \frac{n_{etr,htr}}{N_{etr,htr}} \tag{11}$$

where $\nu = kT/h$ [7] being the attempt-to-escape frequency and h indicating Planck's constant. The dynamics of filling/releasing traps are described by Equation (6).

In the model, it is assumed that recombination of charges of opposite polarities is mainly between trapped and mobile charges and takes place at trapping sites acting as recombination centers. Probability of recombination between two types of mobile charges is significantly lower [1,8] and can be neglected. In general, the recombination processes lead to the loss in quantity of charged species that are expressed using the rates:

$$\begin{aligned} R_{eh} &= r_{eh} n_e n_h \\ R_{etrh} &= r_{etrh} n_{etr} n_h \\ R_{ehtr} &= r_{ehtr} n_e n_{htr} \\ R_{etrhtr} &= r_{etrhtr} n_{etr} n_{htr} \end{aligned} \tag{12}$$

Here, r indicates recombination coefficient and the subscripts *eh*, *etrh*, *ehtr*, *etrhtr* represent recombination between mobile electrons and mobile holes, trapped electrons and mobile holes, mobile electrons and trapped holes, trapped electrons and trapped holes, respectively.

The total rates of generation and losses of mobile and trapped charges in Equations (5) and (6) above can be expressed as:

$$\begin{aligned} S_e &= -R_{eh} - R_{ehtr} - T_e + DT_e \\ S_h &= -R_{eh} - R_{etrh} - T_h + DT_h \\ S_{etr} &= -R_{etrh} - R_{etrhtr} + T_e - DT_e \\ S_{htr} &= -R_{ehtr} - R_{etrhtr} + T_h - DT_h \end{aligned} \tag{13}$$

Note the signs of the terms in Equations (13) which indicate generation (positive rate) or loss (negative rate) mechanisms. Thus, the mobile charges are lost through trapping and recombination and are gained through de-trapping while the latter is the sink of trapped charges.

Finally, the total measurable time-dependent conduction current density through the sample summarizing the contributions from both types of charge carriers is found as:

$$J_{cond}(t) = \frac{1}{L}\int_0^L [j_h(x,t) + j_e(x,t)]\,\mathrm{d}x \tag{14}$$

It is well-known that the measured charging current constitutes two components, namely the displacement and conduction currents. As the polarization is modelled by a constant permittivity, the integration of the displacement current over space leads to a term proportional to the time derivative of the voltage, which vanishes exactly for dc applied voltage. Therefore, Equation (14) gives the total current even in the transient phase. Hence, the simulated current density $J_{\mathrm{cond}}\,(t)$ is used below for comparison with experimentally obtained current density.

The initial and boundary conditions are described as follows. Since a high electric field (32.5 kV/mm) was applied to the insulation in the experiments, the density of charge carriers in the material corresponding to thermal equilibrium prior to voltage application is assumed to be insignificant as compared to the density of injected carriers. Therefore, the densities $n_{\mathrm{e,h}}$ and $n_{\mathrm{etr,htr}}$ are set to zero at $t = 0$. Additionally, if charge carriers of certain polarity reach the counter electrode, no extraction barrier for their ejection is specified in the model. In other words, all electrons arriving to the anode and holes arriving to the cathode disappear from the insulation domain. For this, the outward current densities at corresponding electrodes (*i.e.*, j_{e} at the anode and j_{h} at the cathode) are determined in accordance to Equation (4).

2.2. Computer Implementation

The presented model was utilized for simulations of charge transport in 80 μm thick films of LDPE with and without nanofillers under conditions corresponding to the experiments [17]. It was implemented in finite element software COMSOL Multiphysics. Numerical solutions of the equation system (5)–(7) were obtained in one-dimensional computational domain. Suitable application modes provided in the software were selected for solving the continuity equation (5), ordinary differential equation (6), and Poisson's equation (7). The external conduction current density through the sample was calculated by substituting the transport equation (4) into Equation (14). A non-uniform mesh was created with extremely small elements in the vicinity of both electrodes (the smallest element size 0.1 μm), whereas coarser mesh was kept in the middle of the sample. The coupling of different application modes was implemented so that the densities of charge carriers obtained as solutions of Equations (5) and (6) at every time step were updated in Equation (8) for gaining the total space charge density. This was further utilized in Poisson's equation (7) for deriving the electric field distribution.

3. Results of the Simulations and Discussion

3.1. Charge Transport in LDPE without Nanofillers

The set of model parameters provided an agreement between the computed and measured results is presented in Table 1. The mobility of holes was set close to the values deduced from the measurements [17], while the effective mobility of electrons was approximately one order of magnitude higher than the mobility of holes (as has been found in [20,21]). It should be noted that the potential barrier height at the anode was set to be lower than that at the cathode as the injection of holes from a semiconducting anode was alleviated as compared to the electron injection from a metal cathode [21]. Furthermore, the barrier heights for de-trapping ~1.0 eV were selected in accordance to trap depth level revealed by the results of thermally stimulated currents [22,23] and our calculations [17] based on demarcation energy model. These levels of trap depth are also in agreement with the values used in other numerical model [6]. The trap densities ~10^{21} m^{-3} were set based on the results obtained in [24]. The recombination coefficients were adopted from [6]. Finally, the trapping coefficients were adjusted to achieve the best fit. The commonly accepted relative permittivity ε_r = 2.3 was used for LDPE.

The results of the simulations are presented in Figure 1 together with experimental data. Note that the rapid reduction of the measured currents within first 50–70 s particularly prominent at room temperature and 40 °C in Figure 1, is most likely associated with the decaying displacement current arising due to the application of a step voltage. The conduction current component becomes

dominating only at longer instants after voltage application ($t \geqslant 10^2$–10^3 s) and, hence, simulated and experimental currents can be compared only in this stage. As seen in the figure, the current density at room temperature (~22 °C) predicted by the model agrees well with the measured one. At higher temperatures, the computed characteristics are still in line with experimental data but the agreement is getting worse. Broad maxima appear in the simulated currents and the peaks are shifted to a shorter time as the temperature rises.

Table 1. Parameters used in models for fitting the measured conduction currents on LDPE and its nanocomposites at various temperatures. RT stands for room temperature (~22 °C).

parameters	LDPE			LDPE Nanocomposites		
	RT	**40 °C**	**60 °C**	**RT**	**40 °C**	**60 °C**
Effective mobility						
μ_e, $m^2 \cdot V^{-1} \cdot s^{-1}$	3.0×10^{-14}	1.5×10^{-13}	5.5×10^{-13}	1.0×10^{-14}	3.0×10^{-14}	7.0×10^{-14}
μ_h, $m^2 \cdot V^{-1} \cdot s^{-1}$	2.5×10^{-15}	1.2×10^{-14}	5.0×10^{-14}	2.0×10^{-15}	6.0×10^{-15}	1.4×10^{-14}
Trapping coefficients						
t_e, s^{-1}	0.02	0.08	0.25	0.002	0.022	0.13
t_h, s^{-1}	0.01	0.03	0.08	0.002	0.022	0.13
De-trapping barrier height						
ϕ_{etr}, eV	0.93	0.96	1.00		1.00	
ϕ_{htr}, eV	0.93	0.96	1.00		1.00	
Deep trap density						
N_{etr}, m^{-3}		1.25×10^{21}			6.25×10^{21}	
N_{htr}, m^{-3}		1.25×10^{21}			6.25×10^{21}	
Schottky injection barriers						
ϕ_K, eV		1.22			1.31	
ϕ_A, eV		1.16			1.26	
Recombination coefficients						
r_{etrhtr}, $m^3 \cdot s^{-1}$		6.4×10^{-22}			6.4×10^{-22}	
r_{etrh}, $m^3 \cdot s^{-1}$		6.4×10^{-22}			6.4×10^{-22}	
r_{ehtr}, $m^3 \cdot s^{-1}$		6.4×10^{-22}			6.4×10^{-22}	
r_{eh}, $m^3 \cdot s^{-1}$		0			0	
Relative permittivity						
ε_r		2.3			2.3	

Distributions of space charges in the material bulk obtained from the simulations at room temperature are illustrated in Figure 2. As seen, the positive carriers dominated over the negative ones throughout the simulated time interval. The dynamics of the space charges in the material can be characterized by their transit times determined as the time duration required for charges traversing through the insulation bulk. The arrival of holes to the cathode and electrons to the anode can be traced by using the profiles of mobile charge density shown in Figure 3. Based on that, the transit time ~100 s for electrons and ~1000 s for holes can be identified that

is consistent with the higher (almost one order of magnitude) mobility of electrons as indicated in Table 1. Additionally, the obtained transit times of charge carriers are very close to values calculated as $t_{tr} = L^2/(\mu V_0)$ assuming insignificant accumulation of space charges in the bulk. As it is observed in Figure 2c, the latter is true for the time shorter than the transit time.

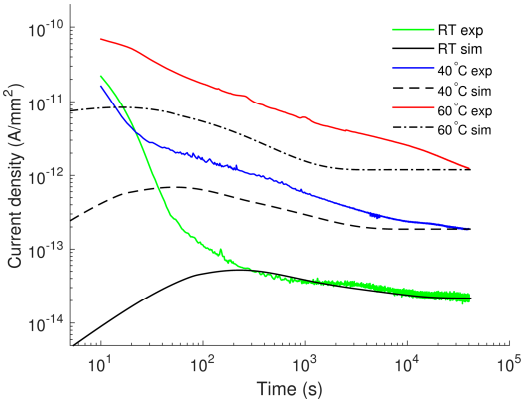

Figure 1. Simulated (referred as "sim" in the legend) and experimental (exp) current densities on LDPE at various temperatures.

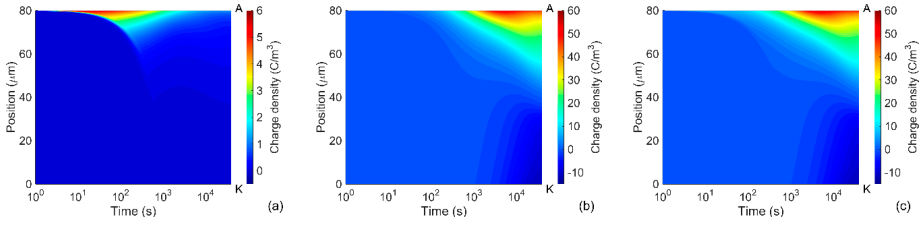

Figure 2. Computed charge density distributions in LDPE at room temperature: (**a**) mobile charges; (**b**) trapped charges; and (**c**) total space charges. Positions of the anode and cathode are indicated by letters A and K, respectively.

During the transport of injected holes towards the cathode, their density reduces remarkably due to the trapping process and most of the mobile carriers concentrate within a thin layer (5–10 μm) at the vicinity of the anode (Figure 2a). The accumulation of mobile positive carriers in the bulk takes place mostly within first 100 s; thereafter, a reduction in their density can be observed. As seen in Figure 2b, immobile positive charges are gradually built up in the vicinity of the anode within the time interval 10^2–10^3 s and its density becomes much higher after 10^3 s. Thus, the immobile charges are strongly dominating over the mobile ones in the material bulk.

The dynamics of positive charge accumulation are controlled by charge injection before 10^2 s and by charge trapping after 10^3 s, while a transition process takes place in the time interval 10^2–10^3 s. A similar tendency is also observed for the negative charges. In particular, the onset of negative charge accumulation in trapping sites close to the cathode is observed at ~10^3 s, which results in a considerable amount of trapped electrons in the bulk after 10^4 s. The variation in the density of the mobile charges leads to the corresponding changes in the simulated conduction current and, hence, a broad maximum appears at time 200–300 s. It should be emphasized that the contribution of mobile electrons to the conduction current cannot be neglected in spite of their remarkably lower density as compared to that of mobile holes. This is because of the higher mobility of electrons than that of holes.

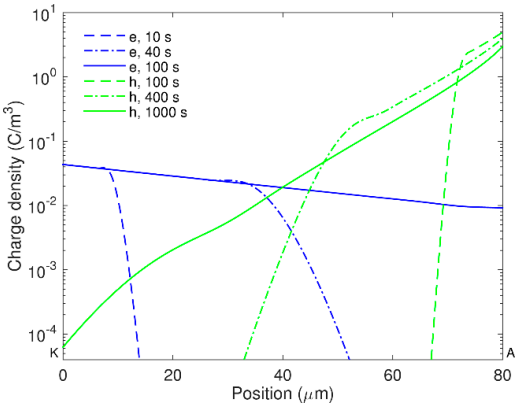

Figure 3. Density profiles of mobile electrons (e) and holes (h) in LDPE at room temperature computed at indicated time.

The distribution and evolution of space charges in LDPE at elevated temperatures are not shown here as the main features presented above are preserved. However, one should mention three distinctions, namely, (a) higher levels of charge densities owing to a larger amount of charges injected at elevated temperatures; (b) faster charge transport processes as charge carriers become more mobile with increasing temperature; and (c) the saturation in the computed conduction currents (see Figure 1) observed at ~10^4 s for 40 °C and at 2×10^3 s for 60 °C. The last feature is not observed within the considered time interval (up to 4×10^4 s) in the simulation at room temperature.

3.2. Charge Transport in LDPE Nanocomposites

In this section, charge transport in LDPE filled with 3 wt % of Al_2O_3 and MgO nanoparticles is studied. As it is indicated [17], the Al_2O_3 particles have

spherical shape with an average diameter of 40 nm, whereas the MgO nanoparticles are in rounded hexagonal shape with an average size of 66 nm and a thickness of 10–20 nm. Since the respective volume fractions of the nanofillers are low (0.7–0.8 vol %), the model used in Section 3.1 can also be employed for heterogeneous materials taking into account the effective medium approximations of properties of the composites. Since the experimental results are very close for both nanocomposites under consideration [17], current densities obtained on LDPE/Al_2O_3 3 wt % are employed for comparison with the simulated ones.

3.2.1. Model Parameterization

As it is shown in the first part of the work [17], the measured dc conductivity is substantially lower for LDPE filled with 3 wt % of nanofillers as compared to the unfilled LDPE that is believed to be associated with the weaken charge transport in the nanofilled materials. By recalling the well-known expression for dc conductivity $\sigma = q\sum n_i\ \mu_i$, (where n_i and μ_i respectively stand for the density and mobility of i^{th} type of charge carriers participating in the transport), the reduction in dc conductivity of nanocomposites can be quantitatively related to the decrease in the density of charge carriers and/or the effective mobility.

Despite the density of mobile charge carriers cannot be monitored separately from trapped carriers in space charge measurements, the concentration of mobile charges is anticipated to be lower in nanocomposites. Significant suppression of space charge accumulation in PE nanocomposites observed in various works [13,18,19] has been interpreted by presence of deep traps. Takada *et al.* [12] explained the origin of the deep traps as potential wells induced at the surface of nanoparticles. The depth of potential wells increases strongly with the applied electric field and the dielectric permittivity of the fillers. Thus for LDPE/MgO nanocomposite, the trap depth may be 1–5 eV with the highest level corresponding to the applied field strength of ~200 kV/mm. Further, the trap depth of ~2 eV has been detected in LDPE/MgO nanocomposite by analyzing results of thermally stimulated currents and the origin of these deep traps have been explained by the effect of nanofillers [25]. Based on these findings, the trap depth should be set higher than that for unfilled LDPE. In addition, increased concentrations of traps has been found in nanofilled PE [24]. Such modifications are expected to enhance capturing of charge carriers injected from the electrodes that may result in thinner layers of homocharges in the vicinity of the electrodes as compared to the case of pure material. These, in turn, may reduce the field strength at the interfaces and so decrease the injected currents [24]. This phenomenon can be identified as a screening effect produced by accumulated homocharges. According to the analysis [13], the screening effect yields a higher barrier height for charge injection at electrodes in case of PE-based nanocomposites as compared to the unfilled counterpart. Considering these modifications in material

properties brought about by nanofillers, the barrier heights for charge injection at both electrodes were increased by up to 0.1 eV and the density of deep traps rose in five times for the nanocomposites as compared to the reference LDPE (see Table 1). As regards the mobility of charge carriers in nanocomposites, reduced values have been found experimentally [17], which can be elucidated by the alternation in the amorphous region of PE by nanoparticles [26].

According to results of dielectric spectroscopy measurements [27] conducted on LDPE and LDPE/Al_2O_3 3 wt % nanocomposite in frequency range 10^{-4}–10^3 Hz and at three temperatures considered in the model, the relative permittivity was slightly higher (maximum 5%) for the nanocomposite than for reference LDPE. Additionally, the frequency dependencies of the relative permittivity were weak for both materials. The relative permittivity of LDPE nanocomposite was therefore set to 2.3 as for the unfilled LDPE.

3.2.2. Results

The experimental and computed currents in the nanomaterial are compared in Figure 4. Unlike the case of pure LDPE, the conduction current densities predicted by the model show good agreement with the measured ones at all three considered temperatures. At each temperature, the localized peak in the simulated conduction current appears later for the nanocomposite as compared to reference LDPE (Figure 1) due to the lower mobility of charge carriers in nanofilled material.

Distributions of charge densities in the bulk of the nanocomposite are shown in Figure 5 for room temperature. Similarly to the reference LDPE, positive charge carriers are dominating in the material and they are mainly concentrated in a thin layer at the vicinity of the anode. As expected, the amount of charges accumulated in the bulk of LDPE nanocomposite is significantly smaller as compared to that in the reference material. Thus, the maximum density of mobile carriers is almost 50 times lower (compare Figures 2a and 5a) while the total space charge density is less than 5 C/m^3 in most part of the nanocomposite (positions 0–70 μm) and its maximum at the anode is below 9 C/m^3, Figure 5c. In the unfilled LDPE, the space charges with density exceeding 5 C/m^3 propagate deeply into the bulk and its maximum is at least six times higher (~55 C/m^3), see Figure 2c. As a result, the electric field is strongly enhanced inside the reference material, but this is not the case for the nanocomposite. As it is seen in Figure 6, the distortion in electric field distribution in the nanofilled material is negligible at 1 h after voltage application and only small (~7%) field enhancement is observed at the vicinity of the cathode at 4×10^4 s. On the contrary, an appreciable enhancement (~25%) can be noticed in the middle of the sample of the unfilled LDPE at 4×10^4 s.

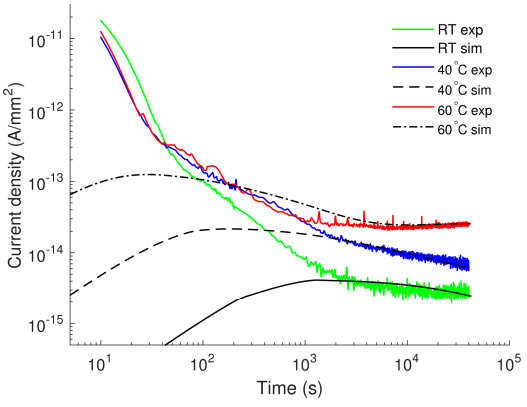

Figure 4. Current densities obtained from simulations (sim) and experiments (exp) on LDPE/Al_2O_3 nanocomposite at various temperatures.

The quantity of accumulated positive space charges (dominating carriers) calculated as:

$$Q(t) = \int_0^L q\left[\mathrm{n}_h\left(x,t\right) + \mathrm{n}_{htr}\left(x,t\right)\right]\mathrm{d}x \tag{15}$$

is presented as a function of time in Figure 7 for all three temperatures. As seen, the amount of charge steadily rises with time and eventually reaches a saturation level ~10^{-3} C/m^2. The charge magnitudes are lower in the LDPE nanocomposite for all studied temperatures and the differences are more than one order of magnitude in the short time interval, whereas they become smaller at longer time. For simulations at elevated temperatures and time exceeding 10^4 s, the total positive charges are comparable in both materials.

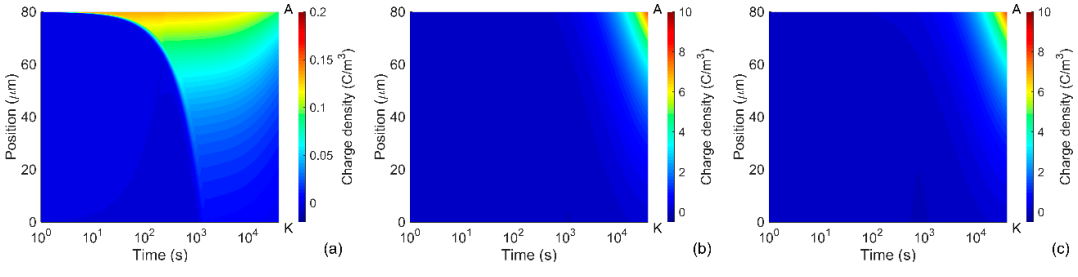

Figure 5. Distributions of charge densities in LDPE nanocomposite obtained from simulations at room temperature: (**a**) mobile charges; (**b**) trapped charges; and (**c**) total space charges. Positions of the anode and cathode are indicated by letters A and K, respectively.

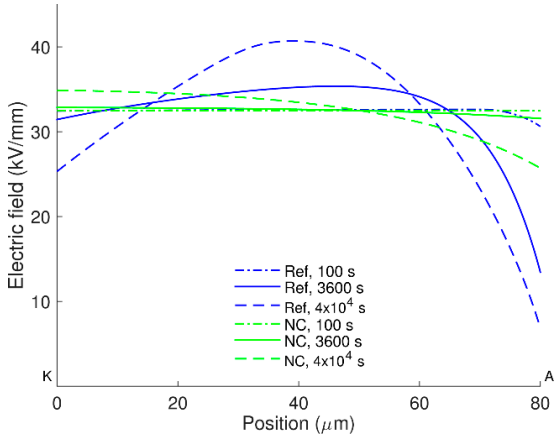

Figure 6. Electric field distributions in LDPE without (Ref) and with (NC) nanofillers at room temperature.

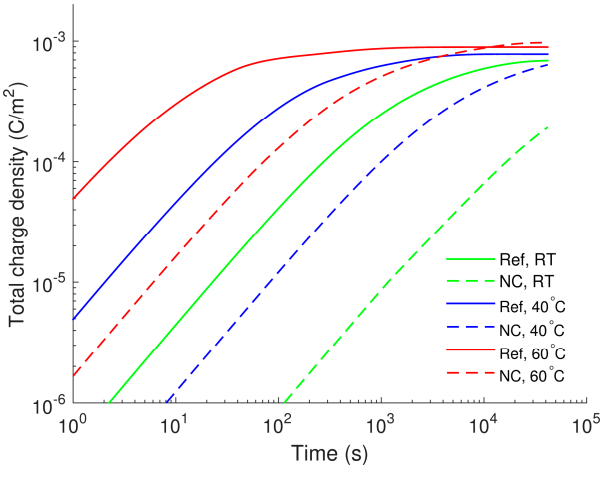

Figure 7. Amount of positive charges accumulated in the bulk of LDPE (Ref) and LDPE nanocomposite (NC).

3.3. Influence of Different Physical Processes on Charge Transport

As discussed above, the weakening in charge transport in nanofilled LDPE as compared to the unfilled one can be attributed to the reduced charge injection at electrode-insulation interfaces, to the decreased charge carrier mobility, to the increased probability of charge capturing in and the decrease of charge release from deep traps. However, it is unclear which process among the above-mentioned mainly contributes to the lowering of the conduction in LDPE nanocomposite. In

other words, what behavior of insulation is changed most noticeable due to the addition of nanofillers into LDPE?

To address this question, we assume that only one type of parameters incorporated in the model for pure LDPE and associated with a certain physical process is modified at a time to the values used in the model of LDPE nanocomposite (Table 1), while all other parameters are kept unchanged. Thus, four scenarios are considered as described in Table 2 and the obtained results (conduction currents at temperature 40 °C) are illustrated in Figure 8, where the simulated currents in LDPE and its nanocomposite are also shown for comparison. As can be seen, the conduction current drops significantly down to the level close to that in the nanocomposite while increasing the injection barriers alone and less pronounced decline is observed in three other situations. The effect of charge mobility on the conduction current is almost the same in the studied time interval, whereas the influence of trap energy (φ_{tr}) and trap density (N_{tr}) is remarkable only at times exceeding 10^4 s. Based on the results of the analysis, we found that the decrease in charge injection at the electrodes mainly accounts for the weakening of conduction in LDPE nanocomposite and so for the suppression of space charge build-up in the bulk.

Table 2. Scenarios for simulations with varying parameters. Model parameters of each scenario are the same as for simulating charge transport in LDPE, except for those provided in the right column. Charge mobilities (in $m^2 \cdot V^{-1} \cdot s^{-1}$) are listed in order of increasing temperature (RT; 40 °C; 60 °C).

Scenario	Description	Model parameters	Modified parameters
#1	Reduction of charge injection at electrodes	Charge injection barrier heights as for the nanocomposite, all other parameters as for LDPE	ϕ_K = 1.31 eV ϕ_A = 1.26 eV
#2	Reduction of charges released from deep traps	De-trapping barrier heights as for the nanocomposite, all other parameters as for LDPE	ϕ_{etr} = 1.00 eV ϕ_{htr} = 1.00 eV
#3	Reduction of charge carrier mobility	Mobility of electrons and holes as for the nanocomposite, all other parameters as for LDPE	$\mu_e = 1 \times 10^{-14}; 3 \times 10^{-14}; 7 \times 10^{-14}$ $\mu_h = 2 \times 10^{-15}; 6 \times 10^{-15}; 1.4 \times 10^{-14}$
#4	Increase of trap densities	Trap densities as for the nanocomposite, all other parameters as for LDPE	$N_{etr} = 6.25 \times 10^{21}$ m^{-3} $N_{htr} = 6.25 \times 10^{21}$ m^{-3}

The contribution of charge recombination to the conduction current is examined by considering charge transport models with and without accounting for this particular process. The simulated conduction currents in both materials are compared in Figure 9. As it is found, charge recombination is essential in pure material and in the nanocomposite at 60 °C. Neglecting this process yields a rapid rise of the simulated currents, especially at elevated temperatures. The marked increase in the conduction currents obtained in the model without recombination is due to the

excess of mobile charges in the bulk, which would be neutralized if recombination is included. In this context, it is interesting to observe that such neutralization is not of importance for the nanofilled material at room temperature and at 40 °C. The differences in the simulated outcomes for LDPE with and without nanoparticles can be attributed to the strong distinctions in the amount of charge carriers generated in these materials. The obtained results also indicate that charge recombination cannot be underestimated in the charge transport model at elevated temperatures, even though its contribution is minor at room temperature.

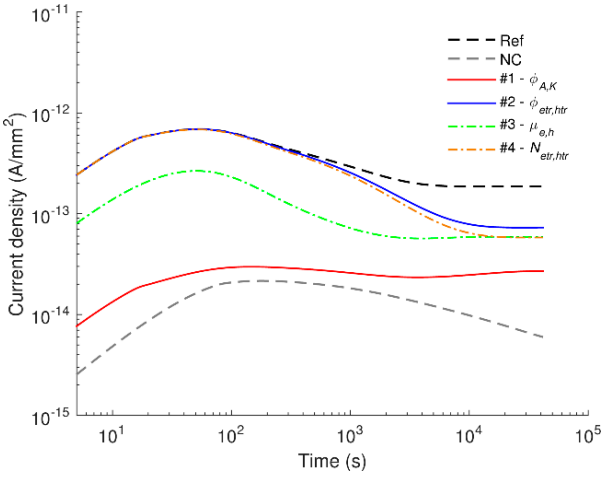

Figure 8. Simulated conduction currents at 40 °C obtained by varying model parameters. Four scenarios are considered as shown in Table 2. The parameters being changed are indicated in the legend.

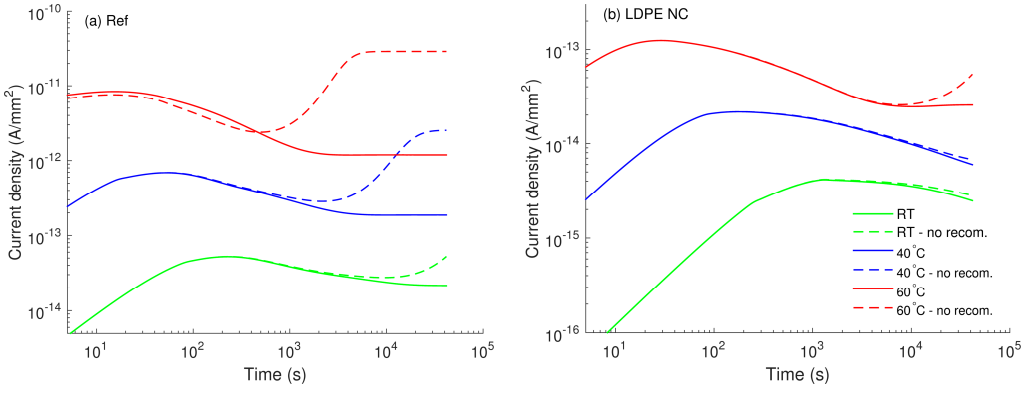

Figure 9. Simulated conduction currents obtained from models with (solid curves) and without (dashed curves) charge recombination.

3.4. Discussion

As mentioned above, broad maxima are observed in the simulated time variations of the current densities and the time t_p corresponding to the current peaks is temperature-dependent (see Figures 1 and 4). These localized peaks are not exhibited in our experimental results [17]. Indeed, localized peaks are often detected in time-domain currents measured on oxidized LDPE [28] rather than on the non-oxidized counterpart [29]. Their appearance has been explained by the high concentration of carbonyl groups (–C=O) in the former material as compared to the latter. The carbonyl groups give rise to the hopping transport of mobile charge carriers in the bulk that eventually increases the conduction current [28]. Current maxima are therefore observed as a consequence of the build-up of significant mobile charges in the bulk [30]. In contrast, lower conduction currents are detected for the non-oxidized PE and the peaks are most probably hidden by the displacement current. The latter arises in transient processes activated by the voltage application due to orientation of polar groups existing in PE. In LDPE samples used in this investigation, the presence of antioxidant is anticipated to suppress the formation of carbonyl groups that explains the absence of the current maxima in the measured charging currents. Nevertheless, the current maxima in the simulated characteristics are of interest. According to the analysis by Many and Rakavy [30] for a single-carrier model in trap-free materials, the peak of transient current corresponds to the arrival of charges at the counter electrode. The peak time t_p can be found as $t_p = 0.787 \times t_{tr}$, where $t_{tr} = L^2/(\mu V_0)$. Unlike the case of trap-free materials, different features are noted in the bipolar charge transport model for materials with traps. As charge trapping strongly reduces the density of mobile carriers, their total density and the current density achieve maxima well before the arrival of the dominating charge carriers at the counter electrode. Thus, in a correlation between t_p and t_{tr} established by using results obtained in Sections 3.1 and 3.2.2 the multiplication factor should be much lower than 0.787.

Another noteworthy feature is that the accumulation of trapped charges in the unfilled LDPE at elevated temperatures becomes saturated after certain time, e.g., at 2×10^3 s at 60 °C. As the trapped charges constitute the main part of the space charges, the same tendency is observed for the latter, yielding unchanged electric field distribution in the insulation bulk afterward. This eventually causes the steady state of simulated current density as seen in Figure 1. In order to avoid the early saturation in the simulated external current density, the trapping coefficients have been adjusted as increasing with temperature, which can be interpreted as the increased probability of charge trapping due to the presence of an increased amount of charges generated at higher temperatures. However, we realized that the steady state in the current density is persistent for simulations at elevated temperatures and it is unavoidable for the described model of charge transport. In fact, the saturation

in the simulated trapped charges has been noted in [5] at 9×10^3 s and the saturated conduction currents are clearly illustrated in [14]. In both cases, the simulations of charge transport were implemented for the conditions of ambient temperature. Note that at room temperature, the steady state in the simulated characteristics is not exhibited within the considered time range in the present study; it only arises at elevated temperatures. The effect of temperature on the saturation of the simulated characteristics could be attributed to the fact that the injected currents described by Schottky's law, Equations (1) and (2), may not fully reflect the physical processes at the electrodes. According to Schottky's law, the amount of injected mobile carriers at the electrodes increases substantially with temperature and, hence, the traps in the insulation bulk can be filled more easily at higher temperatures, yielding the premature saturation in the density of trapped charges and so for the simulated conduction currents.

The applicability of Schottky's mechanism for charge injection at electrode-insulation interfaces is in fact questionable [31]. First of all, the distance x_{max} from the electrode corresponding to the maximum of potential barrier is too long so that an electron may be thermalized by collisions before reaching the barrier [31]. Secondly, the barrier height for injection used in simulations (~1.1–1.3 eV) is much smaller than that at metal-PE interfaces obtained by using density functional theory (DFT) calculations, e.g., [32]. Taylor and Lewis [33] analyzed currents measured on thin films of polyethylene terephthalate (PET) and PE exposed to a wide range of applied electric field at various temperatures and proposed an alternative to Schottky's mechanism where a general form followed Equation (16) instead of the coulombic form by Equation (17) of the potential barrier at electrodes is utilized:

$$\phi_G(x) = -\frac{Kq}{(ax)^n} \tag{16}$$

$$\phi_C(x) = -\frac{q^2}{16\pi\varepsilon x} \tag{17}$$

In Equation (16), K, a, and n are positive constants, K accounts for contributions of the charge q and material permittivity ε presented in the coulombic form of Equation (17). In Equations (16) and (17), x is the distance from the electrode. The widely used Schottky injection law with the coulombic form of the potential barrier is a special case of the general form when the exponent n equals unity. For PET and PE, it has been found that the constant n is much lower than unity. The departure from the image-law potential barrier according to Equation (17) has been explained by space charge build-up at the interfaces and in the insulation bulk as well [33]. Additionally, zero-field activation energies derived for PET and PE were respectively 2.58 and 2.14 eV, which were interpreted as the potential barriers of the general law [33]. These values are closer to the results of DFT calculations obtained recently [32] as

compared to the commonly used ones in the simulations. It should be mentioned that transient processes due to charge trapping, de-trapping, and recombination in the bulk have not been considered in these analyses [33] and, hence, the proposed approach should be reconsidered by taking into account the bulk processes. This may provide better explanation of experimental data obtained for the reference LDPE at elevated temperatures.

4. Conclusions

Charge transport in LDPE and its nanocomposites at different temperatures has been studied by numerical simulations. By achieving a good agreement between simulated and measured conduction currents, we reveal quantitative changes in various physical processes taking place in the insulating materials caused by the presence of nanofillers. In particular, the weakening charge transport in the nanodielectrics as compared to the unfilled LDPE is associated with the increased barrier heights for charge injection at electrodes, the reduced charge mobility, and the increased trap energy and trap density. Simulated results also demonstrate that space charge accumulation and electric field enhancement are less noticeable in LDPE nanocomposites than in the unfilled counterpart. The reduced conduction currents and the suppression of space charge accumulation in nanofilled LDPE are most likely governed by the modification of the barrier heights for charge injection at the dielectric-electrode interfaces. Furthermore, the application of Schottky's mechanism for describing charge injection at electrodes in the simulation is still questionable as it does not fully explain the thermally activated behavior of the conduction currents obtained experimentally.

Acknowledgments: The financial support provided by Chalmers Area of Advance in Energy and Swedish Foundation for Strategic Research is gratefully acknowledged.

Author Contributions: Anh T. Hoang implemented the computer model, performed simulations and analyzed the results. Yuriy V. Serdyuk contributed to the development of the computer model and interpretation of the results. Stanislaw M. Gubanski provided support for the analysis of the data. All authors discussed the results and contributed to the preparation of the manuscript.

Conflicts of Interest: The authors declare no conflict of interest.

References

1. Alison, J.M.; Hill, R.M. A model for bipolar charge transport, trapping and recombination in degassed crosslinked polyethene. *J. Phys. D Appl. Phys.* **1994**, *27*, 1291–1299.
2. Li, Y.; Takada, T. Experimental observation of charge transport and injection in XLPE at polarity reversal. *J. Phys. D Appl. Phys.* **1992**, *25*, 704–716.

3. Fukuma, M.; Nagao, M.; Kosaki, M. Computer Analysis on Transient Space Charge Distribution in Polymer. In Proceedings of the 4th International Conference on Properties and Applications of Dielectric Materials, Brisbane, Queensland, Australia, 3–8 July 1994.
4. Kaneko, K.; Mizutani, T.; Suzuoki, Y. Computer simulation on formation of space charge packets in XLPE films. *IEEE Trans. Dielectr. Electr. Insul.* **1999**, *6*, 152–158.
5. Le Roy, S.; Segur, P.; Teyssedre, G.; Laurent, C. Description of bipolar charge transport in polyethylene using a fluid model with a constant mobility: Model prediction. *J. Phys. D Appl. Phys.* **2004**, *37*, 298–305.
6. Le Roy, S.; Teyssedre, G.; Laurent, C.; Montanari, G.C.; Palmieri, F. Description of charge transport in polyethylene using a fluid model with a constant mobility: Fitting model and experiments. *J. Phys. D Appl. Phys.* **2006**, *39*, 1427–1436.
7. Boufayed, F.; Teyssèdre, G.; Laurent, C.; Roy, S.L.; Dissado, L.A.; Ségur, P.; Montanari, G.C. Models of bipolar charge transport in polyethylene. *J. Appl. Phys.* **2006**, *100*, 104105.
8. Serdyuk, Y.V.; Gubanski, S.M.; Mohammad, A.S. Computer Simulations of Space Charge Dynamics and Electric Fields in HVDC Cable Insulation. In Proceedings of the 15th International Symposium on High Voltage Engineering, Ljubljana, Slovenia, 27–31 August 2007; p. T8-405.
9. Le Roy, S.; Vu, T.T.N.; Laurent, C.; Teyssedre, G. Modelling charge generation and transport in solid organic dielectrics under DC stress. In Proceedings of the European Seminar on Materials for HVDC Cables and Accessories: Performance, Modeling, Testing, Qualification (Jicable HVDC'13), Perpignan, France, 18–20 November 2013; p. 4.1.
10. Taleb, M.; Teyssedre, G.; Le Roy, S.; Laurent, C. Modeling of charge injection and extraction in a metal/polymer interface through an exponential distribution of surface states. *IEEE Trans. Dielectr. Electr. Insul.* **2013**, *20*, 311–320.
11. Baudoin, F.; Laurent, C.; Teyssedre, G.; Le Roy, S. Charge packets modeling in polyethylene. *Appl. Phys. Lett.* **2014**, *104*, 152901.
12. Takada, T.; Hayase, Y.; Tanaka, Y.; Okamoto, T. Space charge trapping in electrical potential well caused by permanent and induced dipoles for LDPE/MgO nanocomposite. *IEEE Trans. Dielectr. Electr. Insul.* **2008**, *15*, 152–160.
13. Zhang, L.; Zhou, Y.; Tian, J.; Sha, Y.; Zhang, Y.; Wu, H.; Wang, Y. Experiment and simulation of space charge suppression in LDPE/MgO nanocomposite under external DC electric field. *J. Electrostat.* **2014**, *72*, 252–260.
14. Min, D.; Wang, W.; Li, S. Numerical analysis of space charge accumulation and conduction properties in LDPE nanodielectrics. *IEEE Trans. Dielectr. Electr. Insul.* **2015**, *22*, 1483–1491.
15. Fleming, R.J.; Ammala, A.; Lang, S.B.; Casey, P.S. Conductivity and space charge in LDPE containing nano- and micro-sized ZnO particles. *IEEE Trans. Dielectr. Electr. Insul.* **2008**, *15*, 118–126.
16. Murakami, Y.; Nemoto, M.; Okuzumi, S.; Masuda, S.; Nagao, M.; Hozumi, N.; Sekiguchi, Y. DC conduction and electrical breakdown of MgO/LDPE nanocomposite. *IEEE Trans. Dielectr. Electr. Insul.* **2008**, *15*, 33–39.

17. Hoang, A.T.; Pallon, L.; Liu, D.; Serdyuk, Y.V.; Gubanski, S.M.; Gedde, U.W. Charge transport in LDPE nanocomposites Part I—Experimental approach. *Polymers* **2016**, *8*, 87.
18. Hayase, Y.; Aoyama, H.; Tanaka, Y.; Takada, T.; Murata, Y. Space Charge Formation in LDPE/MgO Nano-Composite Thin Film under Ultra-High DC Electric Stress. In Proceedings of the 8th International Conference on Properties and Applications of Dielectric Materials, Bali, Indonesia, 26–30 June 2006; pp. 159–162.
19. Kanegae, E.; Ohki, Y.; Tanaka, T.; Sekiguchi, Y.; Murata, Y.; Reddy, C.C. Space Charge Behavior in Multi-Layered Dielectrics with LDPE and LDPE/MgO Nanocomposites. In Proceedings of the 10th IEEE International Conference on Solid Dielectrics (ICSD), Potsdam, Germany, 04–09 July 2010; pp. 1–4.
20. Toomer, R.; Lewis, T.J. Charge trapping in corona-charge polyethylene films. *J. Phys. D Appl. Phys.* **1980**, *13*, 1343–1356.
21. Chen, G.; Tay, T.Y.G.; Davies, A.E.; Tanaka, Y.; Takada, T. Electrodes and charge injection in low-density polyethylene using the pulsed electroacoustic technique. *IEEE Trans. Dielectr. Electr. Insul.* **2001**, *8*, 867–873.
22. Fischer, P.; Röhl, P. Thermally stimulated and isothermal depolarization currents in low-density polyethylene. *J. Polym. Sci.* **1976**, *14*, 531–542.
23. Mizutani, T.; Suzuoki, Y.; Ieda, M. Thermally stimulated currents in polyethylene and ethylene–vinyl-acetate copolymers. *J. Appl. Phys.* **1977**, *48*, 2408–2413.
24. Tian, F.; Lei, Q.; Wang, X.; Wang, Y. Effect of deep trapping states on space charge suppression in polyethylene/ZnO nanocomposite. *Appl. Phys. Lett.* **2011**, *99*, 142903.
25. Ishimoto, K.; Tanaka, T.; Ohki, Y.; Sekiguchi, Y.; Murata, Y. Thermally stimulated current in low-density polyethylene/MgO nanocomposite. On the mechanism of its superior dielectric properties. *Electr. Eng. Jpn.* **2011**, *176*, 1–7.
26. Lewis, T.J. Charge transport in polyethylene nano dielectrics. *IEEE Trans. Dielectr. Electr. Insul.* **2014**, *21*, 497–502.
27. Hoang, A.T.; Serdyuk, Y.V.; Gubanski, S.M. Dielectric spectroscopy measurements in frequency range 10^{-4}–10^{3} Hz and at various temperatures (ambient temperature, 40 and 60 °C) show similarity in the relative permittivities of the reference LDPE and LDPE/Al_2O_3 3 wt % nanocomposite as well as their weak dependencies on frequency, 2015.
28. Fischer, P.; Röhl, P. Transient currents in oxidized low-density polyethylene. In *Mehrphasige Polymersysteme*; Fischer, E.W., Horst Müller, F., Kausch, H.H., Eds.; Steinkopff: Heidelberg, Germany, 1977; Volume 62, pp. 149–153.
29. Pelissou, S.; St-Onge, H.; Wertheimer, M.R. Electrical conduction of polyethylene below and above its melting point. *IEEE Trans. Electr. Insul.* **1988**, *23*, 325–333.
30. Many, A.; Rakavy, G. Theory of transient space-charge-limited currents in solids in the presence of trapping. *Phys. Rev.* **1962**, *126*, 1980–1988.
31. Teyssedre, G.; Laurent, C. Charge transport modeling in insulating polymers: From molecular to macroscopic scale. *IEEE Trans. Dielectr. Electr. Insul.* **2005**, *12*, 857–875.

32. Chen, L.; Tran, D.H.; Quintero, Y.C.; Ramprasad, R. Charge injection barriers at metal/polyethylene interfaces. *J. Mater. Sci.* **2015**, *51*, 506–512.
33. Taylor, D.M.; Lewis, T.J. Electrical conduction in polyethylene terephthalate and polyethylene films. *J. Phys. D Appl. Phys.* **1971**, *4*, 1346–1357.

Crosslinked Poly(2-oxazoline)s as "Green" Materials for Electronic Applications

Martin Fimberger, Ioannis-Alexandros Tsekmes, Roman Kochetov, Johan J. Smit and Frank Wiesbrock

Abstract: Poly(2-nonyl-2-oxazoline)$_{80}$-*stat*-poly(2-dec-9′-enyl-2-oxazoline)$_{20}$ and poly(2-dec-9′-enyl-2-oxazoline)$_{100}$ can be synthesized from the cationic ring-opening polymerization of monomers that can be derived from fatty acids from renewable resources. These (co)poly(2-oxazoline)s can be crosslinked with di- and trifunctional mercapto compounds using the UV-induced thiol-ene reaction. The complex permittivity of the corresponding networks increases with the temperature and decreases with the network density. In a frequency range from 10^{-2} to 10^{6} Hz and at temperatures ranging from -20 to 40 °C, the changes of the real part of the complex permittivity as well as the loss factor can be explained by interfacial polarization within the material. At a temperature of 20 °C and a frequency of 50 Hz, the permittivity of the crosslinked (co)poly(2-oxazoline)s covers a range from 4.29 to 4.97, and the loss factors are in the range from 0.030 to 0.093. The electrical conductivities of these polymer networks span a range from 5×10^{-12} to 8×10^{-9} S/m, classifying these materials as medium insulators. Notably, the values for the permittivity, loss factor and conductivity of these copoly(2-oxazoline)s are in the same range as for polyamides, and, hence, these copoly(2-oxazoline)-based networks may be referred to as "green" alternatives for polyamides as insulators in electronic applications.

Reprinted from *Polymers*. Cite as: Fimberger, M.; Tsekmes, I.-A.; Kochetov, R.; Smit, J.J.; Wiesbrock, F. Crosslinked Poly(2-oxazoline)s as "Green" Materials for Electronic Applications. *Polymers* **2016**, *8*, 6.

1. Introduction

Poly(2-oxazoline)s can be synthesized from the cationic ring-opening polymerization of 2-oxazolines (Scheme 1). Their common structural motif is the amide bond of their side-chains; hence, poly(2-oxazoline)s may be referred to as pseudo-polyamides. The properties of these polymers can be adjusted by *in situ* and polymer analogous reactions [1–3]. In the last decade, crosslinking of these materials by (co)polymerizations with (at least) bifunctional 2-oxazoline monomers (*in situ* approach) [4,5] as well as the UV-induced crosslinking (often by "click" reactions during a polymer analogous approach) [6–8] have received renewed attention, benefiting in part from the increased research activities in the area of poly(2-oxazoline)s that coincides with the advent of microwave reactors in polymer

scientists' laboratories [9,10]. A dedicated focus is directed towards the application of crosslinked poly(2-oxazoline)s in the medicinal sector [11,12].

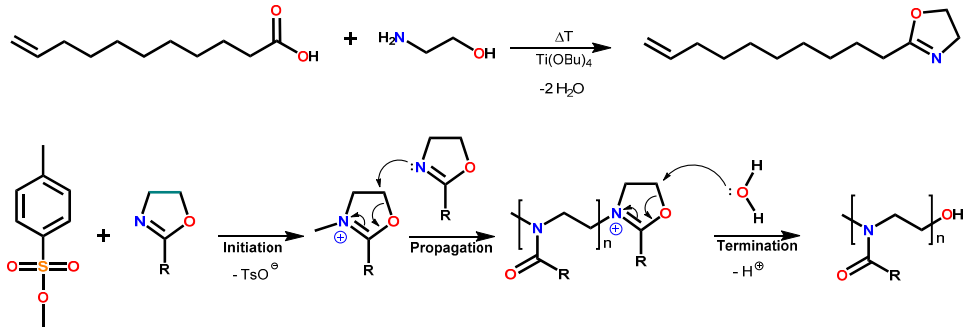

Scheme 1. Schematic representations of the synthesis of 2-oxazoline monomers from carboxylic acids (**top**) and the cationic ring-opening polymerization of 2-oxazolines (**bottom**).

UV-induced polymer analogous crosslinking of (co)poly(2-oxazoline)s by, e.g., the thiol-ene click reaction (Scheme 2), offers numerous advantages over the *in situ* crosslinking, despite the fact that an additional reaction step is required: The formulation containing the "ene" component (commonly a (co)poly(2-oxazoline) with olefinic functionalities in the side-chains), the "thiol" component (which, for crosslinking, must be an oligofunctional thiol), the UV-labile photoinitiator such as Irgacure TPO-L (2,4,6-trimethylbenzoylphenyl phosphinate; Scheme 2), and the solvent may be spin- or dropcast prior to the removal of the solvent, enabling the production of specimen with the envisaged geometry. As the thiol-ene reaction can be initiated by UV stimuli, the crosslinking reaction may proceed at room temperature, and polymer degradation and/or decomposition of temperature-sensitive parts of the network are kept at a minimum. Furthermore, spatial resolution of the crosslinking reaction can be achieved if the UV irradiation is applied through a geometric mask, yielding 2.5-dimensional polymer structures after dissolving the non-crosslinked parts of the polymer film. The term "2.5-dimensional" refers to the fact that a three-dimensional structure cannot be generated by this technique; the surface of the substrate is either covered by a photoresist (with identical height along the substrate) or not covered at all [13–15].

Notably, 2-oxazoline monomers with olefinic functionalities can be synthesized from the reaction of ethanol amine with fatty acids from renewable resources such as undec-10-enoic acid from castor oil [15]. This "green approach" towards the fabrication of polymer-based networks opens a plethora of novel application fields for this type of materials, including electronic devices such as pacemaker leads and high-voltage engineering devices such as "green" transformers.

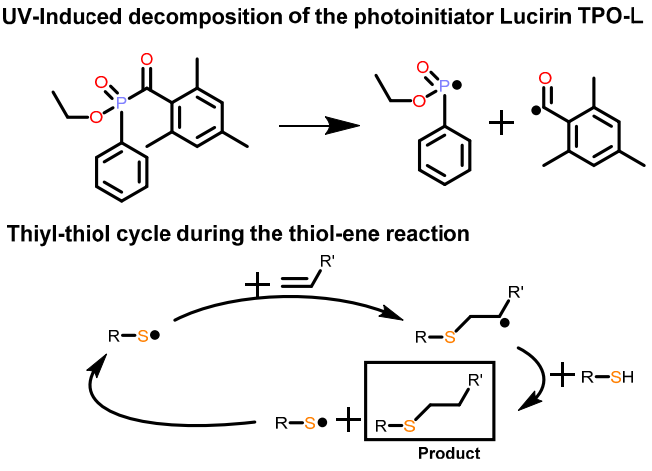

Scheme 2. Schematic representations of the decomposition of the photoinitiator (**top**) and the thiol-thiyl cycle of the thiol-ene reaction (**bottom**).

From this background, the present study aimed at determining the dielectric characteristics of crosslinked (co)poly(2-oxazoline)s from renewable resources. This study was motivated in particular by the demand for novel, polymer-based insulator materials with low or no impact on the production environment and "switchable" crosslinking routines, e.g., crosslinking reactions that take place only after the application of stimuli such as UV irradiation. In contrast to thermally induced crosslinking that commonly starts immediately after the application of the polymer-based insulator formulation, the stimuli-triggered crosslinking renders more flexibility to production routines in general and to their schedule in particular. Furthermore, highly crosslinked polymer networks inherently offer advantages over their non-crosslinked analogues, such as higher rigidity/strength, insolubility, and the absence of a melting point. Consequently, a large field of (potential) applications opens for insulators based on polymer networks, comprising high-voltage outdoor applications [16,17]. Hence, three different poly(2-oxazoline)-based networks (with varying crosslinking degrees and composition of repetition units) were synthesized in this study in order to establish a first (fundamental) data set for the electronic properties of "green" (co)poly(2-oxazoline)-based networks. In particular, the permittivity, loss factor, and electrical conductivity were focused on, with special respect to the comparison with polymer classes such as polyamides, polyesters, and epoxy resins currently used as insulators in electronic applications (Table 1) [18].

Table 1. Density (at 20 °C), dielectric parameters (permittivity and loss factor, both at 20 °C and 50 Hz), and conductivity (20 °C, 50% r.h.) of polyamides, polyesters, and epoxy resins [18].

Parameter	Polymer		
	Polyamides	**Polyesters**	**Epoxy Resins**
Density ($g \cdot cm^{-3}$)	1.13–1.21	1.22–1.26	1.10–1.25
Permittivity	3.6–7	3–4.9	3.7–4.2
Loss factor	0.014–0.15	0.008–0.06	0.007–0.009
Conductivity ($S \cdot m^{-1}$)	10^{-11}–10^{-6}	10^{-13}–10^{-12}	10^{-15}–10^{-14}

2. Experimental Section

2.1. Materials

Unless indicated otherwise, all materials have been purchased from Sigma-Aldrich (Vienna, Austria). Irgacure TPO-L was purchased from ABCR (Karlsruhe, Germany). The 2-oxazoline monomers were prepared according to literature protocols [19,20]. Methyl tosylate was distilled prior to use, all other chemicals were used as received. The solvents acetonitrile and dichloromethane were purchased at Carl Roth (Vienna, Austria).

2.2. Instrumentation

^{1}H-NMR and ^{13}C-NMR spectra were acquired on a Bruker 300 MHz NMR spectrometer (Bruker BioSpin Corporation, Billerica, MA, USA) with a relaxation times of 4 s and 32 scans for ^{1}H-NMR spectra, and a relaxation time of 2 s and 1024 scans for ^{13}C-NMR spectra. The solvent signal of $CDCl_3$ at 7.26 ppm for ^{1}H-NMR spectra (77 ppm for ^{13}C-NMR spectra) was used for referencing. All polymer syntheses were performed with a Biotage Initiator 8 microwave reactor (Biotage, Uppsala, Sweden) at a temperature of 140 °C. The microwave vials were dried prior to use at 80 °C for at least 1 h. FT-IR spectra were recorded on a Bruker Alpha FT-IR spectrometer (Bruker Optics Inc., Billerica, MA, USA) applying an ATR unit over a spectral range from 500 to 4000 cm^{-1}. A background correction was performed prior to the measurements. For each sample, 32 scans were recorded. Size-exclusion chromatography (SEC) measurements were performed on a Shimadzu SEC system (Shimadzu Austria, Vienna, Austria) with a Shimadzu LC-20AD pump, a SIL-20ACHT sampler and an RID202A refractive index detector. A styrene-divinyl benzene copolymer network-based linear XL 5 μm column (PSS-SDV by Polymer Standards Service, Mainz, Germany) was used. As eluent, a mixture of chloroform/triethylamine/*iso*-propanol (94/4/2) was used at a flow rate of 1 mL/min. The results were referenced to polystyrene standards. For

the production of test specimens, a Collin platen press P 200 PV (Dr. Collin GmbH, Ebersberg, Germany) was used. For the irradiation of the samples, a Novacure broadband UV-lamp by EFOS (EFOS, Mississauga, ON, Canada) was applied, and the samples were irradiated at 4500 $mW \cdot cm^{-2}$ from a distance of 10 cm. Conductivity measurements were performed in a three-terminal cell with a Keithley 617 electrometer (Tektronix, Eindhoven, The Netherlands). The cell was equipped with a protective serial resistor. The poling voltage was supplied via a Rogowski-profiled electrode made of aluminum. For the dielectric characterization, a Novocontrol Alpha-A dielectric analyzer (Novocontrol Technologies, Montabaur, Germany) was used applying a ZGS Alpha extension test interface as active cell. For temperature control, a Quatro cryosystem (Novocontrol Technologies, Montabaur, Germany) with an accuracy and stability of 0.1 and 0.01 K, respectively, was used. For the measurement of the dielectric properties, a sinoidal voltage of 3 V was applied to the samples.

2.3. Polymer Syntheses

All poly(2-oxazoline)s and copoly(2-oxazoline)s were synthesized from the corresponding monomers according to literature protocols [21].

2.3.1. Poly(2-nonyl-2-oxazoline)$_{80}$-*stat*-poly(2-dec-9′-enyl-2-oxazoline)$_{20}$, pNonOx$_{80}$-*stat*-pDc$^{=}$Ox$_{20}$

For the experiment, 81.2 mg of methyl tosylate were dissolved in 10 mL of dry dichloromethane in a 20 mL microwave vial. 1.860 g of 2-dec-9′-enyl-2-oxazoline and 6.865 g of 2-nonyl-2-oxazoline were added. Subsequently, the vial was sealed under inert conditions and the mixture heated at 140 °C for 2 h. The product was recovered as a white solid in a quantitative yield by removal of the solvent.

^{1}H-NMR (20 °C, 300 MHz, $CDCl_3$): δ (ppm) = 0.88 (246 H), 1.26 (1198 H), 1.59 (203 H), 2.42–2.33 (205 H), 3.44 (400 H), 4.91–5.01 (41 H), 5.73–5.87 (21 H).

^{13}C-NMR (20 °C, 75 MHz, $CDCl_3$): δ (ppm) = 14.0, 22.6, 25.2, 25.4, 28.9, 29.1, 29.3, 29.5, 31.9, 32.8, 33.0, 33.7, 43.1, 45.2, 114.1, 139.0, 173.2, 173.8.

FT-IR: ν(cm^{-1}) = 2955, 2922, 2857, 1738, 1634, 1539, 1464, 1426, 1417, 1379, 1363, 1242, 1209, 1181, 1158, 1115, 988, 908, 775, 728, 681, 582.

GPC measurements: M_n = 9.7 kDa; M_w = 14.2 kDa; M_w/M_n = 1.47.

2.3.2. Poly(2-dec-9′-enyl-2-oxazoline)$_{100}$, pDc$^{=}$Ox$_{100}$

Seventy-five milligrams of methyl tosylate were dissolved in 9 mL of dry dichloromethane in a 20 mL microwave vial. 8.450 g of 2-dec-9′-enyl-2-oxazoline were added. The vial was closed under inert conditions and the mixture was heated at 140 °C for 2 h. The product was recovered in a quantitative manner as a white solid after removal of the solvent under reduced pressure.

^{1}H-NMR (20 °C, 300 MHz, $CDCl_3$): δ (ppm) = 1.29 (1015 H), 1.59 (218 H), 2.02-2.04 (208 H), 2.32 (208 H), 3.44 (400 H), 4.91–5.01 (201 H), 5.73–5.87 (99 H).

^{13}C-NMR (20 °C, 75 MHz, $CDCl_3$): δ (ppm) = 25.2, 25.4, 25.7, 28.9, 29.1, 29.4, 29.5, 32.8, 32.9, 33.7, 43.4, 45.2, 114.1, 139.0, 173.1, 174.0.

FT-IR: ν(cm^{-1}) = 3079, 2925, 2853, 1737, 1635, 1547, 1462, 1429, 1417, 1317, 1283, 1163, 989, 904, 771, 718, 637, 581.

GPC measurements: M_n = 7.2 kDa; M_w = 16.1 kDa; M_w/M_n = 2.24.

2.3.3. Preparation of the Test Specimens

Crosslinking of the (co)poly(2-oxazoline)s was performed analogously to UV-induced thiol-ene reactions described in the literature [13]. For the samples based on pNonOx$_{80}$-*stat*-pDc$^{=}$Ox$_{20}$ (to be crosslinked with trimethylolpropane tris(3-mercaptopropionate) 3SH), 2.00 g of the polymer were dissolved in 25 g of dichloromethane, and 267 mg of trimethylolpropane tris(3-mercaptopropionate) as well as two drops of Irgacure TPO-L were added (ratio thiol:ene = 1:1). The mixture was stirred for 5 min, and the solvent was removed under reduced pressure (1.5 mbar) at 50 °C for 15 min. Two grams of the dry residue were transferred into a circular mold with a diameter of 50 mm and a height of 0.4 mm, which was situated between two steel plates. For a facilitated removal of the samples from the mold, a teflon foil was put between the mold and the plates. The stack was put into the platen press at 110 °C and 25 bar. The temperature was increased to 125 °C, and heating was continued for 2.5 min under vacuum. Finally, the samples were cooled down to 35 °C and removed from the mold. For the crosslinking of the polymer, the samples were irradiated with UV-light. For the samples based on pDc$^{=}$Ox$_{100}$ (to be crosslinked with trimethylolpropane tris(3-mercaptopropionate) 3SH), 2.05 g of the polymer were dissolved in 10 mL of dichloromethane. Prior to stirring for 5 min, 1.28 g of trimethylolpropane tris(3-mercaptopropionate) and 15 mg of Irgacure TPO-L were added (ratio thiol:ene = 1:1). The solvent was removed under reduced pressure (1.5 mbar) for 15 min. Into a circular mold with a diameter of 50 mm and a height of 0.4 mm, 2.36 g of the solid mixture was placed. The mold was situated between two steel plates, which were covered with Teflon foil for facilitated removal of the samples. The steel plates were put into a preheated platen press at a temperature of 110 °C and 25 bar. After increasing the temperature to 135 °C, the samples were pressed for 10 min under vacuum, subsequently cooled and removed from the mold. Subsequently, the samples were irradiated with UV-light. For the samples based on pDc$^{=}$Ox$_{100}$ (to be crosslinked with 1,3-dimercaptobenzene 2SH), 1.055 g of the polymer were dissolved in 5 mL of dichloromethane and 0.355 g of 1,3-dimercaptobenzene as well as 20 mg of Irgacure TPO-L were added. The solutions were poured into a cast with 50 mm diameter. The solvent was evaporated, and the

samples were illuminated by UV light. Subsequently, the samples were dried in a vacuum oven at 40 °C for 48 h.

3. Results and Discussion

3.1. Choice of Crosslinked (co)poly(2-oxazoline)s

Both types of 2-oxazoline monomers, namely 2-nonyl-2-oxazoline NonOx and 2-dec-9′enyl-2-oxazoline Dc$^{=}$Ox, could be synthesized from the titanium alkoxide-catalyzed reaction of ethanol amine [19,20] with decanoic acid (from renewable resources such as coconut oil [22]) and undec-10-enoic acid (from renewable resources such as castor oil [23]) (Scheme 1). Their cationic ring-opening polymerization and copolymerization (Scheme 1), respectively, can be initiated by initiators such as methyl tosylate and be conveniently performed in microwave reactors [10,24] within reasonably short reaction times of 2 h. For this study, with respect to subsequent thiol-ene crosslinking (see below), a homopolymer of Dc$^{=}$Ox and a copolymer of NonOx and Dc$^{=}$Ox were synthesized as ene components (Scheme 3). The corresponding polymers pNonOx$_{80}$-*stat*-pDc$^{=}$Ox$_{20}$ and pDc$^{=}$Ox$_{100}$ can be crosslinked in UV-induced polymer analogous thiol-ene reactions employing the unsaturated side-chain functionalities of the pDc$^{=}$Ox repetition units. This approach inherently bears the advantage that the thiol and the (co)poly(2-oxazoline) (as well as the photoinitiator) can be cast into the targeted shape from, e.g., solution-based processes, and be crosslinked in that shape, enabling the straightforward production of test specimen with dedicated geometry. For crosslinking, at least bisfunctional thiols and "enes" (polymers with at least two repetition units of pDc$^{=}$Ox) must be employed.

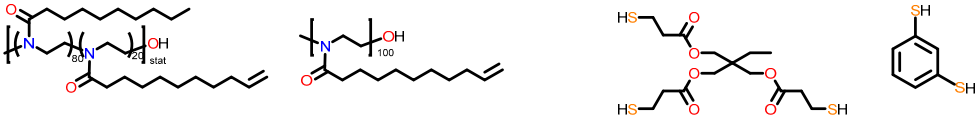

(**a**) (**b**) (**c**) (**d**)

Scheme 3. Reactants for the thiol-ene reactions used in this study: (co)poly(2-oxazoline)s as ene components (**a** and **b**) and di- and trimercapto compounds as thiol components (**c** and **d**).

In order to investigate the effect of crosslinking on the electrical conductivity and the permittivity, pNonOx$_{80}$-*stat*-pDc$^{=}$Ox$_{20}$ and pDc$^{=}$Ox$_{100}$ were crosslinked with a trisfunctional thiol 3SH (trimethylolpropane tris(3-mercaptopropionate)); in addition, pDc$^{=}$Ox$_{100}$ was also crosslinked with a bisfunctional thiol 2SH

(1,3-dimercaptobenzene) (Scheme 3). All reaction mixtures were calculated such that a thiol:ene ratio = 1:1 was maintained, assuming quantitative reactions [25]. Notably, a ratio of 80:20 = 4:1 of "crosslinkable" *vs.* "non-crosslinkable" repetition units (as in pNonOx$_{80}$-*stat*-pDc$^{=}$Ox$_{20}$) had been found to yield insoluble polymer networks in a previous study [13] and was therefore included in these investigations as well. Prior to electrical characterization, all samples were dried thoroughly in order to exclude the effect of moisture on the polarization.

The maximum degree of crosslinking can be calculated from the averaged molecular weight per polymer analogously formed bond (M_{BOND}): The (maximum) number of novel (crosslinking) bonds per polymer chain is equal to the number of its Dc$^{=}$Ox repetition units; for the formation of these bonds, one polymer chain and the corresponding number of thiols are required (maintaining the ratio thiol:ene = 1:1) (Equation (1)).

$$\mathrm{M_{BOND}} = \frac{\mathrm{M\,[(co)\,poly\,(2-oxazoline)]} + \left\{\mathrm{M\,[thiol]} \cdot \frac{\text{number of pDc}^{=}\text{Ox repetition units}}{\text{functionality of the thiol}}\right\}}{\text{number of pDc}^{=}\text{Ox repetition units}} \quad (1)$$

From the as-calculated values of M_{BOND} for the three types of polymer networks investigated in this study (Table 1), the (experimentally determined) density of the crosslinked (co)poly(2-oxazoline)s, and the functionality of the thiol, the "knot density" ρ_{KNOT} can be calculated correspondingly (Equation (2), Table 2).

$$\rho_{\mathrm{KNOT}} = \frac{\rho}{M_{\mathrm{BOND}}} \cdot (\text{functionality of the thiol}) \quad (2)$$

Table 2. Molecular weights per polymer analogously formed bond in the three (co)poly(2-oxazoline)-based networks investigated in this study.

Type of Network	M_{BOND} (g·mol^{-1})	ρ (g·cm^3) at 25 °C	ρ_{KNOT} (mmol·cm^{-3})
pNonOx$_{80}$-*stat*-pDc$^{=}$Ox$_{20}$ (CL:3SH)	1663	0.992	1.8
pDc$^{=}$Ox$_{100}$ (CL:2SH)	281	1.116	8.0
pDc$^{=}$Ox$_{100}$ (CL:3SH)	342	1.184	10.5

3.2. Relative Permittivity

The relative permittivity quantifies the ratio of the capacitance of a capacitor filled with a dielectric material to that of the same capacitor in vacuum. The relative permittivity increases with the polarizability of the material, in particular with its ability to store charges [26]. As the material's polarization does not react instantaneously to external stimuli, the response to an applied frequency commonly

occurs with a phase shift, and the relative permittivity is best described as a complex function (Equation (3)), in which ε_R' is the real part of the permittivity (quantifying the capability of the material to store energy), and ε_R'' is the imaginary part of the permittivity (quantifying the loss of energy from the material) [26].

$$\varepsilon_R = \varepsilon'_R - i \cdot \varepsilon''_R \quad (3)$$

Both the real and the imaginary part of the complex permittivity, are commonly dependent on the temperature and the frequency. The relative permittivity of the three types of (co)poly(2-oxazoline)-based networks has been measured at four different temperatures (−20, 0, 20, and 40 °C) and frequencies ranging from 10^{-2} to 10^6 Hz (Figures 1 to 2). The permittivity at 50 Hz (the industrial standard; Table 3) of all network types increases with the temperature. At 20 °C, a permittivity from 4.29–4.97 can be observed, which is in the expected range for polymers with low to medium polarity such as polyamides, polyesters, or epoxy resins (Table 1).

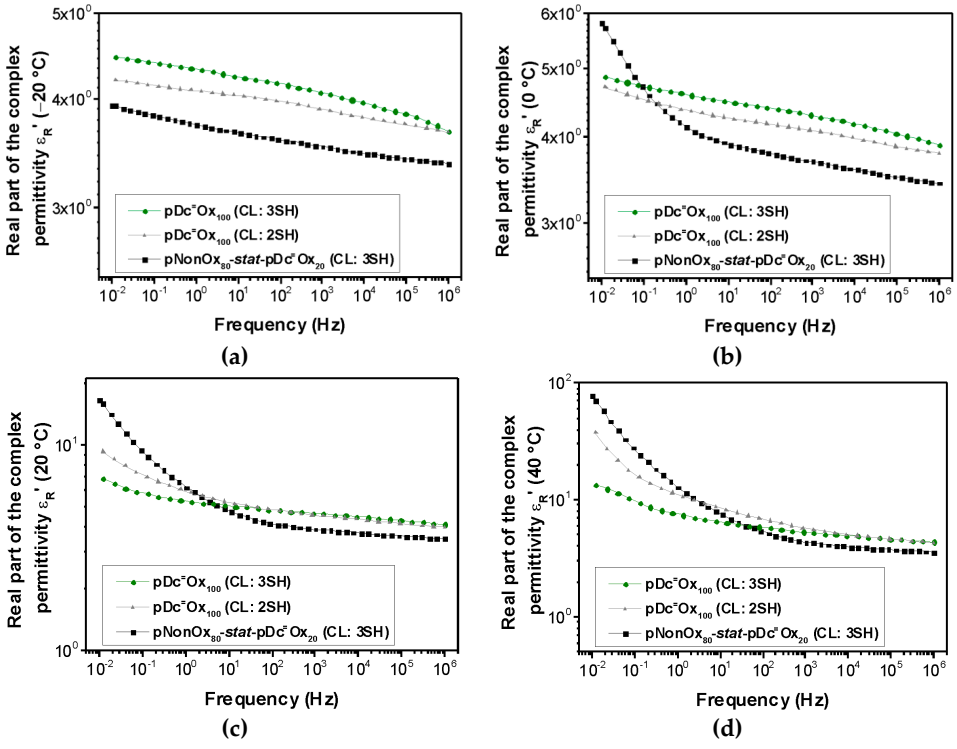

Figure 1. Frequency-dependent real part of the complex permittivity of pNonOx$_{80}$-*stat*-pDc$^{=}$Ox$_{20}$ (CL:3SH), pDc$^{=}$Ox$_{100}$ (CL:2SH), and pDc$^{=}$Ox$_{100}$ (CL:3SH) at −20 °C (**a**), 0 °C (**b**), 20 °C (**c**) and 40 °C (**d**).

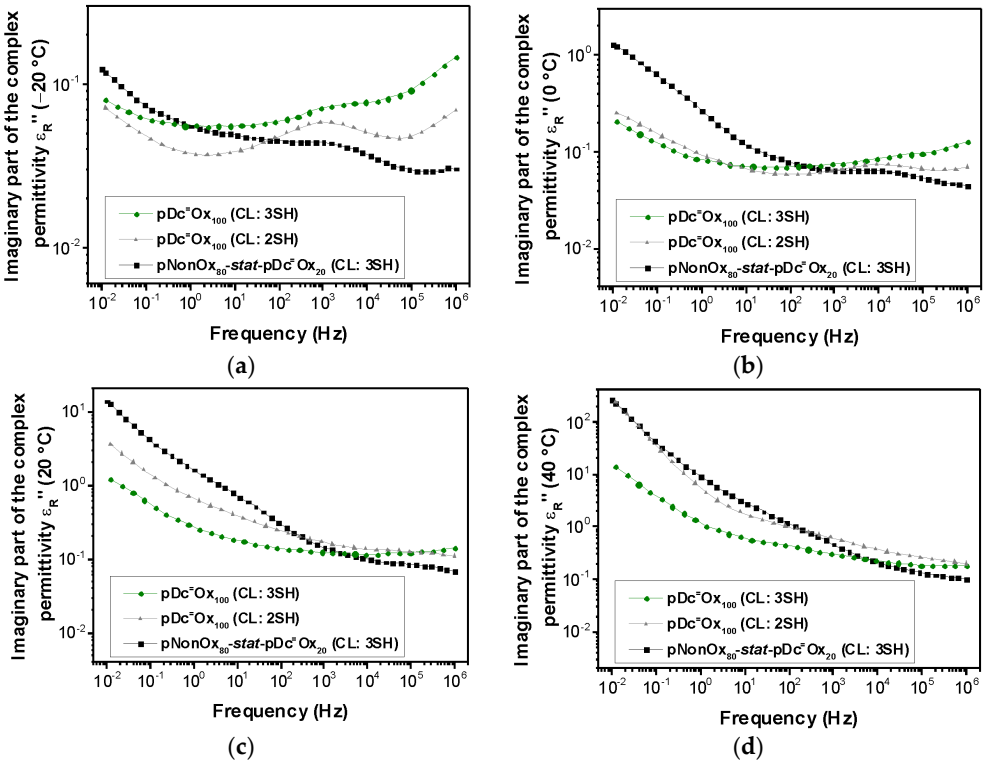

Figure 2. Frequency-dependent imaginary part of the complex permittivity of pNonOx$_{80}$-*stat*-pDc$^{=}$Ox$_{20}$ (CL:3SH), pDc$^{=}$Ox$_{100}$ (CL:2SH), and pDc$^{=}$Ox$_{100}$ (CL:3SH) at −20 °C (**a**), 0 °C (**b**), 20 °C (**c**) and 40 °C (**d**).

Table 3. Permittivity of the poly(2-oxazoline)-based networks at 50 Hz.

Polymer Network	Permittivity			
	T = −20 °C	T = 0 °C	T = 20 °C	T = 40 °C
pNonOx$_{80}$-*stat*-pDc$^{=}$Ox$_{20}$ (CL:3SH)	3.62	3.81	4.29	5.81
pDc$^{=}$Ox$_{100}$ (CL:2SH)	4.00	4.19	4.97	7.28
pDc$^{=}$Ox$_{100}$ (CL:3SH)	4.19	4.42	4.97	6.04

Notably, while the magnitude of the real part of the complex permittivity at 50 Hz is not altered significantly within the temperature range from −20 to 40 °C (maximum increase in the case of pDc$^{=}$Ox$_{100}$ (CL:2SH) by a factor of 1.8), the imaginary part of the complex permittivity increases significantly (details of these phenomena have been summarized hereinafter; Section 3.3.). A more detailed investigation of the frequency-dependent real part of the complex permittivity

(Figure 1) reveals that, at −20 °C, an overall linear correlation between the (logarithmic) frequency and the (logarithmic) real part of the complex permittivity can be observed. At 0 °C, this linear correlation along the whole range of frequencies can be only observed for pDc$^{=}$Ox$_{100}$ (CL:2SH) and pDc$^{=}$Ox$_{100}$ (CL:3SH); for pNonOx$_{80}$-*stat*-pDc$^{=}$Ox$_{20}$ (CL:3SH), deviations from the linear correlation occur for frequencies lower than 1 Hz. At 20 and 40 °C, all types of networks show significant deviation from the linear correlation for frequencies lower than 1–10 Hz (20 °C) and 10–100 Hz (40 °C). In summary, the occurrence of this phenomenon depends on the temperature and the type of polymer network (pNonOx$_{80}$-*stat*-pDc$^{=}$Ox$_{20}$ (CL:3SH) with a comparably low network density *vs.* pDc$^{=}$Ox$_{100}$ (CL:2SH) and pDc$^{=}$Ox$_{100}$ (CL:3SH) with a high degree of crosslinking; Table 2).

Hence, the relative permittivity and, as its origin, the polarizability can be significantly influenced by the temperature and network density. While a significant influence of the temperature on the permittivity and polarizability was expected, the influence on the polarizability by the network density requires a detailed inspection: electronic polarization (caused by frequencies in the range of 10^{15} Hz), atomic polarization (caused by frequencies in the range of 10^{13} Hz), and orientation polarization (caused by frequencies in the range of 10^{9} Hz) can be excluded to cause these phenomena [26].

At the lower range of frequencies measured in this study (lower than 1–10 Hz at 20 °C and 10–100 Hz at 40 °C, respectively), only interfacial polarization with typical frequencies of 10^{-5} to 10^{2} Hz can be assumed to cause the polarization effects. For frequencies higher than 10^{2} Hz, interfacial polarization decreases significantly, which is also observed in this study for that range of frequencies (Figures 1 to 2). As a rule of thumb, interfacial polarization occurs in all polymers with structural inhomogenities. Notably, water contaminations may also affect polarization in that range of frequencies; this origin of low-frequency polarization, however, can be excluded due to extended drying procedures prior to the measurements. The frequency at which interfacial polarization starts to occur increases with the temperature and the "degree of inhomogeneity" [26]. Due to the fact the observed phenomena are most pronounced in the case of pNonOx$_{80}$-*stat*-pDc$^{=}$Ox$_{20}$ (CL:3SH), both the composition of the (co)poly(2-oxazoline)s and the network density seem to influence this polarization.

3.3. Loss Factor

While ε_R' (Figure 1) quantifies the material's capability to store energy and, hence, is indicative of the material's polarizability (see hereinabove), the imaginary part ε_R'' (Figure 2) quantifies the losses of energy. Commonly, the conductivity of a material is classified based on the loss factor tan δ, which is defined as the ratio

of the imaginary part of the complex permittivity and the real part of the complex permittivity (Equation (4)) [26].

$$\tan\delta = \frac{\varepsilon_R''}{\varepsilon_R'} \quad (4)$$

An ideal dielectric would show no loss of energy ($\tan\delta = 0$), while a perfect conductor would not store any energy ($\tan\delta = \infty$), As a rule of thumb, materials with $\tan\delta << 1$ can be considered as good dielectrics and, consequently, as poor conductors. A detailed investigation of the loss factors (Figure 3) reveals that, at −20 °C, all poly(2-oxazoline)-based networks are poor conductors (independent of the frequency). At 0 °C, only pDc$^{=}$Ox$_{100}$ (CL:2SH) and pDc$^{=}$Ox$_{100}$ (CL:3SH) may be considered good dielectrics over the whole range of frequencies; at frequencies lower than 1 Hz, pNonOx$_{80}$-*stat*-pDc$^{=}$Ox$_{20}$ (CL:3SH) starts to become a conducting material. At 20 and 40 °C, only pDc$^{=}$Ox$_{100}$ (CL:3SH) acts as a good dielectric (for frequencies higher than 1 Hz); pNonOx$_{80}$-*stat*-pDc$^{=}$Ox$_{20}$ (CL:3SH) and pDc$^{=}$Ox$_{100}$ (CL:2SH), on the other hand, may be classified as lossy conducting materials for frequencies lower than 1 Hz (at 40 °C). In summary, the trends observed for the polarizability of the poly(2-oxazoline)-based networks (Section 3.2.) are well reproduced with the loss factor; the interfacial polarization, hence, suffices to explain the dielectric properties of these network in the range of frequencies from 10^{-2} to 10^{6} Hz. The standardized values of the loss factor (at 20 °C and 50 Hz; Table 4) emphasize the classification of poly(2-oxazoline)s as (pseudo-)polyamides. Both polyesters as well as epoxy resins typically have lower loss factors (Table 1).

Table 4. Loss factors of the poly(2-oxazoline)-based networks at 50 Hz.

Polymer Network	Loss Factor			
	T = −20 °C	T = 0 °C	T = 20 °C	T = 40 °C
pNonOx$_{80}$-*stat*-pDc$^{=}$Ox$_{20}$ (CL:3SH)	0.014	0.024	0.093	0.262
pDc$^{=}$Ox$_{100}$ (CL: 2SH)	0.010	0.014	0.054	0.159
pDc$^{=}$Ox$_{100}$ (CL:3SH)	0.014	0.016	0.030	0.076

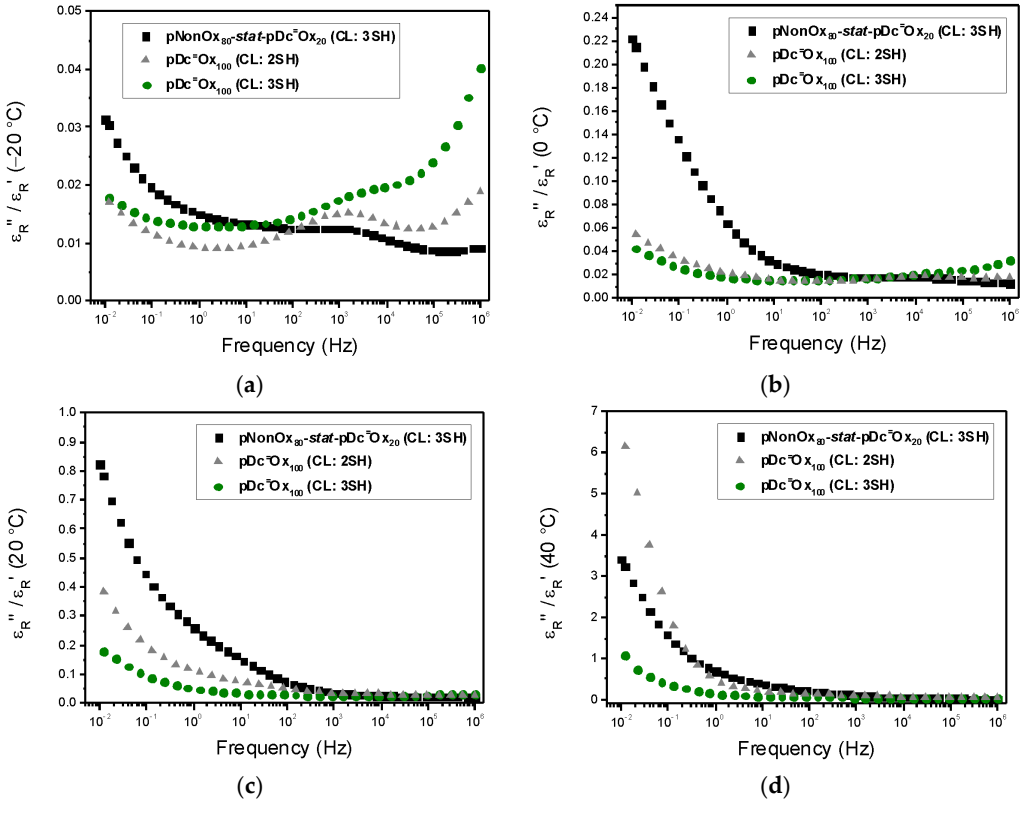

Figure 3. Frequency-dependent loss factors of pNonOx$_{80}$-*stat*-pDc$^{=}$Ox$_{20}$ (CL:3SH), pDc$^{=}$Ox$_{100}$ (CL:2SH), and pDc$^{=}$Ox$_{100}$ (CL:3SH) at −20 °C (**a**), 0 °C (**b**), 20 °C (**c**) and 40 °C (**d**).

3.4. Electrical Conductivity

In order to thoroughly characterize these poly(2-oxazoline)-based networks, also their electrical conductivity was measured. These measurements were performed on (thoroughly dried) polymer disks at 30, 40, and 50 °C. Constant current conditions (quasi steady-state conditions) were achieved for all samples in the range of days due to slow polarization and conduction procedures, while, on the other hand, pseudo steady-state conditions were achieved in the range of hours (Figure 4; left). As expected, the electric conductivity was found to correlate positively with the temperature (Figure 4; right). pDc$^{=}$Ox$_{100}$ (CL:3SH) showed the lowest electrical conductivity of all samples in the range from 5×10^{-12} to 10^{-10} S/m. In total, a range of electrical conductivities in the range from 5×10^{-12} to 8×10^{-9} S/m was covered by the poly(2-oxazoline)-based networks. However, these values might be (slightly) lowered if the time range of multiple days or even weeks was

allowed for determining the steady-state conditions. For the range of electrical conductivities measured for the poly(2-oxazoline) networks, again their similarity with polyamides becomes discernible; polyesters and epoxy resins commonly have lower conductivities (Table 1). The range of conductivities classifies these materials as medium insulators (semiconducting and conducting polymers have conductivities higher than 10^{-9} S/m [27]).

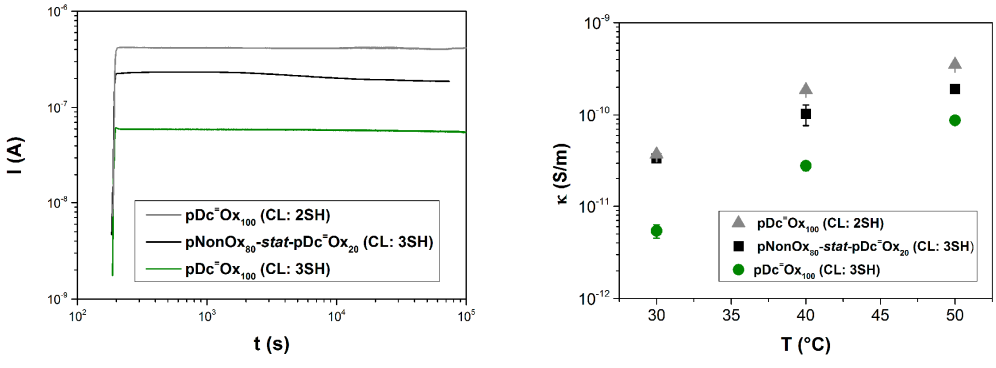

Figure 4. Measurements of the electrical conductivity of the poly(2-oxazoline)-based networks. **(Left)**: Time-dependent set-up of constant current conditions; (**Right**): Electrical conductivities for the polymer networks at 30, 40, and 50 °C.

4. Conclusions

Two types of (co)poly(2-oxazoline)s, namely pNonOx$_{80}$-*stat*-pDc$^{=}$Ox$_{20}$ and pDc$^{=}$Ox$_{100}$, were prepared by the cationic ring-opening polymerization of 2-oxazoline monomers, which were synthesized by the reaction of ethanol amine with fatty acids from renewable resources. These polymers could be crosslinked by the UV-induced thiol-ene reaction with a di- or a trithiol, respectively. The corresponding polymer networks exhibited permittivities in the range of 4.29–4.79 and loss factors in the range of 0.030–0.093 (20 °C, 50 Hz). Interfacial polarization within the materials was found to alter the real part of their permittivity and their loss factor from frequencies lower than 100 Hz. The electrical conductivity of these networks is in the range from 5×10^{-12} to 8×10^{-9} S/m, which renders these materials medium insulators. These first data of the dielectric and electronic properties of the investigated (co)poly(2-oxazoline)-based networks, which may be described as pseudo-peptides, show a high degree of similarity to polyamides, which qualifies the (co)poly(2-oxazoline)s as potential "green" alternatives to polyamides as insulators in electronic applications.

Acknowledgments: The research work was performed within the K-Project "PolyComp" at the Polymer Competence Center Leoben GmbH (PCCL, Leoben, Austria) within the framework of the COMET-program (Competence Centers for Excellent Technologies) of the Federal Ministry for Transport, Innovation and Technology and Federal Ministry for Economy, Family and Youth with contributions by the Delft University of Technology and the Graz University of Technology. Funding is provided by the Austrian Government and the State Government of Styria.

Author Contributions: Martin Fimberger synthesized all monomers and (co)poly(2-oxazoline)s and prepared the test specimens; Ioannis-Alexandros Tsekmes and Roman Kochetov performed the dielectric characterization; Johan J. Smit and Frank Wiesbrock discussed the results and prepared the manuscript.

Conflicts of Interest: The authors declare no conflict of interest.

References

1. Luef, K.P.; Hoogenboom, R.; Schubert, U.S.; Wiesbrock, F. Microwave-assisted cationic ring-opening polymerization of 2-oxazolines. *Adv. Polym. Sci.* In press.
2. Rossegger, E.; Schenk, V.; Wiesbrock, F. Design strategies for functionalized poly(2-oxazoline)s and derived materials. *Polymers* **2013**, *5*, 956–1011.
3. Hoogenboom, R.; Schlaad, H. Bioinspired poly(2-oxazoline)s. *Polymers* **2011**, *3*, 467–488.
4. Kelly, A.M.; Hecke, A.; Wirnsberger, B.; Wiesbrock, F. Synthesis of poly(2-oxazoline)-based hydrogels with tailor-made swelling degrees capable of stimuli-triggered compound release. *Macromol. Rapid Commun.* **2011**, *32*, 1815–1819.
5. Schenk, V.; Rossegger, E.; Ebner, C.; Bangerl, F.; Reichmann, K.; Hoffmann, B.; Höpfner, M.; Wiesbrock, F. RGD-functionalization of poly(2-oxazoline)-based networks for enhanced adhesion to cancer cells. *Polymers* **2014**, *6*, 264–279.
6. Hoogenboom, R.; Thijs, H.M.L.; Fijten, M.W.M.; Schubert, U.S. Synthesis, characterization, and cross-linking of a library of statistical copolymers based on 2-"soy alkyl"-2-oxazoline and 2-ethyl-2-oxazoline. *J. Polym. Sci. Polym. Chem.* **2007**, *45*, 5371–5379.
7. Dargaville, T.R.; Forster, R.; Farrugia, B.L.; Kempe, K.; Voorhaar, L.; Schubert, U.S.; Hoogenboom, R. Poly(2-oxazoline) hydrogel monoliths via thiol-ene coupling. *Macromol. Rapid Commun.* **2012**, *33*, 1695–1700.
8. Kelly, A.M.; Wiesbrock, F. Strategies for the synthesis of poly(2-oxazoline)-based hydrogels. *Macromol. Rapid Commun.* **2012**, *33*, 1632–1647.
9. Kempe, K.; Becer, C.R.; Schubert, U.S. Microwave-assisted polymerizations: Recent status and future perspectives. *Macromolecules* **2011**, *44*, 5825–5842.
10. Ebner, C.; Bodner, T.; Stelzer, F.; Wiesbrock, F. One Decade of microwave-assisted polymerizations: Quo vadis? *Macromol. Rapid Commun.* **2011**, *32*, 254–288.
11. De la Rosa, V.R. Poly(2-oxazoline)s as materials for biomedical applications. *J. Mater. Sci. Mater. Med.* **2014**, *25*, 1211–1225.
12. Luxenhofer, R.; Han, Y.; Schulz, A.; Tong, J.; He, Z.; Kabanov, A.V.; Jordan, R. Poly(2-oxazoline)s as polymer therapeutics. *Macromol. Rapid Commun.* **2012**, *33*, 1613–1631.

13. Schenk, V.; Ellmaier, L.; Rossegger, E.; Edler, M.; Griesser, T.; Weidinger, G.; Wiesbrock, F. Water-developable poly(2-oxazoline)-based negative photoresists. *Macromol. Rapid Commun.* **2012**, *33*, 396–400.
14. Fimberger, M.; Schenk, V.; Rossegger, E.; Wiesbrock, F. UV-Induced crosslinking of poly[2-(2′-norbornenyl)-2-oxazoline]s. *Period. Polytech. Chem. Eng.* **2014**, *58*, 69–74.
15. Petit, C.; Luef, K.P.; Edler, M.; Griesser, T.; Kremsner, J.M.; Stadler, A.; Grassl, B.; Reynaud, S.; Wiesbrock, F. Microwave-assisted syntheses in recyclable ionic liquids: Photoresists based on renewable resources. *ChemSusChem* **2015**, *8*, 3401–3404.
16. Slama, M.E.A.; Beroual, A. Behavior of AC High voltage polyamide insulators: Evolution of leakage current in different surface conditions. *Power Eng. Electr. Eng.* **2015**, *13*, 74–80.
17. Hackam, R. Outdoor HV composite polymeric insulators. *IEEE Trans. Dielectr. Electr. Insul.* **1999**, *6*, 557–585.
18. Notingher, P.V. *Materiale Pentru Electrotehnică: Proprietăţi Tehnice Utilizări (2)*; Editura Politehnica Press: Bucharest, Romanian, 2005; p. 140.
19. Beck, M.; Birnbrich, P.; Eicken, U.; Fischer, H.; Fristad, W.E.; Hase, B.; Krause, H.-J. Polyoxazoline auf fettchemischer Basis. *Angew. Makromol. Chem.* **1994**, *223*, 217–233.
20. Krause, H.-J.; Neumann, P. Process for the preparation of 2-alkyl and 2-alkenyl oxazolines. European Patent EP0315856 (B1), 19 April 1995.
21. Wiesbrock, F.; Hoogenboom, R.; Leenen, M.; van Nispen, S.F.G.M.; van der Loop, M.; Abeln, C.H.; van den Berg, A.M.J.; Schubert, U.S. Microwave-assisted synthesis of a 4^2-membered library of diblock copoly(2-oxazoline)s and chain-extended homo poly(2-oxazoline)s and their thermal characterization. *Macromolecules* **2005**, *38*, 7957–7966.
22. Mol, J.C. Application of olefin metathesis in oleochemistry: An example of green chemistry. *Green Chem.* **2002**, *4*, 5–13.
23. Van der Steen, M.; Stevens, C.V. Undecylenic acid: A valuable and physiologically active renewable building block from castor oil. *ChemSusChem* **2009**, *2*, 692–713.
24. Wiesbrock, F.; Hoogenboom, R.; Abeln, C.H.; Schubert, U.S. Single-mode microwave ovens as new reaction devices: Accelerating the living polymerization of 2-ethyl-2-oxazoline. *Macromol. Rapid Commun.* **2004**, *25*, 1895–1899.
25. Hoyle, C.E.; Bowman, C.N. Thiol–ene click chemistry. *Angew. Chem. Int. Ed.* **2010**, *49*, 1540–1573.
26. Ku, C.C.; Liepins, R. *Electrical Properties of Polymers*; Hanser Publishers: Munich, Germany, 1987.
27. Elias, H.G. *Makromoleküle, Band 4: Anwendungen von Polymeren*; Wiley-VCH Verlag GmbH & Co. KgaA: Weinheim, Germany, 2003; p. 479.

Preparation of Highly Dispersed Reduced Graphene Oxide Modified with Carboxymethyl Chitosan for Highly Sensitive Detection of Trace Cu(II) in Water

Sheng Chen, Rui Ding, Xiuling Ma, Liqun Xue, Xiuzhu Lin, Xiaoping Fan and Zhimin Luo

Abstract: In this article, reduced graphene oxide (RGO)/carboxymethyl chitosan (CMC) composites (RGO/CMC) were synthesized by a hydrothermal method through *in-situ* reduction and modification of graphene oxide (GO) in the presence of CMC. An electrochemical sensor for the determination of Cu(II) by differential pulse anodic stripping voltammetry (DPASV) was constructed by an electrode modified with RGO/CMC. The fabricated electrochemical sensor shows a linear range of 0.02–1.2 μmol· L^{-1}, a detection limit of 3.25 nmol· L^{-1} (S/N = 3) and a sensitivity of 130.75 μA· μmol· L^{-1}· cm^{-2}, indicating the sensor has an excellent detection performance for Cu(II).

Reprinted from *Polymers*. Cite as: Chen, S.; Ding, R.; Ma, X.; Xue, L.; Lin, X.; Fan, X.; Luo, Z. Preparation of Highly Dispersed Reduced Graphene Oxide Modified with Carboxymethyl Chitosan for Highly Sensitive Detection of Trace Cu(II) in Water. *Polymers* **2016**, *8*, 78.

1. Introduction

Copper is an essential element for human beings and plays an important role in various physiological processes at trace level [1,2]. However, due to its toxicity and non-degradation, the contamination of natural water by copper from mining, metal smelting and machinery manufacturing has become serious and attracted more attention [3,4]. The excessive copper intake from food chain can interact with lipid hydroxyperoxides, thereby disrupting cellular functions and causing extremely negative health diseases, such as Wilson's disease and kidney damage [5–8]. Therefore, real-time, rapid and sensitive detection of Cu(II) in water environment is of significance [9]. Until now, there have been many detection methods for Cu(II), including flame atomic absorption spectrometry (AAS), ultraviolet-visible spectroscopy (UV-Vis), atomic fluorescence spectrometry (AFS) and inductively coupled plasma mass spectrometry (ICP-MS) [10]. Nevertheless, the tedious pretreatments like enrichment and extraction, and the high cost for these methods cannot meet the requirements of development of detecting heavy metal ion. Electrochemical analysis has become an

ideal method for detecting metal ions in water due to the easy to transport apparatus, high sensitivity, fast response and low cost [11–13].

Graphene, the basic unit of carbonaceous materials, has been reported as an outstanding and promising material for the fabrication of electrochemical sensors due to its unique nanostructure, extraordinary electronic transport properties, excellent electrocatalytic activities and large surface area [14–16]. For instance, an electrochemical sensor fabricated by a gold electrode modified with graphene for the determination of Cu(II) and Pb(II) shows high sensitivity, good reusability and repeatability [17]. Wonsawat *et al.* [18] developed a bismuth-modified graphene-carbon paste electrode for detecting Cd(II) and Pb(II) in the automated flow system, and the detection limits reached 0.07 and 0.04 $\mu g \cdot L^{-1}$, respectively. However, the van der Waals and π-π stacking interactions between adjacent graphene sheets make them easy to agglomerate, which weakens the advantage of large surface area of graphene and limits its applications [19]. Chitosan, extracted from outer shells of shrimps, carbs and lobsters, was widely used for electrochemical determinations of metals ions [7]. Carboxymethyl chitosan (CMC) is a water-soluble and biodegradable derivate of chitosan, containing a large number of hydroxyl and carboxyl groups, which can make carbon nanomaterials such as carbon nanotube highly dispersed in the aqueous solution [20].

In this study, we prepared a functional nanocomposite through chemical modification of reduced graphene oxide with CMC. GO was reduced to RGO and *in-situ* modified with CMC in the procedure of synthesis. The chemical functionalization of RGO by CMC can efficiently inhibit the aggregation of RGO nanosheet in aqueous solution. RGO/CMC was used for modifying glassy carbon electrode (GCE) to detect Cu(II) in water by differential pulse anodic stripping voltammetry (DPASV). The results show that the electrochemical sensor has a linear range of 0.02–1.2 $\mu mol \cdot L^{-1}$, a low detection limit of 3.25 $nmol \cdot L^{-1}$ (S/N = 3), high sensitivity of 130.75 $\mu A \cdot \mu mol \cdot L^{-1}$ cm^{-2}, high selectivity and excellent reproducibility with the relative standard deviation (RSD) of 0.55%. Because RGO/CMC has high affinity towards metal ions and good conductivity, it has much potential for applications in the electrochemical sensors to detect trace Cu(II) in the water environment.

2. Materials and Methods

2.1. Chemical Reagents

Carboxymethyl chitosan (carboxylation degrees $\geqslant$60%) was purchased from Zhejiang golden shell biological chemical Co. Ltd. (Hangzhou, China). Graphite powder was purchased from Aladdin (Shanghai, China). Hydrazine hydrate (50%), potassium ferricyanide and glacial acetic acid (100%) were purchased from

Guoyao Chemicals Co. Ltd. (Shanghai, China). Nafion (5%) was purchased from Sigma-Aldrich (St. Louis, MO, USA).

2.2. Instruments and Measurements

The electrochemical experiments were performed on a CHI660D electrochemical workstation (CH Instrumental Co., Shanghai, China). The morphology of RGO/CMC was observed by transmission electron microscopy (TEM, JEM-2010F UHR, JEOL Ltd., Tokyo, Japan). The spectral properties were characterized by ultraviolet-visible spectroscopy (UV-Vis, TU-1800PC, Puxi Tongyong Instrument, Beijing, China), Fourier-transform infrared spectroscopy (FT-IR, Nicolet-380, Thermo Electron Co., Waltham, MA, USA), Raman spectra instrument (Olympus FV1000, Olympus Co., Tokyo, Japan). The surface property of RGO/CMC colloidal aqueous solution was studied by Zeta potential analyzer (Zetasizer Nano, Malvern Instruments Ltd., Worcestershire, UK). The component percentage of sample were measured through thermal gravimetric analysis (TGA, SDTA851e, Mettler-Toledo Co., Zurich, Switzerland) with a heating rate of 10 °C· min^{-1} using pure nitrogen as a carrier gas. The crystal structures of GO and RGO/CMC were characterized by X-ray diffraction (XRD, X'Pert, Philips Co., Eindhoven, The Netherlands).

2.3. Preparation of RGO/CMC Composite

GO was prepared by a modified Hummers method (See Supplementary Information). Two milliliters of GO (2 mg· mL^{-1}), 2 mL of CMC (3 mg· mL^{-1}) and 16 mL of deionized water were well mixed by ultrasonication for 2 h. Then, 1.4 μL of hydrazine hydrate were added to the solutions and the mixture was heated at 90 °C for 1.5 h. The reacted solution was filtered by microfiltration membrane (aperture < 0.22 μm) and washed by deionized water for at least three times. Finally, the as-prepared RGO/CMC sheet was dried at 60 °C for further use.

2.4. RGO/CMC/Nafion Modified GCE

As shown in Scheme 1, the fabrication of Cu(II) sensor was completed as briefly described in the following.

2.4.1. Fabrication of Cu(II) Sensor by RGO/CMC/Nafion

Prior to the modification of electrode, the bare GCE was sequentially polished with 1.0, 0.3 and 0.05 μm alumina powder (α-Al_2O_3) and followed by ultrasonically rinsing with ethanol and deionized water in turn.

The prepared RGO/CMC was dispersed in deionized water by ultrasonicaction. RGO/CMC/Nafion suspension was obtained by mixing the RGO/CMC solution (1 mg· mL^{-1}) and Nafion solution (0.5%) with volume ratio of 1:1 through ultrasonication.

Then, RGO/CMC/Nafion was casted on the surface of GCE through dropping a certain amount of mixture suspension.

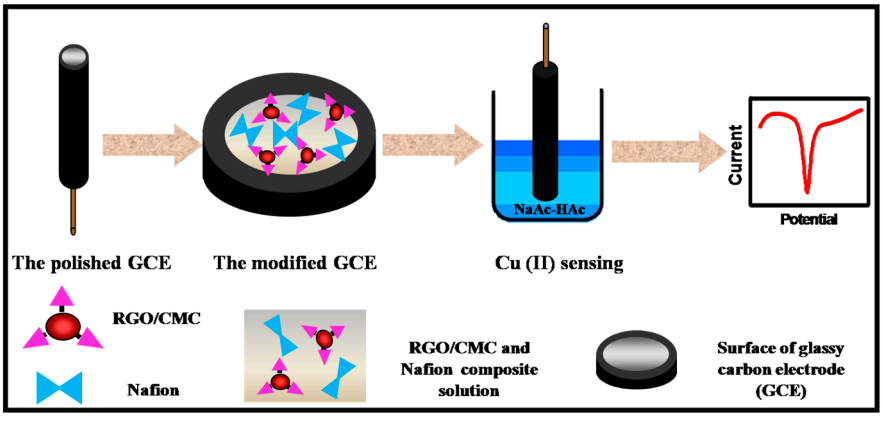

Scheme 1. Schematic illustration of RGO/CMC/Nafion modified GCE for Cu(II) sensing.

2.4.2. Electrochemical Analysis

A standard three-electrode system connected to the CHI660E was used for Cu(II) detection. The RGO/CMC/Nafion modified GCE acted as the working electrode, an Ag/AgCl (saturated with KCl) as the reference electrode and a platinum wire as the counter electrode. The experiment was performed in a HAc-NaAc buffer solution (pH = 4.4) containing Cu(II). The electrochemical response of RGO/CMC/Nafion modified GCE was measured by DPASV with a scanning potential range from −0.50 to 0.40 V with a step voltage of 4 mV, a pulse amplitude of 50 mV, a pulse width of 0.06 s, and a pulse separation of 0.20 s.

The RGO/CMC/Nafion modified GCE was accumulated for 360 s by DPASV with stirring under the constant potential of −0.6 V. Afterwards, *i-t* method was used for restoring its activity by removing the sediment that adsorbed on the surface of the modified GCE at the potential of 0.60 V.

3. Results and Discussion

3.1. Characterizations of RGO/CMC

As shown in Figure 1a, large RGO/CMC nanosheets are observed in the TEM image without agglomeration. FT-IR spectrum of RGO/CMC (Figure 1b) indicates that GO has been effectively reduced as the absorption intensity of the hydroxyl (3428 cm^{-1}) and epoxy (1047 cm^{-1}) were evidently decreased [21]. Furthermore, the

new absorption peak appearing at 2925 cm^{-1} ascribed to the methyl and methylene of CMC, confirms the successful modification of CMC on the surface of RGO [22,23].

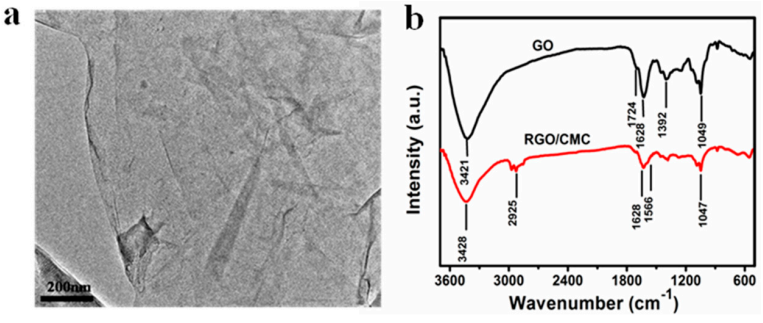

Figure 1. (**a**) A TEM image of RGO/CMC; (**b**) FT-IR spectra of GO and RGO/CMC.

Figure 2a shows UV-Vis absorption spectra of GO, RGO and RGO/CMC. The spectrum of GO presents two characteristic features, a maximum peak at 242 nm assigned to $\pi \rightarrow \pi^*$ transitions of aromatic C–C bonds and a shoulder peak around 301 nm assigned to $n \rightarrow \pi^*$ transitions of C=O bonds [24]. After the reduction of GO, its maximum peak at 230 nm redshifts to 254 nm for RGO and 267 nm for RGO/CMC. Compared with GO, the obvious red-shift of maximum peak of the spectrum of RGO/CMC is due to the reduction of GO and thus restoration of electron [25]. The shoulder peak assigned to carbonyl bond absorption is no longer present because of its chemical reduction by hydrazine hydrate [26–29].

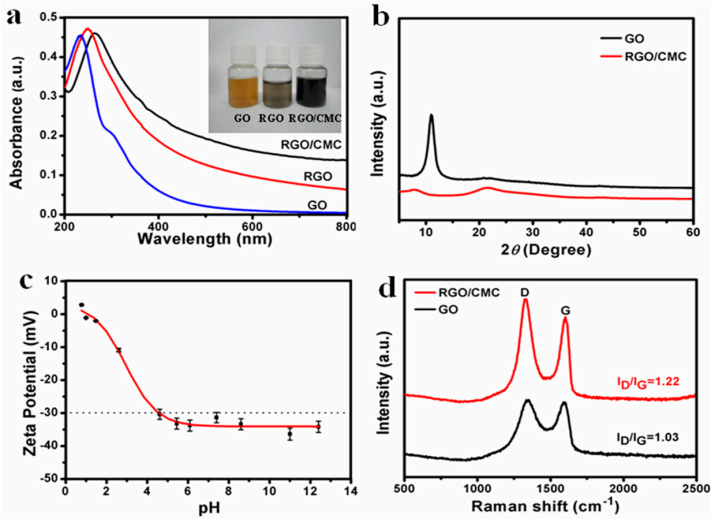

Figure 2. (**a**) UV absorption spectra of RGO/CMC, RGO and GO; (**b**) XRD diffraction patterns of GO and RGO/CMC; (**c**) Zeta potential of RGO/CMC aqueous solution; (**d**) Raman spectra of GO and RGO/CMC.

As seen in the XRD patterns (Figure 2b) of the GO and RGO/CMC, the pattern of GO exhibits a single peak at 11.05° corresponding to an interlayer d spacing of 8 Å, indicating the high degree of oxidation of GO [30]. Compared with GO, the XRD pattern of RGO/CMC shows a broad peak around at 22.35° (d = 4.16 Å). The breaking of the crystal structural integrity is the key factor for widening of the peak [31]. The restoration of electron may leads to the migration of peak [25]. Raman spectra of GO and RGO/CMC (Figure 2d) display two strong bands roughly at ~1346 cm^{-1} (D band) and at ~1590 cm^{-1} (G band) associated with the imperfection of the disordered sp^2 bond structure of carbon materials and the mode of highly ordered pyrolytic graphite, respectively. Raman characterization indicates the main graphene structure of graphene is conserved in RGO/CMC composite [32]. The relative intensity ratio of D/G bands (I_D/I_G) of the GO and RGO/CMC are calculated to be 1.03 and 1.22, respectively, indicating a decrease in the average size of the sp^2 domains after chemical reduction [33].

Zeta potential was used to evaluate the stability of colloidal solution. The higher the absolute value of Zeta potential is, the more stability the nanomaterials have. As shown in Figure 2c, the Zeta potential of RGO/CMC changes from 5 to −35 mV in the pH value range from 1.0 to 12.5. When the pH is between 4.5 and 12.5, the absolute value of Zeta potential is above 30 mV, illustrating the good stability of RGO/CMC in the pH value range from 4.5 to 12.5. According to the relevant literature [34,35],

RGO can keep stable in alkaline environment (pH > 8), while CMC modified RGO can keep stable in a wider range of pH (pH > 4.5).

Figure 3 shows the thermal gravity analysis-differential thermal gravity (TG–DTG) curves of CMC and RGO/CMC. When the temperature rose from room temperature to 800 °C, a broad peak at 334.1 °C appeared in the DTG curve of CMC, corresponding to the 45% of mass loss step of TG curve assigned to the depolymerization and thermal decomposition of indican units in CMC at the temperature range of 250–400 °C [36]. In addition to the agravic peak at 334.1 °C, another obvious peak at 186.4 °C can also be observed from the DTG curve of RGO/CMC, indicating the decomposition of CMC in RGO/CMC [37]. When the temperature reaches to 500 °C, the TG curve of RGO/CMC changes slowly, and the residual mass loss of about 10% is mainly owing to the thermal reduction of graphene oxide. TG and DTG characterizations confirm that there is about 15 wt % of CMC on the surface of RGO.

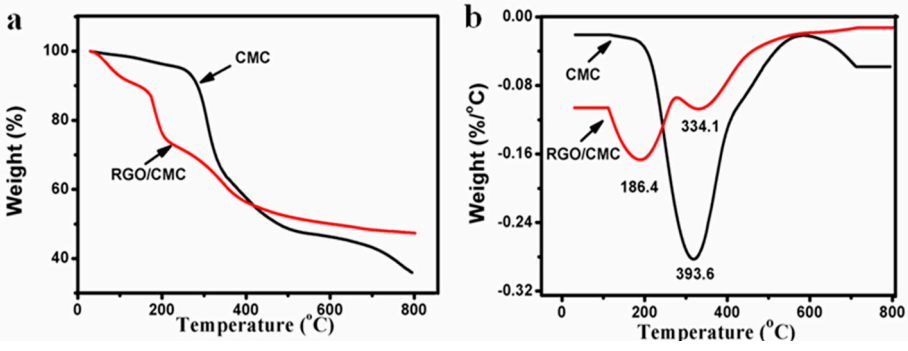

Figure 3. (**a**) TG and (**b**) DTG curves of CMC and RGO/CMC.

3.2. Electrochemical Detection of Cu(II)

For comparison, electrochemical experiments of bare GCE, GCE/Nafion and GCE modified with RGO/CMC/Nafion were carried out by DPASV under the same experimental conditions. Figure 4 depicts the detection performances of electrodes for 1.0 μmol· L^{-1} Cu(II) in 0.1 mol· L^{-1} NaAc-HAc (pH = 4.4). After accumulation for 360 s, the anodic peak current response of the RGO/CMC/Nafion modified GCE (c in Figure 4) is higher than bare GCE (a in Figure 4) and GCE/Nafion (b in Figure 4), indicating RGO/CMC can dramatically improve electroanalytical current response for Cu(II). According to the research of Khomyakov *et al.* [38], the interaction and charge transfer between graphene and metal ions is one of the main reasons for sensitivity of modified electrode. The detection of Cu(II) by the RGO/CMC/Nafion modified GCE may be by two steps and the reaction equations are shown below:

(1) The enrichment process.

(Cu(II)) sol. + (M) surf. — (Cu(II)-M) ads. (Cu(II)-M) ads. + $2e^-$ — (Cu(0)-M) ads.

(2) The dissolution process.

(Cu(0)-M) ads. — (Cu(II)) sol. + (M) surf. + $2e^-$

M in the equation stands for RGO/CMC/Nafion.

During the enrichment process, the chelated Cu(II) will be reduced to elementary copper at the working potential of 0.60 V. After enrichment, with the potential changes from −0.50 to 0.40 V, the copper dissolves and a sensitive anodic stripping peak can be seen at 0.06 V.

The peak potential of RGO/CMC/Nafion modified GCE has a slightly negative shift of −0.06 V (c in Figure 4) as compared to GCE (a in Figure 4) and Nafion/GCE (b in Figure 4), which may due to the accelerated electron transfer process by the functionalization of RGO/CMC [39]. The higher anodic peak current response can be attributed to the function of RGO/CMC, which can offer more sites to chelate Cu(II) for improving current response because of abundant carboxyl groups in CMC and RGO.

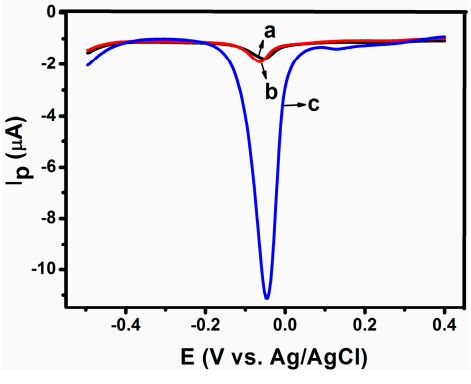

Figure 4. DPASV for 1.0 μmol· L^{-1} Cu (II) in 0.1 M NaAc-HAc (pH = 4.4) with different electrodes: (**a**) Bare GCE; (**b**) Nafion/GCE; and (**c**) RGO/CMC/Nafion/GCE. Detection conditions: amplitude of 0.05 V, pulse width of 0.06 s, and pulse period of 0.20 s.

3.3. Optimization of Detection Conditions

Table 1 shows the effect of various supporting electrolytes, including acid solution, alkaline solution and neutral solution, on different pulse anodic stripping peak current of the Cu(II) on RGO/CMC/Nafion/GCE. It is found that the stripping peak current in NaAc–HAc (0.1 mol· L^{-1}) is the highest, followed by the hydrochloric acid solution, sulfuric acid, potassium chloride, and no response in the sodium hydroxide solution. The electrochemical responses of Cu(II) in different pH values

of NaAc–HAc (0.1 mol· L^{-1}) at RGO/CMC/Nafion/GCE were studied by DPASV. As show in Figure 5a, the stripping peak current of the modified GCE increases with the increase of pH value from 3.6 to 4.4. After that, the peak current decreases with the further increase of pH value, which is consistent with the results of Table 1. Consequently, considering the sensitivity and stability of detection, NaAc–HAc (0.1 mol· L^{-1}) was chosen for this work.

Table 1. Effect of different types of supporting electrolytes on the stripping peak currents.

Supporting Electrolyte	Stripping Peak Current (μA)
KCl (0.1 mol· L^{-1})	0.3670
NaOH (0.1 mol· L^{-1})	No response
H_2SO_4 (0.1 mol· L^{-1})	0.9271
HCl (0.1 mol· L^{-1})	1.056
NaAc–HAc buffer solution	1.568

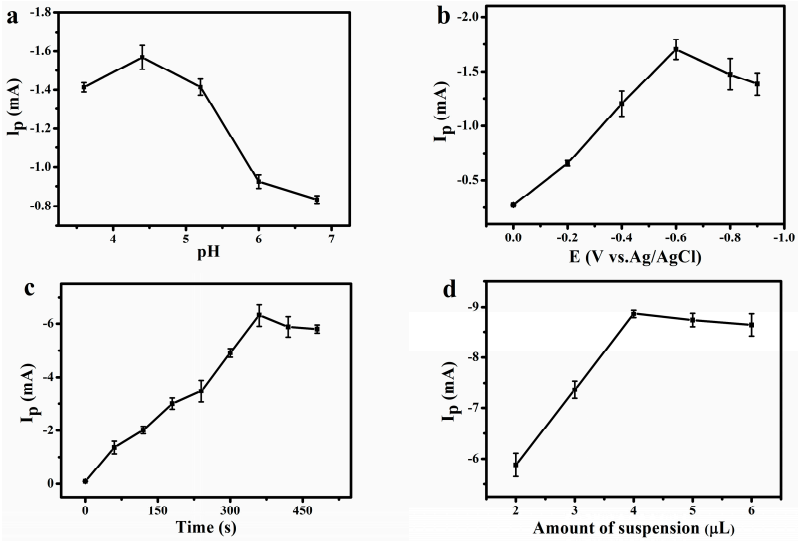

Figure 5. The effect of: (**a**) pH; (**b**) accumulation potential; (**c**) accumulation time; and (**d**) dosage of RGO/CMC/Nafion on the stripping peak current of 1.0×10^{-6} mol· L^{-1} Cu(II).

The influences of accumulation potential, accumulation time and dosage were also investigated. The effect of accumulation potential on peak current is illustrated in Figure 5b. The peak current increases rapidly with the decrease of accumulation potential from 0.0 to −0.60 V. It can be explained that Cu(II) is able to be reduced

at more negative potential. However, with the further decrease of accumulation potential from −0.60 to −0.90 V, the peak current decreases gradually. Parts of the active sites on the modified electrode surface are occupied by some other ions in the negative potential, leading to obstruction of the determination of Cu(II). Figure 5c displays the influence of accumulation time for stripping peak currents. When the accumulation time is 360 s, the response current is the highest because the adsorption of Cu(II) on the surface of modified electrodes has reached saturation [40]. The addition of RGO/CMC/Nafion was studied in the range of 2–6 μL. As shown in Figure 5d, when the dosage of RGO/CMC/Nafion is 4 μL, the response current is the highest. When the dosage continue to increases, the current decrease, which is mainly due to the increase of film thickness obstructing the electron transfer process between Cu(II) and electrode.

The repeated use of RGO/CMC/Nafion modified electrode was examined by *i-t* measurement. Table 2 shows the change of peak currents after repeated measurement of 1.0×10^{-6} mol· L^{-1} Cu(II) for using the same RGO/CMC/Nafion modified electrode ten times. The relative standard deviation is 0.55%, indicating the RGO/CMC/Nafion modified GCE has an excellent reproducibility for the detection of Cu(II).

Table 2. i_p of the RGO/CMC/Nafion modified GCE responding to the 1.0×10^{-6} mol· L^{-1} of Cu(II).

N	1	2	3	4	5	6	7	8	9	10
i_p (μA)	0.723	0.711	0.718	0.714	0.719	0.719	0.722	0.716	0.721	0.723

3.4. Anti-Interference of RGO/CMC/Nafion Modified GCE

Since there are still some other common metal ions in water, the detection of the identification performance of RGO/CMC/Nafion modified GCE is necessary. For practical purposes, 1.0×10^{-6} mol· L^{-1} Cu(II) solutions with different metal ions commonly presenting in natural water were used to examine the anti-interference of RGO/CMC/Nafion modified electrode. As shown in Table 3, the response current of the RGO/CMC/Nafion modified GCE changes within less than ± 5% with the addition of the interfering ions. Therefore, the RGO/CMC modified GCE is suitable for the detection of Cu(II) in real water samples after some pretreatments.

Table 3. $(i_o - i_p)/i_p$ of sensor for 1.0×10^{-6} mol· L^{-1} Cu(II) in the presence of other metal ions.

Concentration (mol· L^{-1})	Species	Interference (%)
5.0×10^{-4}	Na^+	−3.5
	K^+	−2.9
	Ca^{2+}	−4.8
	Mg^{2+}	−1.5
1.0×10^{-4}	Mn^{2+}	−3.1
	Cd^{2+}	−4.6
2.0×10^{-5}	Pb^{2+}	−4.9
	Zn^{2+}	−4.4

3.5. Detection Limit of Cu(II) with RGO/CMC/Nafion Modified GCE

Figure 6 shows the stripping voltammograms under the optimized conditions with the concentration of Cu(II) from 0.02 to 1.2 μmol· L^{-1} and the corresponding calibration curve of the stripping peak current *versus* the concentrations of Cu(II) (inset). The RGO/CMC/Nafion modified electrode shows good detection limit of 3.25 nmol· L^{-1} (S/N = 3) and a sensitivity of 130.75 μA· μmol L^{-1}· cm^{-2}. The limit of detection (LOD) was calculated as follows: LOD = 3 S/m, where S is standard deviation of current value, m is sensitivity, which is the slope of the linear equation. Comparison of other modified electrodes for the determination of Cu(II) is given in Table 4. The present work exhibited better electrochemical analysis performance in detecting trace Cu(II) with lower detection limit in wide linear range.

Table 4. Comparison of different modified electrodes for detecting Cu(II).

Modifier	Electrode	Method	Detection Range (μmol· L^{-1})	Detection Limit (nmol· L^{-1})	Ref.
Tripeptide (Gly-Gly-His)	GCE	DPSV	0.1–30	46	[41]
AMT-g-NGO	CPE	SWASV	0.1–1.0×10^5	40	[42]
Graphene	Gold electrode	OSWV	1.5×10^{-3}–0.02	1.5 ± 0.2	[17]
Propargyl-functionalized ferrocene	Gold electrode	DPV	1.0×10^{-8}–1.0×10^{-3}	3.4×10^{-6}	[43]
Ionic liquid-functionalized orderd mesoporous silica SBA-15	CPE	DPASV	0.3–100	10	[44]
Crosslinked chitosan	CNPE	LSASV	0.079–16	10	[7]
Silica	CPE	DPSV	0.05–0.2	3	[45]
RGO/CMC	GCE	DPASV	0.02–1.2	3.25	Present work

DPSV: Differential pulse stripping voltammetry; AMT-g-NGO: 2-amino-5-mercapto-1,3,4-thiadiazole/Nano graphene oxide; CPE: Carbon paste electrode; SWASV: Square wave anodic stripping voltammetry; OSWV: Osteryoung square wave voltammetry; DPV: Different pulse voltammetry; CNPE: Carbon nanotubes past electrode; LSASV: Linear scan anodic stripping voltammetry.

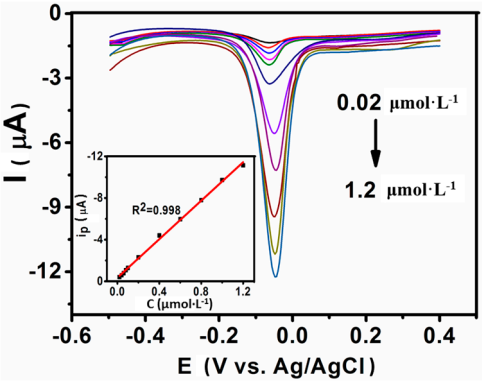

Figure 6. DPASV of the RGO/CMC/Nafion modified GCE in 0.1 M NaAc–HAc (pH = 4.4) with various concentrations of Cu(II). From top to bottom, the different colors of the curves represent the concentration of Cu(II) of 0.02, 0.04, 0.06, 0.08, 0.1, 0.2, 0.4, 0.6, 0.8, 1.0 and 1.2 μmol· L^{-1}, respectively. Inset is the calibration curve of the stripping peak currents *versus* the concentrations of Cu(II).

4. Conclusions

In this article, water-soluble and highly dispersed RGO/CMC was prepared by the chemical reduction of GO and *in-situ* modification with CMC. A simple and effective electrochemical sensor for determination of Cu(II) was constructed by DPASV based on the RGO/CMC/Nafion modified GCE. The RGO/CMC/Nafion modified GCE displays good analytical performance including wide linear range, low detection limit, high sensitivity, good repeatability to Cu(II) and excellent anti-interference ability towards other interfering metal ions. The fabricated sensor based on RGO/CMC/Nafion is promising in the determination of trace Cu(II) in real water samples.

Supplementary Materials: Supplementary materials can be found at www.mdpi.com/2073-4360/8/3/78/s1.

Acknowledgments: This work was financially supported by the National Natural Science Foundation of China (21207018).

Author Contributions: Sheng Chen and Zhimin Luo conceived and designed the experiments; Rui Ding wrote the paper; Xiuling Ma analyzed the data; Xiaoping Fan performed the experiments; Liqun Xue and Xiuzhu Lin contributed materials tools.

References

1. Zhang, J.; Li, B.; Zhang, L.M.; Jiang, H. An optical sensor for Cu (II) detection with upconverting luminescent nanoparticles as an excitation source. *Chem. Commun.* **2012**, *48*, 4860–4862.

2. Liao, Y.; Li, Q.; Yue, Y.; Shao, S.J. Selective electrochemical determination of trace level copper using a salicylaldehyde azine/MWCNTs/Nafion modified pyrolytic graphite electrode by the anodic stripping voltammetric method. *RSC Adv.* **2015**, *5*, 3232–3238.
3. Gupta, V.K.; Singh, L.P.; Singh, R.; Upadhyay, N.; Kaur, S.P.; Sethi, B. A novel copper (II) selective sensor based on dimethyl 4,4′(*o*-phenylene) bis (3-thioallophanate) in PVC matrix. *J. Mol. Liq.* **2012**, *174*, 11–16.
4. Ding, R.; Luo, Z.M.; Ma, X.L.; Fan, X.P.; Xue, L.Q.; Lin, X.Z.; Chen, S. High sensitive sensor fabricated by reduced graphene oxide/polyvinyl butyral nanofibers for detecting Cu (II) in water. *Int. J. Anal. Chem.* **2015**.
5. Cui, S.Q.; Pu, S.Z.; Dai, Y.F. A novel colorimetric sensor based on a diarylethene derivative for selective detection of Cu (II). *Anal. Methods* **2015**, *7*, 3593–3599.
6. Park, G.J.; Hwang, I.H.; Song, E.J.; Kim, H.; Kim, C. A colorimetric and fluorescent sensor for sequential detection of copper ion and cyanide. *Tetrahedron* **2014**, *70*, 2822–2828.
7. Janegitz, B.C.; Marcolino-Junior, L.H.; Campana-Filho, S.P.; Faria, R.C.; Fatibello-Filho, O. Anodic stripping voltammetric determination of copper (II) using a functionalized carbon nanotubes paste electrode modified with crosslinked chitosan. *Sens. Actuators B* **2009**, *142*, 260–266.
8. Gumpu, M.B.; Sethuraman, S.; Krishnan, U.M.; Rayappan, B.B.R. A review on detection of heavy metal ions in water—An electrochemical approach. *Sens. Actuators B* **2015**, *213*, 515–533.
9. Lin, H.; Li, M.X.; Mihailovič, D. Simultaneous determination of copper, lead, and cadmium ions at a $Mo_6S_{9-x}I_x$ nanowires modified glassy carbon electrode using differential pulse anodic stripping voltammetry. *Electrochim. Acta* **2015**, *154*, 184–189.
10. Afkhami, A.; Khoshsafar, H.; Madrakian, T.; Shirzadmehr, A. A new nano-composite electrode as a copper (II) selective potentiometric sensor. *J. Iran. Chem. Soc.* **2014**, *11*, 1373–1380.
11. Cantalapiedra, A.; Gismera, M.J.; Procopio, J.R.; Sevilla, M.T. Electrochemical sensor based on polystyrene sulfonate–carbon nanopowders composite for Cu (II) determination. *Talanta* **2015**, *139*, 111–116.
12. Li, M.; Gou, H.L.; Al-Ogaidi, I.; Wu, N.Q. Nanostructured sensors for detection of heavy metals: A review. *ACS Sustain. Chem. Eng.* **2013**, *1*, 713–723.
13. Afkhami, A.; Soltani-Felehgari, F.; Madrakian, T.; Ghaedi, T.; Rezaeivala, M. Fabrication and application of a new modified electrochemical sensor using nano-silica and a newly synthesized Schiff base for simultaneous determination of Cd^{2+}, Cu^{2+} and Hg^{2+} ions in water and some foodstuff samples. *Anal. Chim. Acta* **2013**, *771*, 21–30.
14. Kang, X.H.; Wang, J.; Wu, H.; Liu, J.; Aksay, I.A.; Lin, Y.H. A graphene-based electrochemical sensor for sensitive detection of paracetamol. *Talanta* **2010**, *81*, 754–759.
15. Wei, Y.; Gao, C.; Meng, F.L.; Li, H.H.; Wang, L.; Liu, J.H.; Huang, X.J. SnO_2/reduced graphene oxide nanocomposite for the simultaneous electrochemical detection of cadmium(II), lead(II), copper(II), and mercury(II): An interesting favorable mutual interference. *J. Phys. Chem. C* **2011**, *116*, 1034–1041.

16. Le, T.X.H.; Bechelany, M.; Champavert, J.; Cretin, M. A highly active based graphene cathode for the electro-fenton reaction. *RSC Adv.* **2015**, *5*, 42536–42539.
17. Kong, N.; Liu, J.Q.; Kong, Q.S.; Wang, R.; Barrow, C.J.; Yang, W.R. Graphene modified gold electrode via π–π stacking interaction for analysis of Cu^{2+} and Pb^{2+}. *Sens. Actuators B* **2013**, *178*, 426–433.
18. Wonsawat, W.; Chuanuwatanakul, S.; Dungchai, W.; Punrat, E.; Motomizu, S.; Chailapakul, O. Graphene-carbon paste electrode for cadmium and lead ion monitoring in a flow-based system. *Talanta* **2012**, *100*, 282–289.
19. Yang, G.H.; Cao, J.T.; Li, L.L.; Rana, R.K.; Zhu, J.J. Carboxymethyl chitosan-functionalized graphene for label-free electrochemical cytosensing. *Carbon* **2013**, *51*, 124–133.
20. Liu, Y.L.; Chen, W.H.; Chang, Y.H. Preparation and properties of chitosan/carbon nanotube nanocomposites using poly(styrene sulfonic acid)-modified CNTs. *Carbohydr. Polym.* **2009**, *76*, 232–238.
21. Afkhami, A.; Moosavi, R.; Madrakian, T.; Keypour, H.; Ramezani-Aktij, A.; Mirzaei-Monsef, M. Construction and application of an electrochemical sensor for simultaneous determination of Cd(II), Cu(II) and Hg(II) in water and foodstuff samples. *Electroanalysis* **2014**, *26*, 786–795.
22. Bao, Q.L.; Zhang, H.; Yang, J.X.; Wang, S.; Tang, D.Y.; Jose, R.; Ramakrishna, S.; Lim, C.T.; Loh, K.P. Graphene-polymer nanofiber membrane for ultrafast photonics. *Adv. Funct. Mater.* **2010**, *20*, 782–791.
23. Le, T.X.H.; Bechelany, M.; Lacour, S.; Oturan, N.; Oturan, M.A.; Cretin, M. High removal efficiency of dye pollutants by electron-Fenton process using a graphene based cathode. *Carbon* **2015**, *94*, 1003–1011.
24. Sun, T.; Xu, P.X.; Liu, Q.; Xue, J.; Xie, W.M. Graft copolymerization of methacrylic acid onto carboxymethyl chitosan. *Eur. Polym. J.* **2003**, *39*, 189–192.
25. Tung, V.C.; Allen, M.J.; Yang, Y.; Kaner, R.B. High-throughput solution processing of large-scale graphene. *Nat. Nanotechnol.* **2009**, *4*, 25–29.
26. Ma, J.K.; Wang, X.R.; Liu, Y.; Wu, T.; Liu, Y.; Guo, Y.Q.; Li, R.Q.; Sun, X.Y.; Wu, F.; Li, C.B.; *et al.* Reduction of graphene oxide with l-lysine to prepare reduced graphene oxide stabilized with polysaccharide polyelectrolyte. *J. Mater. Chem. A* **2013**, *1*, 2192–2201.
27. Li, D.; Mueller, M.B.; Gilje, S.; Kaner, R.B.; Wallace, G.G. Processable aqueous dispersions of graphene nanosheets. *Nat. Nanotechnol.* **2008**, *3*, 101–105.
28. Villar-Rodil, S.; Paredes, J.I.; Martínez-Alonso, A.; Tascon, J.M.D. Preparation of graphene dispersions and graphene-polymer composites in organic media. *J. Mater. Chem.* **2009**, *19*, 3591–3593.
29. Wang, X.; Zhi, L.J.; Tsao, N.; Tomovic, Z.; Li, J.L.; Mullen, K. Transparent carbon films as electrodes in organic solar cells. *Angew. Chem.* **2008**, *120*, 3032–3034.
30. Dubin, S.; Gilje, S.; Wang, K.; Tung, V.C.; Cha, K.; Hall, A.S.; Farrar, J.; Varshneya, R.; Yang, Y.; Kaner, R.B. A one-step, solvothermal reduction method for producing reduced graphene oxide dispersions in organic solvents. *ACS Nano* **2010**, *4*, 3845–3852.

31. Paredes, J.I.; Villar-Rodil, S.; Solis-Fernandez, P.; Martinez-Alonso, A.; Tascon, J.M.D. Atomic force and scanning tunneling microscopy imaging of graphene nanosheets derived from graphite oxide. *Langmuir* **2009**, *25*, 5957–5968.
32. Han, D.X.; Han, T.T.; Shan, C.S.; Ivaska, A.; Niu, L. Simultaneous determination of ascorbic acid, dopamine and uric acid with chitosan-graphene modified electrode. *Electroanalysis* **2010**, *22*, 2001–2008.
33. Stankovich, S.; Dikin, D.A.; Piner, R.D.; Kohlhaas, K.A.; Kleinhammes, A.; Jia, Y.Y.; Wu, Y.; Nguyen, S.T.; Ruoff, R.S. Synthesis of graphene-based nanosheets via chemical reduction of exfoliated graphite oxide. *Carbon* **2007**, *45*, 1558–1565.
34. Konkena, B.; Vasudevan, S. Covalently linked, water-dispersible, cyclodextrin: Reduced-graphene oxide sheets. *Langmuir* **2012**, *28*, 12432–12437.
35. Sreedhar, B.; Aparna, Y.; Sairam, M.; Hebalkar, N. Preparation and characterization of HAP/carboxymethyl chitosan nanocomposites. *J. Appl. Polym. Sci.* **2007**, *105*, 928–934.
36. Jin, M.H.; Kim, T.H.; Lim, S.C.; Duong, D.L.; Shin, H.J.; Jo, J.W.; Jeong, H.K.; Chang, J.; Xie, S.S.; Lee, Y.H. Facile physical route to highly crystalline graphene. *Adv. Funct. Mater.* **2011**, *21*, 3496–3501.
37. Travlou, N.A.; Kyzas, G.Z.; Lazaridis, N.K.; Deliyanni, E.A. Functionalization of graphite oxide with magnetic chitosan for the preparation of a nanocomposite dye adsorbent. *Langmuir* **2013**, *29*, 1657–1668.
38. Khomyakov, P.A.; Giovannetti, G.; Rusu, P.C.; Brocks, G.; Brink, J.V.D.; Kelly, P.J. First-principles study of the interaction and charge transfer between graphene and metals. *Phys. Rev. B* **2009**, *79*, 195425.
39. Sun, W.; Guo, Y.Q.; Ju, X.M.; Zhang, Y.Y.; Wang, X.Z.; Sun, Z.F. Direct electrochemistry of hemoglobin on graphene and titanium dioxide nanorods composite modified electrode and itselectrocatalysis. *Biosens. Bioelectron.* **2013**, *42*, 207–213.
40. Wang, Z.M.; Guo, H.W.; Liu, E.; Yang, G.C.; Khun, N.W. Bismuth/polyaniline/glassy carbon electrodes prepared with different protocols for stripping voltammetric determination of trace Cd and Pb in solutions having surfactants. *Electroanalysis* **2010**, *22*, 209–215.
41. Lin, M.; Hu, X.; Ma, Z.; Chen, L. Functionalized polypyrrole nanotube arrays as electrochemical biosensor for the determination of copper ions. *Anal. Chim. Acta* **2012**, *746*, 63–69.
42. Yuan, X.J.; Chai, Y.Q.; Yuan, R.; Zhao, Q.; Yang, C.L. Functionalized graphene oxide-based carbon paste electrode for potentiometric detection of copper ion(II). *Anal. Methods* **2012**, *4*, 3332–3337.
43. Qiu, S.Y.; Xie, L.D.; Gao, S.; Liu, Q.D.; Lin, Z.Y.; Qiu, B.; Chen, G.N. Determination of copper(II) in the dairy product by an electrochemical sensor based on click chemistry. *Anal. Chim. Acta* **2011**, *707*, 57–61.

44. Zhang, P.H.; Dong, S.Y.; Gu, G.Z.; Huang, T.L. Simultaneous determination of Cd^{2+}, Pb^{2+}, Cu^{2+} and Hg^{2+} at a carbon paste electrode modified with ionic liquid-functionalized ordered mesoporous silica. *Bull. Korean Chem. Soc.* **2010**, *31*, 2949–2954.
45. Etienne, M.; Bessiere, J.; Walcarius, A. Voltammetric detection of copper(II) at a carbon paste electrode containing an organically modified silica. *Sens. Actuators B* **2001**, *76*, 531–538.

Dielectric Properties and Energy Storage Densities of Poly(vinylidenefluoride) Nanocomposite with Surface Hydroxylated Cube Shaped $Ba_{0.6}Sr_{0.4}TiO_3$ Nanoparticles

Shaohui Liu, Shaomei Xiu, Bo Shen, Jiwei Zhai and Ling Bing Kong

Abstract: Ceramic-polymer nanocomposites, consisting of surface hydroxylated cube-shaped $Ba_{0.6}Sr_{0.4}TiO_3$ nanoparticles (BST–NPs) as fillers and poly (vinylidenefluoride) (PVDF) as matrix, have been fabricated by using a solution casting method. The nanocomposites exhibited increased dielectric constant and improved breakdown strength. Dielectric constants of the nanocomposite with surface hydroxylated BST–NPs (BST–NPs–OH) were higher as compared with those of their untreated BST–NPs composites. The sample with 40 vol % BST–NPs–OH had a dielectric constant of 36 (1 kHz). Different theoretical models have been employed to predict the dielectric constants of the nanocomposites, in order to compare with the experimental data. The BST–NPs–OH/PVDF composites also exhibited higher breakdown strength than their BST–NP/PVDF counterparts. A maximal energy density of 3.9 J/cm^3 was achieved in the composite with 5 vol % BST–NPs–OH. This hydroxylation strategy could be used as a reference to develop ceramic-polymer composite materials with enhanced dielectric properties and energy storage densities.

Reprinted from *Polymers*. Cite as: Liu, S.; Xiu, S.; Shen, B.; Zhai, J.; Kong, L.B. Dielectric Properties and Energy Storage Densities of Poly(vinylidenefluoride) Nanocomposite with Surface Hydroxylated Cube Shaped $Ba_{0.6}Sr_{0.4}TiO_3$ Nanoparticles. *Polymers* **2016**, *8*, 45.

1. Introduction

Recently, a great deal of attention has been paid to developing high energy-storage density polymer-based capacitors, due to their potential applications in modern electronic and electrical power systems, such as electronic components, pulsed power sources and hybrid electric vehicles [1–9]. Compared with other electrical energy-storage devices, polymer-based capacitors have several advantages, such as fast charge/discharge (<1 μs), high working voltage, simple processing and cost-effectiveness. However, their energy densities are lower than that of electrochemical devices, such as batteries and double-layer super capacitors, by at least one order of magnitude. For example, the energy density of biaxially oriented polypropylene (BOPP), which is one of the most representative commercial polymer

capacitor films, is only 1–2 J/cm^3. As a result, developing high energy density polymer-based dielectric capacitors has become an active research topic in recent years [5,10–14].

The energy density of dielectric materials is defined as $U = \int EdP$, where E is applied electric field and P is polarization. To obtain high energy density, dielectric materials should have a high E and a high P. However, it is still a challenge to modulate the two parameters simultaneously. In addition, polymers have relatively low dielectric constant (e.g., <10). Although ferroelectric ceramics (e.g., $BaTiO_3$) have high dielectric constant, their applications have been largely limited, due to their low breakdown strength and processing difficulty. In comparison, polymers, such as PVDF and BOPP, are flexible and easy fabrication. Moreover, polymers have much higher breakdown strength than ceramics. Therefore, nanocomposites have been considered to be a unique platform to combine the advantages of polymers (matrix) and ceramics (fillers), so as to achieve high energy density materials.

Ceramic fillers, such as $Pb(Zr,Ti)O_3$, $Ba_{1-x}Sr_xTiO_3$ and $BaTiO_3$, have been widely used to prepare polymer-ceramic composites with increased dielectric constant and enhanced energy density. However, a large quantity of the ceramic fillers is usually needed in order to achieve high dielectric constant. In this case, the breakdown strength and mechanical properties of the composites are seriously deteriorated [8].

Furthermore, it has been widely accepted that the introduction of ceramic fillers reduces the breakdown strength of composites, thus leading to low energy density. The reduction in breakdown strength of composites is mainly attributed to the weak interface interaction between the polymer matrix and ceramic fillers, owing to their poor chemical compatibilities. In this regard, many efforts have been made to improve the dispersing behaviors of ceramic fillers in polymer matrix. One strategy is to modify the surface of ceramic fillers so that a ceramic-polymer interfacial layer can be formed through chemical bonding. As a result, homogeneity of the nanocomposites will be greatly improved, which is essential for them to have excellent energy storage properties [1].

Additionally, particle shape of the ceramic filler also plays a decisive role in determining the energy storage density of polymer nanocomposites [15]. This is because fillers with different particle shapes have different surface areas and, thus, different interfacial areas in the nanocomposites, leading to different interfacial polarization and hence different energy storage properties. At the same time, connectivity of a nanocomposite is closely related to the particle shape of the fillers [16]. Extensive studies have been conducted on the synthesis and characterization of ceramic-polymer nanocomposites, containing $Ba_xSr_{1-x}TiO_3$ particles with different morphologies, including nanospheres [17], nanotubes [18], nanofibers [19], and nanowires [6]. Until now, there has been no report

on PVDF-based nanocomposites with cube-shaped $Ba_{0.6}Sr_{0.4}TiO_3$ nanoparticles (BST–NPs) and surface hydroxylation of BST–NP (BST–NPs–OH) as fillers.

In this work, dielectric and energy storage properties of PVDF nanocomposites with cube shaped BST–NPs–OH fillers were systematically studied. The cube-shaped BST–NPs were synthesized by using a molten salt method. BST–NPs–OH/PVDF nanocomposites were fabricated by using a solution casting method. The effect of content of the BST–NPs–OH on the microstructure, dielectric property and energy storage properties of the nanocomposites were investigated. Dielectric properties of nanocomposites have also been analyzed theoretically.

2. Experimental Section

Barium hydroxide ($Ba(OH)_2$; 99%), strontium hydroxide ($Sr(OH)_2$; 99%) and titanium dioxide (TiO_2; 99%) were obtained from Alfa Aesar (Beijing, China). NaOH and KOH were purchased from Sinopharm Chemical Reagent Co., Ltd. (Shanghai, China). PVDF powders were purchased from 3F Co. (Shanghai, China). All chemicals were used as received without further purification.

Cube-shaped BST–NPs were synthesized by using a molten salt method, with NaOH–KOH mixture as the molten flux. High purity $Ba(OH)_2$, $Sr(OH)_2$ and TiO_2 were used as raw materials to form $Ba_{0.6}Sr_{0.4}TiO_3$. The raw materials were mixed with NaOH–KOH mixture. The mixtures were heated to 200 °C for 12 h. After reaction, the solidified melts were washed with distilled water at room temperature. The washed powders were then dried at 100 °C overnight in air. The final products were cube-shaped BST–NPs.

The BST–NPs were dispersed in an aqueous solution of H_2O_2 (35%, 350 mL), which were stirred and heated at 100 °C for 3 h. The suspensions were subsequently centrifuged at 3000 rpm for 10 min. The collected powder were washed with distilled water and ethanol and then dried at 80 °C for 12 h to obtain surface hydroxylated BSTs NP (BST–NP–OH).

PVDF powders (3F Co., China) were dissolved in dimethylformamide (DMF) first and then the BST–NPs–OH were introduced under constant stirring at 40 °C for 10 h to form stable suspensions. Volume fractions of BST–NPs–OH in the composites were varied from 0 to 40 vol %. Thin film samples were prepared by using tape-casting method with the suspensions on indium tin oxides (ITO) glass. The wet tapes were dried in vacuum at 60 °C for 10 h and then heated at 200 °C for 10 min, followed by quenching in ice-water. The samples were subsequently dried at 40 °C for 24 h. Thickness of the films was controlled in the range of 10–15 μm.

3. Characterization

X-ray diffraction (XRD) was used to study phase composition of the samples, with Cu-Kα radiation by using a RIGAKU D/max2550 diffractometer (Beijing,

China). Fourier-transform infrared spectroscopy (FTIR) was recorded by using a Bruker Tensor 27 spectrometer (Ettlingen, Germany) over 450–4000 cm^{-1}. X-ray photoelectron spectroscopy (XPS) was used to verify the surface-hydroxylated BST–NPs with Al Ka radiation (160 eV) using a Kratos Axis Ultra DLD multi-technique XPS equipment (Manchester, UK). Thermogravimetric analysis (TGA) was conducted using a using a NETZSCH STA449C instrument (Bavaria, Germany) at a heating rate of 10 °C· min^{-1} in N_2 flow (20 mL· min^{-1}). Microstructure of the samples was observed by using scanning electron microscopy (SEM, XL30FEG, Philips, The Netherlands) and transmission electron microscopy (TEM, CM200FEG, Philips, The Netherlands). For SEM measurement, a proper amount of BST-NPs power was dispersed in ethanol and then dropped onto the surface of Si wafer slides. The cross-section SEM of samples were prepared by fracturing the composites films in liquid nitrogen and the fractured surface was sputtered with thin layers of gold to avoid the accumulation of charge. Broadband frequency dielectric properties of the composites were measured by using a 4980A LCR meter (Agilent, Palo Alto, CA, USA) over 0.1–1000 kHz at various temperatures. DC breakdown strength was measured by using a breakdown strength tester (ENTAI, Nanjing, China) in silicone oil at room temperature (25 °C) by applying a DC voltage ramp at a rising rate of 200 V s^{-1} and a limit current of 5 mA. 10 samples were measured for each condition. The nanocomposite films were cut into square of 1 × 1 cm^2, with a thickness of about 10 μm. The top gold electrodes with diameter of 2 mm and thickness of 40 nm were sputtered with a shadow mask, while bottom electrodes were sputtered without the use of shadow mask. Samples were placed between two stainless steel columnar electrodes (Φ = 1 mm). Polarization–electric field loops (*P-E*) were measured by using a Premier II ferroelectric test system in silicone oil to avoid electrical discharges.

4. Results and Discussion

Figure 1 shows XRD patterns of the as-synthesized BST–NPs and the BST–NPs–OH. It was shown that the strong peaks at 2θ that corresponded to 22° (100), 31° (110), 39° (111), 45° (200), 56° (211), and 66° (220) were assigned to BST with a perovskite structure (PDF#34-0411). No visible signal of the presence of secondary phases was observed. XRD results exhibit no changes in the sample of the crystal structure of both BST–NPs–OH and untreated BST–NPs. SEM image revealed that the BST–NPs have a faultless cubic morphology, with an average size (side length) of about 110 nm (inset of Figure 1).

The faultless cubic shape of the BST–NPs is confirmed by the TEM observation, as shown in Figure 2. The cubic nanoparticles have an average size of about 110 nm, in a good agreement with the SEM result.

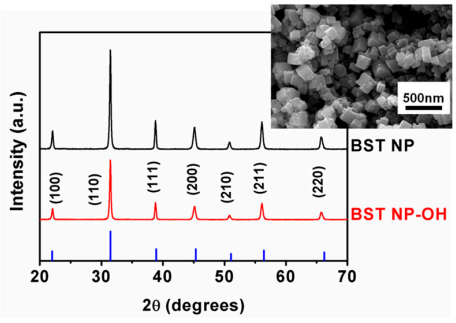

Figure 1. XRD patterns of the as-synthesized BST–NPs and BST–NPs–OH. The inset shows a SEM image of the BST–NPs.

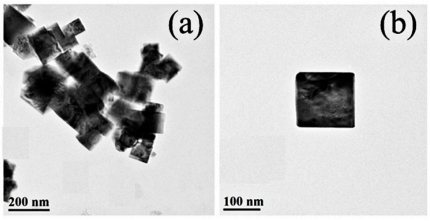

Figure 2. TEM images of the BST–NP at low (**a**) and high (**b**) magnifications.

Figure 3 shows FTIR spectra of the as-obtained BST–NPs and the BST–NPs–OH. The band at 550 cm^{-1} is associated to the bond vibration of Ti–O [20]. The new band at 3450 cm^{-1} corresponded to the stretcing mode of –OH [21], confirming the surface hydroxylation of the BST–NPs. The surface modification of the BST–NPs by the H_2O_2 are demonstrated to act as a bridge to between the F atoms on the PVDF and the –OH groups on the surface BST–NPs–OH (Figure 4).

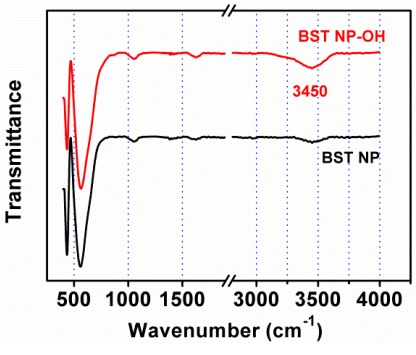

Figure 3. FT-IR spectra of the as-synthesized BST–NPs and the BST–NPs–OH.

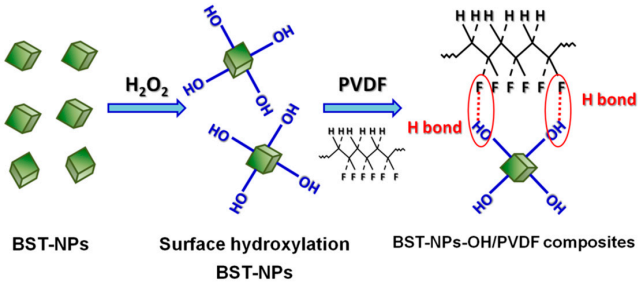

Figure 4. Schematic diagram illustrating hydroxylation of the BST–NPs and formation of a bond between the F atoms on the PVDF chains and the –OH groups on surface of the BST–NPs–OH.

Figure 5 shows the O1s spectra for BST–NPs–OH. We can see the peaks of O1s (529.4 and 531.5 eV) corresponding to the O atoms in $Ba_{0.6}Sr_{0.4}TiO_3$ (O_{-BST}) and free –OH (O_{-OH}) [22], which confirming that the hydroxylate groups were introduced onto the surface of BST–NPs–OH.

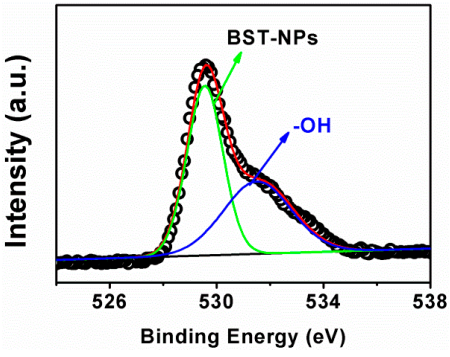

Figure 5. XPS spectra of O 1s of BST–NPs–OH.

TGA curves provided further evidence of the presence of the surface hydroxylation. A difference in the weight loss between the BST–NPs and BST–NPs–OH is obviously observed in TG curves, as shown in Figure 6. The weight loss of the BST–NPs–OH is larger than that of the BST–NPs by a value of 1.35% at 800 °C, which can be attribute to the vaporization of the hydroxyl groups. Moreover, the large weight loss before 300 °C of the BST–NPs–OH sample indirectly confirms that the hydroxylate groups were grafted onto the surface of BST–NPs [23].

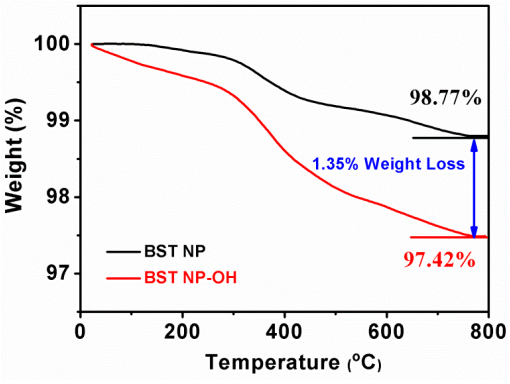

Figure 6. TGA curves of the untreated BST–NPs and the BST–NPs–OH.

Figure 7 shows the surface SEM and cross-section SEM of BST–NPs/PVDF and BST–NPs–OH/PVDF nanocomposites (all the nanocomposites contain 10 vol % nanoparticles). It can be observed in Figure 7b,d that most of the BST–NPs–OH are well-dispersed in BST–NPs–OH/PVDF. However, in the BST–NPs/PVDF nanocomposite sample (Figure 7a,c), the aggregations of BST–NPs are clearly observed. Some voids and pores can be observed in BST–NPs/PVDF. The BST–NPs–OH/PVDF nanocomposites have hardly any small voids between the BST–NPs–OH and PVDF. This result indicates the surface hydroxylation could not only facilitate its dispersion in the polymer matrix but also strongly chain with the polymer matrix by hydroxyl bonds in the interface.

PVDF is a ferroelectric polymer, which has a complex structure and exhibits five crystalline phases, in which α, β, and γ are the most possible phases. Therefore, it is of importance to know the effects of fillers on the structure of the PVDF matrix. FT-IR techniques were used to obtain the structure information on PVDF in nanocomposites. The peaks of 840, 878, 1171, and 1232 cm^{-1} indicate the β-phase of PVDF, whereas the absorption bands at 611, 765, and 975 cm^{-1} indicate the α-phase of PVDF. The peaks of 794 and 1284 cm^{-1} indicate the γ-phase of PVDF. Figure 8 shows the FT-IR spectra of the PVDF, BST–NPs/PVDF and BST–NPs–OH/PVDF nanocomposite films at a filler concentration of 10 vol %. Each nanocomposite exhibits the characteristic absorption bands of α, β, and γ phases, indicating the PVDF matrix is composed of these three phases in the nanocomposites.

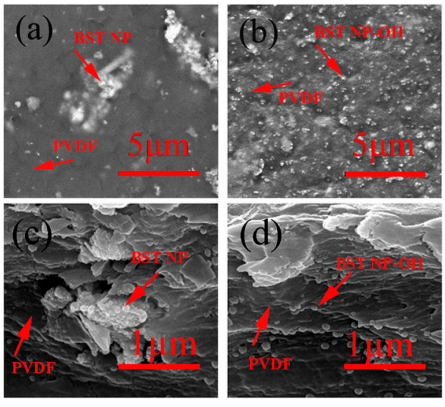

Figure 7. Surface SEM images of the PVDF nanocomposites: (**a**) BST-NPs/PVDF, (**b**) BST–NPs–OH/PVDF. Cross-section SEM of the PVDF nanocomposites: (**c**) BST-NPs/PVDF, (**d**) BST–NPs–OH/PVDF. All samples contain 10 vol % filler.

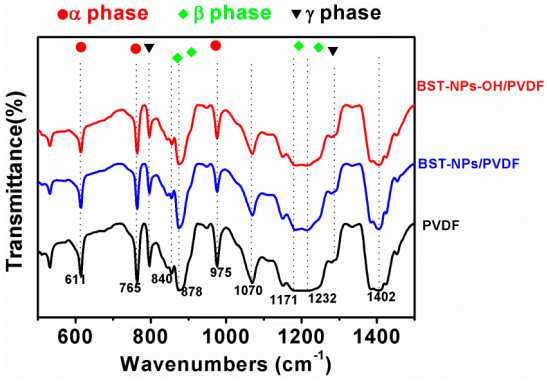

Figure 8. FT-IR spectra of the PVDF, BST–NPs/PVDF and BST–NPs–OH/PVDF nanocomposite films at a filler concentration of 10 vol %.

Figure 9 shows dielectric constants of the composites at 1 kHz as a function of the filler content. Pure PVDF has a relatively low dielectric constant of 7.9. In both composite samples, the dielectric constant gradually increases with increasing filler content. The same with 40 vol % BST–NPs–OH has a dielectric constant of 36, which is 3.6 times higher than that of pure PVDF. This enhancement is obviously attributed to the considerably higher dielectric constant of BST in comparison with that of the polymer matrix [18]. Additionally, the dielectric constant of our composites filled with the cube-shaped BST–NPs–OH is much higher than that of the composites filled with spherical fillers [24]. This is because cube-shaped fillers have higher surface area, which is helpful to increase the connectivity of composites. In addition, the

samples made with the BST–NPs–OH always have slightly larger dielectric constant than those with the BST–NPs. In addition, the loss of the BST–NPs–OH/PVDF is lower than that of the BST–NPs/PVDF. The result should be attributed to the effect of the surface modification. As discussed above, hydroxyl groups on surface of the BST–NPs–OH facilitated homogenous particle distribution in the polymer matrix. Combining with the results of SEM discussed above, the BST–NPs/PVDF have many defects such as voids in the nanocomposites, which is mean that the air was introduced in nanocomposites. The dielectric constant of air is low. Therefore, the BST–NPs–OH composite films exhibited less agglomeration and defects (such as voids), thus leading to higher dielectric constants [14,25].

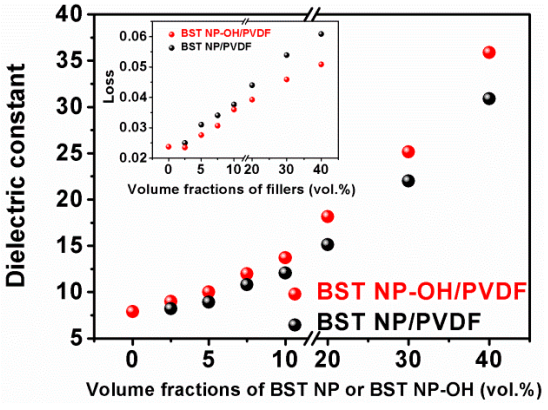

Figure 9. Dielectric constants of the BST–NPs/PVDF and BST–NPs–OH/PVDF nanocomposite films as a function of filler concentration measured at 1 kHz.

Various theoretical models have been proposed to explain the dielectric behaviors of composite materials. Figure 10 shows experimental and theoretical dielectric constants of the BST–NPs–OH nanocomposites at 1 kHz and room temperature as a function of filler volume fraction, where the theoretical values were predicted by the Maxwell–Garnett model, Lichtenecker model and Yamada model. Maxwell–Garnett model is given by:

$$\varepsilon_{eff} = \varepsilon_p \frac{2\varepsilon_p + \varepsilon_c + 2f(\varepsilon_c - \varepsilon_p)}{2\varepsilon_p + \varepsilon_c - f(\varepsilon_c - \varepsilon_p)} \quad (1)$$

where f_c is the volume fraction of fillers, while ε_{eff}, ε_p and ε_c represent the dielectric constants of the nanocomposites, PVDF and BST–NPs, respectively. Lichtenecker model is described as:

$$\ln\varepsilon_{eff} = \ln\varepsilon_p + f(1-k)(\ln\varepsilon_c - \ln\varepsilon_p) \quad (2)$$

where k is a shape-dependent parameter. Yamada model is presented as:

$$\varepsilon_{eff} = \varepsilon_p[1 + \frac{nf_c(\varepsilon_c - \varepsilon_p)}{n\varepsilon_p + (1 - f_c)(\varepsilon_c - \varepsilon_p)}] \quad (3)$$

where n is a shape-dependent parameter. From Figure 10, it is found that the experimental data are in a harmonious agreement with those given by the Maxwell–Garnett model and Lichtenecker model when the volume fraction of BST–NPs–OH powder was less than 10%. At higher contents of BST–NPs–OH powder, more interfaces were present in the nanocomposites, while these such interfaces are not taken into account by these two models. Therefore, their predictions are deviated from the experimental data of the samples with high filler contents. In contrast, the Yamada model is applicable over the whole concentration range in this study. The shape-dependent parameter of n = 15, ε_f = 1000 (reported in the literature [26]) and ε_p = 7.9 are in a good agreement with the measured data. This is because, in the Yamada model, the interactions between the neighboring particles have been taken into account and a shape-dependent parameter has been used. Shape-dependent parameter values related to the geometry of the ceramic particles from 8 to 9.5 have been reported in the literature [27,28]. One reason for this disparity is the difference size of fillers. The ceramic fillers reported in the literature have an average size of about 3 μm [27,28], while the size of BST–NPs fillers in this article is about 110 nm.

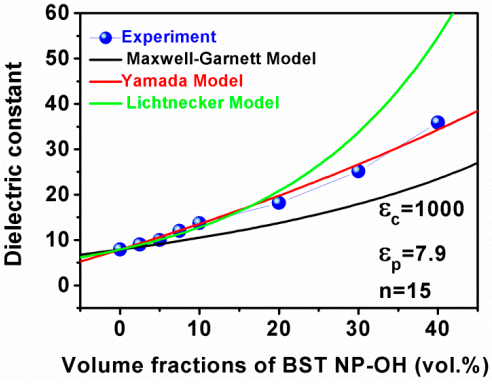

Figure 10. Theoretical and experimental dielectric constants of the composites as a function of content of the BST–NPs–OH powder.

Figure 11 shows breakdown strengths for the nanocomposites as a function of the filler content. The breakdown strength of both nanocomposites monotonically decreases with increasing filler volume fraction. The breakdown strength is strongly influenced by morphology of ceramic fillers, interface areas, agglomerations,

increasing air voids, and the large difference of the dielectric constant between the ceramic fillers and the PVDF. This can be generally attributed to the increase in inhomogeneous electrical field, agglomeration and defects in the nanocomposites [29]. When the ceramic fillers are introduced into the polymer matrix, a distortion in the distribution of the electric field is produced, due to the large difference in dielectric properties between the two phases. In this case, the electrical field in the PVDF matrix is much higher than the average electric field. Therefore, overall breakdown strength of the nanocomposites is decreased. On the other hand, the breakdown strength of the polymer–matrix composites could be largely reduced, if agglomerations and defects are formed. As stated earlier, with increasing filler content, particle agglomeration and for the formation of voids cannot be avoided.

Specifically, the nanocomposites with the BST–NPs–OH always have a higher breakdown strength than the BST–NP counterparts. For example, at 40 vol %, the breakdown strength of the nanocomposite with the BST–NPs–OH is 1210 kV/cm, about two times that of the BST–NP sample (605 kV/cm). This observation is attributed the effect of the surface hydroxylation. The surface hydroxylation benefits the homogenous distribution of BST–NPs–OH in the polymer matrix as seen in SEM images and decreases the defects such as voids in the nanocomposites. This factor contributes to the improvement of the breakdown strength of the nanocomposites [30].

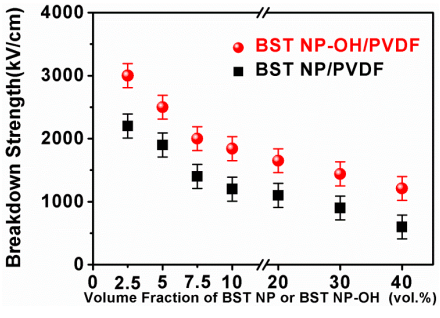

Figure 11. Breakdown strengths the BST–NP/PVDF and BST–NP–OH/PVDF nanocomposites as a function of the filler concentration.

Energy-storage density is related to not only dielectric constant and breakdown strength, but also the polarization and applied electric field. It is well known that the polarization of ferroelectrics is not linearly dependent on electric field, while both the polarization and dielectric constant of ferroelectric materials are strongly dependent on a variety of external conditions. The energy-storage density of ferroelectric materials can be calculated from the *P-E* loops, with the formula, $U = \int EdP$ (where

E and *P* are applied electric field and polarization, respectively). Figure 12 shows *P–E* loops at 100 Hz of the BST–NPs–OH/PVDF nanocomposites. At 1000 kV/cm, the polarization of the nancomposites increases constantly with the filler volume fraction and reaches a maximum value of 3.1 μC/cm^2 at 30 vol %, which should be attributed to the increase in dielectric constant of the nanocomposites. However, the remnant polarization of the composites is also increased with increasing content of BST–NPs–OH. A high remnant polarization means a low energy-storage density, because the integrated area of the *P-E* curve associated with the discharge cycle is decreased.

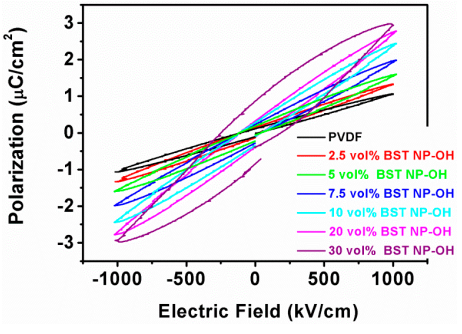

Figure 12. *P-E* loops of the BST–NsP–OH/PVDF nanocomposites with different filler contents.

Figure 13 shows room-temperature energy-storage density of the nanocomposites. Obviously, the energy-storage density is strongly dependent on the BST–NPs–OH content, which is maximized at 5 vol %, with a value of 3.9 J/cm^3 (at 2500 kV/cm). This value is higher than that of the pure PVDF (2.8 J/cm^3) at 4000 kV/cm.

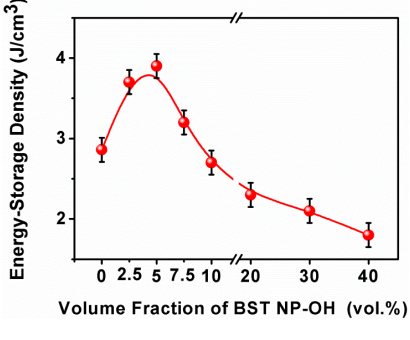

Figure 13. Energy storage density of the BST–NP–OH/PVDF nanocomposites as a function of the filler concentration.

5. Conclusions

Surface hydroxylation of BST–NPs ceramic fillers has a positive effect on dielectric properties, breakdown strength and energy storage densities of the PVDF based nanocomposites, due to the improvement in homogeneity of the nanocomposites. A maximum dielectric constant of 36 (1 kHz) was observed in the BST–NPs–OH sample with a filler concentration of 40 vol %. The sample had a breakdown strength of 1210 kV/cm, two times higher than that the BST–NPs counterpart. A maximal energy density of 3.9 J/cm^3 was obtained in the composite sample with 5 vol % BST–NPs–OH. It is believed that the finding of this study can be extended to other composites in order to achieve high energy storage density for potential applications in energy storage and power capacitor components.

Acknowledgments: This research was supported by the Ministry of Sciences and Technology of China through 973-project under Grant (2015CB654601).

Author Contributions: Shaohui Liu wrote the main manuscript text. Shaomei Xiu prepared Figures 3 and 4. Bo Shen, Ling Bing Kong and Jiwei Zhai revised this manuscript. All authors reviewed the manuscript.

Conflicts of Interest: The authors declare no conflict of interest.

References

1. Yu, J.H.; Huang, X.Y.; Wu, C.; Wu, X.F.; Wang, G.L; Jiang, P.K. Interfacial modification of boron nitride nanoplatelets for epoxy composites with improved thermal properties. *Polymer* **2012**, *53*, 471–480.
2. Liu, S.H.; Xue, S.X.; Zhang, W.Q.; Zhai, J.W.; Chen, G.H. The influence of crystalline transformation of $Ba_{0.6}Sr_{0.4}TiO_3$ nanofibers/poly(vinylidene fluoride) composites on the energy storage properties by quenched technique. *Ceram. Int.* **2015**, *41*, S430–S434.
3. Zhang, X.; Shen, Y.; Zhang, Q.; Gu, L.; Hu, Y.; Du, J.; Lin, Y.; Nan, C.W. Ultrahigh energy density of polymer nanocomposites containing $BaTiO_3$@TiO_2 nanofibers by atomic-scale interface engineering. *Adv. Mater.* **2015**, *27*, 819–824.
4. Wu, L.; Wang, X.; Gong, H.; Hao, Y.; Shen, Z.; Li, L. Core-satellite $BaTiO_3$@$SrTiO_3$ assemblies for a local compositionally graded relaxor ferroelectric capacitor with enhanced energy storage density and high energy efficiency. *J. Mater. Chem. C* **2015**, *3*, 750–758.
5. Liu, S.H.; Xue, S.X.; Shen, B.; Zhai, J.W. Reduced energy loss in poly(vinylidene fluoride) nanocomposites by filling with a small loading of core-shell structured $BaTiO_3/SiO_2$ nanofibers. *Appl. Phys. Lett.* **2015**, *107*, 032907.
6. Wang, G.; Huang, X.; Jiang, P. Increasing the energy efficiency and breakdown strength of high-energy-density polymer nanocomposites by engineering the $Ba_{0.7}Sr_{0.3}TiO_3$ nanowire surface via reversible addition—fragmentation chain transfer polymerization. *J. Phys. Chem. C* **2015**, *7*, 18017–18027.

7. Shen, Y.; Hu, Y.; Chen, W.; Wang, J.; Guan, Y.; Du, J.; Zhang, X.; Ma, J.; Li, M.; Lin, Y. Modulation of topological structure induces ultrahigh energy density of graphene/$Ba_{0.6}Sr_{0.4}TiO_3$ nanofiber/polymer nanocomposites. *Nano Energy* **2015**, *18*, 176–186.
8. Liu, S.H.; Xiao, S.; Xiu, S.M.; Shen, B.; Zhai, J.W.; An, Z. Poly(vinylidene fluoride) nanocomposite capacitors with a significantly enhanced dielectric constant and energy density by filling with surface-fluorinated $Ba_{0.6}Sr_{0.4}TiO_3$ nanofibers. *RSC Adv.* **2015**, *5*, 40692–40699.
9. Tang, H.; Zhou, Z.; Bowland, C.C.; Sodano, H.A. Synthesis of calcium copper titanate ($CaCu_3Ti_4O_{12}$) nanowires with insulating SiO_2 barrier for low loss high dielectric constant nanocomposites. *Nano Energy* **2015**, *17*, 302–307.
10. Chu, B.J.; Zhou, X.; Ren, K.L.; Neese, B.; Lin, M.R.; Wang, Q.; Bauer, F.; Zhang, Q.M. A dielectric polymer with high electric energy density and fast discharge speed. *Science* **2006**, *313*, 334–336.
11. Liu, S.H.; Zhai, J.W. Improving the dielectric constant and energy density of poly(vinylidene fluoride) composites induced by surface-modified $SrTiO_3$ nanofibers by polyvinylpyrrolidone. *J. Mater. Chem. A* **2015**, *3*, 1511–1517.
12. Dang, Z.M.; Yuan, J.K.; Yao, S.H.; Liao, R.J. Preparation and dielectric properties of core–shell structured Ag@polydopamine/poly(vinylidene fluoride) composites. *Adv. Mater.* **2013**, *25*, 6334–6365.
13. Huang, X.; Jiang, P. Core–shell structured high-*k* polymer nanocomposites for energy storage and dielectric applications. *Adv. Mater.* **2015**, *27*, 546–554.
14. Liu, S.H.; Zhai, J.W.; Wang, J.W.; Xue, S.X.; Zhang, W.Q. Enhanced energy storage density in poly(vinylidene fluoride) nanocomposites by a small loading of suface-hydroxylated $Ba_{0.6}Sr_{0.4}TiO_3$ nanofibers. *ACS. Appl Mater. Inter.* **2014**, *6*, 1533–1540.
15. Tang, H.X.; Zhou, Z.; Sodano, H.A. Relationship between $BaTiO_3$ nanowire aspect ratio and the dielectric permittivity of nanocomposites. *ACS. Appl Mater. Interfaces* **2014**, *6*, 5450–5455.
16. Dang, Z.M.; Yuan, J.K.; Zha, J.W.; Zhou, T.; Li, S.T.; Hu, G.H. Fundamentals, processes and applications of high-permittivity polymer–matrix composites. *Prog. Mater. Sci.* **2012**, *57*, 660–723.
17. Luo, B.; Wang, X.; Wang, Y.; Li, L. Fabrication, characterization, properties and theoretical analysis of ceramic/PVDF composite flexible films with high dielectric constant and low dielectric loss. *J. Mater. Chem A* **2014**, *2*, 510–519.
18. Liu, S.H.; Xue, S.X.; Zhang, W.Q.; Zhai, J.W.; Chen, G.H. Significantly enhanced dielectric property in PVDF nanocomposites flexible films through a small loading of surface-hydroxylated $Ba_{0.6}Sr_{0.4}TiO_3$ nanotubes. *J. Mater. Chem A* **2014**, *2*, 18040–18046.
19. Song, Y.; Shen, Y.; Hu, P.H.; Lin, Y.H.; Li, M.; Nan, C.W. Significant enhancement in energy density of polymer composites induced by dopamine-modified $Ba_{0.6}Sr_{0.4}TiO_3$ nanofibers. *Appl Phys. Lett* **2012**, *101*.

20. Liu, S.H.; Zhai, J.W. A small loading of surface-modified $Ba_{0.6}Sr_{0.4}TiO_3$ nanofiber-filled nanocomposites with enhanced dielectric constant and energy density. *RSC. Adv.* **2014**, *4*, 40973–40979.
21. Xie, L.Y.; Huang, X.Y.; Wu, C.; Jiang, P.K. Core-shell structured poly(methyl methacrylate)/$BaTiO_3$ nanocomposites prepared by in situ atom transfer radical polymerization: A route to high dielectric constant materials with the inherent low loss of the base polymer. *J. Mater. Chem* **2011**, *21*, 5897–5906.
22. Xie, L.Y.; Huang, X.Y.; Huang, Y.H.; Yang, K.; Jiang, P.K. Core-shell structured hyperbranched aromatic polyamide/$BaTiO_3$ Hybrid filler for poly(vinylidene fluoride-trifluoroethylene-chlorofluoroethylene) nanocomposites with the dielectric constant comparable to that of percolative composites. *ACS Appl. Mater. Interfaces* **2013**, *5*, 1747–1756.
23. Xie, L.Y.; Huang, X.Y.; Yang, K.; Li, S.T.; Jiang, P.K. "Grafting to" route to PVDF-HFP-GMA/$BaTiO_3$ nanocomposites with high dielectric constant and high thermal conductivity for energy storage and thermal management applications. *J. Mater. Chem A* **2014**, *2*, 5244–5251.
24. Kim, P.; Doss, N.M.; Tillotson, J.P.; Hotchkiss, P.J.; Pan, M.J.; Marder, S.R.; Li, J.Y.; Calame, J.P.; Perry, J.W. High energy density nanocomposites based on surface-modified $BaTiO_3$ and a ferroelectric polymer. *ACS Nano* **2009**, *3*, 2581–2592.
25. Yu, K.; Niu, Y.J.; Zhou, Y.C.; Bai, Y.Y.; Wang, H. Nanocomposites of surface-modified $BaTiO_3$ nanoparticles filled ferroelectric polymer with enhanced energy density. *J. Am. Ceram. Soc.* **2013**, *96*, 2519–2524.
26. Wang, Z.P.; Nelson, J.K.; Hillborg, H.; Zhao, S.; Schadler, L.S. Dielectric constant and breakdown strength of polymer composites with high aspect ratio fillers studied by finite element models. *Compos. Sci. Technol.* **2013**, *76*, 29–36.
27. Hu, G.; Gao, F.; Kong, J.; Yang, S.; Zhang, Q.; Liu, Z.; Zhang, Y.; Sun, H. Preparation and dielectric properties of poly(vinylidene fluoride)/$Ba_{0.6}Sr_{0.4}TiO_3$ composites. *J. Alloy. Compd.* **2015**, *619*, 686–692.
28. Thomas, P.; Varughese, K.; Dwarakanath, K.; Varma, K. Dielectric properties of poly(vinylidene fluoride)/$CaCu_3Ti_4O_{12}$ composites. *Compos. Sci. Technol.* **2010**, *70*, 539–545.
29. Yang, K.; Huang, X.Y.; Huang, Y.H.; Xie, L.Y.; Jiang, P.K. Fluoro-polymer@$BaTiO_3$ hybrid nanoparticles prepared via RAFT polymerization: Toward ferroelectric polymer nanocomposites with high dielectric constant and low dielectric loss for energy storage application. *Chem. Mater.* **2013**, *25*, 2327–2338.
30. Wang, Y.; Cui, J.; Yuan, Q.; Niu, Y.; Bai, Y.; Wang, H. Significantly enhanced breakdown strength and energy density in sandwich-structured barium titanate/poly(vinylidene fluoride) Nanocomposites. *Adv. Mater.* **2015**, *27*, 6658–6663.

Structural and Spectroscopic Characterization of A Nanosized Sulfated TiO_2 Filler and of Nanocomposite Nafion Membranes

Valentina Allodi, Sergio Brutti, Marco Giarola, Mirko Sgambetterra, Maria Assunta Navarra, Stefania Panero and Gino Mariotto

Abstract: A large number of nano-sized oxides have been studied in the literature as fillers for polymeric membranes, such as Nafion®. Superacidic sulfated oxides have been proposed and characterized. Once incorporated into polymer matrices, their beneficial effect on peculiar membrane properties has been demonstrated. The alteration of physical-chemical properties of composite membranes has roots in the intermolecular interaction between the inorganic filler surface groups and the polymer chains. In the attempt to tackle this fundamental issue, here we discuss, by a multi-technique approach, the properties of a nanosized sulfated titania material as a candidate filler for Nafion membranes. The results of a systematic study carried out by synchrotron X-ray diffraction, transmission electron microscopy, thermogravimetry, Raman and infrared spectroscopies are presented and discussed to get novel insights about the structural features, molecular properties, and morphological characteristics of sulphated TiO_2 nanopowders and composite Nafion membranes containing different amount of sulfated TiO_2 nanoparticles (2%, 5%, 7% w/w).

Reprinted from *Polymers*. Cite as: Allodi, V.; Brutti, S.; Giarola, M.; Sgambetterra, M.; Navarra, M.A.; Panero, S.; Mariotto, G. Structural and Spectroscopic Characterization of A Nanosized Sulfated TiO_2 Filler and of Nanocomposite Nafion Membranes. *Polymers* **2016**, *8*, 68.

1. Introduction

Among the different polymer electrolytes proposed as proton exchange membranes (PEM) for fuel cell (FC) applications, one of the best choices is represented by perfluorinated polymers, such as Dupont's Nafion®, due to their high proton conductivity and the excellent mechanical and chemical stability. Unfortunately, ionic conduction of Nafion is strongly dependent on the membrane hydration, and a sharp decrease in conductivity is observed at working temperatures above 80–100 °C due to dehydration and polymer structure relaxation. An upgrade of the Nafion properties in critical conditions (high temperature, low relative humidity) can be achieved by

loading the pristine Nafion with hydrophilic inorganic acids, which can both act as a water reservoir, into the polymer matrix (thus increasing the membrane water uptake) and, in virtue of their acidity, provide additional pathways for proton hopping inside the polymer. Among the inorganic acids, sulfated transition-metal oxides have become the subject of intensive studies, due to the high stability and extraordinary acidity of some of these compounds, as, for instance, sulfated zirconium oxide [1–3], sulfated tin oxide [4,5], and sulfated titanium oxide [6]. The latter has been widely studied in the past as a catalyst and as a proton conductor [7,8]. Recently, sulfated titania nanoparticles have been added to various polymers to form composite membranes with improved thermal and mechanical properties and enhanced proton conductivity [9].

This work reports on the results of a multi-technique characterization of nanosized sulfated TiO_2 powders obtained through a direct one-step synthesis and their incorporation as fillers in Nafion-based polymer electrolytes. To the best of our knowledge, the inclusion of one-step synthesized S-TiO_2 in Nafion membranes has never been reported before, with the exception of our recent work where water dynamics inside S-TiO_2-added Nafion membranes were investigated by NMR spectroscopy [10]. In the present paper, structural features, molecular properties, as well as morphological characteristics of TiO_2 nanopowders, both before and after the incorporation in Nafion membranes, have been investigated by a variety of advanced techniques, such as synchrotron X-ray diffraction (XRD), transmission electron microscopy (TEM), thermogravimetry (TGA), and vibrational spectroscopies (both Raman scattering and infrared absorption), paying particular attention to the effects caused by their exposure to a high humidity. Finally, the homogeneity degree of both structure and morphology of composite Nafion membranes with different amounts of sulfated TiO_2 nanoparticles (2%, 5%, 7% w/w) has been probed in the micrometric scale by Raman mapping. Our goal is to illustrate how the incorporation of sulfated nanostructured titania into Nafion membranes alters the local environment of the ionic and hydrophobic domains of the membranes in terms of bonding and molecular interactions.

2. Materials and Methods

Sulfated titania (S-TiO_2) was obtained through a one-step sol-gel procedure by adapting the synthesis proposed by Swaminathan and co-workers [11]. A solution of titanium isopropoxide in 2-propanol was used as Ti source and an aqueous sulfuric acid solution was adopted for both hydrolysis and sulfating processes. H_2SO_4 (0.5 M; 6.4 mL) was added to a mixture of 12.5 mL of titanium(IV) isopropoxide (Sigma-Aldrich, St. Louis, MO, USA) and 100 mL of 2-propanol (Sigma-Aldrich, St. Louis, MO, USA) with vigorous stirring. After 2 h, the solution was filtered, then calcined for 3 h at 400 °C to obtain an inorganic powder. Plain

and composite Nafion membranes were prepared according to a solvent-casting procedure already reported in a previous work [3]. A proper dispersion of commercial Nafion (5 wt % in water/alcohol, E.W. 1100, Ion Power, GmbH) was treated with *N*,*N*-dimethylacetamide at 80 °C in order to replace the solvents. As for the composite membranes, the inorganic powder was added to the final Nafion solution and stirred to homogenize the dispersion. Filler concentrations of 2%, 5%, and 7% *w*/*w* of S-TiO_2 with respect to Nafion content were chosen. Each mixture was casted on a Petri dish and dried at 100 °C to obtain self-standing membranes. After that, dry membranes were hot-pressed at 175 °C and 50 atm for 15 min in order to improve their thermo-mechanical properties. They were finally activated by immersion in a boiling solution of hydrogen peroxide (3%), sulfuric acid (0.5 M), and water. All of the membrane samples were stored in distilled water after preparation. Membrane samples are labeled here as N for plain Nafion and as nTiO_2-S (*n* = 2, 5, 7) for composite Nafion membranes filled by different nominal amounts of sulfated inorganic powder. Table 1 summarizes the samples investigated in this work and the acronyms used to identify them.

Table 1. Plain Nafion and composite Nafion membranes investigated in this work.

Sample	Filler	Filler content (wt %)	Sample acronym
Plain Nafion	None	0	N
Composite Nafion	Superacid S-TiO_2	2	2-TiO_2-S
Composite Nafion	Superacid S-TiO_2	5	5-TiO_2-S
Composite Nafion	Superacid S-TiO_2	7	7-TiO_2-S

Synchrotron X-ray diffraction experiments were carried out at the ELETTRA synchrotron radiation source (MCX beamline) on capillarized S-TiO_2 powders. An X-ray wavelength of 1.204 Å has been used in a diffractometer equipped with a four-circle Huber goniometer (2θ precision better than 0.0001°) in full circle configuration. The diffraction spectra were recorded in the 15–67 degree 2-theta (2θ) range, with a step size of 0.01 degrees and a time per step of two seconds. The structural refinement has been carried out by the GSAS code [12] starting from the anatase polymorphic lattice of TiO_2 [13].

Transmission electron microscopy measurements were performed by a FEI G2 20 HR-TEM instrument equipped with a LaB6 electron beam source and two 2D flat cameras (low-resolution and high-resolution). Samples have been suspended in acetone in an ultrasonic bath and dispersed on copper holey carbon film grids for observation.

Thermal properties of the powders were evaluated by means of thermogravimetric analysis (TGA) performed in air flux (60 mL·min^{-1}) at a heating rate of 5 °C·min^{-1} with a TGA/SDTA 851 Mettler-Toledo (Greifensee, Switzerland). In order to investigate the hydro-thermal stability of the synthesized oxide, TGA measurements were performed on both pristine and hydrolyzed powders, these latter obtained according to the following protocol. S-TiO_2 powder was dispersed in boiling water (1 mL of water for 1 mg of powder) under vigorous stirring for 1 h, filtered, and washed three times with cold water, and finally calcined at 400 °C for 3 h.

Vibrational characterization of both sulfated titania nanopowders and composite membranes was carried out by means of FT-IR and Raman spectroscopy measurements. FT-IR spectra were obtained at room temperature, using a JASCO spectrometer (FT/IR-660 plus, JASCO, Easton, MD, USA) equipped with a Tri-Glycine-Sulfate (TGS) detector, either in attenuated total reflection (ATR) configuration (using a germanium crystal for both kinds of samples, spectral range between 4000 and 900 cm^{-1}), or in transmission configuration in KBr pellets. All of the IR spectra were recorded with a resolution of 4 cm^{-1}, and a polystyrene film was used as reference for wavenumber calibration. In order to allow for a better comparison between different samples, a proper baseline has been carefully subtracted from each FT-IR spectrum. Prior to the measurement each membrane was dried in vacuum for 30 min to avoid the occurrence of spectral differences between the samples due to a different hydration degree.

Micro-Raman spectroscopy measurements were carried out in backscattering geometry at room temperature using, in turn, two different Horiba-Jobin Yvon micro-sampling spectrometers (Horiba, Kyoto, Japan): a LABRAM HR, consisting of a single monochromator, for spectra detection extended to a very high wavenumber region and a triple-axis monochromator (model T64000) in order to probe the spectral region below 200 cm^{-1} down to a few wavenumbers from the laser excitation line. The single monochromator spectrometer was equipped with a He–Ne laser as excitation source (632.8 nm) and a notch filter for the Rayleigh line cut-off. The scattered radiation was dispersed by a removable diffraction grating having 600 or 1800 lines/mm and detected at the spectrograph output by a multichannel device, a CCD with 1024 × 256 pixels, cooled by liquid nitrogen, and with its maximum efficiency occurring in the red region. The spectral resolution was about 1 cm^{-1}/pixel when the 1800 lines/mm grating was used, while the spectral limit on the side of low wavenumbers, due to the notch filter, was about 200 cm^{-1}. In order to investigate the low-wavenumber spectral region, the triple-axis monochromator, set in double subtractive/single configuration, and equipped with holographic gratings having 1800 lines/mm, was exploited. For most measurements carried out by means of this spectrometer, the excitation source was the 514.5-nm line of a mixed Ar-Kr ion gas

laser. The scattered radiation detection was ensured by a multichannel detector an open-electrode CCD, consisting of a matrix of 1024 × 256 pixels, cooled by liquid nitrogen, whose maximum efficiency occurred in the green/yellow region. In these conditions the spectral resolution was about 0.4 cm^{-1}/pixel. Both micro-Raman setups were coupled to a camera which allowed for the exploration and selection of the sample region worth to be measured. Independently of the spectrometer used to carry out the Raman measurements, the spectra were obtained by focusing the laser beam onto a spot of about 2 μm in size through a long-working distance 50× objective, with medium numerical aperture (N.A. = 0.5), or through a 80× objective with high numerical aperture (N.A. = 0.9). The laser power at the samples surface was kept below 5 mW. All the spectra were calibrated in wavenumber using the emission lines of an Ar spectral lamp. In order to verify the spectra reproducibility over the sample surface, repeated micro-Raman spectra were carried out under the same experimental conditions from different points of the investigated sample. The recorded spectra were processed to remove artifacts due to cosmic rays, while the luminescence background, consisting of a continuous line, underlying the overall Raman spectrum and having both the shape and the intensity dependent of the probed sample region, was subtracted before starting the analysis of the experimental data.

3. Results and Discussion

3.1. Structural and Thermal Characterization of the Sulfated Powders

A typical diffraction pattern of the synthesized powders recorded at the synchrotron radiation source is shown in the Figure 1. The synthesized material consists of nanosized nanoparticles of anatase as confirmed by synchrotron diffraction. The Rietveld refinement suggests a slightly deformed trigonal anatase lattice with crystal parameters of a = 3.791 Å and c = 9.439 Å to be compared to a = 3.784 Å and c = 9.514 Å literature values, respectively (convergence parameters Rwp = 4.9% RF_2 = 1.0%, DWd = 1.74) [13,14]. Occupancies and Debye-Waller factors have been fixed in the refinement (x(Ti) = x(O) = 1; B(O) = 2.0; and B(Ti) = 1.0). The refined crystal structure is in a satisfactory agreement with literature data, e.g., the atomic site position of oxygen (x = 0.926) to be compared with that of [13,15,16]. The undulations of the background suggest the presence also of minor content of nanosized particles with TiO_2-B structure [17–19]. The final crystallite size obtained by size-strain analysis suggests a diameter of about 10.1 ± 0.6 nm.

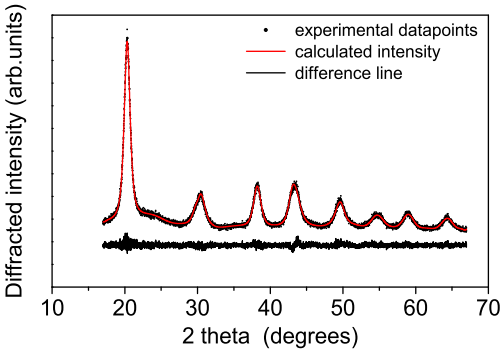

Figure 1. Synchrotron diffraction patters of the synthesized samples fitted by Rietveld method using the GSAS software.

The morphology of the S-TiO_2 ceramic material has been investigated by TEM: two typical micrographs at different magnifications are presented in Figure 2. The low magnification TEM image highlights a highly homogeneous sample constituted by nanometric round-shaped particles of very similar size. The powder is morphologically very pure: apparently no contaminations by larger particles, chunks, or other morphologies can be observed. The size distribution obtained by analyzing 10 micrographs and more than 500 particles by using the ImageJ software [20,21] indicates a mean diameter of about 7.6 $\pm$ 2.5 nm in fair good agreement with the value derived from XRD size-strain analysis (10.1 $\pm$ 0.6 nm). High-resolution TEM imaging confirms the uniform morphology of the nanoparticles and evidences their crystalline nature, too. Diffraction fringes have been observed throughout the entire sample and the corresponding Fast Fourier Transform (FTT) pattern easily indexed to the crystal lattice planes of anatase TiO_2 [13].

The thermal response of S-TiO_2 is reported in Figure 3: in addition to the pristine S-TiO_2 material, a second sample has also been studied by TG, namely hydrolyzed-S-TiO_2. The latter sample has been obtained by a drastic hydrolysis treatment after the standard synthesis, as reported in the experimental section, in order to highlight eventual losses of weakly bonded and physisorbed sulfate surface groups. Both pristine (red curve) and hydrolyzed (black curve) samples present two main weight losses. The first loss, starting just above room temperature until about 500 °C, can be ascribed to removal of water and surficial OH^- anions, while the second main loss, occurring above 500 °C, is due to thermal decomposition of SO_4^{2-} groups. It is worth noticing that a high sulfation degree is detected in pristine S-TiO_2 powder (*i.e.*, *ca.* 8%) confirming the effectiveness of the synthetic route. Moreover, a certain extent of sulfation is retained after the severe hydrothermal stability test. Indeed, a weight loss of about 2% is observed for the hydrolyzed sample above 500 °C.

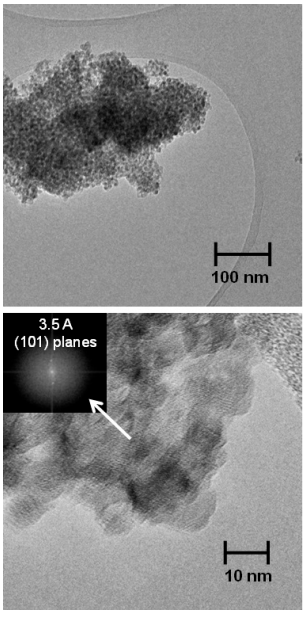

Figure 2. Transmission electron micrographs of the synthesized powders. In the inset of the bottom micrograph a FFT pattern of the periodic arrangement of the crystal planes is shown with an indexing for the trigonal anatase lattice.

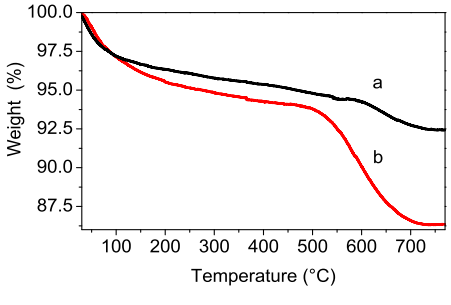

Figure 3. TGA of hydrolyzed (**a**) and pristine (**b**) powders.

Derivative thermal gravimetric (DTG) curves of pristine and hydrolyzed powders are reported in Figure 4 in the 300–750 °C temperature region in order to better highlight the different thermal processes of sulfate decomposition occurring in the two samples. A shift of the derivative peak minimum towards higher temperature occurs when moving from pristine (*ca.* 600 °C, red curve) to hydrolyzed (*ca.* 650 °C, black curve) powder. This shift can be explained by assuming the presence of differently-bonded sulfate species: the weakly bonded ones, decomposing at lower

temperature, are hydrolyzed, whereas the more strongly-bonded sulfate species are retained even at higher temperature as evidenced by their DTG response.

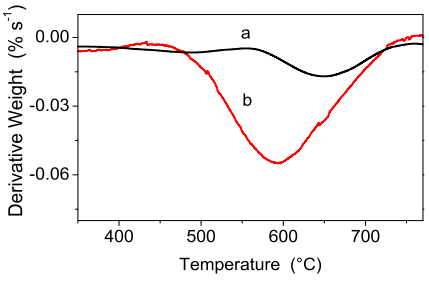

Figure 4. DTG curves of hydrolyzed (**a**) and pristine (**b**) powders.

3.2. Vibrational Characterization of the Synthesized Powders

The vibrational characterization of the synthesized sample was carried out both by Raman and Infrared absorption spectroscopy. A typical Raman spectrum of the S-TiO_2 powder carried out in the low wavenumber region is shown in the Figure 5a. This spectrum consists of several Raman bands, having quite different spectral amplitude. At first sight it looks very similar to that of nanocrystalline anatase TiO_2 reported in literature [22], thus indicating that this titania phase is the paramount component of the synthesized powders. However, a deeper insight also reveals the occurrence of some weak Raman modes besides the five ones of anatase TiO_2, which suggest the presence of a second minor component, probably related to a TiO_2-B phase, as revealed by the x-ray diffraction results. Therefore, in order to discuss in depth the Raman spectrum measured from the synthesized nanopowders, we shall refer to both of these crystalline titania phases.

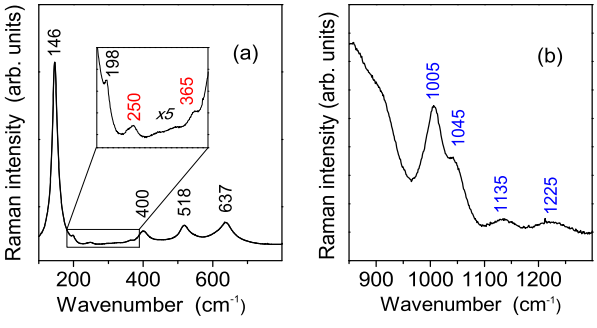

Figure 5. Experimental Raman spectra of the synthesized sample showing typical features of TiO_2 (panel **a**) and of sulfate group SO_4^{2-} (panel **b**). The details about the spectra detection are provided in the text.

Crystalline anatase TiO_2 has a tetragonal structure which belongs to the space group $D_{4h}{}^{19}$ (I41/amd). Among them six modes are Raman active (1 A_{1g}, 2 B_{1g} and 3 E_g). In micro-crystalline TiO_2 anatase they occur at about 143 cm^{-1} (E_g), 198 cm^{-1} (E_g), 395 cm^{-1} (B_{2g}), 512 cm^{-1} (A_{1g}), 518 cm^{-1} (B_{1g}), 639 cm^{-1} (E_g) [23]. All of these vibrational modes are present in the spectrum of S-TiO_2 powders (see Figure 5a), although slightly shifted in wavenumber with respect to single crystal due to the nanocrystalline character of our powders. On the other hand, TiO_2-B phase is characterized by four formula units per unit cell and, thus, a total of 36 vibrations, among which 12 A_g and 6 B_g are Raman active modes [24,25]. However, only two TiO_2-B modes are unambigously observed in S-TiO_2 Raman spectra, respectively at about 250 and 365 cm^{-1} (see Figure 5a, quoted in red). The missing peaks of this titania phase are probably hidden under the much stronger ones due to anatase. As for the Raman spectra of the S-TiO_2 powder recorded in the higher wavenumber region, Figure 5b shows the spectral features related to sulfate functionalization: the peak at about 1005 cm^{-1}, is assigned to the stretching mode ν_1 of the $SO_4{}^{2-}$ groups, while the three bands (one of which occurring at about 1045 cm^{-1} and two weaker at about 1135 and 1225 cm^{-1}) are associated to the splitting of the ν^3 mode of the $SO_4{}^{2-}$ units. The splitting, due to a lowering of the free $SO_4{}^{2-}$ anion symmetry, suggests the formation of bidentate sulfate groups coordinated to TiO_2 nano-particles [26]. Raman spectroscopy therefore confirms that the sample consists of a predominant phase, *i.e.* anatase, and a minor component, *i.e.*, TiO_2-B, in fair agreement with X-ray diffraction results. Moreover, it clearly reveals the sulphated functionalization of the synthesized powders.

The vibrational spectrum of sulfate groups of the S-TiO_2 powder was also detected by ATR FT-IR spectroscopy. Figure 6a clearly shows the occurrence of the ν_1 vibrational mode at about 1000 cm^{-1} and the three ν^3 modes at about 1047, 1136 and 1224 cm^{-1}, respectively. The number and position of these modes fairly correlate with the above Raman spectroscopy findings, as well as with the observations of Arata and Hino [27] who attributed them to bidentate sulfate coordination at the titania surface.

In order to investigate the nanopowder interaction with water, and, at the same time, to simulate the condition of a Nafion membrane in a working fuel cell, samples were stored in a high relative humidity (RH) environment (close to 100% RH) for at least 12 h. The FT-IR spectra recorded on the powder after the exposure to moisture, shown in Figure 6b, shows evidence of remarkable changes of the spectral features with regard to both their number and their relative intensity. In particular, the disappearance of the mode at about 1224 cm^{-1} indicates a different arrangement of $SO_4{}^{2-}$ groups in presence of a higher water content, which turns out to promote the switch from a bidentate coordination to a monodentate one of the same groups inside S-TiO_2 nanoparticles. This change of the sulfate coordination suggests

the occurrence of an interaction mechanism between S-TiO_2 and water molecules similar to that proposed by Bolis *et al.* for sulfated ZnO_2 [27]. Similar changes on vibrational spectrum of S-TiO_2 powders exposed to high relative humidity are observed by Raman spectroscopy, which in addition reveals the occurrence of an extra peak at 981 cm^{-1} (Figure 7). This is attributed to the stretching vibrational mode of a quasi-isolated SO_4^{2-} ion [28,29], which is not detected by IR spectroscopy for symmetry reasons. The Raman spectrum evolution is in accordance with TGA results obtained on the sample before and after the hydrolysis. Therefore, the picture emerging from both Raman and TGA measurements is the following: due the hydrolysis treatment a part of the sulfate groups is released, and, in a high RH environment, this part of sulfate groups shows the spectrum typical of isolated SO_4^{2-}. Moreover, the sulfate ions having a monodentate coordination in the high RH conditions most probably represent the remaining fraction after the hydrolysis treatment.

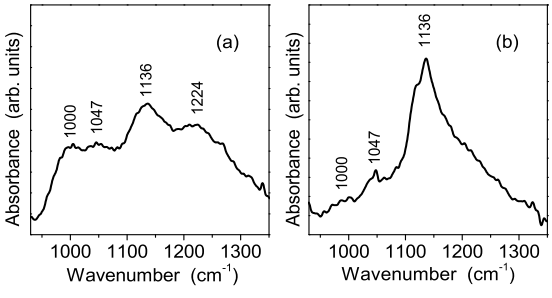

Figure 6. FT-IR ATR spectra of the synthesized sample showing typical features of the sulfate group SO_4^{2-} recorded before (panel **a**) and after (panel **b**) the storage in high relative humidity environment. The details about the spectra detection are provided in the text.

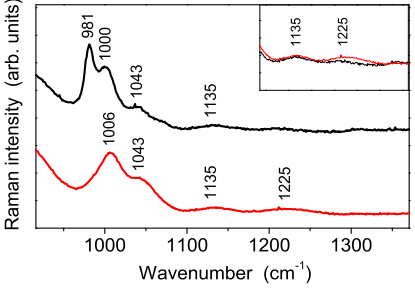

Figure 7. Raman spectra of the synthesized sample before (red) and after (black) the storage in high humidity environment. Inset: direct comparison of the 1225 cm^{-1} peak intensity.

3.3. Vibrational Characterization of Composite Membranes

The vibrational properties of Nafion membranes (pure and composite with three different amounts of filler) were also investigated. The related Raman spectra, observed in the wavenumber region above 380 cm^{-1}, are reported in Figure 8. All of the samples show the characteristic bands of Nafion at about 385 cm^{-1} [$\delta(CF_2)$], 731 cm^{-1} [$ns(CF_2)$], 804 cm^{-1} [n(C–S)], 971 cm^{-1} [ns(C–S)], 1059 cm^{-1} [$ns(SO_3^-)$], 1212 cm^{-1} [$nas(CF_2)$], 1295 cm^{-1} [n(C–C)] and 1375 cm^{-1} [ns(C–C)] [30]. No significant shift of the Nafion peaks was detected in composite membranes with respect to the pure one. Likewise, the peaks of TiO_2 anatase incorporated within the composite membranes spectra occur at the same wavenumbers as in the S-TiO_2 powder. Moreover, a spatial inhomogeneity, over the scale of 10 μm, of the S-TiO_2 distribution within the membranes, was present in all the nanocomposite samples, so that the spectra reported in Figure 8 should be considered as the representative spectra of the three composite membranes.

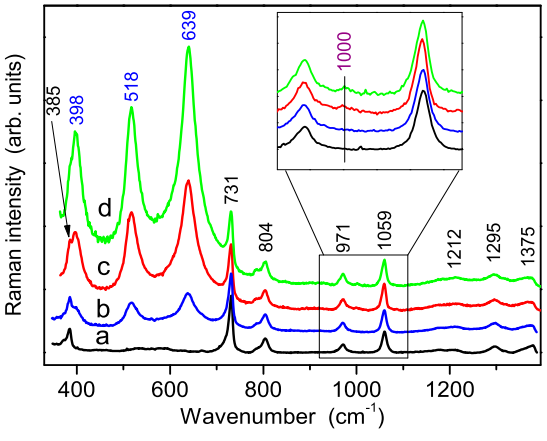

Figure 8. Experimental Raman spectra, carried out in the high wavenumber region, of pure Nafion membrane (**a**) and of three composite membranes with increasing amounts of TiO_2 nanopowders: 2% (**b**) 5% (**c**) and 7% (**d**). The inset report the spectra of SO_4^{2-} groups in the region 950–1090 cm^{-1} after proper magnification.

As for the Raman spectrum of sulfate groups, shown after proper magnification in the inset of Figure 8, a weak peak occurring at about 1000 cm^{-1} is clearly observed in composite membranes heavily loaded by S-TiO_2 (*i.e.*, with 5% and 7% *w*/*w*), thus confirming the persistence of sulfate groups in composite samples after the powder incorporation. Moreover, the comparison between the Raman spectra carried out in the low wavenumber region from S-TiO_2 nanopowders and from composite membranes, see Figure 9, indicates the occurrence of an important phase

rearrangement of the TiO_2 component incorporated into the Nafion membrane, which results in a remarkable decrease of the TiO_2-B phase, while the anatase one seems to be unaffected.

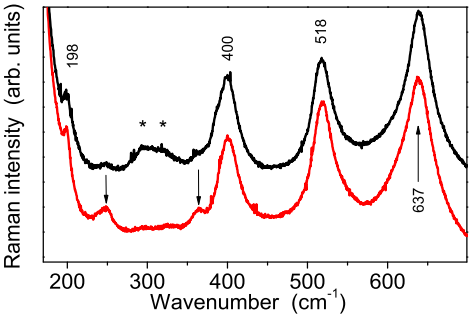

Figure 9. Experimental Raman spectra carried out in the low wavenumber region on S-TiO_2 nanopowder sample (red trace) and on nanocomposite membrane loaded by 7% *w*/*w* of S-TiO_2 (black trace). The two arrows indicate the TiO_2-B phase modes at about 250 and 310 cm^{-1}, respectively, while the pair of stars (*) labels the Nafion peaks at about 292 cm^{-1} (t(CF_2)) and 310 cm^{-1}, assigned to the t(CF_2) mode [25].

The FT-IR ATR spectra of pure and loaded Nafion show five main peaks (Figure 10), all related to Nafion membrane, at about 965, 983, 1060, 1153, and 1212 cm^{-1}, respectively. They turn out in good agreement with the assignments reported in the literature [31]. A small, but systematic, spectral difference is observed for all the loaded samples at about 1220 cm^{-1}.

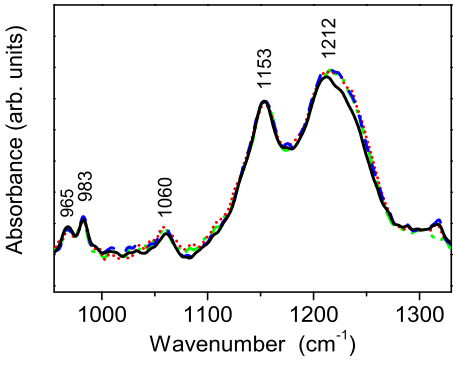

Figure 10. FT-IR ATR spectra of the pure Nafion (black line) and loaded composite *n*-TiO_2-S-N (*n* = 2, 5, 7) membranes showing small, but significant, differences in the spectral region near 1220 cm^{-1}. For the details refer to the text.

In principle the origin of the observed difference in the spectral shape in this region might be related either to a rearrangement of the Nafion local structure (and thus of its vibrational properties) due to the powder incorporation or, in alternative, to a contribution of the S-TiO_2 sulfate peak at 1224 cm^{-1}. However, in the latter case, one should expect to observe an additional change in the spectrum of the composite membrane near 1136 cm^{-1}, related to the sulfate peak observed in powders with intensity even higher than that of the peak at 1220 cm^{-1} (see Figure 6). Unfortunately, this is not the case, so the spectral change is likewise due to a change in the Nafion local structure within the composite membrane, thus suggesting an interaction effect between filler and Nafion.

3.4. Membrane Morphology Related Raman Mapping

Optical microscopy images of the composite membranes revealed the non-homogeneous nature of the systems on the micrometric scale. In fact, while pure Nafion looks homogenous, the filler distribution inside the Nafion membranes turns out to not be uniform independently of the incorporated amount since it originates morphologically, unlike regions inside the polymer matrix. Raman micro-spectroscopy allows for the analysis of the different micro-region in the membranes surface in order to probe the S-TiO_2 distribution. The results of this hand-made Raman mapping, carried out from the three investigated composite membrane, are cumulatively reported in Figure 11.

Raman spectra, displayed in the three middle panels of this composite figure, were taken step-by-step, moving along a straight line on the surface of the three composite samples, respectively, from the regions serially numbered in the top panels of the figure. The obtained spectra were fitted with Lorentzian curves in order to estimate the weight of each spectral component. Afterwards, the intensity (I) ratios between the membrane peak at about 731 cm^{-1} and each of the two S-TiO_2 peaks at about 639 and 518 cm^{-1}, respectively, were determined. The choice to exploit the area of two powder peaks, in order to derive the intensity ratios, allowed to obtain two independent checks of the fitting procedure validity. The results of this analysis revealed a quite sharp correspondence between the morphology characteristics of the composite membranes and their S-TiO_2 content, both the intensity ratios I_{639}/I_{731} and I_{518}/I_{731} showing the same behavior. In particular, for the two samples with higher filler content (5% and 7%) the brighter circular zones are richer in S-TiO_2, while the surrounding areas have a lower filler amount. In contrast, in the case of the membrane loaded with 2% of filler, the filler-dense regions look darker, due to a different image contrast. Moreover, it was possible to assess that in the case of 2-TiO_2-S a part of the membrane remained almost filler-free while, for the higher S-TiO_2 percentages, the filler was present in the whole membrane surface, although not homogeneously distributed.

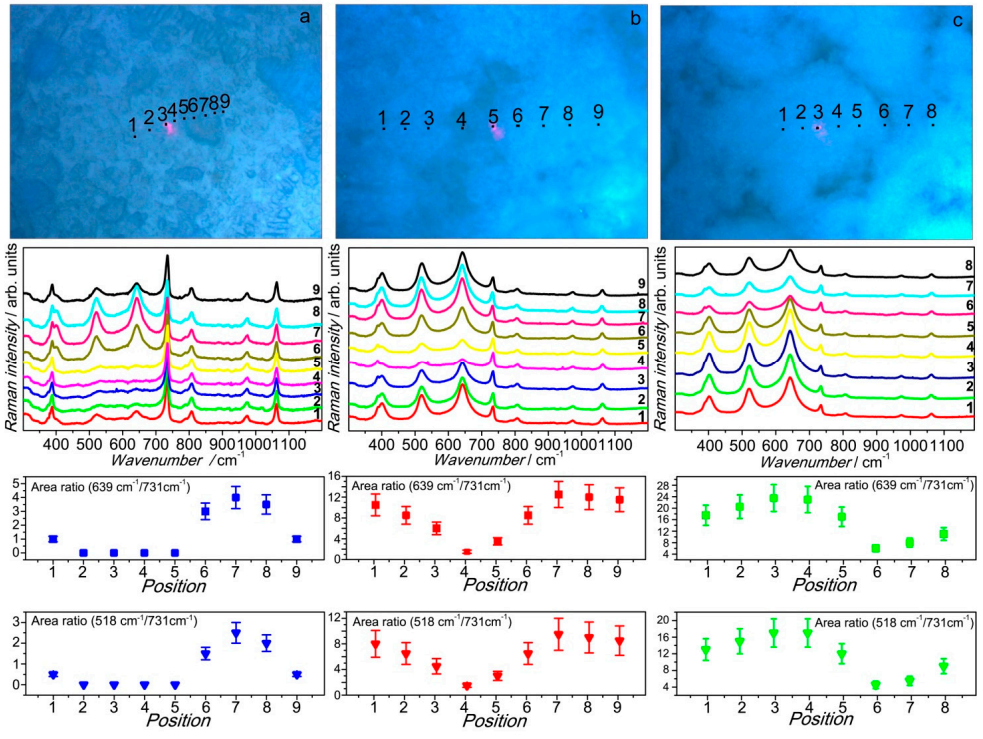

Figure 11. Raman mapping of the three composite membranes: 2-TiO_2-S (**a**) 5-TiO_2-S (**b**) and 7-TiO_2-S (**c**). For each sample, the upper panel shows the optical microscopy image, the middle one the Raman spectra in the different samples. The red spot observed in the optical images is the laser beam, whose size is of the order of 1 micron.

4. Conclusions

This paper presents and discusses the results of systematic investigations, carried out by means of a multi-techniques approach, on sulfated TiO_2 nano-powders synthesized via a novel one-step method and three composite Nafion-based membranes, obtained by the incorporation of different amounts of these S-TiO_2 powder. Both X-rays diffraction and Raman scattering measurements of sulfated nanopowders indicated the formation of an almost pure titania anatase phase with only a minor amount of TiO_2-B phase, typical of nanometric samples. TEM microscopy revealed that the powders obtained through the one-step synthesis are composed by spherical nanoparticles with an average dimension of about 8 nm and a very sharp size distribution. Moreover, vibrational spectroscopy (Raman scattering and FT-IR ATR) allowed the analysis of the sulfate functionalization of the nanopowders either as synthesized or after the exposure to water vapor. The powder

functionalization by sulfate groups was also confirmed by TGA analysis, and turn out to be still present even after a severe hydrothermal stability test. This is a crucial condition in order to exploit the use of the powder in presence of a high relative humidity environment, as it occurs in a working proton-conducting membrane fuel cell. The functionalization persistence was confirmed also after the S-TiO_2 incorporation inside the Nafion membrane. Evidence of an interaction effect between the filler and the host polymeric network was revealed by FTIR spectroscopy for each one of the filler percentages explored, with a partial rearrangement of the Nafion local structure due to the powder incorporation. The inclusion of the inorganic fillers during the recast procedure induces at microscopic level the formation of zones with different S-TiO_2 concentration inside the polymer matrix, although, at least for the case of 5% and 7% filler inclusion, sulfated titania seems to be present over the whole membrane surface. In the case of 2% S-TiO_2 membrane, the surface structure consists of filler-rich regions, in form of islands, separated by areas of almost pure Nafion. This structural arrangement does not easily provide any proton percolation path, which in contrast requires a continuous filler presence, as it occurs for membranes loaded with higher inclusion content. Therefore, if the percolation mechanism is the predominant way for protons to conduct, a higher resistance would be expected for the 2% membrane compared to the 5% and 7% ones. Future investigations will be focused on the membranes' electrochemical behavior, in the aim to verify this hypothesis and, possibly, highlight the influence of hydration on their conduction properties.

Acknowledgments: This work has been performed in the framework of the NAMEDPEM Project "Advanced nanocomposite membranes and innovative electrocatalysts for durable polymer electrolyte membrane fuel cells" (PRIN 2010-2011, project 2010CYTWAW), funded by the Italian MIUR (Ministry of Instruction, University and Research).

Author Contributions: Stefania Panero and Gino Mariotto conceived and designed the experiments; Sergio Brutti and Valentina Allodi performed the experiments (XRD, vibrational spectroscopies, electron microscopy); Valentina Allodi and Marco Giarola analyzed the data; Mirko Sgambetterra and Maria Assunta Navarra synthesized materials, prepared samples and took care of thermogravimetric analyses; Gino Mariotto, Stefania Panero, Sergio Brutti and Maria Assunta Navarra revised data analysis and discussion of results; Valentina Allodi and Gino Mariotto wrote the paper.

Conflicts of Interest: The authors declare no conflict of interest. The founding sponsors had no role in the design of the study; in the collection, analyses, or interpretation of data; in the writing of the manuscript, and in the decision to publish the results.

References

1. Giffin, G.A.; Piga, M.; Lavina, S.; Navarra, M.A.; D'Epifanio, A.; Scrosati, B.; di Noto, V. Characterization of sulfated-zirconia/Nafion composite membranes for proton exchange membrane fuel cells. *J. Power Sources* **2012**, *198*, 66–75.

2. Tominaka, S.; Akiyama, N.; Croce, F.; Momma, T.; Scrosati, B.; Osaka, T. Sulfated zirconia nanoparticles as a proton conductor for fuel cell electrodes. *J. Power Sources* **2008**, *185*, 656–663.
3. Navarra, M.A.; Croce, F.; Scrosati, B. New, high temperature superacid zirconia-doped Nafion™ composite membranes. *J. Mater. Chem.* **2007**, *17*, 3210–3215.
4. Scipioni, R.; Gazzoli, D.; Teocoli, F.; Palumbo, O.; Paolone, A.; Ibris, N.; Brutti, S.; Navarra, M.A. Preparation and characterization of nanocomposite polymer membranes containing functionalized SnO_2 additives. *Membranes* **2014**, *4*, 123–142.
5. Brutti, S.; Scipioni, R.; Navarra, M.A.; Panero, S.; Allodi, V.; Giarola, M.; Mariotto, G. SnO_2-Nafion® nanocomposite polymer electrolytes for fuel cell applications. *Int. J. Nanotechnol.* **2014**, *11*, 882–896.
6. Sgambetterra, M.; Panero, S.; Hassoun, J.; Navarra, M.A. Hybrid membranes based on sulfated titania nanoparticles as low cost proton conductors. *Ionics* **2013**, *19*, 1203–1206.
7. Colón, G.; Hidalgo, M.C.; Munuera, G.; Ferino, I.; Cutrufello, M.G.; Navío, J.A. Structural and surface approach to the enhanced photocatalytic activity of sulfated TiO_2 photocatalyst. *Appl. Catal. B* **2006**, *63*, 45–59.
8. Sakai, T.; Kajitani, S.; Hamagami, S.J.; Oda, H.; Matsuka, M.; Matsumoto, H.; Ishihara, T. Proton conduction properties of hydrous sulfated nano-titania synthesized by hydrolysis of titanyl sulfate. *Solid State Ionics* **2010**, *181*, 1746–1749.
9. Aslan, A.; Bozkurt, A. An investigation of proton conductivity of nanocomposite membranes based on sulfated nano-titania and polymer. *Solid State Ionics* **2013**, *239*, 21–27.
10. Nicotera, I.; Kosma, V.; Simari, C.; Ranieri, G.A.; Sgambetterra, M.; Panero, S.; Navarra, M.A. An NMR study on the molecular dynamic and exchange effects in composite Nafion/sulfated titania membranes for PEMFCs. *Int. J. Hydrogen. Energ.* **2015**, *40*, 14651–14660.
11. Krishnakumar, B.; Velmurugan, R.; Swaminathan, M. TiO_2-SO_4^{2-} as a novel solid acid catalyst for highly efficient, solvent free and easy synthesis of chalcones under microwave irradiation. *Catal. Commun.* **2011**, *12*, 375–379.
12. Larson, A.C.; Von Dreele, R.B. *General Structure Analysis System (GSAS)*; Los Alamos National Laboratory Report LAUR: Los Alamos, NM, USA, 1994.
13. Banfield, J.F.; Veblen, R. Conversion of perovskite to anatase and TiO_2(B): A TEM study and the use of fundamental building blocks for understanding relationships among the TiO_2 minerals. *Am. Miner.* **1992**, *77*, 545–557.
14. Young, R.A. *The Rietveld Method*; Oxford University Press: London, UK, 1993.
15. Cromer, D.T.; Herrington, K. The structures of anatase and rutile. *J. Am. Chem. Soc.* **1955**, *77*, 4708–4709.
16. Kavan, L.; Grätzel, M.; Gilbert, S.E.; Klemenz, C.; Scheel, H.J. Electrochemical and photoelectrochemical investigation of single-crystal anatase. *J. Am. Chem. Soc.* **1996**, *118*, 6716–6726.

17. Liu, Z.; Andreev, Y.; G. Armstrong, A.R.; Brutti, S.; Ren, Y.; Bruce, P.G. Nanostructured TiO_2(B): The effect of size and shape on anode properties for Li-ion batteries. *Progr. Nat. Sci.* **2013**, *23*, 235–244.
18. Beuvier, T.; Richard-Plouet, M.; Brohan, L. Accurate methods for quantifying the relative ratio of anatase and TiO_2(B) nanoparticles. *J. Phys. Chem. C* **2009**, *113*, 13703–13706.
19. Gentili, V.; Brutti, S.; Hardwick, L.J.; Armstrong, A.R.; Panero, S.; Bruce, P.G. Lithium insertion into anatase nanotubes. *Chem. Mater.* **2012**, *24*, 4468–4476.
20. Abramoff, M.D.; Magalhaes, P.J.; Ram, S.J. Image processing with Image. *J. Biophotonics. Int.* **2004**, *11*, 36–42.
21. Rasband, W.S. *Image J.*; National Institutes of Health: Bethesda, MD, USA, 1997.
22. Bersani, D.; Lottici, P.P.; Ding, X.-Z. Phonon confinement effects in the Raman scattering by TiO2 nanocrystals. *Appl. Phys. Letts* **1998**, *82*, 73–75.
23. Giarola, M.; Sanson, A.; Monti, F.; Mariotto, G.; Bettinelli, M.; Speghini, A.; Salviulo, G. Vibrational dynamics of anatase TiO_2: Polarized Raman spectroscopy and ab initio calculations. *Phys. Rev. B* **2010**, *81*.
24. Ben Yahia, M.; Lemoigno, F.; Beuvier, T.; Filhol, J.; Richard-Plouet, M.; Brohan, L.; Doublet, M.-L. Updated references for the structural, electronic, and vibrational properties of TiO_2(B) bulk using first-principles density functional theory calculations. *J. Chem. Phys.* **2009**, *130*, 204501.
25. Kobayashi, M.; Petrykin, V.V.; Kakihana, M. One-step synthesis of TiO_2(B) nanoparticles from a water-soluble titanium complex. *Chem. Mater.* **2007**, *19*, 5373–5376.
26. Nakamoto, K. Infrared and raman spectra of inorganic and coordination compounds. In *Handbook of Vibrational Spectroscopy*; J. Wiley&Sons: New York, NY, USA, 1986.
27. Arata, K.; Hino, M. Preparation of superacids by metal-oxides and their cathalitic action. *Mater. Chem. Phys.* **1990**, *26*, 213–237.
28. Bolis, V.; Magnavacca, G.; Cerrato, G.; Morterra, C. Surface heterogeneity on hydrophilic and hydrophobic silicas: Water and alcohols as probes for H-bonding and dispersion forces. *Langmuir* **1997**, *13*, 888–894.
29. Myhre, C.E.L.; Christensen, D.H.; Nicolaisen, F.M.; Nielsen, C.J. Spectroscopic study of aqueous H_2SO_4 at different temperatures and compositions: Variations in dissociation and optical properties. *J. Phys. Chem. A* **2003**, *107*, 1979–1991.
30. Gruger, A.; Régis, A.; Schmatko, T.; Colomban, P. Nanostructure of Nafion (R) membranes at different states of hydration—An IR and Raman study. *Vibr. Spectrosc.* **2001**, *26*, 215–225.
31. Kunimatsu, K.; Bae, B.; Miyatake, K.; Uchida, H.; Watanabe, M. ATR-FTIR study of water in Nafion membrane combined with proton conductivity measurements during hydration/dehydration cycle. *J. Phys. Chem. B* **2011**, *115*, 4315–4321.

MDPI AG
St. Alban-Anlage 66
4052 Basel, Switzerland
Tel. +41 61 683 77 34
Fax +41 61 302 89 18
http://www.mdpi.com

Polymers Editorial Office
E-mail: polymers@mdpi.com
http://www.mdpi.com/journal/polymers

MDPI AG
St. Alban-Anlage 66
4052 Basel
Switzerland

Tel: +41 61 683 77 34
Fax: +41 61 302 89 18

www.mdpi.com

ISBN 978-3-03842-293-8